



UNIVERSITAT POLITÈCNICA DE CATALUNYA
BARCELONATECH

Departament d'Enginyeria Electrònica

Fixed-Switching Frequency Sliding Mode Control Applied To Power Converters

*Thesis submitted in partial fulfillment of the
requirement for the PhD Degree issued by the
Universitat Politècnica de Catalunya, in its
Electronic Engineering Program.*

Víctor Repecho Del Corral

Advisor: Domingo Biel Solé

Barcelona, December 2017

Aknowlegdements

This thesis is the result of almost four years of intensive work, dedication and efforts. All the hours spent in the laboratory, the discussions around a blackboard or the realization of scientific articles have led to the present thesis, of which I am proud of. I would like to show my gratitude to all people that have helped and supported me during this exciting time, without whom the development of this thesis would not have been possible.

First of all, i would like to express my grateful thanks to my advisor Dr. Domingo Biel, who not only gave me the opportunity to become a part of the electronics and control laboratory in the University, but also have managed this thesis with dedication, effort and patience.

I feel truly grateful to Rafel Cardoner, for his valuable advices about power electronics implementations and micro controllers programming, which have been indispensable for the experimentation evaluations of this work. Many thanks also to Enric Miró for his help in the daily work at the laboratory.

I would like to express my gratitude towards Rafael Ramos, who provided me his knowledge about FGPA programming required in one of the experimental tests.

I am also grateful to the Advanced Control of Energy Systems (ACES) group, which have contributed to this work with the support of its research members. Specifically, i would like to show my gratitude to Josep María Olm, Antoni Arias, Enric Fossas, Robert Griñó and Arnau Dòria for their collaboration in several aspects of the thesis development.

Finally, i want to thank my girl Pili for her understanding and encouragement and, most of all, i would like to thank my family and specially my parents, Isidro and Daniela, to whom this thesis is dedicated.

Víctor Repecho del Corral,
Barcelona, January 2018

Abstract

The application of the sliding mode control in power converters has a well-known inconvenient from the practical point of view, which is to obtain fixed switching frequency implementations. This thesis deals with the development of a hysteresis band controller in charge of fixing the switching frequency of the sliding motions in power electronics applications. The proposed control measures the switching period of the control signal and modifies the hysteresis band of the comparator in order to regulate the switching frequency of the sliding motion. The proposed structure becomes in an additional control loop aside from the main control loop implementing the sliding mode controller. In the first part of the thesis, the switching frequency control system is modelled and a design criteria for the control parameters are derived for guaranteeing closed-loop stability, under different approaches and taking into account the most expectable working scenarios. In the second part of the thesis, the proposed strategies are validated in several power converters. Specifically, DC-to-DC and DC-to-AC power converters are assembled and the experimental results are shown. In this part, the procedures used for implementing the controllers are also deeply discussed.

Contents

| | |
|---|------------|
| Contents | vii |
| I Introduction and Problem Statement | 1 |
| 1 Introduction | 3 |
| 1.1 The switched power converters | 3 |
| 1.2 Control techniques in Switched Power Converters | 5 |
| 1.3 Ideal Sliding Motion | 7 |
| 1.4 Real Sliding Motion | 9 |
| 1.5 Proposed Solutions to the Variable Switching Frequency Problem | 11 |
| 1.5.1 Variable Hysteresis Band | 12 |
| 1.5.2 External Synchronization Signal | 12 |
| 1.5.3 Zero Average Dynamics | 13 |
| 1.5.4 PWM-Based SMC | 15 |
| 1.5.5 Additional Control Loop | 15 |
| 1.6 Thesis objectives | 16 |
| 1.7 Thesis structure | 18 |
| II Theoretical Analysis of the Proposed Solution and Study of the resulting Sliding Dynamics | 21 |
| 2 Modelling and stability analysis of the switching frequency control loop | 23 |
| 2.1 Open loop case: The fixed hysteresis band comparator | 23 |
| 2.2 Closed-loop case: A discrete-time modelling. | 25 |
| 2.2.1 The regulation case | 27 |
| 2.2.2 The tracking case | 29 |
| 2.3 Closed-loop case: A continuous-time modelling. | 34 |
| 3 A case of study: SFC design and simulation results | 39 |
| 3.1 Design of the sliding mode controller | 39 |
| 3.2 The regulation case in the discrete-time approach | 41 |

| | | |
|------------|--|-----------|
| 3.3 | The regulation case in the continuous-time approach | 43 |
| 3.4 | The tracking case | 46 |
| 4 | Real sliding dynamics in a switching frequency control loop | 53 |
| 4.1 | The regular form approach | 54 |
| 4.2 | Fixed hysteresis band | 56 |
| 4.3 | Case study: the Buck converter | 59 |
| 4.3.1 | Mathematical model | 59 |
| 4.3.2 | Simulation results | 60 |
| 4.4 | Time-varying hysteresis band | 64 |
| 4.4.1 | The regulation case | 64 |
| 4.4.2 | The tracking case | 68 |
| 4.4.3 | Simulation results | 70 |
| III | Application of the Proposed Solution to Power Converters. | 77 |
| 5 | Voltage Regulation in a Buck Converter. | 79 |
| 5.1 | The Buck Converter | 79 |
| 5.2 | Sliding mode control of the Output voltage | 80 |
| 5.2.1 | Switching surface design | 80 |
| 5.2.2 | Sliding dynamics | 81 |
| 5.2.3 | Control law | 82 |
| 5.3 | Switching frequency regulation | 82 |
| 5.3.1 | Evaluation of ρ_k^\pm | 82 |
| 5.3.2 | SFC design | 83 |
| 5.4 | Implementation Details | 83 |
| 5.5 | Experimental results | 86 |
| 5.6 | Conclusions | 92 |
| 6 | Voltage Regulation in a Multiphase Buck Converter. | 93 |
| 6.1 | The multiphase converter | 93 |
| 6.2 | Interleaved sliding mode control of the output voltage | 95 |
| 6.2.1 | Master switching surface design | 95 |
| 6.2.2 | Sliding dynamics of the Master phase | 96 |
| 6.2.3 | Master phase control law | 97 |
| 6.2.4 | Slaves switching surfaces design. Interleaved Sliding Mode | 97 |
| 6.3 | Switching frequency regulation | 98 |
| 6.3.1 | Evaluation of ρ_k^\pm | 98 |
| 6.3.2 | SFC design | 99 |
| 6.4 | Implementation Details | 100 |
| 6.5 | Experimental results | 102 |
| 6.6 | Conclusions | 108 |

| | |
|--|------------|
| 7 Voltage Regulation in a Boost Converter. | 109 |
| 7.1 The Boost Converter | 109 |
| 7.2 Sliding mode control of the output voltage | 110 |
| 7.2.1 Switching surface design | 110 |
| 7.2.2 Sliding dynamics | 111 |
| 7.2.3 Control law | 113 |
| 7.3 Switching frequency regulation | 113 |
| 7.3.1 Evaluation of ρ_k^\pm | 113 |
| 7.3.2 SFC design | 113 |
| 7.4 Implementation Details | 114 |
| 7.5 Experimental results | 116 |
| 7.6 Conclusions | 120 |
| | |
| 8 Voltage Tracking in a Voltage Source Inverter. | 121 |
| 8.1 The voltage source inverter | 121 |
| 8.2 Sliding mode tracking of the output voltage | 123 |
| 8.2.1 Switching surface design | 123 |
| 8.2.2 Ideal sliding dynamics | 126 |
| 8.2.3 Control law | 127 |
| 8.2.4 Sliding dynamics for pure resistive load | 127 |
| 8.2.5 Sliding dynamics for reactive linear load | 131 |
| 8.2.6 Sliding dynamics for nonlinear load | 134 |
| 8.3 Switching frequency regulation | 139 |
| 8.4 Implementation details | 141 |
| 8.4.1 Effects of the hysteresis comparator discretization | 141 |
| 8.4.2 Digital emulation of the ideal hysteresis comparator | 143 |
| 8.4.3 Switching function digitalization issues | 145 |
| 8.4.4 Digital emulation of the SFC for a tracking control task | 146 |
| 8.4.5 Estimation of switching function slopes | 147 |
| 8.4.6 Controller implementation | 149 |
| 8.4.7 Assembled converter and devices employed | 150 |
| 8.5 Experimentation results | 152 |
| 8.5.1 SFC performance | 152 |
| 8.5.2 SMC performance | 154 |
| 8.5.3 Nonlinear load test | 159 |
| 8.6 Conclusions | 161 |

| | | |
|-----------|---|------------|
| IV | Conclusions and Future Research. | 163 |
| 9 | Conclusions and Future Research. | 165 |
| 9.1 | Conclusions | 165 |
| 9.1.1 | Theoretical analysis of the proposed solution and study of the resulting sliding dynamics | 166 |
| 9.1.2 | Application of the proposed solution to power converters. | 167 |
| 9.2 | Future research | 168 |
| 9.2.1 | Open problems in the theoretical part | 168 |
| 9.2.2 | Open problems in the application part | 169 |
| | Bibliography | 170 |

Part I

Introduction and Problem Statement

Chapter 1

Introduction

1.1 The switched power converters

The energy conversion systems have played a key role in the technological development in the recent years. All the energy sources that currently exist such as oil, gas, nuclear or renewable (solar, hydropower, wind power, etc.) require some level of transformation in order to generate and distribute the electrical energy through the alternate current (AC) grid. The energy distribution system is based on AC since it allows the employment of electrical transformers for voltage conversions, being simple to adequate the voltage levels with a very good efficiency. The aforementioned energy sources can generate electricity by different ways. Mostly, the power plants are based on turbines connected to an AC generator which directly injects the energy to the AC grid (this is the case for power plants of fossil fuels, nuclear energy, hydropower or wind power). Alternatively, the photovoltaic power plants generate direct current (DC), that requires to be converted to AC for being injected to the grid through a DC/AC converter. Besides, some energy systems as wind turbines generate AC that cannot be directly injected to the grid due to the different frequency they produce, requiring an AC/AC conversion.

The necessity of power conversion is not only present in the generation and distribution stage, but also in the final consumption stage. Both for industrial or domestic use, a lot of equipment work with DC and require an AC/DC conversion when consume energy from the grid. In all households can be found a lot of systems like TV, PC or different appliances that include AC/DC converters. Even such systems include more than one converter, using a main AC/DC converter firstly, and several DC/DC converters to supply different subsystems. Generally speaking, the power conversion is required in everywhere: transport, industrial, communication, residential, etc.

A power conversion process scheme is depicted in Figure 1.1. The desirable scenario would be a conversion with no losses, in the sense that all the input power of the conversion process is successfully delivered at the output. Unfortunately, this is not physically realizable. Indeed, one of the most important characteristic of the power converters is its energy efficiency. The energy costs money and if the power conversion wastes energy, then wastes

money as well. Not only the cost is the inconvenient, the lost energy produces heat, and if this heat is not properly dissipated, it can incur in a reduction of the system reliability and life time. Initially, the first developed power supplies were based on linear structures [1], but the excessive power losses limited their use. Those linear structures use transistors working in the active zone, being the voltage-current product different from zero in all the cases, leading to the aforementioned low efficiency.

The switched power converters [2–4] have the capability to transform the energy with a good efficiency. Their operation is based on to control, at high frequency, transistors acting as switches (with only two possible states, open or closed), where ideally the voltage-current product always remains null. Together with the transistors, the switched power converters include reactive elements as inductors and capacitors. These elements do not dissipate active power (from an ideal point of view) providing the possibility to perform the power conversion with low power losses (ideally speaking, without losses). Although neither the transistors can operate as ideal switches nor the reactive components do not dissipate power, the achievable efficiencies are really high. Nowadays, the good efficiency of the switched power converters have become predominant their utilization in the energy conversion field.

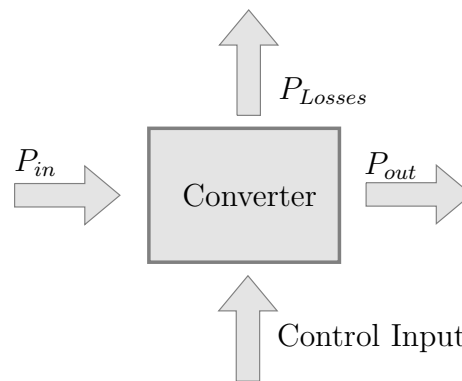


Figure 1.1: Power conversion scheme.

A design key point of the switched power converters is their operation switching frequency. As it was introduced previously, the transistors work as switches, commutating between two states at high frequency. In general, to increase the switching frequency leads to a smaller reactive components, which, in turn, reduces the size, weight and cost of the converter. As a consequence, the switching frequency has to be fixed as high as possible. In fact, the switching frequency of a power converter is usually limited by the switching transistors. These devices are selected according to the converter voltage and current levels, their maximum switching frequency and their conduction and switching losses. Once the switching elements have been selected, the converter switching frequency is accordingly defined.

With a given switching frequency, the rest of the converter elements can be optimized. Mainly the design of the capacitors and the inductors can be optimized in order to pro-

duce low losses at the working switching frequency, since the current and voltage ripples are totally determined. Even the copper wires, circuit board, power connections and used transistors drivers have implications with respect to the working switching frequency. Besides, the converters sometimes include line filters, which are also designed for a known switching frequency. Therefore, for operating a power converter with a different switching frequency than the one it was designed for can incur in a loss of efficiency, a noise increment and even a converter malfunctioning. Therefore, it is clear the relevance of keep the switching frequency fixed.

1.2 Control techniques in Switched Power Converters

As systems exposed to disturbances, the switched power converters require controllers in order to suitably perform their tasks. For instance, an AC/DC power converter connected to the grid have to regulate a DC output voltage in order to supply a specific load. Such regulation has to be robust with respect to variations in the grid voltage and also to the supplied load in the DC side, which could suffer variations in the power consumption. Another example where the inclusion of a control system is required could be a DC/AC converter injecting energy from a photovoltaic installation to the AC grid, where the power generation is variant, and the synchronization with the grid frequency is essential.

The most common control technique used in the switched power converters is the linear control theory [5,6]. This control can be applied to power converters through a pulse width modulation (PWM), which in turn imposes a fixed switching frequency. The Figure 1.2 shows the PWM modulation idea. The power transistors have to be driven by a digital waveform, u , with two possible discrete states, which will be the control signal, in order to act them as switches. The PWM modulation will generate this control input using a sawtooth signal, f_c , known as carrier signal, that fixes the switching frequency, and a modulation signal, which corresponds to the average values of the control input, d , known as duty cycle. The duty cycle can be considered a continuous-time signal, since it does not have discontinuities as the real control signal has. Such consideration is the basis for the application of linear control theory to the power converters.

In general, the converters can be described in the state space as bilinear systems, with discontinuities in the right-hand side. The discontinuities are produced by the transistors control inputs, u . In order to remove the discontinuity from the equations, an averaged state space modelling is performed, substituting such discontinuous signal by the corresponding duty cycles, d . As a consequence, the resulting state space vector of the averaged models does not include high frequency ripples. Moreover, very often, an additional small signal analysis is required in order to get linear models, which restricts the expected dynamics to specific working conditions. This strategy is the most popular technique for controlling power converters, where the desired performance is in general achieved using a linearized model, and the duty cycle is generated by a linear controller. In [2] can be found such procedures, together with the resulting transfer functions for the most popular DC/DC converters.

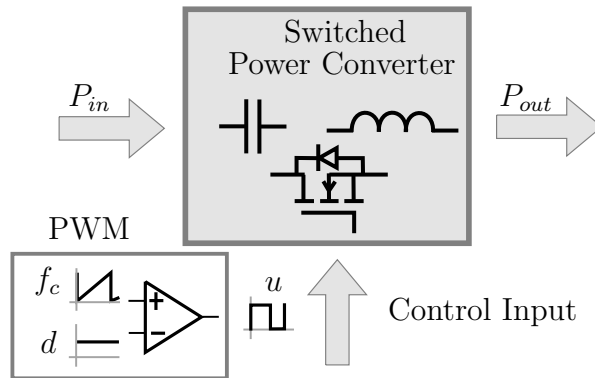


Figure 1.2: Switched power converter scheme, where the real control input, u , and the averaged control input, d , are depicted.

For most of the applications, the PWM-based linear control theory is enough to provide a desirable performance in the systems, but, for specific applications, a different control technique could be necessary. Mainly, the drawbacks of the PWM-based linear control techniques come from the used linearized model. Since the considered models for the controllers design are local, when the power converter moves away from the nominal conditions the performance can be compromised. Additionally, the averaged models assume known the elements affecting the systems dynamics as inductors and capacitors. Whatever drift in these values from the nominal ones can also negatively affect the control performance. The Sliding Mode Control (SMC) [7] constitutes an alternative to the classical PWM-based linear controllers. This methodology, which can be classified as a nonlinear control technique [8,9], provides benefits to the power converters control. Besides the well-known robustness, the order reduction and a fast transient response, the first order SMC uses as control outputs non-continuous signals with two allowable states, which perfectly matches with the physical structure of the power converters, transistors acting as switches. Moreover, the methodology works with the system state space equations without linearization process, and as a consequence, the provided stability conditions are, in general, more global. Of course, it exists an important inconvenient that historically has limited its practical application: how to achieve a bounded switching frequency of operation.

This chapter briefly introduces the main idea of the sliding mode control theory. This analysis not only help us to demonstrate that in a real application the switching frequency under sliding motion becomes variable but also to justify the basis of the new proposal in order to get a fixed switching frequency. Finally, a short list of the proposed approaches for solving this inconvenient found in the literature until now is reviewed.

1.3 Ideal Sliding Motion

First of all, an affine nonlinear system is considered

$$\dot{x} = f(x) + g(x)u \quad (1.1)$$

where the control signal u takes values from a discrete set with two values $\{u^-, u^+\}$. The state space equation matches with whatever switched power converter with a single control input. Indeed, such equation could represent arbitrary systems, not only power converters.

The basis of the SMC is to design a switching function, $\sigma(x)$, which depends on the state vector, and enforces this function to be in a state space region where the desired system dynamics is achieved, in general $\sigma(x) = 0$. The most simple switching function definition is $\sigma(x) = e_x$, where $e_x = x^* - x$ is the tracking error, being x^* the desired value of the state space vector. It is immediate to demonstrate that if the control guarantees that $\sigma(x) = 0$, the desired and real state space vector are equal. Therefore, the control objective is to ensure that the function $\sigma(x) = x^* - x$ always converges to the space region defined by $\sigma(x) = 0$. This condition is satisfied when

$$\dot{\sigma}(x)\sigma(x) < 0 \quad (1.2)$$

is fulfilled.

The previous consideration can be proved just taking the *Lyapunov* function candidate $V(x) = 0.5\sigma(x)^2$, where the first time derivative yields $\dot{V}(x) = \dot{\sigma}(x)\sigma(x)$. As the function $V(x) = 0.5\sigma(x)^2$ fulfils all the conditions to be a *Lyapunov* function [8], the condition defined in (1.2) is enough to ensure that $\sigma(x) = 0$ is an attractive region for $\sigma(x)$. When the switching function $\sigma(x)$ is on the desired switching surface $\sigma(x) = 0$, it is called that the system is under sliding motion.

Nevertheless, according to the system relative degree [7], the construction of the surface may include higher orders elements of the tracking error. It is simple to figure out that the way to impose the condition $\dot{\sigma}(x)\sigma(x) < 0$ will be through $\dot{\sigma}(x)$, since $\sigma(x)$ does not depend on control. In other words, in order to enforce sliding motion on $\sigma(x) = 0$, the control action, u , has to appear in $\dot{\sigma}(x)$. The equation (1.3) shows the case where the switching function includes the tracking error and its first time derivative

$$\sigma(x) = \phi_1 e_x + \phi_2 \dot{e}_x \quad (1.3)$$

where ϕ_1, ϕ_2 are strictly positive constants. In the initial case, where $\sigma(x) = e_x$, when the system is under sliding motion automatically implies that $e_x = 0$ and x tracks x^* without dynamics. This fact does not happen for the switching function defined in (1.3), since, when the switching function is on the surface $\sigma(x) = 0$, the following first order linear differential equation governs the error dynamics:

$$\phi_1 e_x + \phi_2 \dot{e}_x = 0 \quad (1.4)$$

which has $e_x = 0$ as unique asymptotically stable equilibrium point. Therefore, it is clear that the error dynamics under sliding motion will be determined by the selected switching surface. Regardless of the switching function order, the control law of u has to ensure that condition (1.2) always holds. The previous condition will be guaranteed by a discontinuous control law, taking the available discrete values, previously defined (u^+ and u^-). It is very common to use a sign function as the control, since this function generates the values 1 or -1, which match with values for u^+ and u^- for several converters. In general, the control law will be of the form

$$u = \text{sign}(\sigma(x)) \quad (1.5)$$

where the function $\text{sign}()$ provides 1 when $\sigma \geq 0$ and -1 when $\sigma < 0$. Nevertheless, some converters have control input states that do not correspond to 1 or -1, being for instance 1 or 0. In these cases, the control law will be modified accordingly. In any case, since u is discontinuous, from a theoretical point of view, this signal will switch at infinite switching frequency when $\sigma(x)$ is zero. This assumption allows to analyse the ideal sliding dynamics, since at infinite switching frequency the switching function will be placed exactly on $\sigma(x) = 0$. Studying the ideal sliding dynamics is the process to derive the dynamics of the system defined in (1.1) with the dynamics imposed by $\sigma(x) = 0$. This task can be carried out using the equivalent control method proposed by Professor Vadim Utkin [7]. The equivalent control, u_{eq} , is defined as the solution of the equations

$$\sigma = 0, \quad \dot{\sigma}(x, u_{eq}) = 0. \quad (1.6)$$

Taking as switching function an expression depending on the error, $e_x = x - x^*$, as:

$$\sigma(x) = \mu(e_x), \quad (1.7)$$

the switching function first time derivative is found as:

$$\dot{\sigma}(x) = \frac{\partial \sigma(x)}{\partial x} f(x) + \frac{\partial \sigma(x)}{\partial x} g(x)u. \quad (1.8)$$

According to (1.6), the equivalent control can be obtained solving the equation

$$0 = \frac{\partial \sigma(x)}{\partial x} f(x) + \frac{\partial \sigma(x)}{\partial x} g(x)u_{eq}, \quad (1.9)$$

which yields

$$u_{eq} = - \left[\frac{\partial \sigma(x)}{\partial x} g(x) \right]^{-1} \frac{\partial \sigma(x)}{\partial x} f(x). \quad (1.10)$$

Notice that (1.10) implies a continuous-time solution, which u cannot attain. Finally, u is replaced by u_{eq} in (1.1) in order to find the ideal sliding dynamics. Placing (1.10) into (1.1), one gets:

$$\dot{x} = f(x) + g(x)u_{eq}. \quad (1.11)$$

Furthermore, according to [7], the space region where the sliding motion occurs, which is called sliding domain, is characterized by the inequality

$$u^- < u_{eq}(x, t) < u^+. \quad (1.12)$$

1.4 Real Sliding Motion

The real sliding motion can be understood as the system dynamics that arises when the control action, u , is forced to operate at finite switching frequency. The employment of a sign function in real systems leads to a finite switching frequency, due to unmodelled dynamics and delays. However, this switching frequency can be too high for some systems, like power converters. Substitute the sign function on (1.5) by a comparator with hysteresis, allows to bound the switching frequency. The control law, therefore, will be of the form:

$$u = \begin{cases} u^+ & \text{if } \sigma < -\Delta, \\ u^- & \text{if } \sigma > \Delta, \end{cases} \quad (1.13)$$

being Δ the hysteresis width. This approach can be found in sliding mode control literature in order to study the real sliding dynamics [10–12]. From a rigorous point of view, the previous control law is not defined within the hysteresis bands, so an alternative expression can be used instead:

$$u = \begin{cases} u^+ & \text{if } \sigma < -\Delta \quad \text{or } (|\sigma| < \Delta \ \& \ \dot{\sigma} > 0) \\ u^- & \text{if } \sigma > \Delta \quad \text{or } (|\sigma| < \Delta \ \& \ \dot{\sigma} < 0). \end{cases} \quad (1.14)$$

The different behaviour of the system trajectories on the phase plane can be observed in Figure 1.3.

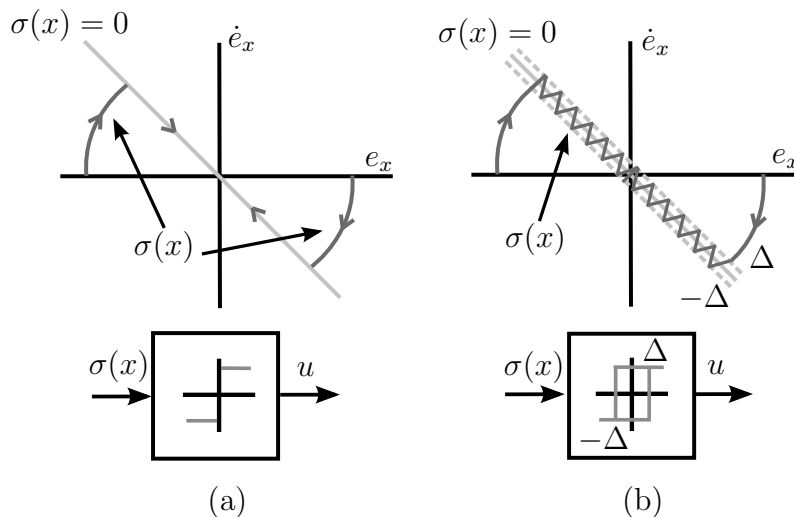


Figure 1.3: Phase plane system trajectories. (a) Ideal sliding motion. (b) Real sliding motion within a boundary layer Δ .

As Figure 1.3 shows in the right side, the real switching function, $\sigma(x)$, is not on the sliding surface, $\sigma = 0$, but chatters in its vicinity. In this scenario, the condition $|\sigma(x)| < \Delta$ holds. It is a designer task to keep the hysteresis band value small enough, in the way that this dynamics can be neglected with respect to the low frequency dynamics, determined by the equivalent control. Analysing the high frequency dynamics of $\sigma(x)$ provides the expression that allows to study and control the switching frequency of the control action. A good approach consists in defining the control action as a continuous low frequency component, which is u_{eq} , plus a high frequency component, u_{hf} , which takes values in the set $\{u^-, u^+\}$.

$$u = u_{eq} + u_{hf} \quad (1.15)$$

Let us just combine the expressions (1.15) and (1.8).

$$\dot{\sigma}(x) = \frac{\partial \sigma(x)}{\partial x} f(x) + \frac{\partial \sigma(x)}{\partial x} g(x) u_{eq} + \frac{\partial \sigma(x)}{\partial x} g(x) u_{hf} \quad (1.16)$$

By definition, $\dot{\sigma}(x, u_{eq}) = 0$, therefore

$$\dot{\sigma}(x) = \frac{\partial \sigma(x)}{\partial x} g(x) u_{hf} \quad (1.17)$$

The motion of $\sigma(x)$ in the vicinity of $\sigma(x) = 0$ is governed by (1.17). From this expression it is clear that this dynamics depends on the system. Of course, the dynamics of the state space vector can be also stated as:

$$\dot{x} = f(x) + g(x) u_{eq} + g(x) \left[\frac{\partial \sigma(x)}{\partial x} g(x) \right]^{-1} \dot{\sigma}(x). \quad (1.18)$$

The switching function trajectories within the hysteresis band are governed by the last term of the right hand side of equation (1.18). Figure 1.4 depicts the expected behaviour.

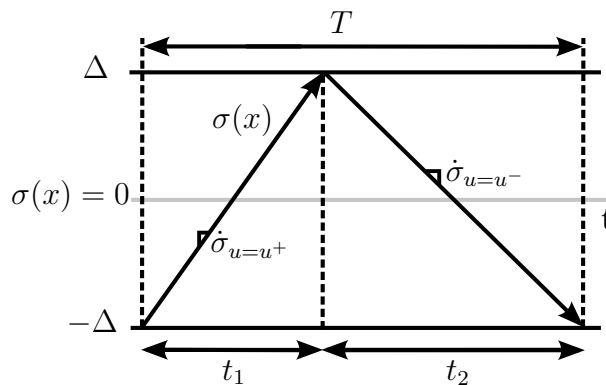


Figure 1.4: Switching function behaviour within the hysteresis band in the vicinity of $\sigma(x) = 0$.

From Figure 1.4 the switching period of the control action is derived:

$$T = t_1 + t_2 = \frac{2\Delta}{\dot{\sigma}_{u=u^+}} - \frac{2\Delta}{\dot{\sigma}_{u=u^-}} \quad (1.19)$$

Expression (1.19) can be written in different ways. One interesting approach is to formulate it as a function of the equivalent control. Recalling (1.15) and (1.17), one gets:

$$\dot{\sigma}(x) = \frac{\partial\sigma(x)}{\partial x} g(x)(u - u_{eq}) \quad (1.20)$$

and, therefore, assuming that $u^+ = 1$ and $u^- = -1$, (1.19) boils down to

$$T = 4\Delta \left[\frac{1}{(1 - u_{eq}^2)} \right] \left[\frac{\partial\sigma(x)}{\partial x} g(x) \right]^{-1}. \quad (1.21)$$

Notice that from (1.21) the hysteresis band of the comparator can be calculated as a function of the equivalent control and the desired switching period, T^* , as:

$$\Delta = \frac{\partial\sigma(x)}{\partial x} g(x) \frac{T^*}{4} (1 - u_{eq}^2). \quad (1.22)$$

However, this approach has an important limitation, which will be discussed later. Moreover, expression (1.21) confirms the well-known problem of the SMC applied to switched power converters, the switching frequency is variable and system dependent, as (1.21) states.

A very important aspect should be remarked at this point. In the previous methodology, it has been assumed that the slopes of $\sigma(x)$ remain constant along the switching interval, that is $\ddot{\sigma}(x) = 0$. This is a very reasonable assumption that is often taken in the sliding mode control literature [11, 13, 14]. The basis of this hypothesis relies in consider the switching period of the control action small enough with respect to the system time constants. If this consideration holds, it is reasonable to assume that the switching function slopes are locally constant during a switching interval. Indeed, the switching frequency in the power converters are designed as high as possible, due to the reason introduced in Section 1.1, which perfectly fits with this assumption.

1.5 Proposed Solutions to the Variable Switching Frequency Problem

At this stage, some solutions proposed in the literature in order to set the switching frequency in the power converters under SMC are reviewed.

1.5.1 Variable Hysteresis Band

An intuitive solution is to adjust the comparator hysteresis band using the expression (1.22), modifying its level in accordance with the system state. Such approach has been proposed by different authors [15–21]. An equivalent scheme is depicted in Figure 1.5.

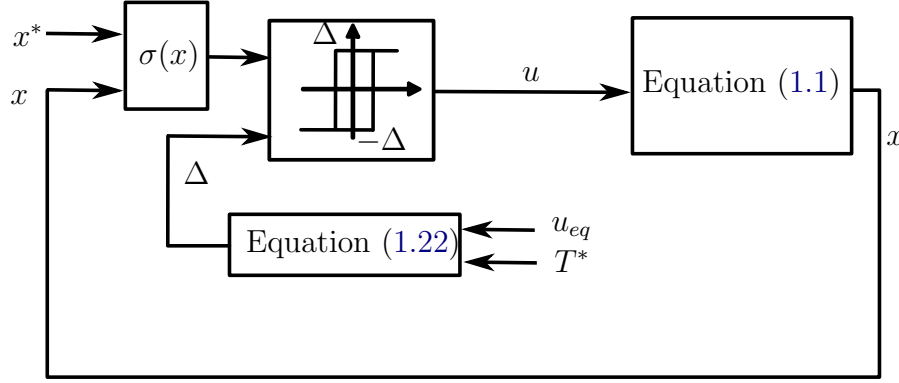


Figure 1.5: System for operating at fixed switching period under sliding motion based on a variable hysteresis band.

From Figure 1.5, and as equation (1.22) shows, the hysteresis computation requires a high level of the plant knowledge since the term

$$\frac{\partial \sigma(x)}{\partial x} g(x)$$

should be known. Furthermore, the measurement of the equivalent control or, alternatively, its estimation based on expression (1.10) should be also performed, which entails an evident complexity.

The procedure provides good results in general, although it is difficult to achieve the desired switching frequency accurately, due to the complexity for generating the hysteresis. This complexity is, in fact, its main drawback. Additionally, it is evident that if in the hysteresis calculation some system parameters are assumed known and constant, the system will not be robust in the face of parametric variations. In order to improve the robustness, additional sensors and/or observers have to be included to get a proper adaptation of the hysteresis band amplitude, leading to a further system complexity, decreasing the reliability and increasing the cost up to unmanageable levels.

1.5.2 External Synchronization Signal

Fixed switching frequency can also be achieved by using an external signal to force the switching instants [22, 23]. The idea is sketched at Figure 1.6, specifically in the left side. The synchronization signal, $D(t)$, is added to the switching function in the way that such signal controls the switching events. As it is depicted in the Figure, the peak values of signal $D(t)$ should be higher than the hysteresis values, Δ , as $D(t)$ can control the

switching events. Through a complicated tuning process, it is possible to adjust the signal $D(t)$ fixing the switching frequency of the control action. However this process is extremely sensitive, and it is usual that steady-state errors appear in the system when the working conditions change. The right part of Figure 1.6 tries to show this phenomenon. Notice how the switching function (grey lines) does not reach the upper bound of the hysteresis band, entailing an average value different from zero of $\sigma(x)$, leading to the aforementioned steady-state error.

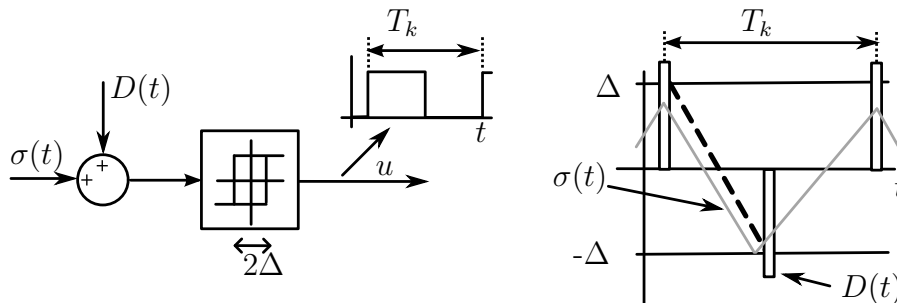


Figure 1.6: External Signal Synchronization scheme for a fixed frequency sliding mode control.

Moreover, this approach needs some additional hardware on the controller in order to generate the synchronization signal. As a consequence, the usage of this method is, in general, not recommended.

1.5.3 Zero Average Dynamics

As it was introduced in the previous Section, and noted in different works available in the literature, a switching function describing piecewise linear behaviour within a symmetric hysteresis band comparator implies that its average value, along the switching interval, is zero. This is the concept exploited by the Zero Average Dynamics (ZAD), which was presented in [24]. The method computes a duty cycle that guarantees zero T -periodic mean value of the switching function, with T denoting the switching period. The Figure 1.7 shows this idea.

From the Figure, it is possible to develop the formulation delivering the duty cycle to be used in the next switching interval that leads to a zero averaged value of $\sigma(x)$. The results are shown in Table 1.1.

Therefore, fixed switching frequency is reached in the steady-state, and the averaged behaviour is close to the ideal sliding mode one. The ZAD strategy has been successfully implemented in [25]. The results presented therein show a good performance of the ZAD, but also point out the requirement of a fast digital processor to solve the complex calculations involved in the duty cycle computation, as expressions in Table 1.1 corroborate. In fact, such computation complexity constitutes the main drawback of ZAD-based SMC fixed switching frequency implementations.

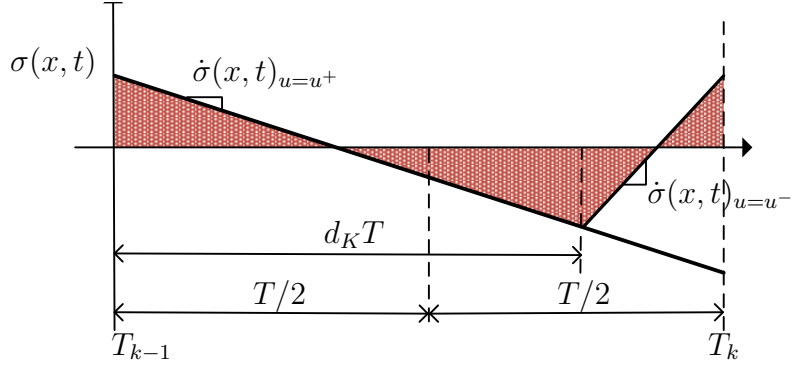


Figure 1.7: Zero Average Dynamics trajectories detail.

Table 1.1: Zero Average Dynamics control action formulas

| | |
|---|--|
| $\sigma(x(T_k), T_k)$ and $\sigma(x(T_k), T_k) + \frac{T}{2}\dot{\sigma} _{k,u^+} \geq 0$ | $u(T_k) = u^+; d_k = 1$ |
| $\sigma(x(T_k), T_k)$ and $\sigma(x(T_k), T_k) + \frac{T}{2}\dot{\sigma} _{k,u^+} < 0$ | $u(T_k) = u^+; d_k = 1 - \sqrt{\frac{ \dot{\sigma} _{(K,u^+)} - 2\frac{ \sigma[x(T_k), T_k] }{T}}{ \dot{\sigma} _{(K,u^+)} + \dot{\sigma} _{(K,u^-)}}}$ |
| $\sigma(x(T_k), T_k)$ and $\sigma(x(T_k), T_k) + \frac{T}{2}\dot{\sigma} _{k,u^+} \leq 0$ | $u(T_k) = u^-; d_k = 1$ |
| $\sigma(x(T_k), T_k)$ and $\sigma(x(T_k), T_k) + \frac{T}{2}\dot{\sigma} _{k,u^+} > 0$ | $u(T_k) = u^-; d_k = 1 - \sqrt{\frac{ \dot{\sigma} _{(K,u^+)} - 2\frac{ \sigma[x(T_k), T_k] }{T}}{ \dot{\sigma} _{(K,u^+)} + \dot{\sigma} _{(K,u^-)}}}$ |

1.5.4 PWM-Based SMC

This proposal is based on the use of PWM at fixed switching frequency to implement the so-called PWM-SMC. Initially proposed in [26, 27], the method directly implements the equivalent control and obtains the switching instants by comparing the equivalent control with the fixed frequency sawtooth waveform at the PWM. The method is equivalent to the traditional PWM implementation according to a linear controller design, but using the equivalent control u_{eq} instead of the duty cycle provided by the linear controller. The corresponding scheme is depicted in Figure 1.8.

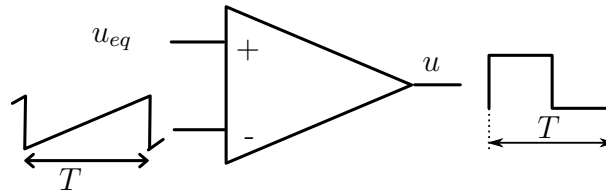


Figure 1.8: PWM-based sliding mode controller.

It should be noted that the expression for the equivalent control depends on the system state and on its parameters for a given working conditions, as (1.10) states. It is important to notice that this equation holds from the ideal point of view.

The results presented in [28] show overall good performance, but it should be highlighted that the same solution can also be derived by calculating the required duty cycle to obtain the desired system dynamics. Indeed, from our point of view, the equivalent control is more a theoretical concept than a practical method. From its definition, the equivalent control is the continuous control action that places the system trajectories exactly on the sliding surface. In a practical implementation, this includes whatever unmodelled dynamics, delays and uncertainties in the power converter. Besides, power converters commonly suffer external disturbances, which generally can only be bounded. In other words, there is no way to determine the equivalent control a priori. The equivalent control could be measured low pass filtering the hysteretic control action enforcing sliding motion in a certain switching surface ($|\sigma(x)| < \Delta$), but not vice versa. Hence, equation (1.10) should be used only for theoretical issues. Moreover, in this method, some sliding mode properties, such as order reduction or robustness in the face of disturbances, could be lost.

1.5.5 Additional Control Loop

Hysteretic controllers are often applied to power converters without using SMC theory. However, like occur in SMC approaches, the switching frequency becomes variable. Indeed, in most of the hysteretic controllers, sliding motion naturally occurs. Under this research field, some interesting solutions in order to fix the switching frequency were provided [29–32]. These proposals are based on adding an additional loop in order to properly adjust the hysteresis band, as Figure 1.9 shows. The system uses a period sensor or a

switching frequency sensor, generating an outer loop in charge of adjusting the hysteresis band of the comparator.

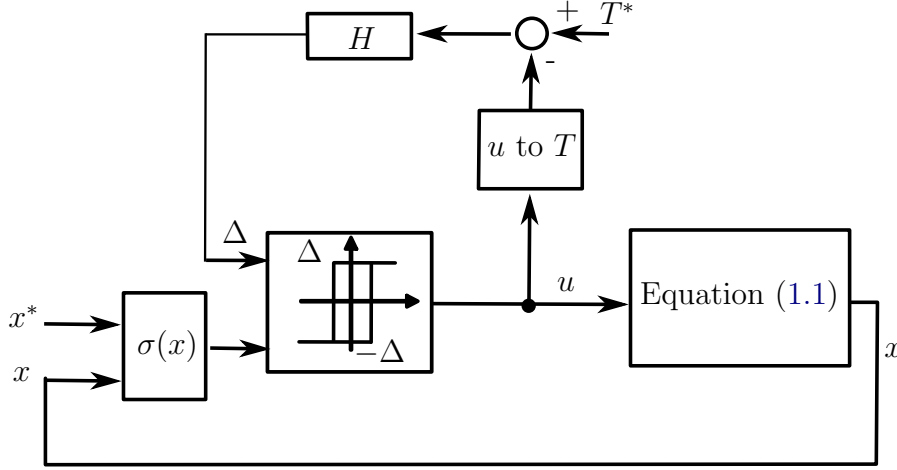


Figure 1.9: Closed loop regulation of the hysteresis band.

However, in the works previously cited, the additional loop analysis was not deeply treated, being the stability conditions only useful under strict conditions. Generally, the loop is tuned with extremely slow dynamics, and such loop behaviour is not related with the main system. Moreover, the problem has been addressed exclusively from a regulation point of view, not dealing with the tracking problem scenario.

1.6 Thesis objectives

This thesis proposes a solution to solve the problem of the variable switching frequency in SMC. The idea consists in using an additional loop capable of regulating such switching frequency to the desired level. The complete control structure is shown in Figure 1.10. The SMC will be designed and implemented as it was described in Sections 1.3, 1.4, adding a second loop for the purpose of controlling the switching frequency. The main parts of this second loop are, basically: a variable hysteresis band comparator, a switching period sensor, and the controller, called SFC (Switching Frequency Controller). The control structure responds to a classical feedback loop, measuring the signal to be controlled, T , comparing it with the desired value, T^* , and generating the hysteresis band value, Δ , through a properly designed controller, SFC.

This solution is similar to be one proposed in the Subsection 1.5.5 but, in this case, the sliding mode control theory will be applied, and the SFC stability conditions will be found for regulation and tracking scenarios. Therefore, the objectives of the thesis can be divided in two main subjects, namely, the theoretical developments and practical applications, which are detailed as follows:

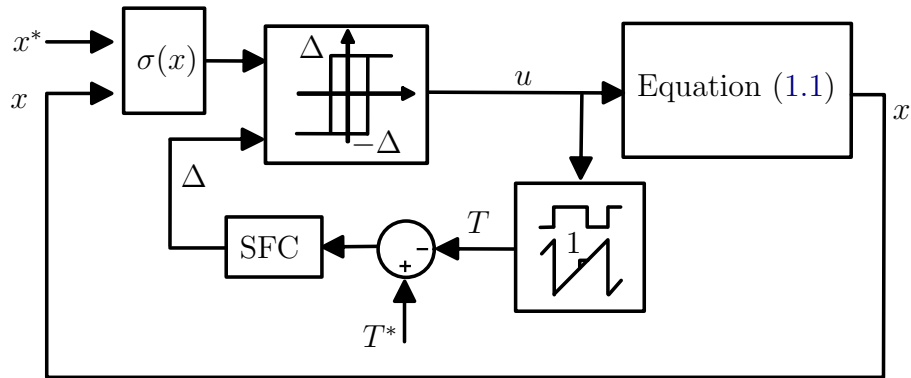


Figure 1.10: Overall controller architecture of the proposed solution for switching frequency regulation.

1. Theoretical contributions

- (a) Modelization of the proposed control loop for the switching frequency regulation.
- (b) Study of different possibilities for the SFC, which contains a discrete-time approach and a continuous-time one.
- (c) Analysis of the resulting SFC dynamics of the proposed approaches to the most expectable SMC working scenarios, namely: regulation and tracking tasks. These cases include some configurations of the power converters, specifically: DC/DC and DC/AC.
- (d) Derivation of the stability conditions of the SFC dynamics for the different approaches and working scenarios.
- (e) Establish design guidelines for the different SFC approaches.
- (f) Validation of the aforementioned objectives through numerical simulations.
- (g) Study of the real sliding dynamics when the SFC is included in the classical implementation of a SMC.

2. Power electronics applications

- (a) Implementation of the SFC by means of analog circuitry and by digital devices as μC (micro-controller) or FPGA (Field Programmable Gate Array).
- (b) Application of the SFC to a DC/DC Buck converter.
- (c) Application of the SFC to a DC/DC multiphase converter.
- (d) Application of the SFC to a DC/DC Boost converter.
- (e) Application of the SFC to a DC/AC VSI (Voltage Source Inverter).

1.7 Thesis structure

The thesis is organized in four parts, being the first one this introductory part. The second part is dedicated to the theoretical developments and stability analysis, and the third one is focused on the experimental evaluation of the SFC in power converters. Finally, the fourth part contains the conclusions of the thesis and the future researches. Within the parts, the thesis is structured in Chapters, where all the previous objectives defined in Section 1.6 are addressed. Specifically, the thesis structure is:

- Part I. *Introduction and Problem Statement*. Containing the present Chapter, where the SMC concepts and the open problem regarding the switching frequency has been introduced.
- Part II. *Theoretical Analysis of the Proposed Solution and Study of the resulting Sliding Dynamics*.
 - Chapter 2. *Modelling and stability analysis of the switching frequency control loop*. This Chapter deals with the objectives 1a, 1b, 1c and 1d. In the Chapter, the theoretical tools needed to design the SFC that ensures the proper switching frequency regulation are provided.
 - Chapter 3. *A case of study: SFC design and simulation results*. In this Chapter the objectives 1e and 1f are achieved. Apart from the simulation results corroborating the proper operation of the SFC, this Chapter also includes design guidelines for the SFC approaches contemplated in the thesis.
 - Chapter 4. *Real sliding dynamics in a switching frequency control loop*. The objective 1g is developed in this Chapter. Additionally, some interesting results about the real sliding mode and the piecewise linear behaviour of the switching function are also obtained.
- Part III. *Application to power converters*.
 - Chapter 5. *Voltage Regulation in a Buck Converter*. This Chapter, as its name indicates, essentially meets the objective 2b. The SFC in a regulation control problem, employing the discrete-time approach, is validated through experimental tests. In the same way, the objective 2a is partially contained in this Chapter, since the practical implementation of the SFC is detailed. Indeed, Objective 2a is distributed along Chapters 6, 7 and 8. With regard to the SMC, its design and implementation are discussed as well.
 - Chapter 6. *Voltage Regulation in a Multiphase Buck Converter*. Objective 2c is addressed in this Chapter, where a 8 phases synchronous Buck converter with interleaving operation is assembled in the laboratory. The SFC is designed and implemented using the continuous-time approach, thus providing additional results to the Objective 2a. With respect to the SMC, eight different switching

functions are designed, one regulating the output voltage and the remaining seven ensuring interleaving operation. The implementation of these switching functions are also discussed in the Chapter.

- Chapter 7 *Voltage Regulation in a Boost Converter*. The nonlinear structure of a Boost converter is tested in the Chapter, covering the results stated in the Objective 2d. In this case, the used structure for the SFC is the continuous-time approach, as it was employed in Chapter 6. Again, the SMC design and its implementation is duly justified.
- Chapter 8 *Voltage Tracking in a Voltage Source Inverter*. The performance of the SFC under a tracking control problem is confirmed in this Chapter, validating Objective 2e. Despite of the design of the SFC in the tracking case from a theoretical point of view, the Chapter deals with the issues related to digital implementation of the SFC. To do that, some approximations are required in order to successfully implement the SFC, leading to additional results for the Objective 2a. Moreover, in the Chapter, a switching function with a low output impedance sensitivity is designed for the SMC, making possible to connect different types of impedances at the inverter output with a good tracking performance. Both controllers (SMC and SFC) are implemented using the same μC (micro-controller), providing a compact solution for sliding mode controllers operating at fixed switching period.
- Part IV. *Conclusions and Future Research*. In the Final part, the Conclusions of the work and the generated research lines are commented.

Part II

Theoretical Analysis of the Proposed Solution and Study of the resulting Sliding Dynamics

Chapter 2

Modelling and stability analysis of the switching frequency control loop

This chapter deals with the modelling and the analysis of the structure for the SFC presented in the Chapter 1. As it was previously introduced, the control methodology is based on the adjustment of the hysteresis band value of the comparator through an additional control loop, as Figure 1.10 shows. Since the control loop will vary such hysteresis band, the analysis of the switching period presented in Section 1.4 needs to be revisited. Furthermore, this structure has an additional peculiarity: the SFC structure used to adjust the hysteresis band value will affect the relation between the applied hysteresis and the corresponding switching period. In this thesis two different approaches have been applied, namely:

1. A discrete-time approach, where the hysteresis band can be updated just once per switching cycle.
2. A continuous-time approach, assuming that the hysteresis band will be a time-varying signal.

The chapter is structured as follows: In Section 2.1, the analysis of the time invariant hysteresis case done in Section 1.4 is revisited, being used to define some essential parameters for the analysis performed hereafter of the SFC structure. In Section 2.2 the discrete-time approach is presented and the two most expectable working scenarios in power converters, the regulation and the tracking case problems, are analysed. Finally, in Section 2.3 a continuous-time approach for the SFC, particularizing it only to the regulation control problem, is presented.

2.1 Open loop case: The fixed hysteresis band comparator

The time invariant hysteresis band amplitude case was already analysed in the Section 1.4. However, the resulting expression for the switching period (see equations (1.19), (1.21)) is

redefined at this point, including some important definitions.

Assume that a switching function, $\sigma(x)$, has been defined in order to enforce sliding motion in the subspace $\sigma(x) = 0$, with the objective to control the dynamics of a power converter (voltage, current,..). Suppose also that the control law provided by the SMC theory, which guarantees convergence of $\sigma(x)$ to $\sigma(x) = 0$, is implemented using a fixed band hysteresis comparator, as (1.13) states. Once the sliding motion is reached, the expected behaviour of $\sigma(x)$ within the hysteresis band is shown in Figure 2.1. Notice that, as it was justified in Chapter 1, the switching function $\sigma(x)$ has been represented by straight lines.

Under these conditions, the k -th switching period, T_k , can be deduced from Figure 2.1. The subindex k holds for any switching interval that will occur.

$$T_k = T_k^+ + T_k^- = 2\Delta (\rho_k^+ - \rho_k^-), \quad (2.1)$$

where ρ_k^+ and ρ_k^- are defined as the inverses of $\dot{\sigma}(x)$ for each control input state:

$$\rho_k^+ := \frac{1}{\dot{\sigma}(x)_k^+}, \quad \rho_k^- := \frac{1}{\dot{\sigma}(x)_k^-}. \quad (2.2)$$

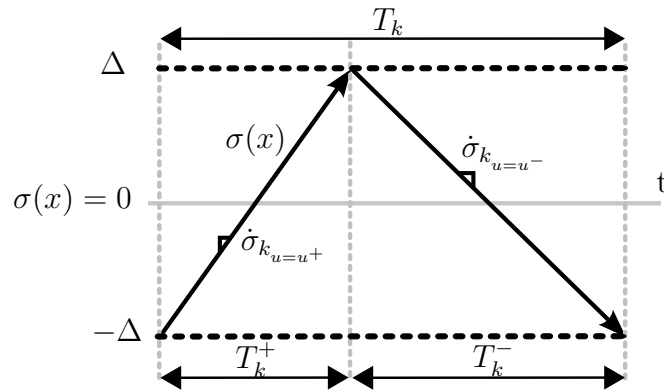


Figure 2.1: Switching function behaviour within a time invariant hysteresis band.

The time derivative of $\sigma(x)$ was already shown in the Chapter 1, specifically by equation (1.20). From the definitions of ρ_k^\pm , it is required to evaluate $\dot{\sigma}(x)^\pm$ at any switching interval k for the two possible control input states, u^+ and u^- . Therefore the expressions for $\dot{\sigma}(x)_k^\pm$ respond to

$$\dot{\sigma}(x)_k^+ = \left(\frac{\partial \sigma(x)}{\partial x} \right)_k g(x)_k (u^+ - u_{eq}(x)_k) \quad (2.3)$$

$$\dot{\sigma}(x)_k^- = \left(\frac{\partial \sigma(x)}{\partial x} \right)_k g(x)_k (u^- - u_{eq}(x)_k) \quad (2.4)$$

where the subindex k holds for the corresponding sampled counterparts of the original

signals in the specific time instant. In Chapter 1, it was introduced that for the sliding motion to exist, the equivalent control, u_{eq} , has to be within u^- and u^+ (see inequality (1.12)). As a consequence, the right hand sides of expressions (2.3) and (2.4) are always different from zero. Furthermore, taking into account the fulfilment of the transversality condition (see for details [33]), which defines

$$\frac{\partial \sigma(x)}{\partial x} g(x) \neq 0, \quad (2.5)$$

it is obvious that condition $\dot{\sigma}(x)_k^\pm \neq 0 \forall k$ holds under sliding motion.

Therefore, from (2.3), (2.4) and (2.5) it results that the values of ρ_k^+ and ρ_k^- always exist under sliding motion, according to their definitions in (2.2). Assuming that (2.5) is not only non null but positive, and $u^+ > 0$ and $u^- < 0$, it follows immediately that

$$\rho_k^+ > 0, \quad \rho_k^- < 0, \quad \forall k \geq 0. \quad (2.6)$$

The analyses developed in the next subsections assume that ρ_k^+ is always positive definite, meanwhile ρ_k^- is negative definite, as the inequalities in (2.6) state. However, in some applications the term

$$\frac{\partial \sigma(x)}{\partial x} g(x)$$

could result negative definite. In these cases, in order to keep the methodologies developed in this work, a slightly different definition for $\dot{\sigma}(x)_k^\pm$ must be used as:

$$\dot{\sigma}(x)_k^+ = \left(\frac{\partial \sigma}{\partial x} \right)_k g(x)_k (u^- - u_{eq}(x)_k) \quad (2.7)$$

$$\dot{\sigma}(x)_k^- = \left(\frac{\partial \sigma}{\partial x} \right)_k g(x)_k (u^+ - u_{eq}(x)_k). \quad (2.8)$$

Which such alternative definitions, the inequalities defined in (2.6) always hold.

2.2 Closed-loop case: A discrete-time modelling.

According to (2.1), the switching period becomes in a series of discrete-time measurements. Thus, it is reasonable to modify the hysteresis band amplitude only at the beginning of each switching period. Assuming that the hysteresis band amplitude is updated at the beginning of each switching interval and remains constant up to the next switching event, the expected switching function behaviour within the hysteresis band can be depicted as the Figure 2.2 shows.

In order to establish a standard methodology, the beginning of the switching interval will be considered when the slope of $\sigma(x)$ changes from the negative value to the positive one, as Figures 2.1, 2.2 display, regardless of the control action state. As it was commented in the previous Section, the values of ρ_k^+ will be always strictly positive and ρ_k^- strictly

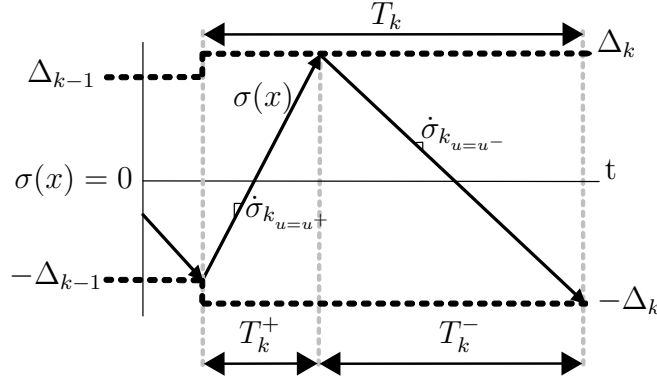


Figure 2.2: Switching function behaviour within a time-varying hysteresis band.

negative. Therefore the beginning of the switching interval is fully determined.

Since, in this approach, the hysteresis value will change between two consecutive switching intervals, the expression found in (2.1) should be revisited. From Figure 2.2 the new relation between Δ_k and T_k can be found

$$T_k = T_k^+ + T_k^- = \rho_k^+ (\Delta_k + \Delta_{k-1}) - 2\rho_k^- \Delta_k = \hat{\rho}_k \Delta_k + (\tilde{\rho}_k - \hat{\rho}_k) \Delta_{k-1}, \quad (2.9)$$

with

$$\begin{aligned} \hat{\rho}_k &:= \rho_k^+ - 2\rho_k^-, \\ \tilde{\rho}_k &:= 2(\rho_k^+ - \rho_k^-). \end{aligned}$$

Expression (2.9) constitutes the discrete-time model for the switching frequency control loop, and relates the k -th switching period and the hysteresis band value. Due to the used methodology to update the hysteresis band, such relation includes the hysteresis band values in the interval k and $k - 1$. In Figure 2.3 the resulting model of the SFC, which includes the model found in (2.9), is shown. From Figures 2.2, 2.1 an important aspect to be taken into account can be deduced. It is easy to figure out that the measured value of T_k will not be available until the k -th switching interval ends. This phenomenon is included to the system through an asynchronous discrete delay, z^{-1} (see bottom part of Figure 2.3).

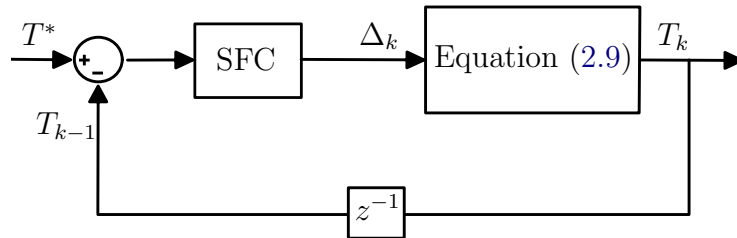


Figure 2.3: Detail of the switching frequency control loop. Discrete-time model.

At this point, using the loop shown in Figure 2.3, the closed-loop behaviour of the

system can be studied. Let us define the switching period error as $e := T^* - T$, where T^* is the reference switching period. From (2.9), the error equation of the SFC can be easily found as

$$e_k - e_{k-1} = \hat{\rho}_k (\Delta_{k-1} - \Delta_k) + \rho_{k-1}^+ (\Delta_{k-2} - \Delta_{k-1}) + (\tilde{\rho}_{k-1} - \tilde{\rho}_k) \Delta_{k-1}. \quad (2.10)$$

Once the discrete-time model is achieved, the control objective will be the proper design of the SFC in such a way that e_k converges to zero, thus implying T_k tends to T^* . The controller design procedure and the corresponding stability condition derivation will be carried out in the next subsections particularizing expression (2.10) in two different working conditions, namely: the regulation case and the tracking case. The analysis will be based on to substitute the expression provided by the SFC, which will be of the form $\Delta_k = f(e_k)$, in equation (2.10) and analyse the conditions for e_k to converge to zero as $k \rightarrow \infty$. It is clear that a specific controller expression, $\Delta_k = f(e_k)$, could deliver arbitrary values in presence of power converter transients, compromising the SMC itself (Δ_k could become too high or negative). Moreover, in Chapter 1 it was explained that in order to approximate the real sliding motion to the ideal one, it is required that the Δ_k value should be small enough (see Section 1.4). As a consequence, it is important to define an allowable range of the hysteresis band values used by the SFC in order to preserve the good performance of the SMC. This idea is expressed in the Remark 1.

Remark 1. *Arbitrarily hysteresis band values may take the system far away from the real sliding regime. Hence, a specific range $\mathcal{I}_\Delta := [\Delta_{min}, \Delta_{max}]$ such that $\Delta_k \in \mathcal{I}_\Delta, \forall k \geq 0$, has to be defined for preserving the existence of the sliding motion. In order to establish the suitable hysteresis range for a certain system, the following design criterion is proposed: Δ_{min} may be obtained from the maximum allowable switching frequency, while the maximum acceptable ripple for the state variables would be used to set Δ_{max} and, consequently, the minimum switching frequency. In turn, the switching frequency reference should be accordingly selected within these limiting values.*

2.2.1 The regulation case

In the power electronics field, it is very common to regulate the output voltage of a given converter to a DC value. In some applications the output current of a converter is also controlled to a fixed value, acting the converter as a constant current source. These two cases correspond to a regulation case. In the regulation case the state vector reference, x^* , is constant. Assume that a SMC has been designed to regulate such voltage or current, and that through a proper design of the \mathcal{I}_Δ (see Remark 1), the oscillations of $\sigma(x)$ in the vicinity of $\sigma(x) = 0$ are small, such that $x \simeq x^*$ holds. Therefore, considering the state vector x constant, the switching function derivatives and their inverses are also constant under steady-state sliding motion. Hence, from a certain discrete-time instant k_0 the following relations are fulfilled:

$$\rho_k^\pm = \rho(x^*, u^\pm) := \rho_*^\pm, \quad \hat{\rho}_k := \hat{\rho}^*, \quad \tilde{\rho}_k := \tilde{\rho}^*, \quad \forall k \geq k_0, \quad (2.11)$$

for a given steady-state working point. With these definitions, (2.10) can be simplified up to the following expression:

$$e_k - e_{k-1} = \hat{\rho}^* (\Delta_{k-1} - \Delta_k) + \rho_*^+ (\Delta_{k-2} - \Delta_{k-1}). \quad (2.12)$$

Now the goal is to properly design the SFC generating the value for Δ_k as a function of the measured switching period error, e_k , in order to get the convergence of the error to zero. Let us try as SFC controller a pure discrete-time integrator, which corresponds to:

$$\Delta_k = \Delta_{k-1} + \gamma e_{k-1}, \quad (2.13)$$

being $\gamma > 0$ the integral constant. Replacing the control action, (2.13), in the closed-loop error dynamics, (2.12), one gets

$$e_k = (1 - \gamma \hat{\rho}^*) e_{k-1} - \gamma \rho_*^+ e_{k-2}. \quad (2.14)$$

The arisen equation in (2.14) is an homogeneous linear difference equation, which implies that the only solution of the equilibrium is $e_k = 0$. The integral gain γ , is the design parameter which should be selected to get the equilibrium point of (2.14) stable. In order to rigorously define the conditions for γ to achieve a stable behaviour of the equilibrium point $e_k = 0$, the Assumption A is defined.

Assumption A. *A real sliding motion has been enforced over a specific switching surface, $\sigma(x) = 0$, in such a way $|\sigma(x)| < \Delta$ with a given control law defined as (1.5) depicts. Moreover, after the sliding mode transient, the system reaches the steady-state where $x \simeq x^*$, and the relations shown in equations (2.11) are fulfilled.*

Once the Assumption A is defined, the Theorem 1 states the condition for γ to achieve stability of the SFC.

Theorem 1. *Let Assumption A be fulfilled, and let the hysteresis band amplitude, Δ_k , be updated according to (2.13). If γ fulfils that*

$$0 < \gamma < \min \left\{ |\rho_*^+|^{-1}, |\rho_*^-|^{-1} \right\}, \quad (2.15)$$

with ρ_^\pm defined in (2.11), then the switching period, T_k , converges asymptotically to the reference value, T^* , in the steady-state.*

Proof. It follows applying Jury stability criterion [34] to the characteristic polynomial associated to the difference equation (2.14), which results in

$$p(z) = z^2 + z(\gamma \hat{\rho}^* - 1) + \gamma \rho_*^+. \quad (2.16)$$

The conditions to be fulfilled, according to the criterion, are:

1. $p(1) > 0 \rightarrow \gamma > 0$

2. $p(-1) > 0 \rightarrow \gamma < |\rho_*^-|^{-1}$
3. $|\gamma\hat{\rho}^* - 1| < |\gamma\rho_*^+| \rightarrow \gamma < |\rho_*^+|^{-1}$

□

In this case, since the values of ρ_*^\pm can be considered parameters, the z transform has been used in order to find the stability conditions of (2.14). Finally, the equivalent model in the z domain is shown in Figure 2.4. Notice how the inherent delay produced when the switching period is measured has been considered for the proper implementation of (2.13).

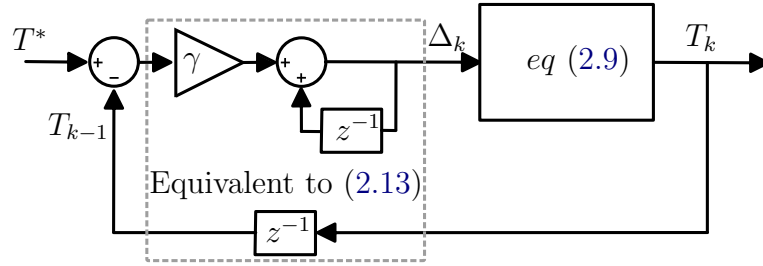


Figure 2.4: Equivalent model in the z domain of the control loop for the discrete-time approach in the regulation case.

2.2.2 The tracking case

The power converters usually have to work connected to the AC grid, sometimes injecting power from a renewable plant, sometimes consuming power from the grid. In these cases, the power converters are working with references (of voltage or currents) that vary with time. These applications are classified as tracking control problems. When the SMC is tracking a time-varying reference, $x^* = f(t)$, it exists a variation of the switching function time derivatives with k , i.e. $\rho_k^+ \neq \rho_{k-1}^+$, $\rho_k^- \neq \rho_{k-1}^-$. As a consequence, the simplification made in (2.11) does not apply.

Before progressing with the tracking case stability analysis, an important consideration about the variations of ρ_k^\pm with k is discussed in Remark 2.

Remark 2. *Although in the tracking case it is assumed that the values of ρ_k^\pm vary with k , such variations must be sufficiently slow so that these values can be considered locally constant during a switching interval. This fact will be achieved when the effective switching period of the control action is small enough with respect to the system time constants. This hypotheses is equivalent to assume that the behaviour of $\sigma(x)$ in Figures 2.1, 2.2 can be considered piecewise linear even when the system is tracking a time-varying reference $x^* = f(t)$. Therefore, the switching period has to be small enough as the condition:*

$$\frac{df(t)}{dt} \approx \frac{f(T_k) - f(T_{k-1})}{T_k} \rightarrow 0$$

is met. Notice how in this case the last term on the right side in equation (2.10) does not vanish.

The chosen SFC structure for the regulation case was a pure discrete-time integrator (equation (2.13)), which was characterized by:

$$\Delta_k = \Delta_{k-1} + \gamma e_{k-1}.$$

Keeping such structure as SFC, and without the aforementioned simplifications for ρ_k^\pm , the new expression for the error dynamics in the tracking case is found. The dynamics is governed by (2.17):

$$e_k = (1 - \gamma \hat{\rho}_k) e_{k-1} - \gamma \rho_{k-1}^+ e_{k-2} + \Delta_{k-1} (\tilde{\rho}_{k-1} - \tilde{\rho}_k). \quad (2.17)$$

The difference between expression (2.12) and (2.17) is the last term on the right side of expression (2.17). It should be highlighted that this term makes the expression (2.17) non-homogeneous and, as a consequence, it losses $e_k = 0$ as equilibrium solution. Thus, in order to recover the homogeneous characteristic of expression (2.14), this work proposes the design of a feedforward action in order to cancel this term in the closed-loop dynamics. This idea is sketched in Figure 2.5.

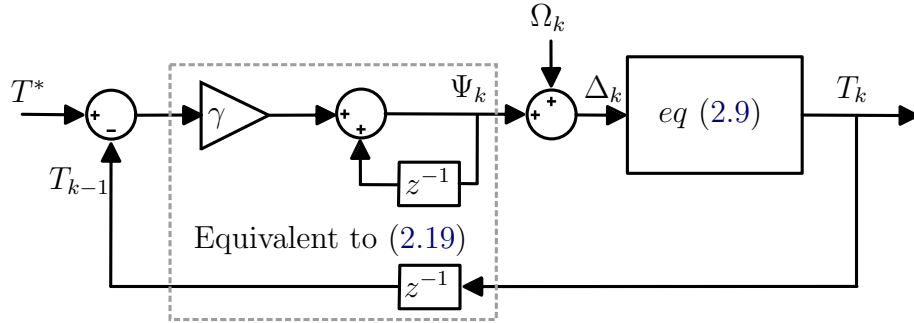


Figure 2.5: Switching frequency regulation control loop with feedforward action. The inherent time delay due to the switching period measurement is represented by z^{-1} .

The analysis is simple, the new control action includes the feedforward term Ω_k , as

$$\Delta_k = \Psi_k + \Omega_k, \quad (2.18)$$

where Ψ_k keeps the structure of a discrete-time integrator

$$\Psi_k = \Psi_{k-1} + \gamma e_{k-1}. \quad (2.19)$$

The value for Ω_k is derived placing (2.18) in (2.10) and equalling all the terms that do not depend on e_k to zero. The result of the proposed procedure is given by equation (2.20):

$$\Omega_k = \frac{\hat{\rho}_{k-1} - \rho_k^+}{\hat{\rho}_k} \Omega_{k-1} + \frac{\rho_{k-1}^+}{\hat{\rho}_k} \Omega_{k-2} + \frac{\tilde{\rho}_{k-1} - \tilde{\rho}_k}{\hat{\rho}_k} \Psi_{k-1}. \quad (2.20)$$

The proposed modified structure for the tracking control problem is depicted in Figure 2.6, according to (2.18), (2.19) and (2.20), where the detail of Ω_k computation has been highlighted.

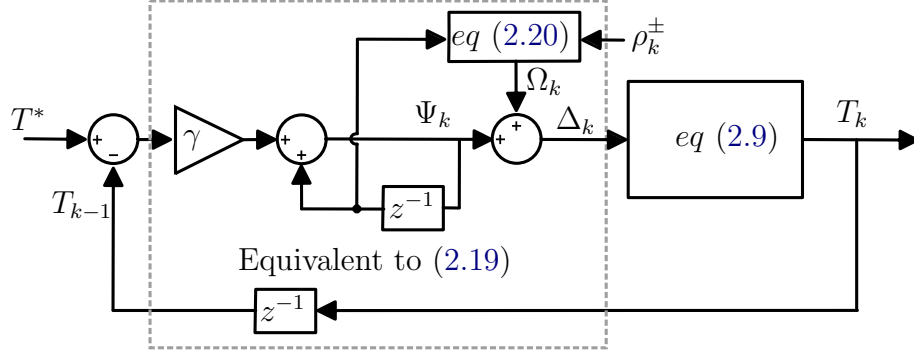


Figure 2.6: Switching frequency regulation control loop with feedforward action. Detail of new controller structure including the feedforward action.

From the obtained expression for Ω_k , some considerations should be taken into account, which are mainly noted in Remark 3.

Remark 3. *An important remark should be made at this point with regards to the expression found for Ω_k in (2.20). Looking carefully the expression, it is simple to note how the k -th value for Ω_k depends on the k -th values of $\hat{\rho}$, $\tilde{\rho}$ and ρ^+ . Such result is not realizable from a practical point of view since it depends on samples that are not available yet. Besides, the values $\hat{\rho}$, $\tilde{\rho}$ and ρ^+ should be properly estimated. As a consequence, some approximations will be required when the proposed controller is implemented, both in the simulation and in the experimentation cases, which will be discussed later.*

Assuming that the expression for Ω_k can be properly obtained, the final error dynamics for the proposed controller with feedforward action can be evaluated. It follows replacing (2.18), (2.19) and (2.20) in (2.10), which provides the resulting closed-loop error dynamics in (2.21).

$$e_k = (1 - \gamma \hat{\rho}_k) e_{k-1} - \gamma \rho_{k-1}^+ e_{k-2}. \quad (2.21)$$

Now the equation of the switching period error boils down to an homogeneous time-varying discrete-time linear system, recovering $e_k = 0$ as the equilibrium solution. It should be noted that $\hat{\rho}_k$, ρ_{k-1}^+ cannot be treated as constant parameters in this case.

Although the ρ_k^\pm are not constant with k , it can be defined an expectable range of values related to a certain working conditions. Under steady-state sliding motion, the state vector profile $x^* = f(t)$ will produce the following time-varying values:

$$\begin{aligned} \rho_k^+ &= \rho_k(x^*(t), u^+) = \rho_{*k}^+, \\ \rho_k^- &= \rho_k(x^*(t), u^-) = \rho_{*k}^-, \\ \hat{\rho}_k &= \hat{\rho}_k(x^*(t)) := \hat{\rho}_k^*, \\ \tilde{\rho}_k &= \tilde{\rho}_k(x^*(t)) := \tilde{\rho}_k^*, \end{aligned} \quad (2.22)$$

$\forall k \geq k_0$, and the previous error definition is particularized to such specific steady-state sliding motion as:

$$e_k = (1 - \gamma \hat{\rho}_k^*) e_{k-1} - \gamma \rho_{*k-1}^+ e_{k-2}. \quad (2.23)$$

In this case, the error expression to be analysed, (2.23), is considerably different than (2.14). In the previous analysis, the z transform was used in order to derive the stability conditions for the regulation case, as Theorem 1 states. Since, in the tracking case, the values of ρ_{*k}^\pm vary with k , they cannot be treated as constant values in steady-state, hindering the usage of the z transform. A different procedure is applied instead. The stability conditions for the tracking control case are found by means of a Lyapunov-based discrete-time approach [35]. The Theorem 2 enunciates the stability conditions according to this Lyapunov-based criterion.

Theorem 2. *Let Assumption A be fulfilled, with $x^* = f(t)$ being a time-varying reference signal, and assume that the hysteresis band amplitude, Δ , is calculated according to (2.18), (2.19) and (2.20). If the integral gain γ is selected within the range values delimited by $\gamma_m < \gamma < \gamma_M$, with:*

$$\gamma_m := \max \left\{ \frac{\hat{\rho}_k^* - \sqrt{\frac{1}{2} (\hat{\rho}_k^{*2} - \rho_{*k}^{+2})}}{\hat{\rho}_k^{*2} + \rho_{*k}^{+2}}, \forall k \geq 0 \right\}, \quad (2.24)$$

$$\gamma_M := \min \left\{ \frac{\hat{\rho}_k^* + \sqrt{\frac{1}{2} (\hat{\rho}_k^{*2} - \rho_{*k}^{+2})}}{\hat{\rho}_k^{*2} + \rho_{*k}^{+2}}, \forall k \geq 0 \right\}, \quad (2.25)$$

being defined $\hat{\rho}_k^*$, $\tilde{\rho}_k^*$ and ρ_{*k}^\pm according to (2.22), the switching period, T_k , converges asymptotically to the reference value, T^* , in the steady-state.

Proof. It follows using a Lyapunov-based discrete-time criterion according to [35]. Using the change of variables $y_{1k} = e_{k-1}$, $y_{2k} = e_k$, and defining $y = (y_1, y_2)^\top$, the second-order difference equation (2.23) can be equivalently written as the first order system

$$y_{k+1} = A_k y_k, \quad (2.26)$$

with

$$A_k = \begin{pmatrix} 0 & 1 \\ -\gamma \rho_{*k}^+ & 1 - \gamma \hat{\rho}_{k+1}^* \end{pmatrix} := \begin{pmatrix} 0 & 1 \\ \alpha_k & \beta_{k+1} \end{pmatrix}. \quad (2.27)$$

Hence, the problem boils down to the stability analysis of the trivial solution $y = 0$ of (2.26).

Following [35], let us consider the Lyapunov function candidate

$$V_k = y_k^\top Q_k y_k, \quad \text{with } Q_k = \begin{pmatrix} 2\alpha_k^2 + \frac{\delta}{2} & 0 \\ 0 & 1 \end{pmatrix}, \quad (2.28)$$

$\delta > 0$ being a real constant.

On the one hand, as $\{\rho_{*k}^+\}$ belongs to a closed interval in \mathbb{R}^+ by hypothesis, for any $\gamma \in \mathbb{R}$ there exist $\eta_1, \eta_2 \in \mathbb{R}^+$ such that, $\forall k \geq 0$,

$$\eta_1 \mathbb{I}_2 \leq Q_k \leq \eta_2 \mathbb{I}_2, \quad (2.29)$$

with \mathbb{I}_2 standing for the 2×2 identity matrix. On the other hand, the Lyapunov equation

$$A_k^\top Q_{k+1} A_k - Q_k \leq -\eta \mathbb{I}_2, \quad \text{with } \eta > 0, \quad \forall k \geq 0,$$

becomes

$$\begin{pmatrix} \alpha_k^2 + \frac{\delta}{2} - \eta & -\alpha_k \beta_{k+1} \\ -\alpha_k \beta_{k+1} & 1 - 2\alpha_{k+1}^2 - \beta_{k+1}^2 - \frac{\delta}{2} - \eta \end{pmatrix} \geq 0.$$

A Schur complement-based sufficient condition for the preceding matrix to be positive semidefinite is:

$$\alpha_k^2 + \frac{\delta}{2} - \eta > 0 \quad (2.30)$$

$$\left(\alpha_k^2 + \frac{\delta}{2} - \eta \right) \left(1 - 2\alpha_{k+1}^2 - \beta_{k+1}^2 - \frac{\delta}{2} - \eta \right) \geq \alpha_k^2 \beta_{k+1}^2. \quad (2.31)$$

Recalling again the hypothesis on the evolution of ρ_{*k}^+ , the fulfillment of (2.30) follows selecting $\delta > 2\eta$. In turn, it is sufficient for (2.31) to be satisfied that

$$\alpha_k^2 + \frac{\delta}{2} - \eta \geq \alpha_k^2, \quad (2.32)$$

$$1 - 2\alpha_{k+1}^2 - \beta_{k+1}^2 - \frac{\delta}{2} - \eta \geq \beta_{k+1}^2. \quad (2.33)$$

Notice that $\delta > 2\eta$ also guarantees (2.32), while for small enough values of δ, η inequality (2.33) is guaranteed by the demand

$$1 - 2(\alpha_{k+1}^2 + \beta_{k+1}^2) > 0$$

or, equivalently,

$$\frac{1}{2} > \gamma^2 \rho_{*k+1}^{+2} + (1 - \gamma \hat{\rho}_{*k+1}^*)^2.$$

Therefore, γ has to be selected within the interval with bounds given by the roots of the corresponding second-order equation, namely

$$\frac{\hat{\rho}_{k+1}^* \pm \sqrt{\frac{1}{2} (\hat{\rho}_{k+1}^{*2} - \rho_{*k+1}^{+2})}}{\hat{\rho}_{k+1}^{*2} + \rho_{*k+1}^{+2}}, \quad \forall k \geq k_0. \quad (2.34)$$

It is then immediate that the selection of γ within (γ_m, γ_M) implies asymptotically conver-

gence of T_k to the reference value T^* , $\forall k \geq k_0$. \square

The result of Theorem 2 differs from the obtained in Theorem 1 for the regulation case in the sense that, in this case, the values for γ ensuring stability have a lower bound besides an upper one. Moreover, the found condition is sufficient but not necessary, which means that values outside this range could also produce stable behaviour of the SFC in the proposed structure.

2.3 Closed-loop case: A continuous-time modelling.

The previous solutions perfectly fit with a controller implementation by means of discrete-time devices, as FPGA (Field Programmable Gate Array), DSP (Digital Signal Processors) or μ C (micro-controllers). An alternative approach would be to adjust the hysteresis band value by means of a classical linear controller, as it could be the well-known PID (Proportional Integral Derivative action), implemented by analogue circuitry. This approach could be cheaper than the solution based in digital devices (FPGA, DSP) and it becomes the optimum solution for low power converters.

Unlike the discrete-time approach, to use a P type, PI type or whatever combination present in the continuous-time linear control theory, will demand a specific analysis, since the dynamics of Δ will affect the switching period itself. In this thesis only the I-type based controller has been analysed, under the regulation control case, but, of course, following an equivalent procedure to the one developed hereafter, different models for different linear control structures could be also derived.

As it was proposed in the previous Section, the first approximation for the SFC is an integral type action. The expected behaviour of the switching function with a SFC based on a continuous-time integrator generating the hysteresis band values is depicted in Figure 2.7.

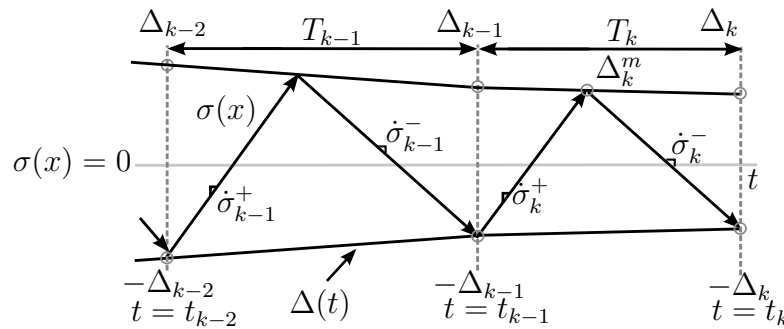


Figure 2.7: Switching function behaviour within a continuous-time variant hysteresis band.

The expression which determines the value of $\Delta(t)$ is given by:

$$\Delta(t) = \gamma_L \int e(\tau) d\tau \quad (2.35)$$

where $\gamma_L > 0$ is the integral gain and e is the switching period error. It should be noted that although the hysteresis band is a continuous-time function, both the switching periods and the period errors result again in a set of discrete-time values. As a consequence, the evolution of $\Delta(t)$ will be characterized by sections of constant slopes. For instance, in the time interval $[t_{k-1}, t_k)$ one gets:

$$\Delta(t) = \Delta_{k-1} + \gamma_L e_{k-1} (t - t_{k-1}) \text{ for } t_{k-1} \leq t < t_k \quad (2.36)$$

where Δ_{k-1}, Δ_k are the values of $\Delta(t)$ at the corresponding time instants (see Figure 2.7). According to the Figure, and assuming that the switching function, $\sigma(x)$, keeps the piecewise linear behaviour, the k -th switching period can be obtained as follows:

$$T_k = \frac{-2\Delta_k}{\gamma_L e_{k-1} - (\rho_k^-)^{-1}} + \frac{2\Delta_{k-1}}{(\rho_k^+)^{-1} - \gamma_L e_{k-1}}. \quad (2.37)$$

Equation (2.37) constitutes the model relating Δ_k and T_k in this approach. Using the expressions (2.35) and (2.37) the resulting control loop for this SFC structure can be obtained, which is shown in Figure 2.8.

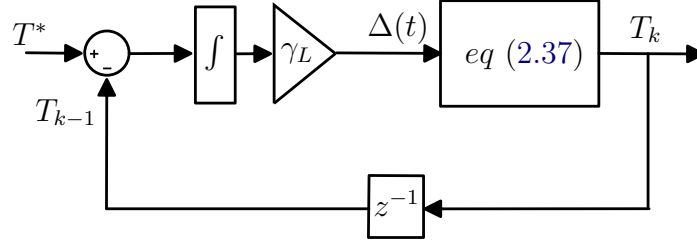


Figure 2.8: Switching frequency control loop model with a continuous-time integrator.

Expression (2.37) gives a nonlinear relation between Δ_k and T_k , which entails a certain level of complexity in the derivation of the stability conditions. In order to facilitate such procedure, the non-linear response is approximated by a linear one by applying the Assumption B.

Assumption B. Let Assumption A be fulfilled, also assume that under a regulation control problem the values of ρ_k^\pm can be replaced by the corresponding steady-state values ρ_*^\pm . Assume also that the following inequality holds:

$$\gamma_L |e_k| \ll \min \left\{ |\rho_*^+|^{-1}, |\rho_*^-|^{-1} \right\}, \quad \forall k \geq k_0 \quad (2.38)$$

which entails that the rate of change of Δ is much slower than the $\sigma(x)$ one from a specific time instant $k_0 \geq 0$.

Under Assumption B, the term $\gamma_L |e_k|$ can be neglected and the expression (2.37) can be simplified up to (2.39)

$$T(t) = \lambda \Delta(t) \quad (2.39)$$

where

$$\lambda = 2 (\rho_*^+ - \rho_*^-). \quad (2.40)$$

The resulting linearised continuous-time model is shown in Figure 2.9. For the linearization, the discrete delay has been modelled using the *Padé* approximation [36], assuming that the real switching periods, T_k , will be always close to the reference one, T^* . Moreover, since the switching period will be measured by analog electronics, a first order transfer function has been considered in order to include the dynamics added by the sensor.

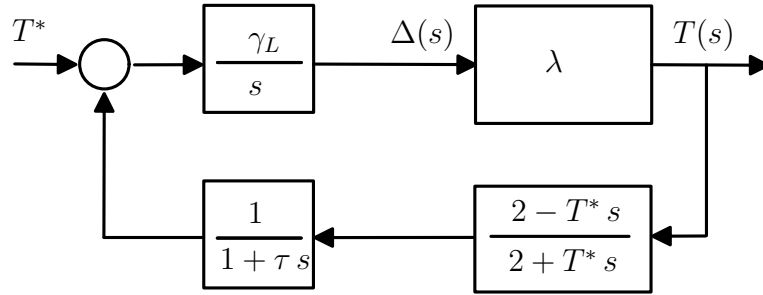


Figure 2.9: Switching frequency control loop linearized model with a continuous-time integrator in the s domain.

Taking into account the closed-loop system in the s domain (see Figure 2.9), the stability conditions can be deduced, which are stated at Theorem 3.

Theorem 3. *Let Assumption B be fulfilled. Let also the SFC be implemented as expression (2.35) denotes and assume that the discrete delay and the dynamics of the switching period sensor can be modelled as it is shown in Figure 2.9. Then, the switching period of the sliding mode controller tends asymptotically to the reference value T^* when*

$$\gamma_L < \frac{2(T^* + 2\tau)}{\lambda T^*(T^* + 4\tau)} \quad (2.41)$$

is fulfilled.

Proof. It follows from the characteristic polynomial of the closed-loop system shown in Figure 2.9, which is given by:

$$p(s) = \tau T^* s^3 + (T^* + 2\tau) s^2 + (2 - \gamma \lambda T^*) s + 2 \gamma \lambda \quad (2.42)$$

and applying the Routh's stability criterion, taking into account that $T^*, \tau > 0$. \square

In the experimental results shown later in this thesis, the used sensor adds dynamics to the system, being the reason why it is considered in the preceding stability analysis. However, the stability condition found in (2.42) could be also particularized for the cases

where the added dynamics related to the switching period sensor could be neglected, i. e. $\tau = 0$. This scenario would correspond for example to the simulation case shown in this document, or if a resettable digital counter together with a digital to analog converter were implemented instead of an analog sensor in an experimentation. In such cases, it results evident that the stability condition is given by:

$$\gamma_L < \frac{2}{\lambda T^*}. \quad (2.43)$$

It is important to note the implications of the linearised method shown above, since not only the stability conditions in (2.42), (2.43) have to be evaluate but also the fulfilment of Assumption B. The following Remark states the recommended design steps when this approach is employed.

Remark 4. *It has to be remarked that the aforementioned equivalent model can be used only when Assumption B can be taken as a fact, specifically, the relation between the grade of changes of Δ and $\sigma(x)$. The recommended design rule is to select a value of γ_L such that (2.38) is ensured for the expected working point, where a range of Δ has been defined according to Remark 1, leading to a bounded values for e_k as $|e_k| < e_M \forall k$, where e_M is the maximum allowable period error. Once the Assumption (2.38) is ensured, the stability condition given by the Theorem 3 has to be evaluated as well.*

Chapter 3

A case of study: SFC design and simulation results

In this Section, a very simple system is introduced in order to show the complete process for the SFC loop design, including the aforementioned practical approaches. The design and simulation of the proposed strategies will be tested in a linear system. Firstly, an sliding mode controller will be designed using the classical approach, through the equivalent control method, as it was introduced in Sections 1.3 and 1.4. Such SMC controller will be applied for both regulation and tracking tasks. The next step shows the derivation of the expressions for the ρ^\pm , allowing to properly design the SFC in the different cases, namely: the discrete-time approach for regulation and tracking cases, and the continuous-time approach in a regulation scenario. Finally, the simulations results of all the designed approaches are presented.

3.1 Design of the sliding mode controller

Let us introduce the single-input single-output linear system

$$\dot{x}_1 = -x_1 + x_2, \quad (3.1)$$

$$\dot{x}_2 = -x_1 + Mu, \quad (3.2)$$

where M is a system parameter, which could be interpreted as the system gain and u is the discontinuous input, taking values in the discrete set $\{-1, 1\}$. The control objective is to control the dynamics of x_2 to a desired behaviour, $x_2^*(t)$. Taking into account the relative degree of the system (3.1), (3.2) (see Section 1.3), a switching surface based on the tracking error is enough. Therefore, the switching surface is chosen as (3.3) states.

$$\sigma(x, t) := x_2 - x_2^*(t) = 0. \quad (3.3)$$

The desired dynamics for x_2 is

$$x_2^*(t) := A + B \sin \omega t, \quad (3.4)$$

with $A, B \geq 0$. It should be noticed that the switching function can create a regulation control case, ($B = 0$), or a tracking control case, ($B \neq 0$). The sliding motion will be enforced in $|\sigma(x, t)| < \Delta$ with a hysteretic control law of the type shown in equation (1.13), being $u^+ = 1$ and $u^- = -1$.

As it was presented in Section 1.3, the sliding mode control design is based on the first time derivative of the switching function. Once the first time derivative is found, the equivalent control can also be derived (see expressions (1.9) and (1.10)). These operations result in:

$$\dot{\sigma} = Mu - (x_1 + \dot{x}_2^*), \quad (3.5)$$

and, hence,

$$u_{eq} = \frac{1}{M} (x_1 + \dot{x}_2^*). \quad (3.6)$$

From (3.5) the control law can be derived. The control law enforcing $\sigma \dot{\sigma} < 0$ is:

$$u = \begin{cases} u^+ & \text{if } \sigma < -\Delta, \\ u^- & \text{if } \sigma > \Delta, \end{cases} \quad (3.7)$$

Recalling the sliding mode domain condition defined in (1.12), the ideal sliding motion on $\sigma = 0$ (or the real sliding motion on $|\sigma(x, t)| < \Delta$) can be enforced if

$$-1 < \frac{1}{M} (x_1 + \dot{x}_2^*) < 1$$

holds. The ideal sliding dynamics is determined placing the equivalent control in the state space equations. Therefore using (3.6) in (3.1), (3.2) one gets

$$x_2 = x_2^*(t), \quad (3.8)$$

$$\dot{x}_1 = -x_1 + x_2^*(t). \quad (3.9)$$

The dynamic of x_2 is directly imposed by the sliding motion, which is equal to $x_2^*(t)$. The remaining dynamics characterizing x_1 on sliding motion, x_1^* , is asymptotically stable. Hence, it is also possible to find the steady-state solution of the differential equation (3.9) in the time domain, $x_1^*(t)$, which is

$$x_1^*(t) = A + \frac{B}{1 + \omega^2} (\sin \omega t - \omega \cos \omega t). \quad (3.10)$$

Once the ideal steady-state sliding regime $x^* = (x_1^*, x_2^*)^\top$ has been reached, the switching function time derivatives allow to find the values for ρ_*^\pm , which can be derived using (3.4),

(3.5) and (3.10), resulting in

$$\rho_*^\pm(t) = \left(\pm M - A - \frac{B}{1 + \omega^2} (\sin \omega t + \omega^3 \cos \omega t) \right)^{-1} \quad (3.11)$$

for the tracking case. The regulation case is determined by $B = 0$, and therefore

$$\rho_*^\pm = \frac{1}{\pm M - A}. \quad (3.12)$$

Notice that the previous values, ρ_*^\pm , are the key for the SFC design, as it was presented in Chapter 2.

Thereupon, the simulation results for the system defined in (3.1),(3.2) with the different approaches presented in Chapter 2 for the SFC will be shown. Specifically, the regulation control problem is simulated for the discrete-time approach (Section 2.2.1) and for the continuous-time one (Section 2.3). Analogously, the tracking case is simulated for the discrete-time approach using the feedforward action (Section 2.2.2). The simulations have been performed with Matlab-Simulink using the following parameters: $M = 3$, $A = 1$, and $\omega = 2\pi \cdot 0.02$, while the desired switching period is $T^* = 0.1$ s. The parameter B will be selected depending on the used approach.

3.2 The regulation case in the discrete-time approach

First of all, the design of the SFC for the discrete-time regulation control case is performed. In this case, the value of B is set to 0. For the design of the γ value of the SFC, it is required to use the values of ρ^\pm at the corresponding steady-state sliding motion. As it was derived in (3.12), the values of ρ^\pm at the specific steady-state sliding motion, ρ_*^\pm , can be evaluated with the given data for M and A . Therefore, it stems from (3.12) that $\rho_*^+ = 0.5$ and $\rho_*^- = -0.25$. Recalling Theorem 1, the characteristic polynomial detailed in (2.16), for the case of study is found:

$$p(z) = z^2 + z(\gamma - 1) + 0.5\gamma. \quad (3.13)$$

Hence, following Theorem 1 and equation (2.15), under the SFC with the structure given by (2.13), the closed-loop system of the SFC is stable for values in the range $0 < \gamma < 2$. Furthermore, using the equation (3.13), the root locus for different values of γ can be studied. Figure 3.1 depicts the poles placement in the complex plane for different γ values, together with the responses, in the time domain, of the system in front of a step reference (from $T^* = 0.05$ s to $T^* = 0.1$ s). From the Figure 3.1, it can be seen how values below $\gamma = 0.3$ deliver responses with the poles in the real axis, being such responses underdamped for values from 0.3 to 2. For $\gamma > 2$ the SFC loop reaches the unstable region. Notice that the response for $\gamma = 2$ is omitted due to the oscillating behaviour, showing the one for $\gamma = 1.8$ instead. It is obvious that, for this case, the system is close to the stability limit.

In Figure 3.2 it can be seen the response of the SFC and the SMC for two values of γ and T^* , specifically for $\gamma = 0.1$ and $\gamma = 1$ with a reference value that changes, again,

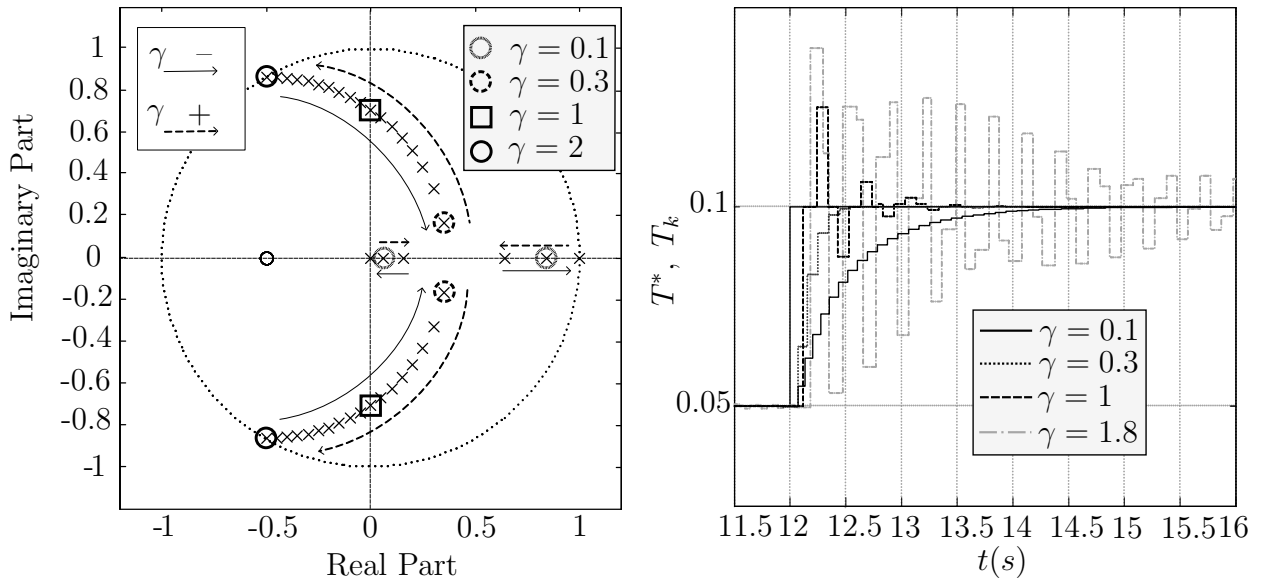


Figure 3.1: Left Plot: Root locus of $p(z)$ for the simulation case of study. Right Plot: response in the time domain for different values of γ .

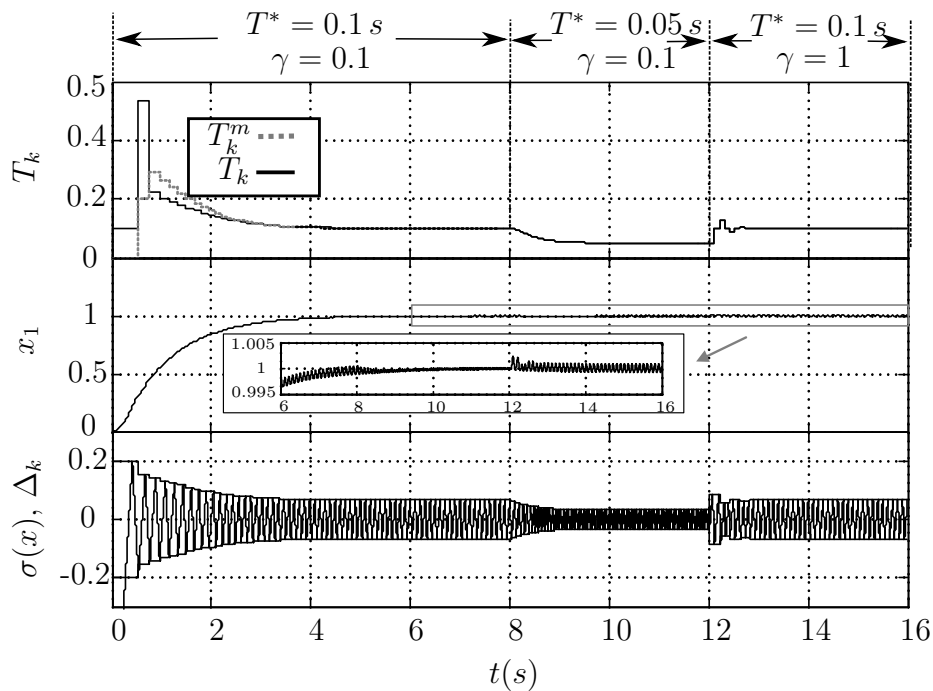


Figure 3.2: Regulation: performance of the SFC, with the discrete-time approach, for different values of γ and T^* .

between $T^* = 0.1$ s and $T^* = 0.05$ s. The values that take T^* and γ during the simulation are depicted in the top of Figure 3.2. The top plot of the Figure contains the switching period of the simulated system (3.1),(3.2), i.e. T_k , as well as the switching period arising from the model developed in Section 2.2.1 and detailed in Figure 2.4, which is labelled as T_k^m . The mid plot shows the resulting dynamics of x_1 , while the x_2 one is directly derived from σ (see equation (3.3)), which is plotted at the bottom plot of the Figure. Notice in the zoomed view of this mid plot how the ripple of x_1 changes as the switching period does. This ripple is the consequence of the different value of Δ generated by the SFC for different desired switching periods. However, in all the cases such ripples are small with respect to the DC value of x_1 , as expected.

The third plot illustrates how Δ_k is updated until T_k attains the reference value T^* , confirming that the desired switching period is achieved in steady-state. Moreover, the model response, T_k^m , always fits with the real switching period, T_k , except for the start-up, where the steady-state sliding motion is still not reached and, as a consequence, $\rho^\pm \neq \rho_*^\pm$. Once the system reaches the steady-state sliding motion, i.e. $\rho^\pm = \rho_*^\pm$, both responses perfectly match, even under switching period reference variations occurring at $t = 8$ s and $t = 12$ s; thus validating the mathematical model of the switching period behaviour presented in Section 2.2. Finally, it has to be noted that the hysteresis band amplitude achieves a constant value in the steady-state, as it can be inferred from (2.13). The asymptotic convergence of the state variable x_1 to the reference one x_1^* is illustrated in the mid part of the Figure 3.2, thus corroborating an overall good performance of the full system (SMC+SFC).

3.3 The regulation case in the continuous-time approach

In the continuous-time approach, the main difference with respect to the analysis performed in the previous section are focused in the SFC implementation. The analysis of the SMC is shared by the two approaches, since the control goal is the same for both, that is to regulate x_2 to x_2^* . Even the evaluation of the parameters ρ_*^\pm are exactly the same, because such values are related to the same steady-state sliding motion. The analysis differences rely on the SFC approach. In this case, the stability conditions and the design guideline of the SFC were defined in Section 2.3. It should be remembered that in the continuous-time approach, an important assumption was taken (Assumption B) in order to develop the equivalent model of the SFC loop. Thus, the equivalent diagram in the s domain shown in Figure 2.9 only can be used under certain conditions, when Assumption B is met. At this stage, we assume that the error of the switching period in the simulation performed hereunder, will be limited by a known value, being this bound $|e_k| < 0.05$ s. Let us study the grade of fulfilment of the Assumption B, which is:

$$\gamma_L |e_k| \ll \min \left\{ |\rho_*^+|^{-1}, |\rho_*^-|^{-1} \right\}, \forall k \geq k_0.$$

In this case, a factor of 20 is proposed. This implies the following relation

$$20 \cdot |e_k| \gamma_{L20} = \min \left\{ |\rho_*^+|^{-1}, |\rho_*^-|^{-1} \right\}.$$

According to Section 3.2, the values for ρ_*^\pm are $\rho_*^+ = 0.5$ and $\rho_*^- = -0.25$, therefore:

$$20 \cdot |e_k| \gamma_{L20} = 2.$$

Hence,

$$\gamma_{L20} = \frac{2}{20 \cdot 0.05} = 2.$$

Thus, ensuring that the designed value for γ_L is within the range $0 < \gamma_L < \gamma_{L20}$, the model of Figure 2.9 holds. Additionally, Theorem 3 allows to check if the equivalent model is stable. Since in the simulations presented hereafter the switching period sensor is ideal, the stability conditions must be determined by (2.43). This stability condition is stated as:

$$\gamma_L < \frac{2}{\lambda T^*},$$

being $\lambda = 2(\rho_*^+ - \rho_*^-)$, yielding

$$\gamma_L < \frac{2}{2(0.5 + 0.25) \cdot 0.1} = 13.3.$$

In the following simulation the switching period reference will be also varied to $T^* = 0.05$ s, thus the corresponding stability condition is also checked

$$\gamma_L < \frac{2}{2(0.5 + 0.25) \cdot 0.05} = 26.667.$$

From this result, the stability for values of $\gamma_L \leq 2$ are guaranteed. Notice that in this case, it does not make sense to show the resulting root locus for different values of γ_L since the model not always applies.

The simulation shown in Figure 3.3 corresponds to the same simulation set-up of the previous Section, but in this case, the SFC is implemented by means of a continuous-time integrator, as it has already commented. In the test, two different values of γ_L are used, specifically $\gamma_L = 1$ and $\gamma_L = 10$, corresponding one to a value within the values where Assumption B is fulfilled, and another outside this range. In the simulation, the ideal response of the switching period according to Figure 2.9, labelled as T_k^m , is shown. During the simulations, two transients in the reference switching period are applied, specifically from $T^* = 0.1$ s to $T^* = 0.05$ s and vice versa. In fact, from these transients arise the bound for the period error, previously used in the analysis performed over the γ_L values fulfilling Assumption B.

During the start-up, the real period, T_k , and the ideal one, T_k^m , do not match since the steady-state sliding motion has not been established, and $\rho_k^\pm \neq \rho_*^\pm$. Once the system

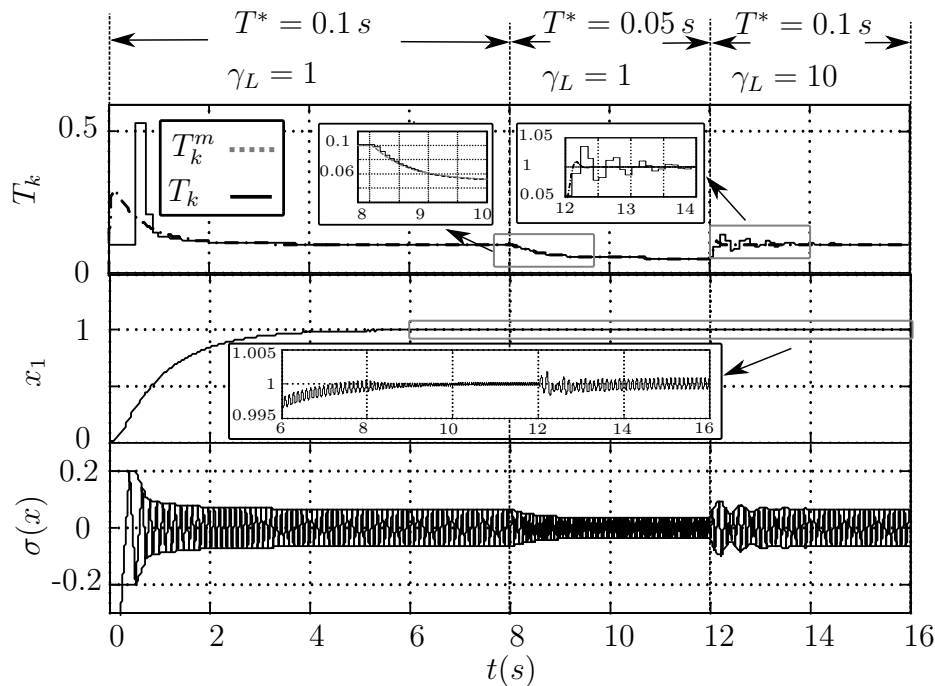


Figure 3.3: Regulation: performance of the SFC, with the continuous-time approach, for different values of γ and T^* .

reaches the steady-state, the responses T_k , T_k^m converge. Despite of the start-up, the behaviour during the transients at time instant $t = 8$ s and $t = 12$ s deserve a special attention. In the first transient (reference change at $t = 8$ s), the value for integral gain is $\gamma_L = 1$. During this transient, it is evident that T_k and T_k^m match, thus validating the model and also confirming that, in this case, the Assumption B is met. It should be noted that since the response is underdamped, the fulfilment of the hypothesis in the initial condition ($|e_0| < 0.05$ s) implies that the transients are exactly the same for T_k and T_k^m . However, this does not happen in the second transient (reference change at $t = 12$ s), where a gain of $\gamma = 10$ is used, and, as expected, the responses of T_k and T_k^m do not overlap. Indeed, since the initial error does not meet the Assumption B, the responses T_k and T_k^m will not fit along the transient, as it could be observed from the zoomed view of the top plot. As a conclusion, with a reasonable known bound for $|e_k| \forall k$, it is possible to successfully design the SFC in the continuous-time approach, obtaining the expected dynamics for T_k . Notice that the no fulfilment of Assumption B does not imply an unstable response, it just means that the developed model is not valid.

Despite of the range of application of the model developed in Section 2.3, the switching period is properly regulated (even when $\gamma_L = 10$) in the entire test, being negligible the impact over the SMC which regulates x_2 , and as a consequence, x_1 . In the zoomed area of the mid plot, it can be appreciated the different ripple levels in x_1 according to the variation in the switching period, being in both cases negligible when comparing with the DC value.

3.4 The tracking case

A tracking performance is obtained when $B \neq 0$. It should be noticed again that the SMC design is the same as the one presented in Section 3.1 so, it is omitted here for the sake of brevity. Since the reference for x_2^* is a time-varying signal, the values for ρ_k^* will also have dependency with k . It is simple to evaluate the expected values for $\rho_*^\pm(t)$ just replacing the given values of M , A , B and ω in (3.11). The values for the ρ_{*k}^\pm will be the corresponding ones of $\rho_*^\pm(t)$ at the specific time instant k . As a result, the functions $\tilde{\rho}_k^*$ and $\hat{\rho}_k^*$, can be derived, following their definitions in Section 2.2 (equation (2.9)). The expression for $\rho_*^\pm(t)$ are:

$$\rho_*^\pm(t) = \left(\pm M - A - \frac{B}{1 + \omega^2} (\sin \omega t + \omega^3 \cos \omega t) \right)^{-1}$$

The values for M , A and ω were already defined, being the selected amplitude of the reference signal $B = 0.5$. Therefore:

$$\rho_*^\pm(t) = \left(\pm 3 - 1 - \frac{0.5}{1 + (2\pi \cdot 0.02)^2} (\sin (2\pi \cdot 0.02) t + (2\pi \cdot 0.02)^3 \cos (2\pi \cdot 0.02) t) \right)^{-1}.$$

The previous expressions are the tools required for the SFC design in the tracking case. From these expressions $\tilde{\rho}_k^*$ and $\hat{\rho}_k^*$ are computed, and the stable range for γ according to Theorem 2 is found. With the goal of clarifying the result provided by Theorem 2, and how to apply it, a graphical approach is shown in Figure 3.4. In this plot can be seen, from top to bottom, the reference signal, $x_2^*(t)$, the resulting signals ρ_{*k}^+ , ρ_{*k}^- and the set of solutions obtained applying Theorem 2. The mid plot corroborates the expected variations of ρ_{*k}^\pm with k and also shows that the time evolution of such values are slow with respect to the desired switching period. Once such signals are plotted, the solution according to Theorem 2 can be graphically found, finding the minimum value and the maximum one of the corresponding solutions (see bottom plot of Figure 3.4). Notice how in the bottom plot the minimum value, γ_m , and the maximum one, γ_M , delimiting the stable range for γ are graphically determined. These values result in $0.314 < \gamma < 1.0315$. It is worth remarking that numerical simulations show that stability is indeed guaranteed for $0 < \gamma < 1.6$. The reader has to keep in mind that the stability condition provided by Theorem 2 is sufficient but not necessary.

Once the stable range for γ is found, the remaining task is to implement the feedforward action. Recalling the Subsection 2.2.2, the SFC for tracking cases includes a feedforward action Ω (see equation (2.18)). As it was commented in Remark 3, the implementation of such function implies an important limitation, since due to the inherent delay of the switching period measurement, it is not possible to exactly implement the theoretical value found for Ω_k . Besides, the feedforward action needs to estimate the values of ρ_{*k}^\pm (see equation (2.20)) which also inherit the problem of the measuring delay of T_k . In order to

overcome these problems the following approximation is used:

$$\Omega_k \simeq \Omega_{k-1}, \quad (3.14)$$

where the corresponding values for ρ_{k-1}^\pm are estimated using the expressions:

$$\rho_{k-1}^+ = \frac{T_{k-1}^+}{\Delta_{k-1} + \Delta_{k-2}}; \quad \rho_{k-1}^- = \frac{T_{k-1}^-}{2 \Delta_{k-1}}.$$

The basis of this approximation is again the idea expressed in Remark 2, in the sense that the system dynamics is slow enough with respect to the switching period, and, hence, the variation between consecutive k samples is small. Such phenomena will be highlighted later in the simulation results.

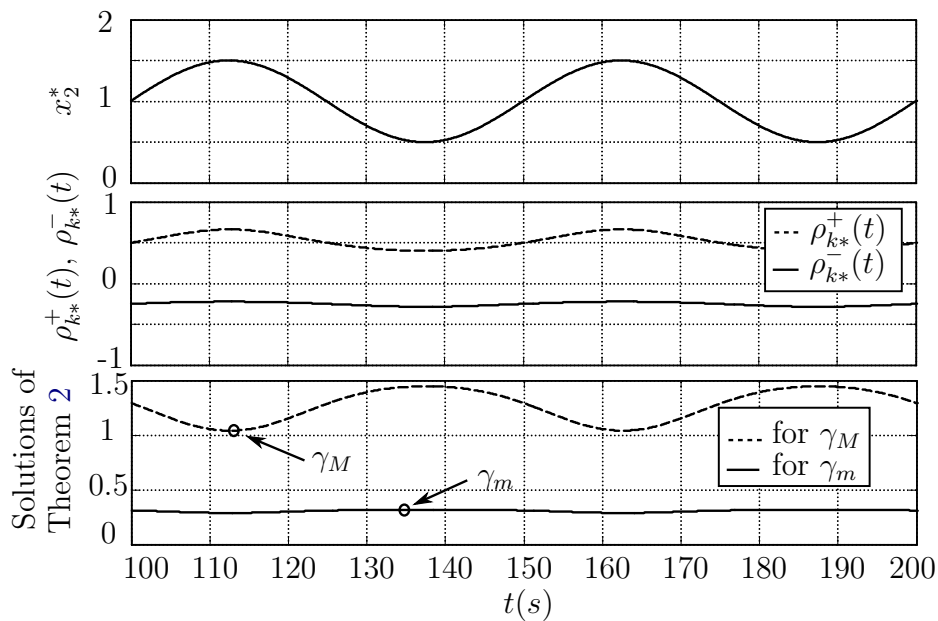


Figure 3.4: From top to bottom: Reference signal x_2^* ; temporal evolution of the signals ρ_k^+, ρ_k^- , measured from the system; solutions according to Theorem 2.

For the evaluation of the performance of the designed SFC for the tracking case, different tests are performed. The results are detailed in the simulations shown in Figures 3.5, 3.6 and 3.7. The selected value for the integral gain of the SFC is $\gamma = 0.4$.

Figure 3.5 compares the performance of the system without and with SFC action, and highlights the effect of the SFC. The SMC operates with fixed hysteresis band for the first 150 s. The SFC with $\gamma = 0.4$ is enabled at $t = 150$ s. It should be noticed that it is not until the activation of the SFC that T_k is able to attain the reference value $T^* = 0.1$ s. Indeed, the switching period with a fixed band value is time-varying, as expected from (1.19), taking into account that the values of σ_k^\pm vary with k . Notice how, in the same way,

for the correct regulation of the switching period, a time variant hysteresis band value is produced by the controller, as it can be extracted from the σ envelope in the bottom plot of Figure 3.5. Another drawn conclusion from the result is that the switching period model response, which is obtained solving (2.18)-(2.23), and represented by T_k^m perfectly fits with the real switching period, T_k . Similarly, the piecewise linear behaviour of the switching function can also be appreciated in the zoomed area that plots the switching function.

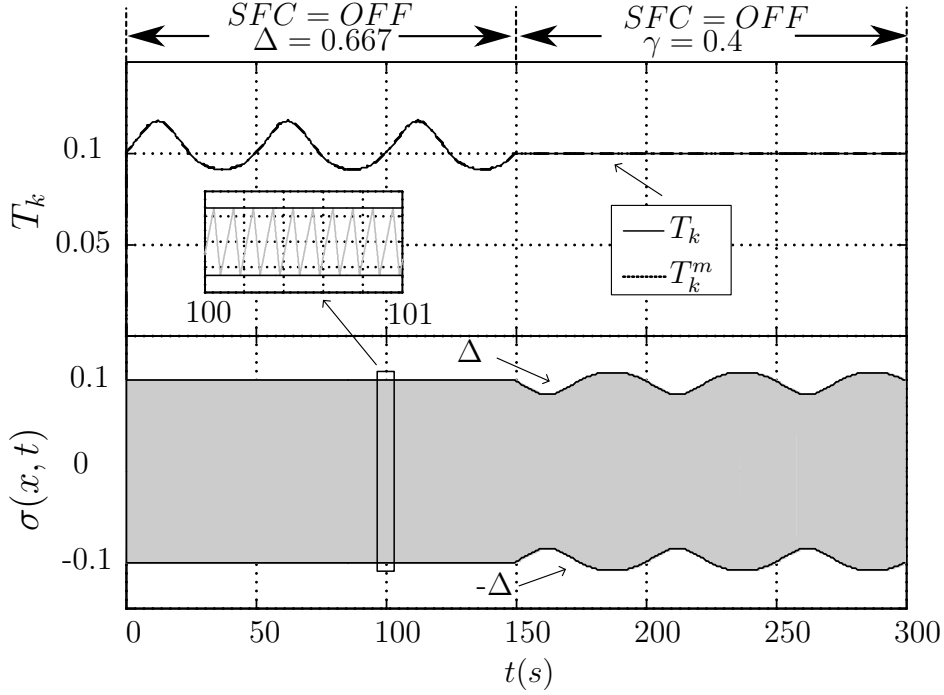


Figure 3.5: Tracking: evolution of T_k and $\sigma(x, t)$ with fixed hysteresis for $t < 150$ s and SFC for $t \geq 150$ s. Step change reference, $\gamma = 0.4$.

The test shown in Figure 3.6 presents the transient response of the SFC. Specifically, the Figure shows the behaviour when T^* suddenly varies from $T^* = 0.1$ s to $T^* = 0.05$ s. The result illustrates the good performance of the SFC under transients, since the switching period is regulated to the new value with a fast dynamics. Again the responses T_k and T_k^m are essentially the same, even in the transient.

Figure 3.7 presents the dynamics of x_2 , T_k and σ for changes in frequency and amplitude of the reference signal $x_2^*(t)$. From the Figure, a good behaviour of the state variables and a proper regulation of the switching period are confirmed, validating the proposed SFC structure for tracking cases. As it happened in the regulation case, small differences between T_k^m and T_k only arise in sliding mode transients. Through the presented simulation results, the SFC in tracking cases is successfully evaluated.

The final test is aimed to show the effects that can arise if the key condition assumed along the work is not fulfilled, which is that the switching period is small enough with respect to the system time constants. For such purpose, the desired switching period and the fundamental frequency of the tracking signal are varied along the simulation shown in

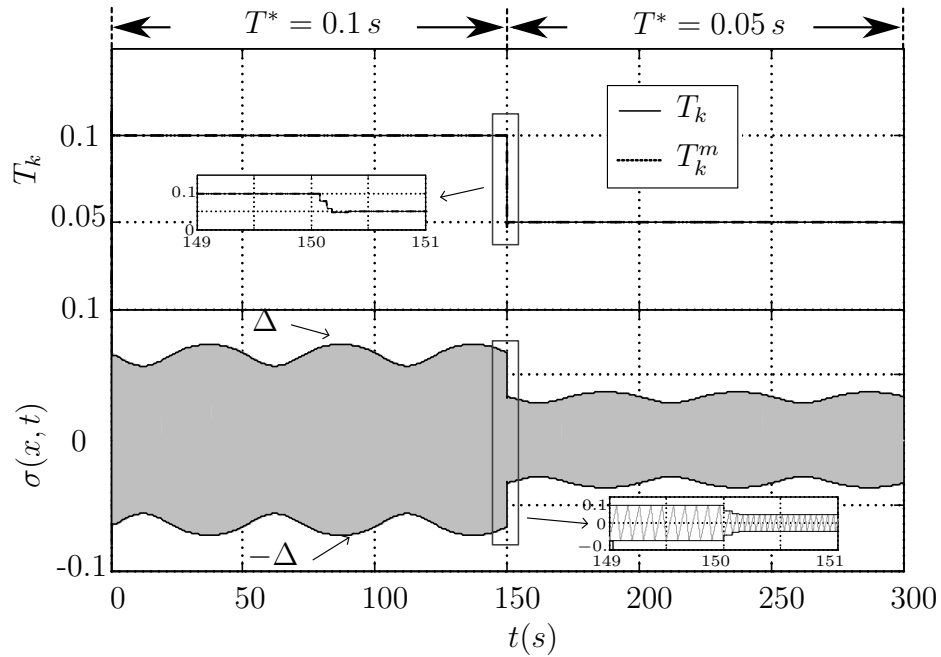


Figure 3.6: Tracking: evolution of T_k and $\sigma(x, t)$ when T^* is changed from 0.1 s to 0.05 s.

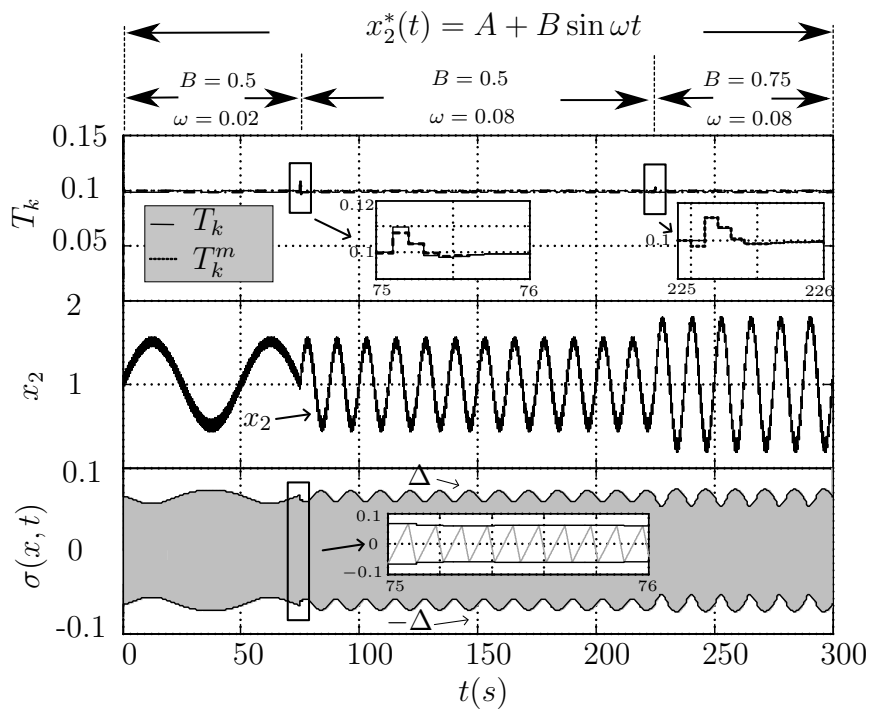


Figure 3.7: Tracking: evolution of T_k , x_2 and $\sigma(x, t)$ when the frequency and amplitude of $x_2^*(t)$ are changed from $\omega = 0.02$ to $\omega = 0.08$ and from $B = 0.5$ to $B = 0.75$, respectively.

Figure 3.8. From the result, different effects can be identified according to the following scenarios:

1. From $t = 0$ to $t = 50$ s.

At the beginning, from the initial time to $t = 50$ s, the relationship between T^* and the signal period is high enough as the aforementioned piecewise linear of the switching function and the approximations made by (3.14) hold. As a result, the proper regulation of T is achieved.

2. From $t = 50$ s to $t = 100$ s

At time instant $t = 50$ s the frequency of the tracking signal is increased ten times. Notice how in this part of the simulation an steady-state error appears in the switching period, which can be seen in the top plot and, specifically, in the zoomed view in the left top side of Figure 3.8. In this case, according to the zoomed view of the switching function in the bottom plot, the switching function keeps the piecewise behaviour and, therefore, the steady-state error is produced by the approximation given by (3.14) when the feedforward action is implemented. We can conclude that the signal period is not low enough with respect to the value of T^* and the approximations is inaccurate.

3. From $t = 100$ s to $t = 200$ s

In this part, the desired switching period is reduced (from $T^* = 0.1$ s to $T^* = 0.05$ s), in order to do again useful the approximations of (3.14). The simulation result confirms how the expected behaviour is recovered, since the steady-state error in the switching period disappears.

4. From $t = 200$ s to $t = 300$ s

In the final part, the desired switching period is considerably increased (from $T^* = 0.05$ s to $T^* = 0.4$ s). With this action, the piecewise linear behaviour of $\sigma(x)$ is lost, as it can be inferred from the zoom view on the right bottom part of Figure 3.8. Additionally, it is evident that the approximation given by (3.14) is neither fulfilled. The consequence of these effects in the switching period regulation are clearly observed in the top plot and, in detail, in the top right zoomed view, where a considerably steady-state error is produced in the switching period. It is clear from these results that when the assumption stated along the thesis is not fulfilled, the SFC fails in its objective. This confirms the importance of keep the relation between the system time constant and the switching period always high enough, in order to get a good switching frequency control.

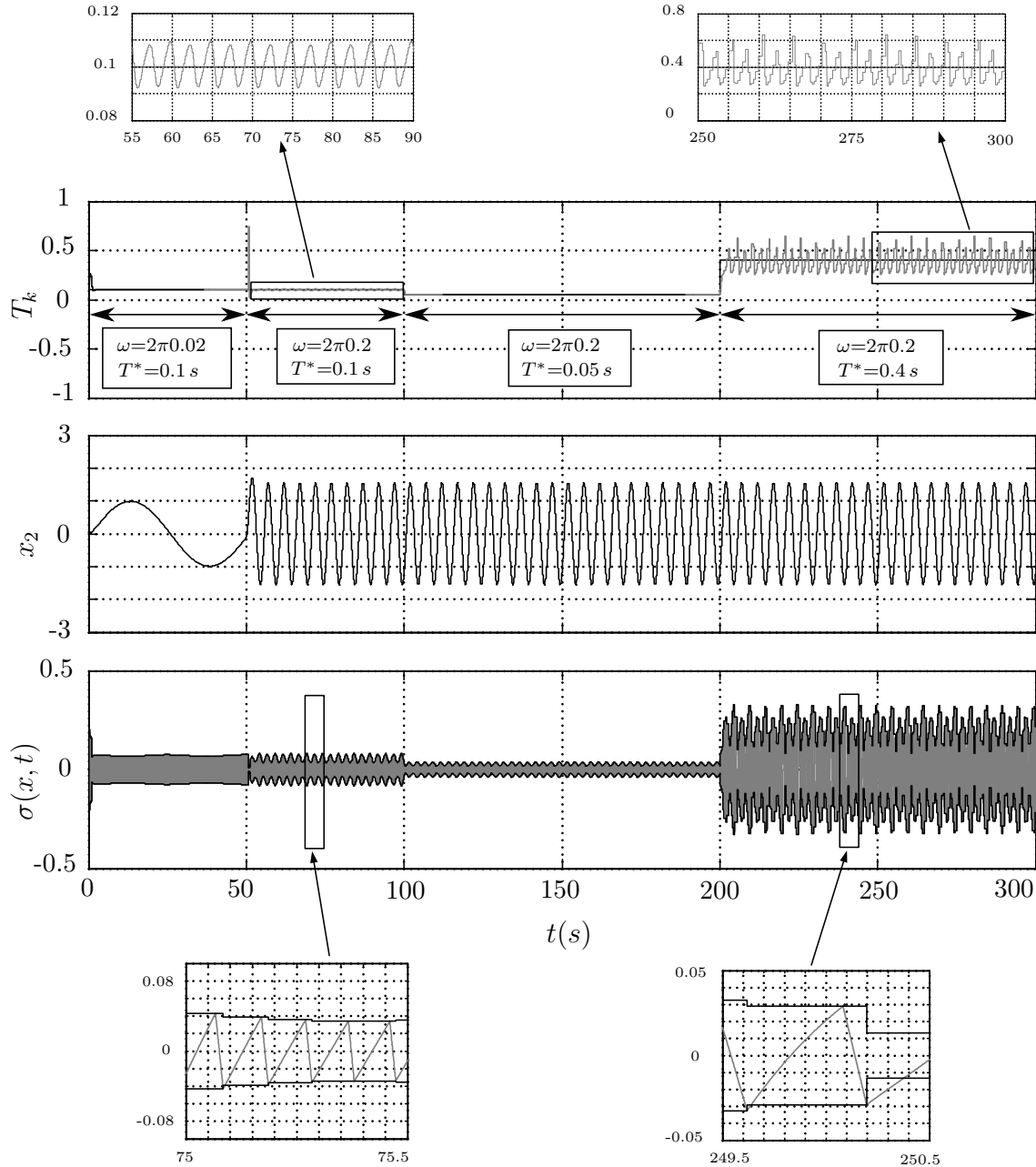


Figure 3.8: Performance of the SFC when the relation between the system time constant and the switching period varies between values high enough and not high enough.

Chapter 4

Real sliding dynamics in a switching frequency control loop

In Chapter 2 a control architecture for regulating the switching frequency under sliding mode has been proposed. The idea can be summarized as a variable hysteresis comparator with an additional control loop. The structure has been particularized for two different approaches, the discrete-time one and the continuous-time one. The stability conditions for the new loops have been obtained taking into account the most expectable working scenarios: regulation and tracking tasks. The question that this Chapter will answer is: How does a variable hysteresis band comparator affect the real sliding dynamics? The ideal sliding dynamics was studied by Professor V. Utkin in [7] by proposing the equivalent control method, which takes advantage of that the switching function is perfectly confined in the desired space region, $\sigma(x) = 0$. This method assumes therein infinite switching frequency, which is not realizable in real systems. In the implementations it is common to add a hysteresis comparator instead of the sign function, and then the switching frequency becomes bounded. This substitution leads to the so-called real sliding dynamics, where $|\sigma(x)| < \Delta$ holds, being Δ the width of the hysteresis used in the comparator (see Section 1.4 for details). According to this interpretation, in [37], it can be found the following result:

In a system with a hysteretic implementation of the control law, for any solution describing a real motion within the boundary layer, $|\sigma(x)| < \Delta$, it exists a solution describing the ideal motion on the switching surface which differs from the real one within the range of Δ , and when Δ tends to zero, the difference between the real and the ideal solutions converges to zero.

This procedure is so-called the classical approach for the analysis of the real sliding motion. Therefore, if $\Delta \rightarrow 0$ cannot be realizable (in general, this is the case), it will exist an error between the real and the ideal solutions, which depends on Δ . Moreover, since the proposed SFC modifies the hysteresis band values, the final impact in the aforementioned accuracy of the solutions must be studied. In [38], an alternative approach was presented in order to study the real sliding dynamics, and in that case, $\sigma(x)$ becomes the "virtual" input to the real dynamics instead of $\dot{\sigma}(x)$ (as it happens in the classical approach, Section

1.4, equation (1.18)). Such description, based on the regular form, will be used in this Chapter in order to analyse the impact of a hysteresis band on the real sliding dynamics.

The chapter is structured as follows. In Section 4.1, the approach based on the regular form is briefly introduced. In Section 4.2, the case $\Delta \neq 0$ is considered, leading to an interesting result regarding the mean value of the switching function and its piecewise linear behaviour. Some simulation results are introduced in Section 4.3 with the aim to validate the result provided in Section 4.2. Finally, in Section 4.4 the case for time-varying Δ is considered, leading to some conclusions about the real sliding mode in systems using SFC, which will be corroborated through numerical simulations as well.

4.1 The regular form approach

Consider the following linear system shown in (4.1).

$$\dot{x} = Ax + Bu + g(t), \quad (4.1)$$

where $x \in \mathbb{R}^n$, $A \in M_n(\mathbb{R})$, $B \in M_{n \times 1}(\mathbb{R})$, $g \in \mathbb{R}^n$ is a vector function representing a smooth external disturbances, and $u \in \mathbb{R}$ is the control action. An associated switching surface to this system would be:

$$\sigma(x) = Cx = 0, \quad (4.2)$$

where $C \in M_{1 \times n}(\mathbb{R})$.

Let the state space equation of the system given by (4.1) be expressed as it is shown in (4.3),(4.4) through a specific state transformation:

$$\dot{x}_1 = A_{11}x_1 + A_{12}x_2 + g_1(t), \quad (4.3)$$

$$\dot{x}_2 = A_{21}x_1 + A_{22}x_2 + B_1u + g_2(t). \quad (4.4)$$

This description is call the *regular form* ([37]). Taking into account the performed change of variables, the switching function, $\sigma(x)$, can also be written in the transformed state space as

$$\sigma(x_1, x_2) = C_1x_1 + C_2x_2, \quad (4.5)$$

where $x_1 \in \mathbb{R}^{n-m}$, $x_2 \in \mathbb{R}^m$, and matrices A_{ij}, C_i, B_1 have appropriate dimensions. Then, the computation of $\dot{\sigma}(x_1, x_2)$ (from now on $\dot{\sigma}$) yields:

$$\begin{aligned} \dot{\sigma} = & C_1\dot{x}_1 + C_2\dot{x}_2 = C_1(A_{11}x_1 + A_{12}x_2 + g_1(t)) + \\ & + C_2(A_{21}x_1 + A_{22}x_2 + B_1u + g_2(t)), \end{aligned}$$

which allows u to be expressed as follows:

$$u = -B_1^{-1}C_2^{-1}C_1(A_{11}x_1 + A_{12}x_2 + g_1(t)) + B_1^{-1}(A_{21}x_1 + A_{22}x_2 + g_2(t)) + B_1^{-1}C_2^{-1}\dot{\sigma}. \quad (4.6)$$

Notice that the previous expression for the control law includes both the low frequency component (related to the equivalent control) and the high frequency one (related to the real sliding motion). The equivalent control is easily found assuming that $\dot{\sigma} = 0$, according to its definition in Section 1.3, equation (1.6), as:

$$u_{eq} = -B_1^{-1}C_2^{-1}C_1(A_{11}x_1 + A_{12}x_2 + g_1(t)) + B_1^{-1}(A_{21}x_1 + A_{22}x_2 + g_2(t)). \quad (4.7)$$

Then, (4.6) can be updated up to:

$$u = u_{eq} + B_1^{-1}C_2^{-1}\dot{\sigma}. \quad (4.8)$$

As a consequence, the real dynamics is governed by the reduced order system:

$$\begin{aligned} \dot{x}_1 &= A_{11}x_1 + A_{12}x_2 + g_1(t), \\ \sigma &= C_1x_1 + C_2x_2, \end{aligned}$$

It is obvious to see that if (4.6) is replaced in (4.3)-(4.4), the second state space equation becomes the desired dynamics imposed by (4.5), since it consists of a linear combination of x_1 and x_2 . Hence, the previous system can also be expressed as:

$$\dot{x}_1 = (A_{11} - A_{12}C_2^{-1}C_1)x_1 + g_1(t) + A_{12}C_2^{-1}\sigma, \quad (4.9)$$

$$x_2 = -C_2^{-1}C_1x_1 + C_2^{-1}\sigma. \quad (4.10)$$

The ideal dynamics can be obtained setting $\sigma = 0$ in (4.9),(4.10), which results in the ideal sliding dynamics for x_1 , x_2 , denoted as x_1^* , x_2^* :

$$\dot{x}_1^* = (A_{11} - A_{12}C_2^{-1}C_1)x_1^* + g_1(t), \quad (4.11)$$

$$x_2^* = -C_2^{-1}C_1x_1^*. \quad (4.12)$$

Notice that now the input signal in the real dynamics is $\sigma = \sigma(t)$, where $\sigma(t)$ is the real evolution of the switching function chattering in the vicinity of $\sigma = 0$. Meanwhile, in the approach presented in Section 1.4 this role was played by $\dot{\sigma}$ (see equation (1.18)).

Remark 5. Notice that initially, in Section 1.4 a more general nonlinear system was considered in equation (1.1). In this chapter a linear system has been considered in the analysis. As a consequence, the results found hereafter only hold for linear systems.

4.2 Fixed hysteresis band

Both on the regular approach and on the classical one, it has been proved that the real and the ideal trajectories of the sliding mode are related in such a way that $\|x(t) - x^*(t)\| \leq N\Delta$, being N a positive number (see [38], [37] for details). Moreover, as the switching function is enforced to chatter around the desired space region $\sigma(x) = 0$, it is reasonable to think that $x(t)$ will chatter around the ideal response $x^*(t)$. Assuming that in the real sliding dynamics $x(t) = x^*(t)$ cannot be attained, let us see if at least, under certain conditions, the average values of both responses match. One could think that if the average value of the switching function, $\sigma(x)$, is zero, the average value of $x(t) - x^*(t)$ should converge to zero as well. The analysis of such hypotheses is developed at this stage using the regular form approach shown in the previous section.

First of all, the average value of the switching function in the case of a fixed hysteresis band is analysed through the averaging operator defined in (4.13).

$$\langle(\cdot)\rangle = \frac{1}{T} \int_{t-T}^t (\cdot) dt. \quad (4.13)$$

Recalling Figure 2.1, and assuming a piecewise linear behaviour of σ , its time evolution can be modelled as:

$$\begin{aligned} \sigma(t) &= \sigma(0) + \dot{\sigma}(x)_k^+ t & \text{for } 0 \leq t < T_k^+ \\ \sigma(t) &= \sigma(T_k^+) + \dot{\sigma}(x)_k^- (t - T_k^+) & \text{for } T_k^+ \leq t < T_k \end{aligned} \quad (4.14)$$

Applying the averaging operator, the mean value of $\sigma(t)$ is found integrating for the two time intervals: $0 \leq t < T_k^+$ and $T_k^+ \leq t < T_k$:

$$\langle\sigma\rangle = \frac{1}{T_k} \left[\left(\int_0^{T_k^+} (\sigma(0) + \dot{\sigma}(x)_k^+ t) dt \right) + \left(\int_{T_k^+}^{T_k} (\sigma(T_k^+) + \dot{\sigma}(x)_k^- (t - T_k^+)) dt \right) \right]. \quad (4.15)$$

Solving the previous integrals one gets:

$$\langle\sigma\rangle = \frac{1}{T_k} \left(\left[\sigma(0)t + \frac{\dot{\sigma}(x)_k^+}{2} t^2 \right]_0^{T_k^+} + \left[\sigma(T_k^+)t + \frac{\dot{\sigma}(x)_k^-}{2} (t - T_k^+)^2 \right]_{T_k^+}^{T_k} \right). \quad (4.16)$$

According to Figure 2.1 the following relations hold: $\sigma(0) = -\Delta$, $\sigma(T_k^+) = \Delta$ and $\sigma(T_k) = -\Delta$. Moreover, it is also obvious that $T_k^+ = 2\Delta/\dot{\sigma}(x)_k^+$, $T_k^- = -2\Delta/\dot{\sigma}(x)_k^-$ and $T_k = T_k^+ + T_k^-$. Therefore, the resulting mean value is:

$$\langle\sigma\rangle = \frac{1}{T_k} \left(-\frac{2\Delta^2}{\dot{\sigma}(x)_k^+} + \frac{2\Delta^2}{\dot{\sigma}(x)_k^+} + \frac{2\Delta^2}{\dot{\sigma}(x)_k^+} - \frac{2\Delta^2}{\dot{\sigma}(x)_k^-} + \frac{2\Delta^2}{\dot{\sigma}(x)_k^-} - \frac{2\Delta^2}{\dot{\sigma}(x)_k^+} \right) = 0. \quad (4.17)$$

Expression (4.17) confirms the suggested result with regard to the average value of σ

when it is confined within a fixed and symmetric hysteresis band. Notice that this result holds assuming a piecewise linear behaviour of σ .

Once the null average value of the switching function is confirmed, the next step is to see if $\langle \sigma \rangle = 0$ entails that $\langle x \rangle = \langle x^* \rangle$ in steady-state. For such purpose, the following assumption is made:

Assumption C. *Once the sliding mode steady-state has been reached, the switching function, σ , becomes T -periodic, with $T \in \mathbb{R}^+$, from a certain time instant.*

Theorem 4. *Assume that equations (4.9), (4.10) and (4.11), (4.12) characterize the real sliding dynamics and the ideal sliding dynamics, respectively. Consider also that Assumption C is fulfilled and that Matrix A_1 , defined as $A_1 = (A_{11} - A_{12}C_2^{-1}C_1)$ (see equations (4.9), (4.11)), is a Hurwitz matrix. Then, both systems admit asymptotically stable, T -periodic solutions \tilde{x} , \tilde{x}^* , respectively, such that*

$$\langle \tilde{x}^* \rangle = \Gamma^* \langle g_1(t) \rangle, \quad (4.18)$$

$$\langle \tilde{x} \rangle = \langle \tilde{x}^* \rangle + \Gamma \langle \sigma(x) \rangle, \quad (4.19)$$

where

$$\Gamma^* = \begin{pmatrix} -A_1^{-1} \\ C_2^{-1}C_1A_1^{-1} \end{pmatrix},$$

$$\Gamma = \begin{pmatrix} -A_1^{-1}A_{12}C_2^{-1} \\ C_2^{-1}(C_1A_1^{-1}A_{12}C_2^{-1} + \mathbb{I}) \end{pmatrix}.$$

then, since $\langle \sigma \rangle = 0$, $\langle \tilde{x} \rangle = \langle \tilde{x}^* \rangle$ holds, with $\langle \tilde{x}^* \rangle$ given by (4.18).

The proof of Theorem 4 is outlined hereunder [38].

Proof. As A_1 is Hurwitz and Assumption C is fulfilled, the existence of T -periodic, asymptotically stable solutions $\tilde{x}^\top = (\tilde{x}_1^\top, \tilde{x}_2^\top)$, $\tilde{x}^{*\top} = (\tilde{x}_1^{*\top}, \tilde{x}_2^{*\top})$ for (4.9), (4.10) and (4.11), (4.12), respectively, is ensured by basic linear systems theory ([39]). In turn, these solutions satisfy:

$$\dot{\tilde{x}}_1 = A_1\tilde{x}_1 + g_1(t) + A_{12}C_2^{-1}\sigma, \quad (4.20)$$

$$\tilde{x}_2 = -C_2^{-1}C_1\tilde{x}_1 + C_2^{-1}\sigma, \quad (4.21)$$

and

$$\dot{\tilde{x}}_1^* = A_1\tilde{x}_1^* + g_1(t), \quad (4.22)$$

$$\tilde{x}_2^* = -C_2^{-1}C_1\tilde{x}_1^*. \quad (4.23)$$

Applying the averaging operator (4.13) to (4.20), (4.22) while taking into account its linearity and the fact that $\langle \dot{\tilde{x}}_1 \rangle = 0$, $\langle \dot{\tilde{x}}_1^* \rangle = 0$, because neither $\dot{\tilde{x}}_1$ nor $\dot{\tilde{x}}_1^*$ have continuous

component but just zero averaged terms, it results that

$$\begin{aligned} 0 &= A_1 \langle \tilde{x}_1 \rangle + \langle g_1(t) \rangle + A_{12} C_2^{-1} \langle \sigma \rangle, \\ 0 &= A_1 \langle \tilde{x}_1^* \rangle + \langle g_1(t) \rangle. \end{aligned}$$

Then, it follows immediately from the Hurwitz character of A_1 that

$$\begin{aligned} \langle \tilde{x}_1^* \rangle &= -A_1^{-1} \langle g_1(t) \rangle, \\ \langle \tilde{x}_1 \rangle &= \langle \tilde{x}_1^* \rangle - A_1^{-1} A_{12} C_2^{-1} \langle \sigma \rangle \end{aligned}$$

and, subsequently from (4.21),(4.23),

$$\begin{aligned} \langle \tilde{x}_2^* \rangle &= C_2^{-1} C_1 A_1^{-1} \langle g_1(t) \rangle, \\ \langle \tilde{x}_2 \rangle &= \langle \tilde{x}_2^* \rangle + C_2^{-1} (C_1 A_1^{-1} A_{12} C_2^{-1} + \mathbb{I}) \langle \sigma \rangle. \end{aligned}$$

Now, gathering terms appropriately, (4.18), (4.19) follow immediately. \square

The previous result confirms that if $\langle \sigma \rangle = 0$, and σ is T -periodic, for a linear system the relation $\langle x \rangle = \langle x^* \rangle$ is fulfilled in steady-state. This result can be applied as long as the average value of σ becomes null in a T -periodic window. It is evident that for regulation cases, i.e. $x^* = ct$, once the steady-state sliding motion has been achieved and the switching period has been successfully regulated to the desired switching period T^* , appears a T^* -periodic behaviour of $\sigma(x)$. Since under these conditions Δ becomes constant, the mean value of σ is null and the previous result applies. Equivalently, in the tracking case scenario, this result could also be applied, even when the switching function does not have a T^* -periodic behaviour it exists a T -periodic behaviour of σ in a larger time window, T_w . In order to fit the conditions of Theorem 4, at steady-state sliding motion and with the SFC properly regulating the switching period, T_w must be a multiple of T^* and the mean value of σ during T_w should be also zero.

However, notice that the previous result does not apply in transients, neither under regulation task nor in the tracking case. Section 4.4 deals with this case, in order to see its impact in the real sliding mode.

Remark 6. *The null mean value of σ obtained in (4.17) and used in Theorem 4 takes an important relevance in this thesis, due to the fact that such null mean value was achieved under the assumption of piecewise linear behaviour of the switching function within a fixed hysteresis band. In all the theoretical developments shown in Chapter 2, the piecewise linear characteristic of σ was the hypothesis supporting the validity of the developed models. Hence, with the last result, a switching function with constant slopes in steady-state is not only useful for the validity of the SFC developments but also to guarantee that $x^* - x$, has a null mean value under certain conditions.*

4.3 Case study: the Buck converter

In order to highlight the importance of the result provided by Theorem 4, some simulations are included below using a similar system than the proposed in (3.1), (3.2).

4.3.1 Mathematical model

The proposed system is given by (4.24), (4.25), where the factor β has been included and the control action, u , takes values in the set $\{0, 1\}$, being $u^+ = 1$, $u^- = 0$.

$$\dot{x}_1 = -\beta x_1 + x_2, \quad (4.24)$$

$$\dot{x}_2 = -x_1 + Mu, \quad (4.25)$$

where M and β are real positive system parameters. Unlike the simulation shown in Chapter 3, in this case the regulated state variable is x_1 instead of x_2 . According to the relative degree, the switching function includes the regulation error and its first time derivative:

$$\sigma = \sigma(x) = \alpha (x_1^* - x_1) + \frac{d}{dt} (x_1^* - x_1), \quad (4.26)$$

being $\alpha > 0$ a surface parameter and x_1^* the reference value. Assume at this point that, following the procedure discussed in Section 3.1, the control law for u ensuring sliding motion on $|\sigma| < \Delta$ has been properly designed. Let us directly follow with the application of the regular form method introduced in Section 4.1.

The new variables are based on the errors $e = (e_1, e_2)^\top$, defined as:

$$e_1 = x_1^* - x_1, \quad e_2 = \beta x_1^* - x_2. \quad (4.27)$$

The selection of the new variables arise from x_1, x_2 related to the steady-state equilibrium point of (4.24), (4.25), which are $x_1 = x_1^*$ and $x_2 = \beta x_1^*$. Therefore, the error dynamics can be found as:

$$\dot{e}_1 = e_2 - \beta e_1 \quad (4.28)$$

$$\dot{e}_2 = -e_1 - M u + x_1^*, \quad (4.29)$$

and the switching function becomes:

$$\sigma(e_1, e_2) = (\alpha - \beta) e_1 + e_2. \quad (4.30)$$

System (4.28), (4.29) is already in regular form and matches (4.3), (4.4), and so does the switching function (4.30) with (4.5). Hence, following the procedure detailed in Section 4.1, the real dynamics (4.9), (4.10) reads in this case as:

$$\dot{e}_1 = -\alpha e_1 + \sigma, \quad (4.31)$$

$$e_2 = (\beta - \alpha) e_1 + \sigma, \quad (4.32)$$

while the ideal dynamics (4.11), (4.12) boils down to

$$\dot{e}_1^* = -\alpha e_1^*, \quad (4.33)$$

$$e_2^* = (\beta - \alpha) e_1^*. \quad (4.34)$$

Notice that, in this case, $g(t) = 0$ and $\alpha > 0$; consequently, when $\sigma = \sigma(t)$ is T -periodic within the hysteresis bandwidth ($|\sigma| < \Delta$), the hypotheses of Theorem 4, including Assumption C, are fulfilled. Hence, the solutions of (4.31), (4.32) tend asymptotically to the periodic solution $\tilde{e} = (\tilde{e}_1, \tilde{e}_2)^\top$, with \tilde{e}_1, \tilde{e}_2 related by (4.32). As for \tilde{e}_1 , a T -periodic solution for (4.31) is given by (see, for example, [40]):

$$\tilde{e}_1(t) = \frac{e^{-\alpha t}}{e^{\alpha T} - 1} \int_0^T e^{\alpha \tau} \sigma(\tau) d\tau + e^{-\alpha t} \int_0^t e^{\alpha \tau} \sigma(\tau) d\tau. \quad (4.35)$$

In turn, the solutions of (4.33), (4.34) tend asymptotically to the equilibrium point $\tilde{e}^* = 0$.

Then, according to Theorem 4, since the disturbance vector $g(t)$ is null in this case, (4.18) becomes $\langle \tilde{e}^* \rangle = 0$, while $\langle \tilde{e} \rangle$ is fulfilling (4.19), i.e.

$$\langle \tilde{e}_1 \rangle = \frac{1}{\alpha} \langle \sigma \rangle, \quad (4.36)$$

$$\langle \tilde{e}_2 \rangle = \frac{\beta}{\alpha} \langle \sigma \rangle. \quad (4.37)$$

Therefore, in case that $\langle \sigma \rangle = 0$, (4.36), (4.37) yield $\langle \tilde{e} \rangle = 0$. This implies that $\langle x_1 \rangle = x_1^*$ and $\langle x_2 \rangle = \beta x_1^*$, meaning that the average value of the real signal is exactly equal to the reference one.

4.3.2 Simulation results

A numerical analysis of system (4.24), (4.25) has been carried out with the parameter values $M = \beta = 3$. For the switching function in (4.26) we have chosen $\alpha = 1$, while the reference value for x_1 has been set to $x_1^* = 1$. In accordance with (4.27), this selection entails that the ideal steady-state value for x_2 is $x_2^* = 3$.

The simulation consists in implementing the control law of the form denoted in equation (1.13), with three different values for the hysteresis bandwidth,

$$\Delta = \begin{cases} 0.1 & \text{when } 0 \leq t < 16s, \\ 0.04 & \text{when } 16s \leq t < 30s, \\ 0.01 & \text{when } 30s \leq t < 40s, \end{cases}$$

and checking that (4.36), (4.37) are fulfilled, i.e. that the average steady-state errors $\langle e_1 \rangle$, $\langle e_2 \rangle$ verify:

$$\langle e_1 \rangle = \langle \sigma \rangle, \quad \langle e_2 \rangle = 3 \langle \sigma \rangle.$$

Let us assume that during the last instants of the time windows in which each of the three

values of Δ is active the variables have achieved a steady-state.

The tests have carried out with the software package MATLAB/Simulink (R2016b) using an ODE 5 solver with a fixed step of 10^{-5} . As for the average values, they have been extracted using a low-pass filter with transfer function

$$H(s) = \left(\frac{100}{s^2 + 18s + 100} \right)^{10}.$$

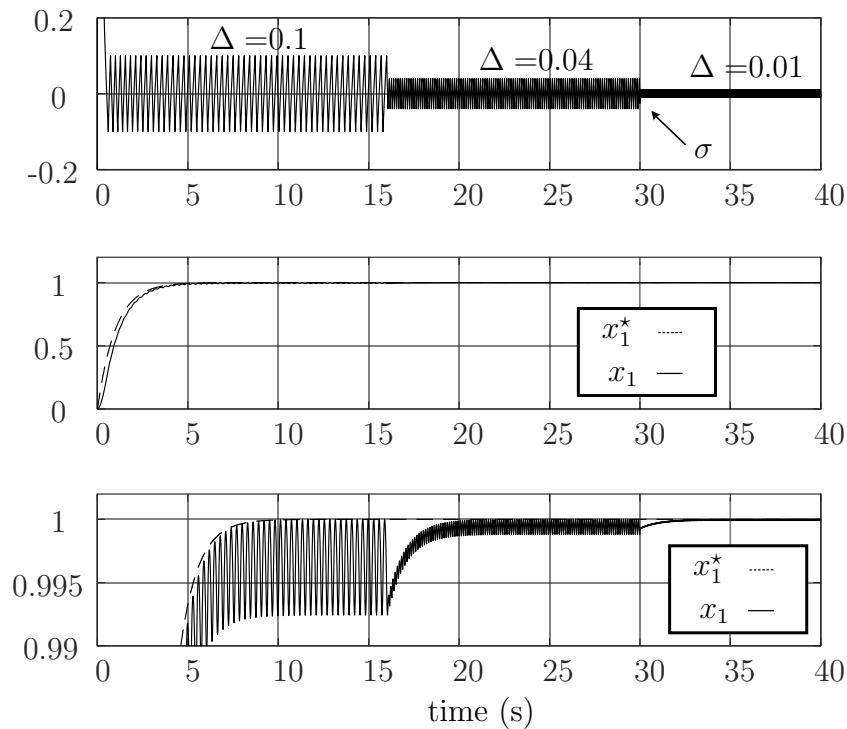


Figure 4.1: System response with different hysteresis band values. Top plot: switching function. Mid plot: state variable x_1 and its reference, x_1^* . Bottom plot: zoom of the mid plot.

The top plot in Figure 4.1 depicts the switching function, σ . As expected, the chattering amplitude is higher when $\Delta = 0.1$, and decreases while Δ does. In turn, the mid plot depicts the behaviour of the state variable x_1 with respect to its reference value and the ideal sliding dynamics one, x_1^* . The zoom in the bottom plot reveals that x_1 stabilizes closer to the reference, i.e. with less average steady-state error, and also with decreasing chattering amplitude, for lower values of Δ . From here it is confirmed how $x_1 \rightarrow x_1^*$ as $\Delta \rightarrow 0$. According to Theorem 4, if this exists a regulation error in x_1 with respect to x_1^* (as Figure 4.1 depicts, mainly when $\Delta = 0.1$), the mean value of σ should not be zero. Let us see such result with detailed zoomed views of the three cases appeared in Figure 4.1.

The top plots in Figures 4.2, 4.3 and 4.4 show the switching function and its mean value for $\Delta = 0.1$, $\Delta = 0.04$ and $\Delta = 0.01$. Notice that the signal envelope allows an easy

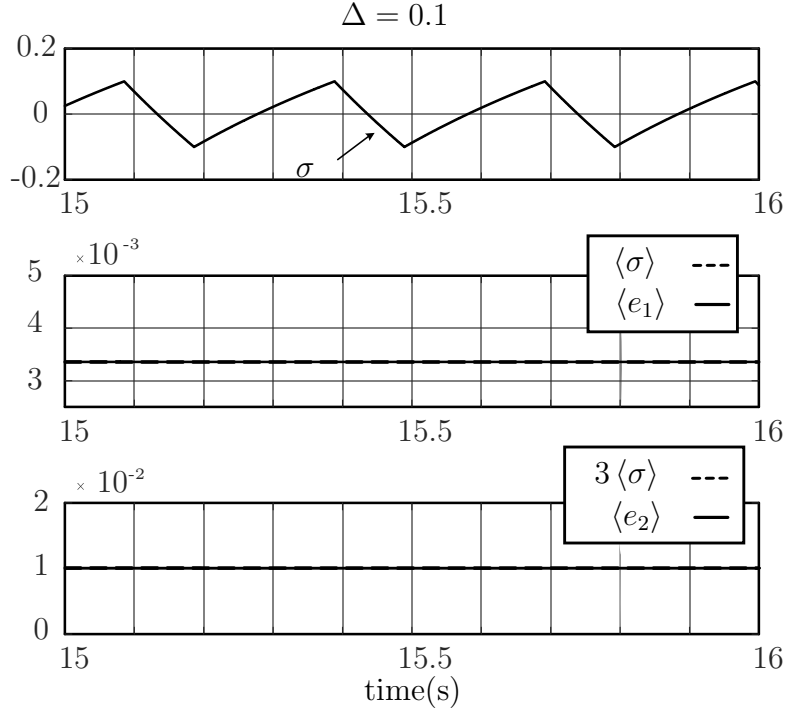


Figure 4.2: Performance for $\Delta = 0.1$ in the steady-state. Top plot: switching function. Mid plot: $\langle e_1 \rangle$ matching $\langle \sigma \rangle$. Bottom plot: $\langle e_2 \rangle$ matching $3 \langle \sigma \rangle$.

identification of the current hysteresis value. It is also worth emphasizing that, as we are in a regulation control problem and the hysteresis band is symmetric with respect to zero, the switching period of the control action achieves a constant value, T , in the steady-state, and the switching function becomes T -periodic, thus meeting Assumption C.

It is clear from the top plot in Figure 4.2 that, for the highest value of the hysteresis, namely $\Delta = 0.1$, the switching function does not show a piecewise linear behaviour. Consequently, its mean value is not zero, as confirmed by the mid plot, where it is shown to match that of e_1 , this resulting in the steady-state error for x_1 observed in the first part of the bottom plot in Figure 4.1. In turn, one can observe in Figures 4.3 and 4.4 that lower values of Δ enforce the piecewise linear character of σ within the hysteresis band, this yielding lower mean values for the respective switching functions and also for the steady-state errors of x_1 arising in Figure 4.1. In all these cases $\langle e_1 \rangle$ matches $\langle \sigma \rangle$. In turn, $\langle e_2 \rangle$ always coincides with $3 \langle \sigma \rangle$, as expected.

Hence, this confirms the theoretical predictions of Theorem 4. When the piecewise linear assumption for $\sigma(x)$ is closer to be fulfilled, the average values of σ tend to zero, and so do the average state errors, $\langle e_1 \rangle$, $\langle e_2 \rangle$. Conversely, steady-state errors appear in the state variables when the piecewise linear assumption for σ does not hold and $\langle \sigma \rangle \neq 0$. In any case $\langle e_1 \rangle$, $\langle e_2 \rangle$, match the expected values $\langle \sigma \rangle$ and $3 \langle \sigma \rangle$, respectively.

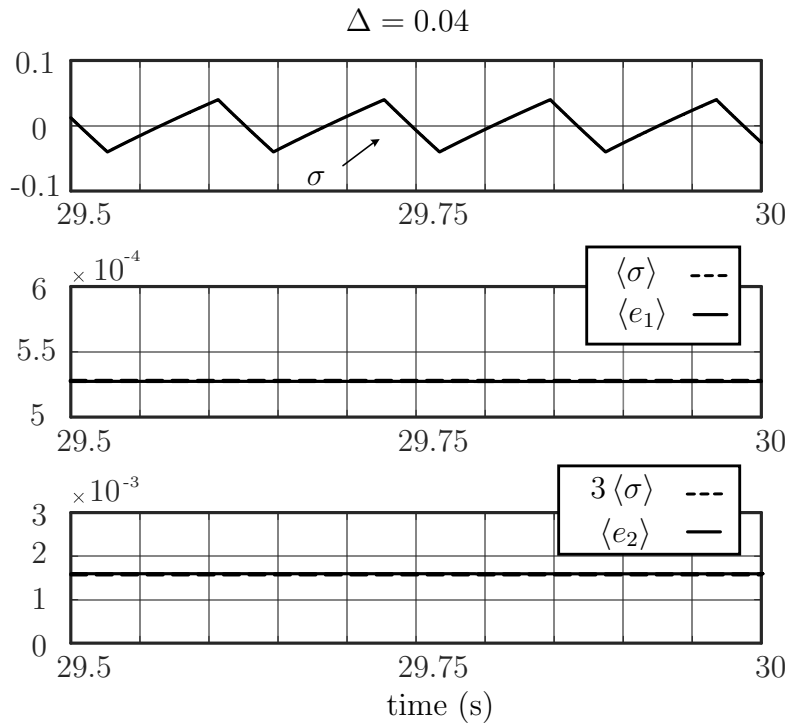


Figure 4.3: Performance for $\Delta = 0.04$ in the steady-state. Top plot: switching function. Mid plot: $\langle e_1 \rangle$ matching $\langle \sigma \rangle$. Bottom plot: $\langle e_2 \rangle$ matching $3 \langle \sigma \rangle$.

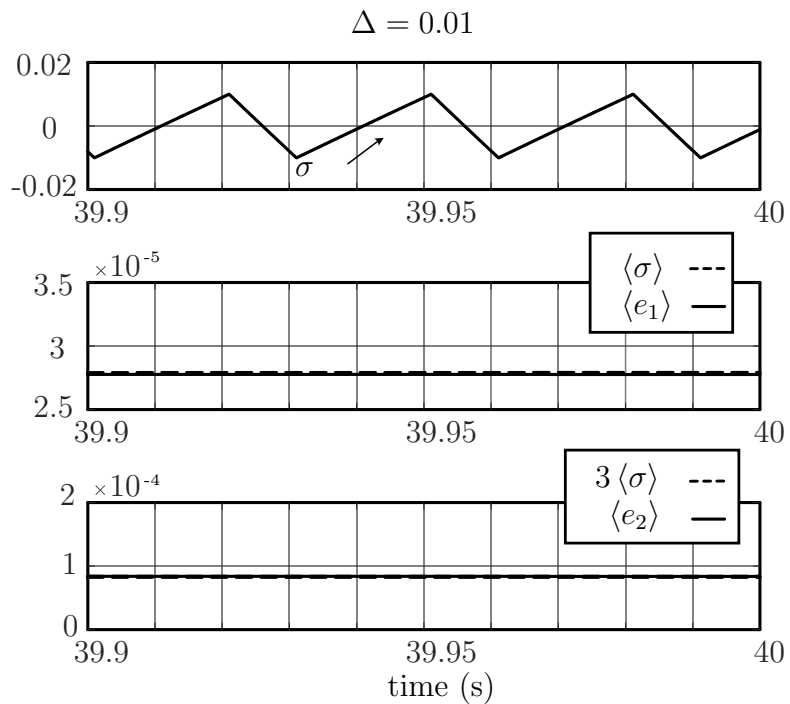


Figure 4.4: Performance for $\Delta = 0.01$ in the steady-state. Top plot: switching function. Mid plot: $\langle e_1 \rangle$ matching $\langle \sigma \rangle$. Bottom plot: $\langle e_2 \rangle$ matching $3 \langle \sigma \rangle$.

4.4 Time-varying hysteresis band

In the face of system transients the hypothesis of T -periodicity of σ does not hold. Thus, the mean value of the solutions for the real and the ideal sliding dynamics could not be equal. Nevertheless, some conclusions can be drawn in these conditions. For the purpose of studying those cases, the mean value of σ is derived for the approaches analysed in Chapter 2 in a transient scenario.

4.4.1 The regulation case

In the regulation case, regardless of the used approach (discrete-time or continuous-time), the mean value of σ will differ from zero only during transients. In the steady-state, as equations (2.13) and (2.36) reveal, the value of Δ becomes constant once the transient has disappeared and the switching period error has vanished. As a consequence, the mean value of σ is now evaluated when $\Delta_k \neq \Delta_{k-1}$.

The discrete-time approach

Related to the discrete-time approach, and as Figure 2.2 reflects, the new relations which arise are $\sigma(0) = -\Delta_{k-1}$, $\sigma(T_k^+) = \Delta_k$ and $\sigma(T_k) = -\Delta_k$. Also, from the Figure, one gets that

$$T_k^+ = \frac{\Delta_k + \Delta_{k-1}}{\dot{\sigma}_*^+}, \quad T_k^- = \frac{-2\Delta_k}{\dot{\sigma}_*^-}.$$

Of course, $T_k = T_k^+ + T_k^-$. Therefore, replacing such values in (4.16), the average value is found:

$$\langle \sigma \rangle_k = \frac{1}{T_k} \left[\frac{\Delta_k^2 - \Delta_{k-1}^2}{2\dot{\sigma}_*^+} \right] \quad (4.38)$$

and replacing (2.13) in (4.38), one gets:

$$\langle \sigma \rangle_k = \frac{\gamma e_{k-1}}{2T_k \dot{\sigma}_*^+} [2\Delta_{k-1} + \gamma e_{k-1}] \quad (4.39)$$

Figure 4.5 plots the expression in (4.39) as a function of γe_{k-1} , with $\Delta_{k-1} = 2$, and $(2T_k \dot{\sigma}_*^+)^{-1} = 1 \cdot 10^{-3}$ (notice that these chosen values are not relevant, they are only used to show the function tendency). It is simple to find out that the function in (4.39) has a minimum on $\gamma e_{k-1} = -\Delta_{k-1}$.

Recalling the controller expression of the SFC:

$$\Delta_k = \Delta_{k-1} + \gamma e_{k-1},$$

and according to Remark 1, the hysteresis values have a minimum on $\Delta_{min} > 0$, and therefore:

$$\Delta_{k-1} + \gamma e_{k-1} > \Delta_{min}, \quad \rightarrow \quad \gamma e_{k-1} > -\Delta_{k-1}.$$

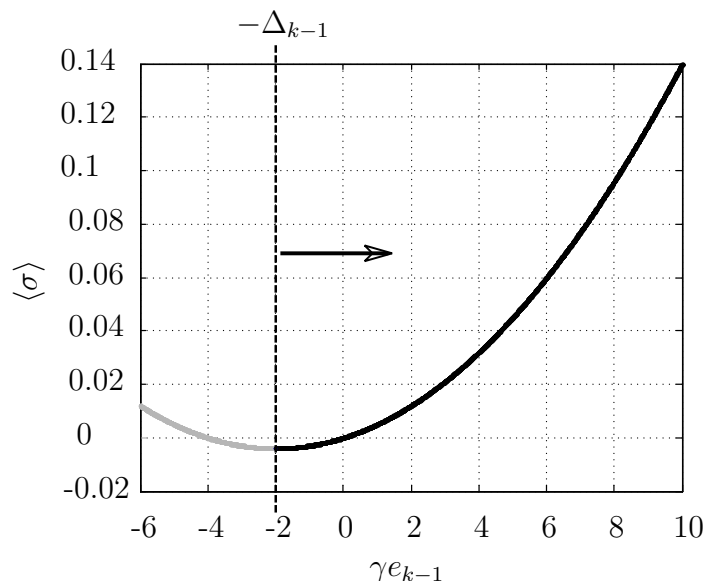


Figure 4.5: Evolution of the mean value of σ as a function of γe_{k-1} for the discrete-time approach.

As a consequence of this restriction, the value of γe_{k-1} will always live in the black zone of the curve shown in Figure 4.5. In such area, the tendency of $\langle \sigma \rangle$ with respect to the value of γ increases monotonically in absolute value. Then, it is clear that under certain conditions, (e_{k-1} can be understood as an initial condition) increasing the value of γ a higher average value (in absolute value) of σ will be produced. This means that with a proper (low enough) design of γ , the effect in the real sliding mode could also be neglected in transients.

The continuous-time approach

Let us now analyse the case for the continuous-time approach. First of all, according to Figure 2.7, the following expressions hold for this case: $\sigma(0) = -\Delta_{k-1}$, $\sigma(T_k^+) = \Delta_k^m$ and $\sigma(T_k) = -\Delta_k$. In the same way, we have:

$$T_k^+ = \frac{\Delta_k^m + \Delta_{k-1}}{\dot{\sigma}_*^+}; \quad T_k^- = \frac{-\Delta_k - \Delta_k^m}{\dot{\sigma}_*^-}. \quad (4.40)$$

Recalling (4.16), the mean value for this case is found as

$$\langle \sigma \rangle_k = \frac{1}{T_k} \left[\frac{(\Delta_k^m)^2 - \Delta_{k-1}^2}{2 \dot{\sigma}_*^+} + \frac{\Delta_k^2 - (\Delta_k^m)^2}{2 \dot{\sigma}_*^-} \right]. \quad (4.41)$$

For a proper evaluation of $\langle \sigma \rangle$, the point Δ_k^m is required (see Figure 2.7). Such point can be expressed, taking into account the $\Delta(t)$ slope given by (2.36), as a function of both Δ_k ,

Δ_{k-1} :

$$\Delta_k^m = \Delta_{k-1} \left(\frac{\dot{\sigma}_*^+ + \gamma_L e_{k-1}}{\dot{\sigma}_*^+ - \gamma_L e_{k-1}} \right) = \Delta_k \left(\frac{\dot{\sigma}_*^- + \gamma_L e_{k-1}}{\dot{\sigma}_*^- - \gamma_L e_{k-1}} \right). \quad (4.42)$$

From (4.42) it could also be derived that:

$$\Delta_k = \Delta_{k-1} \frac{(\dot{\sigma}_*^+ + \gamma_L e_{k-1})(\dot{\sigma}_*^- - \gamma_L e_{k-1})}{(\dot{\sigma}_*^+ - \gamma_L e_{k-1})(\dot{\sigma}_*^- + \gamma_L e_{k-1})}. \quad (4.43)$$

Besides, using the controller expression (see (2.36)) it is possible to find that:

$$\Delta_k = \Delta_{k-1} + \gamma_L e_{k-1} T_k. \quad (4.44)$$

Replacing equations (4.42), (4.43) and (4.44) in (4.41) the averaged values of σ boil down to:

$$\langle \sigma \rangle_k = \Delta_{k-1} \gamma_L e_{k-1} \left[\frac{(\dot{\sigma}_*^- + \dot{\sigma}_*^+) + 2\gamma_L e_{k-1}}{(\dot{\sigma}_*^+ - \gamma_L e_{k-1})(\dot{\sigma}_*^- + \gamma_L e_{k-1})} \right]. \quad (4.45)$$

The goal now is to study the tendency of the average value of σ according to (4.45) depending on γ_L value. Notice that both Δ_{k-1} and e_{k-1} can be treated as initial conditions for the analysis.

First of all, it is difficult to derive a conclusion from (4.45), since it results in a division of polynomial functions where the term of interest, $\gamma_L e_{k-1}$, appears both in the numerator and denominator. Notice that expression (4.45) is equal to zero in two points, in $\gamma_L e_{k-1} = 0$ (the origin) and in $\gamma_L e_{k-1} = -0.5(\dot{\sigma}_*^- + \dot{\sigma}_*^+)$, complicating the analysis. Moreover, in (4.45) appears the switching function slopes $\dot{\sigma}^+$, $\dot{\sigma}^-$ ($\dot{\sigma}^-$ is negative definite). These functions can be interrelated by a α parameter since, recalling (2.3), (2.4) and with $u^- = -1$ and $u^+ = 1$, one gets

$$\alpha = \frac{|\dot{\sigma}_*^-|}{\dot{\sigma}_*^+} = \frac{|-1 - u_{eq}(x)_*|}{1 - u_{eq}(x)_*}.$$

Under sliding motion the inequality $-1 < u_{eq} < 1$ holds (see Section 1.3). Therefore, a reasonable existence range for α will be $0.1 < \alpha < 10$. Thus, expression (4.45) is revisited as

$$\langle \sigma \rangle = x \frac{(1 - \alpha) + 2x}{(1 - x)(x - \alpha)}, \quad (4.46)$$

where $\varphi = \dot{\sigma}_*^+$, $x = \gamma_L e_{k-1} / \varphi$. Notice that in this case, a two variables (x , α) function is obtained. Figure 4.6 shows the different curves resulting from (4.46) when the α parameter is modified. The value of Δ_{k-1} is fixed to 1 in order to obtain a per unit analysis with respect to Δ .

As expected from the obtained expression, all the curves pass through the origin. Let try to find out the region where the term $\gamma_L e_{k-1}$ will live taking into account the design

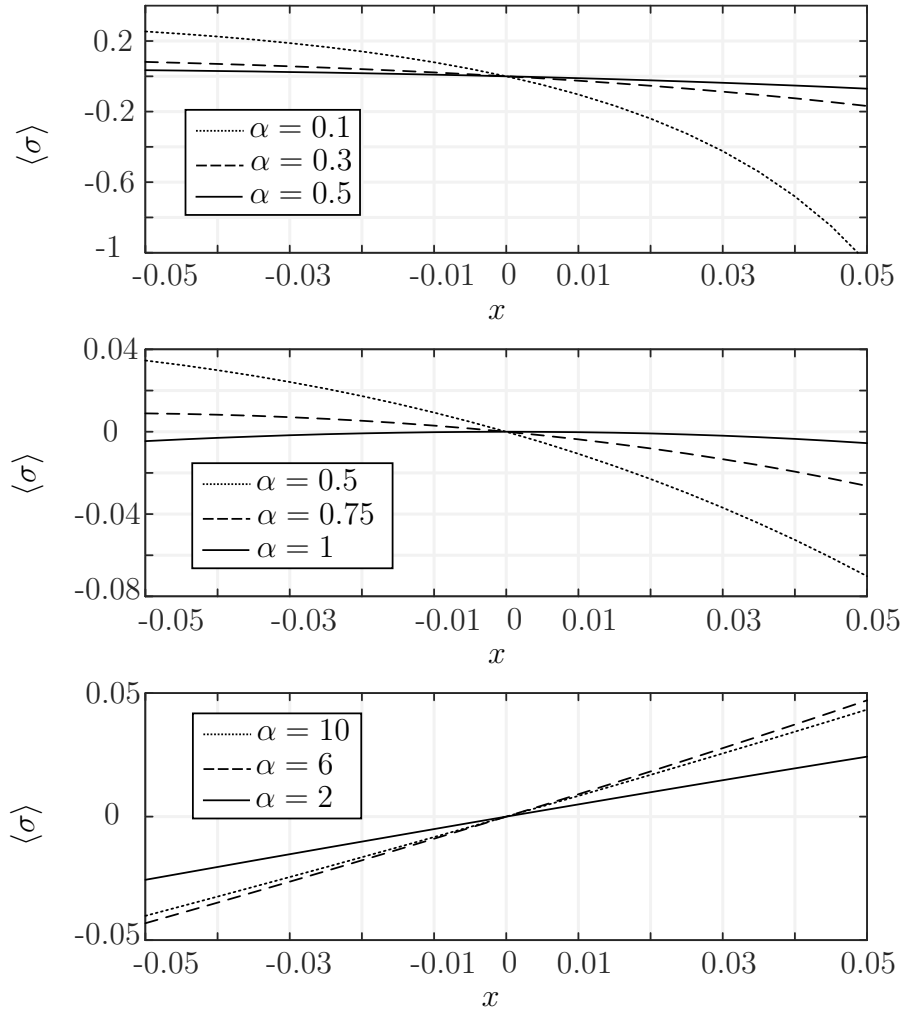


Figure 4.6: Per unit evolution of the mean value of σ as a function of $x = \gamma L e_{k-1} / \varphi$ with α as a parameter.

restrictions imposed by Assumption B. From:

$$x = \frac{\gamma_L e_{k-1}}{\varphi} \quad (4.47)$$

it is obvious that tending the γ_L value to zero, the mean value of σ also does. Moreover, according to Assumption B the design rule to be fulfilled for γ_L is:

$$|\gamma_L e_{k-1}| \ll \min \{ \dot{\sigma}_*^+, |\dot{\sigma}_*^-| \}$$

which yield for $\alpha \geq 1$

$$|\gamma_L e_{k-1}| \ll \varphi,$$

and for $\alpha \leq 1$

$$\frac{|\gamma_L e_{k-1}|}{\alpha} \ll \varphi.$$

From the previous expressions, it can be seen that with a γ_L meeting with Assumption B implies a x small, according to (4.47), even when $e_{k-1} \neq 0$. Therefore, in the allowable range of γ_L , all functions in Figure 4.6 move very close to the origin. It is also clear from the curves that, in this range, the tendency is that the mean value of σ grows in absolute value when γ_L does.

4.4.2 The tracking case

In this case we have $\Delta_k \neq \Delta_{k-1}$ in the steady-state sliding motion. Taking into account that this case was studied under a discrete-time approach, equation (4.38) holds and the mean value for each switching period interval can be computed using (2.18), (2.19) as:

$$\langle \sigma \rangle_k = \frac{1}{T_k} \left[\frac{(\gamma e_{k-1})^2 + 2\gamma e_{k-1} (\Omega_k + \Psi_{k-1}) + \Omega_k^2 - \Omega_{k-1}^2 + 2\Psi_{k-1} (\Omega_k - \Omega_{k-1})}{2\dot{\sigma}_k^+} \right] \quad (4.48)$$

Here, e_{k-1} and Ψ_{k-1} , can be considered as initial conditions, so they do not depend on γ . Similarly, the values of Ω_k , Ω_{k-1} do not vary with γ , as (2.20) confirms. The above result contemplates the steady-state and the transients and, in general, $\Omega_k \neq \Omega_{k-1}$ and $\langle \sigma \rangle$ is always different from zero. However, the function in (4.48) has again a minimum on $\gamma e_{k-1} = -(\Omega_k + \Psi_{k-1})$. In the same way, the controller expression for this approach is:

$$\Delta_k = \Omega_k + \Psi_{k-1} + \gamma e_{k-1},$$

which, according to Remark 1, it is bounded by $\Delta_{min} > 0$ since:

$$\Delta_k = \Omega_k + \Psi_{k-1} + \gamma e_{k-1} > \Delta_{min} \quad \rightarrow \quad \gamma e_{k-1} > \Delta_{min} - (\Omega_k + \Psi_{k-1}),$$

thus implying that:

$$\gamma e_{k-1} > -(\Omega + \Psi_{k-1}).$$

Therefore, in the SFC transients, where $e_{k-1} \neq 0$, if γ is increased the absolute value of $\langle \sigma \rangle$ grows, as (4.48) states (this result coincides with the one shown in (4.39) and Figure 4.5).

Moreover, it is possible to derive the expression that arises once the steady-state sliding motion is reached and the switching period has been properly regulated to the reference value. Thus, in this case, it could be considered that $e_{k-1} = 0$, and accordingly, that $\Psi_k = \Psi_{k-1} = \Psi_*$ (see equation (2.19)), yielding:

$$\langle \sigma \rangle_k = \frac{1}{T_k} \left[\frac{\Omega_k^2 - \Omega_{k-1}^2 + 2\Psi_* [\Omega_k - \Omega_{k-1}]}{2\dot{\sigma}_k^+} \right], \quad (4.49)$$

which does not depend on γ . Therefore, the value of γ values has not effect in the steady-state sliding motion. However, (4.49) discloses that in tracking scenarios there exists a mean value in σ produced by the variations of Ω with k .

As it was previously stated, in some conditions where this exists a periodicity T_w , the result of Theorem 4 could be also applied in tracking cases. Assuming that

$$N_w = \frac{T_w}{T^*}$$

and $N_w \in \mathbb{N}$, using (4.49) it is possible to evaluate the mean value of σ along the time interval T_w as

$$\langle \sigma \rangle_{T_w} = \sum_{i=2}^{N_w+2} \frac{1}{T_i} \left[\frac{\Omega_i^2 - \Omega_{i-1}^2 + 2\Psi_i [\Omega_i - \Omega_{i-1}]}{2\dot{\sigma}_i^+} \right] \quad (4.50)$$

If the previous expression becomes null, the T_w -average value of the ideal and real sliding dynamics converges.

Taking the results obtained in equations (4.39), (4.45) and (4.50) it might seem that the implementation of the SFC always affects the real sliding dynamics. The only logical conclusion that can be drawn from these results is that the real sliding dynamics is modified by the SFC with respect to fixed hysteresis band implementations, mainly during transients. However, it is difficult to state if the SFC improves or degrades the performance of the sliding mode control with respect to the classical approach, i.e the fixed hysteresis band. Nevertheless, such mean value is bounded by the hysteresis band used, as the following Remark indicates.

Remark 7. *The mean value of σ under sliding motion is bounded by the maximum hysteresis band value, Δ_{max} . Thus,*

$$|\langle \sigma \rangle| < \Delta_{max}.$$

According to Remark 1, the maximum value of Δ must be defined so that the produced high frequency ripple on the state variables (x) is small with respect to the low frequency

dynamics of x . As a consequence, whatever mean value appearing on x due to the variation of the hysteresis band, as (4.49) states, will be negligible with respect to x^* .

4.4.3 Simulation results

In order to show the effect of the SFC transients in the SMC performance, a simple simulation is done. Using the system introduced in Section 4.3.2, a sudden variation of the switching period reference is applied enforcing a SFC transient. The values of γ (γ_L) will be designed in order to show how higher values of γ (γ_L) will imply a higher impact in the state variables behaviours. The simulation depicts the transient detail of T_k following the variation of T^* . This transient will be tested with two different values of γ (γ_L), designed so that one of them produces a soft transient in T_k , and the other an underdamped one. Let us calculate the values of ρ_*^\pm (related to the steady-state sliding motion) for the simulated system in Section 4.3.2. Using (4.26) the first time derivative of σ for the steady-state sliding motion can be found assuming that $x_1 = x_1^*$ and $x_2 = \beta x_1^*$:

$$\dot{\sigma}^* = x_1^* - Mu. \quad (4.51)$$

Using the values provided in Section 4.3.2 for x_1^* and M , and according to the ρ_*^\pm definition in (2.2), one gets:

$$\rho_*^+ := \frac{1}{\dot{\sigma}^*|_{u=0}}, \quad \rho_*^- := \frac{1}{\dot{\sigma}^*|_{u=1}}.$$

Hence,

$$\rho_*^+ = 1, \quad \rho_*^- = -0.5.$$

Regulation case: the discrete-time approach

Firstly, the discrete-time approach is simulated (Section 2.2.1, equation (2.13)). The characteristic polynomial of the SFC for this case is (according to (2.16)):

$$p(z) = z^2 + z(2\gamma - 1) + \gamma,$$

and the selected values for γ for the aforementioned purpose are: $\gamma = 0.05$ and $\gamma = 0.5$, which lead to the following closed-loop poles:

$$\gamma = 0.05; \quad p_{z_1} = 0.8405, \quad p_{z_2} = 0.0595$$

$$\gamma = 0.5; \quad p_{z_1} = 0.7071i, \quad p_{z_2} = -0.7071i.$$

Notice how the chosen values for γ provide poles in the real axis for a soft transient response for the case $\gamma = 0.05$, becoming complex for $\gamma = 0.5$. The resulting poles are within the unit circle in both cases, thus confirming stable SFC responses. The simulation for both cases are shown in Figures 4.7, 4.8. The signals depicted in the Figures are structured as follows. In the top plot the switching function, σ , and the hysteresis bandwidth generated

by the SFC are depicted. In the mid plot the switching period reference, T^* , and real switching period, T_k , are shown. Finally, the bottom plot presents the behaviour of x_1 and the mean value of σ . In this case, the low pass filter detailed in Section 4.3.2 measuring the average value is substituted by the operator shown in (4.13) computed one time per switching period. As a consequence, such mean value is delayed one switching interval.

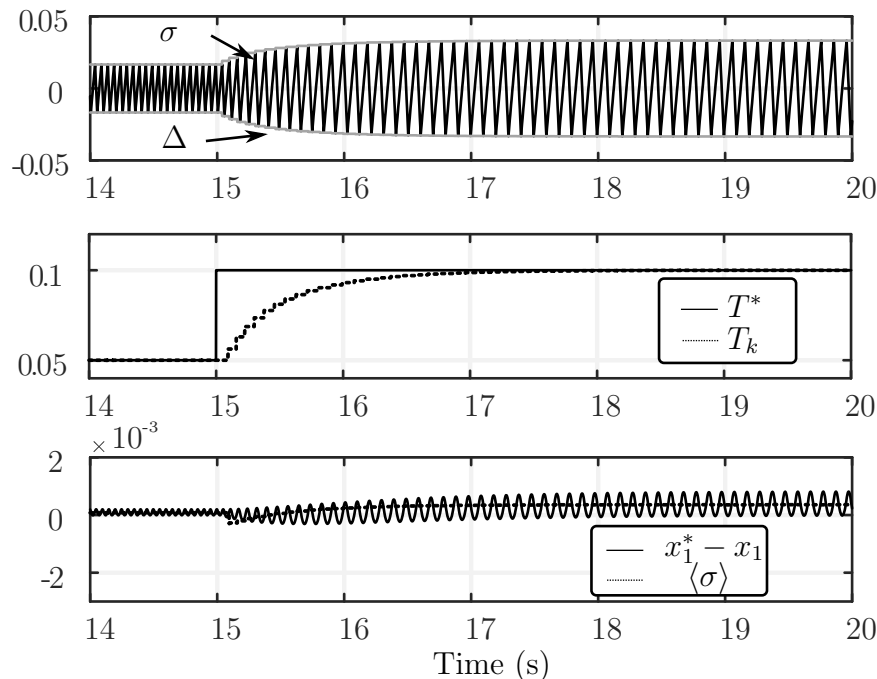


Figure 4.7: Mean value impact on σ in the face of a switching period transient with the discrete-time approach. $\gamma = 0.05$.

First of all, it should be noted that sliding motion is preserved during the entire test, since σ is perfectly confined within the hysteresis bandwidth during the transients (see top plots of Figures 4.7 and 4.8). Similarly, the proper regulation of T_k to T^* in the transients is also confirmed from the mid plots of Figures 4.7, 4.8. From the results on the bottom plots, it is obvious that the signal x_1 is highly perturbed when the transient in the SFC is faster (Figure 4.8, $\gamma = 0.5$), being such perturbation smaller when $\gamma = 0.05$ is used (Figure 4.7). This result coincides with the result obtained in (4.39), as the mean value of σ is proportional to the used γ . Furthermore, it is worth remarking that the simulations in Figures 4.7 and 4.8 corroborate the result of Theorem 4, since the mean values of σ and $x_1^* - x_1$ only match at steady-state, when Δ is constant and σ becomes T^* -periodic.

Regulation case: the continuous-time approach

The same simulation has been performed using the SFC in the continuous-time approach (see Section 2.3, equation (2.35)). The previous calculus for ρ_*^\pm hold for this approach, which yields $\alpha = 2$ ($\dot{\sigma}_*^+ = 1$, $\dot{\sigma}_*^- = -2$). The initial condition of e_{k-1} is 0.05 and the values

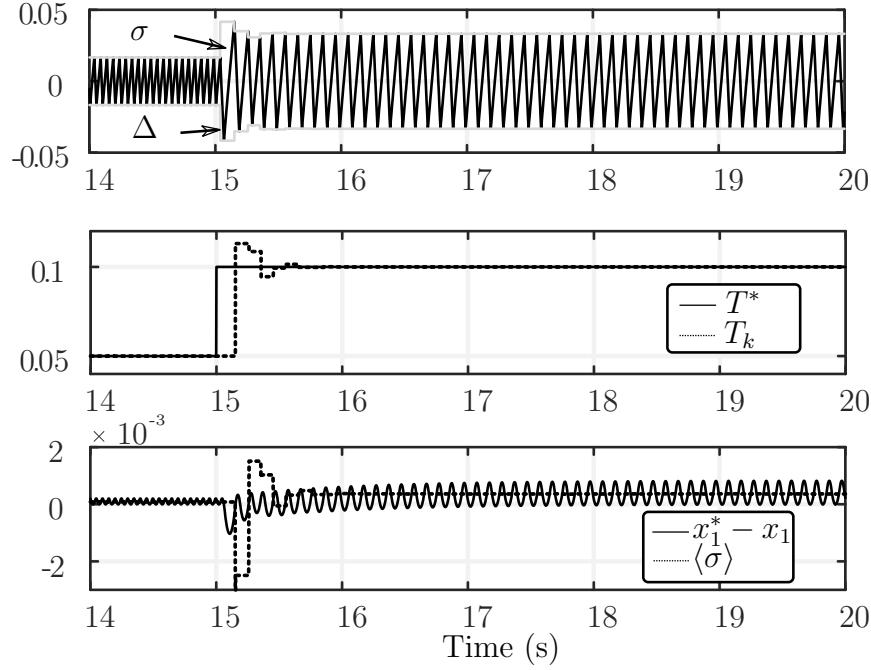


Figure 4.8: Mean value impact on σ in the face of a switching period transient with the discrete-time approach. $\gamma = 0.5$.

for γ_L in order to produce a smooth and a fast transient in T_k are $\gamma_L = 0.5$ and $\gamma_L = 2.5$, respectively.

From the direct comparison of the results in Figures 4.9, 4.10, the analysis made in Section 4.4.1 can be validated, since the use of a higher value of γ_L increases the mean value of σ during the transient.

The tracking case

The system simulated in Section 4.3.2 is now tested with a time-varying reference for x_1 , in order to check the mean value of σ . In this case, the simulation results are focused in the steady-state operation, as the transient effects are essentially the same than the ones shown in Figures 4.7, 4.8, because the approach to adjust the hysteresis values is the same. The objective here is to check if the mean value of σ during a larger time interval, T_w , presents a periodic behaviour, and it could become zero when averaging it in T_w . The time-varying reference for this case is:

$$x_1^* = 2 \sin(2 \cdot 0.02 \pi t),$$

keeping $T^* = 0.1$ s as the desired switching period. For the tracking case, the system is slightly modified, including a control action taking $u^+ = 1$ and $u^- = -1$ (see (4.24), (4.25)). With this configuration, the system is able to track references without offset. The SFC structure is the corresponding to a tracking approach, (Section 2.2.2, Figure 2.6, Equations

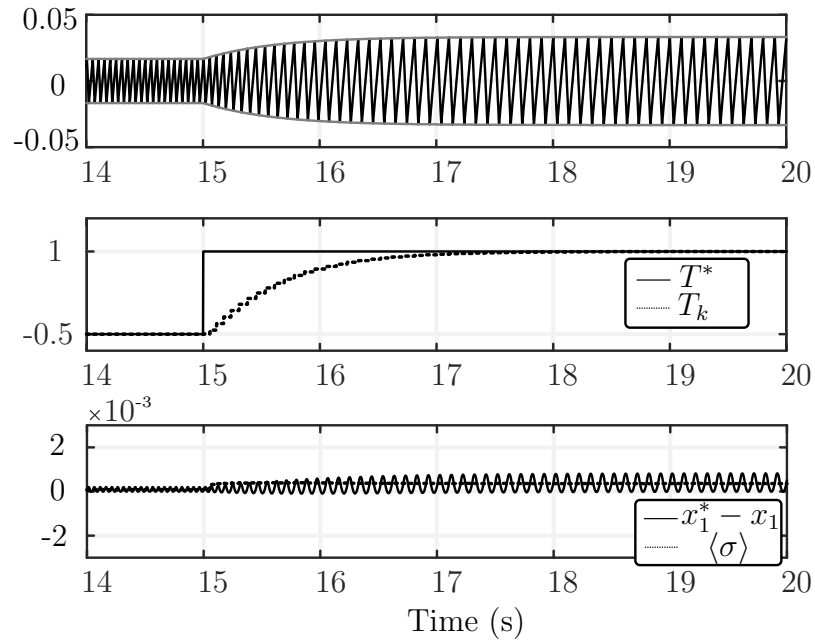


Figure 4.9: Mean value impact on σ in the face of a switching period transient with the continuous-time approach. $\gamma_L = 0.5$.

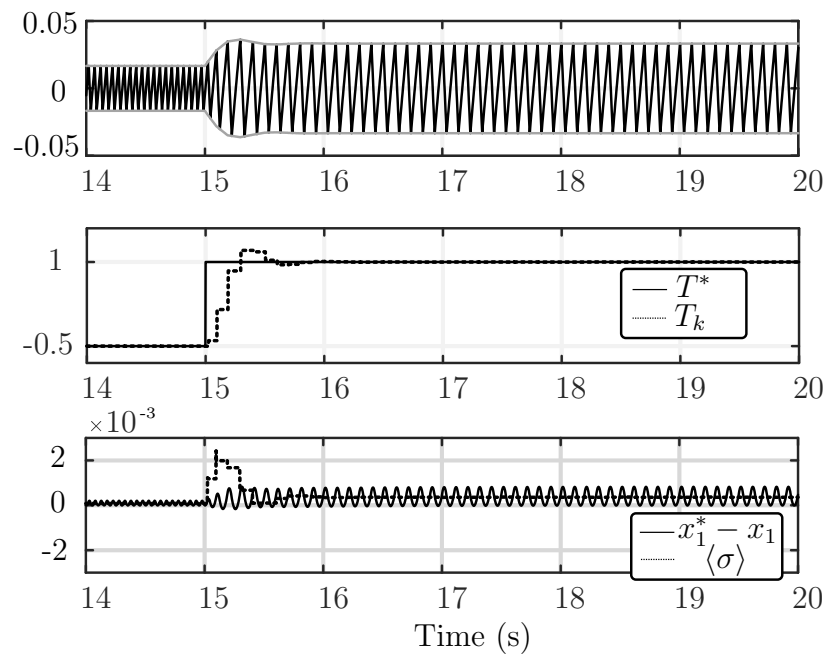


Figure 4.10: Mean value impact on σ in the face of a switching period transient with the continuous-time approach. $\gamma_L = 2.5$.

(2.18), (2.19) and (2.20)). The control gain is set to $\gamma = 0.5$ according to Theorem 2.

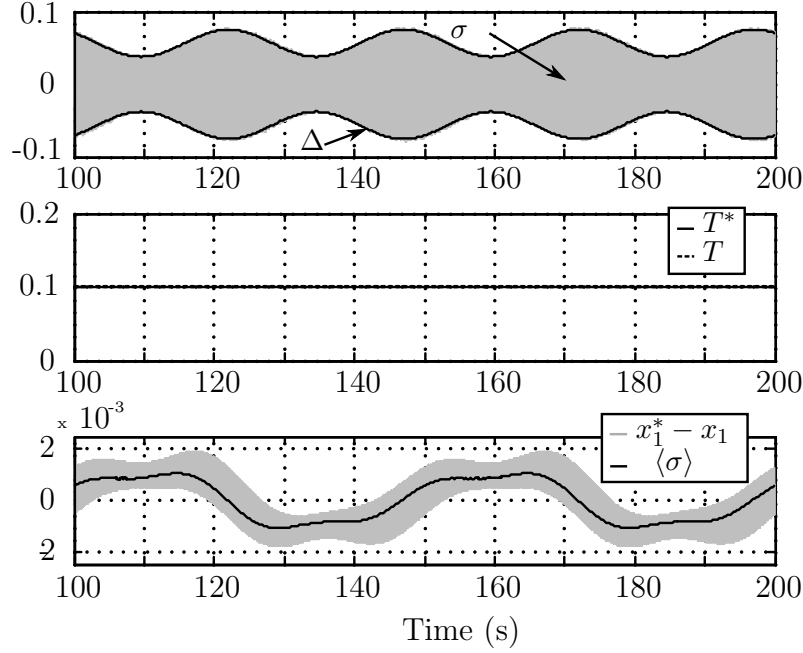


Figure 4.11: Steady-state mean value of σ in the tracking case with SFC, $\gamma = 0.5$.

Figure 4.11 shows: the switching function and the hysteresis band in the top plot, the desired and real switching periods in the mid plot and the tracking error together with the average value of σ in the bottom plot. It should be noticed that the mean value of σ has been calculated using the operator shown in (4.13) at any switching period, T . From Figure 4.11, the proper SFC function is confirmed, since T^* and T perfectly fit (mid plot). The interesting result is located in the bottom plot, where a periodic behaviour of $\langle \sigma \rangle$ is observed (the showed time interval corresponds exactly to a two periods of $T_w = 50$ s). Due to the symmetry of the signal, it is not unreasonable to assume that the mean value of σ along a time interval of $T_w = 50$ s is null.

Notice how $\langle \sigma \rangle$ is close to the averaged tracking error defined as $e_v = x_1^* - x_1$, since the expression enforced by the sliding motion (see (4.26)):

$$\sigma = \alpha e_v + \dot{e}_v,$$

always holds. Performing the Laplace transform, the previous expression reveals that $\langle \sigma \rangle$ is the result of low-pass filtering e_v .

Finally, it has been considered interesting to show the same result in Figure 4.11 but with a fixed hysteresis band. The results are shown in Figure 4.12. The difference, aside that a fixed hysteresis value produces time-varying switching periods, relies in the different mean values produced in σ . By direct comparison with Figure 4.11, it can be noted that the maximum value of the mean value is slightly higher when the hysteresis band is fixed. Again, the mean value of σ matches the averaged tracking error.

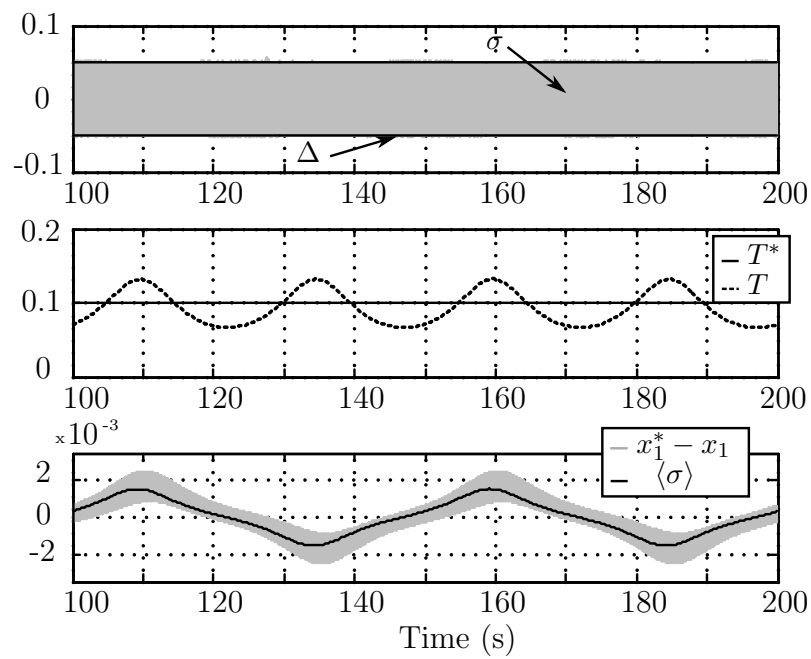


Figure 4.12: Steady-state mean value of σ in the tracking case with fixed hysteresis band, $\Delta = 0.05$.

Part III

Application of the Proposed Solution to Power Converters.

Chapter 5

Voltage Regulation in a Buck Converter.

At this stage, the discrete-time approach of the SFC is experimentally tested in a DC-DC Buck converter for evaluation purpose. The state space equations modelling the Buck converter behaviour correspond to a linear system. In this case, the SMC will regulate the converter output voltage, becoming a regulation task for a time invariant linear system. The SFC will be implemented by a mid-range micro-controller (μC), whereas the SMC will be assembled by means of analog circuitry. The Chapter is structured as follows: in the first Section the power converter is presented, where its state space equations and parametric values are introduced. Then, the SMC controller is designed for regulating the output voltage. The next step develops the studies required for properly tuning the SFC. Finally, the implementation issues and the experimental results are presented.

5.1 The Buck Converter

The Buck converter circuit scheme is shown in Figure 5.1. Table 5.1 lists the parameter values of the experimental prototype.

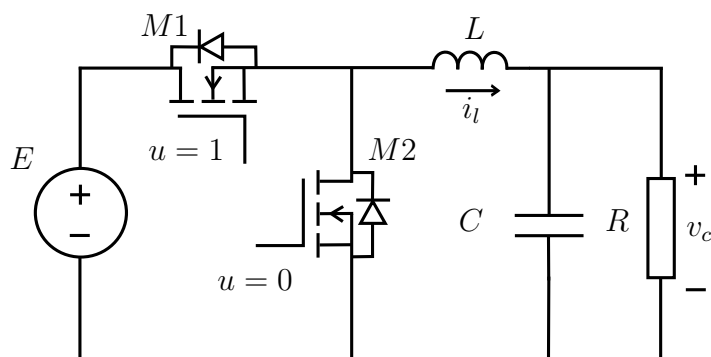


Figure 5.1: Buck converter.

The linear state space equations [2] of the Buck converter are:

$$C \frac{dv_c}{dt} = i_l - \frac{v_c}{R} \quad (5.1)$$

$$L \frac{di_l}{dt} = E u - v_c, \quad (5.2)$$

where the control action u takes values from the set $\{0, 1\}$, E is the input voltage, v_c the output voltage and L, C, R are the inductance, the capacitance and the resistive load, respectively. The power switches $M1$ and $M2$ work in a complementary manner, remaining closed when u takes the value showed in Figure 5.1.

Table 5.1: Buck converter parameters

| Parameter | Symbol | Value |
|----------------------------|---------|------------|
| Input voltage | E | 48 V |
| Desired output voltage | v_c^* | 12-24 V |
| Inductor | L | 22 μ H |
| Output capacitor | C | 50 μ F |
| Nominal load resistance | R | 2 Ω |
| Switching period reference | T^* | 10 μ s |

The Buck converter is characterized by its input-output step-down property, and the output voltage, v_c , is always lower than its input, E . This converter is widely used in several fields such industrial, communications, appliances, etc [41–45]. The control objective usually comes from the necessity to regulate its output voltage for different load levels.

5.2 Sliding mode control of the Output voltage

5.2.1 Switching surface design

Because of the relative degree of the control input with respect to the output voltage is two, in order to make possible the existence of the sliding motion, the chosen switching surface for regulating the output voltage is (see Section 1.3):

$$\sigma(v_c, i_l) := \lambda_1 e_v + C \lambda_2 \dot{e}_v = 0, \quad (5.3)$$

being $\lambda_{1,2} > 0$. The voltage error has been defined as $e_v = v_c^* - v_c$, responding v_c^* to the desired output voltage.

5.2.2 Sliding dynamics

Following the methodology shown at Sections 1.3, 1.4, the switching function time derivative is calculated and shown in (5.4):

$$\dot{\sigma}(v_c, i_l) = f_1(v_c, i_l) - \frac{\lambda_2}{L} E u, \quad (5.4)$$

where

$$f_1(v_c, i_l) = \lambda_1 \dot{v}_c^* + C \lambda_2 \ddot{v}_c^* + i_l \left(\frac{\lambda_2}{RC} - \frac{\lambda_1}{C} \right) + v_c \left(\frac{\lambda_1}{RC} + \frac{\lambda_2}{L} - \frac{\lambda_2}{R^2 C} \right). \quad (5.5)$$

In general, \dot{v}_c^* and \ddot{v}_c^* can be considered null since a regulation control problem is considered. According to equation (5.4), the sliding motion can be enforced in $\sigma(v_c, i_l) = 0$ if

$$0 < f_1 < \frac{\lambda_2 E}{L}. \quad (5.6)$$

The ideal sliding dynamics can be studied through the equivalent control method, which assumes that the system trajectories are exactly on the surface and remain there, entailing $\sigma(v_c, i_l) = 0$ and $\dot{\sigma}(v_c, i_l) = 0$. Hence, the equivalent control is found in (5.7).

$$u_{eq} = \frac{L}{E \lambda_2} f_1(v_c, i_l). \quad (5.7)$$

Under sliding motion, the output voltage dynamics is characterized by (5.3), thus:

$$C \frac{dv_c}{dt} = -\frac{\lambda_1}{\lambda_2} v_c + \frac{\lambda_1}{\lambda_2} v_c^* + C \dot{v}_c^*. \quad (5.8)$$

The remaining dynamics of the inductor current can be derived placing (5.7) in the system equations (5.2), yielding

$$L \frac{di_l}{dt} = \frac{L}{C} \left(\frac{1}{R} - \frac{\lambda_1}{\lambda_2} \right) \left(i_l - \frac{v_c}{R} \right).$$

Therefore, the system dynamics under sliding motion is governed by:

$$C \frac{dv_c}{dt} = -\frac{\lambda_1}{\lambda_2} v_c + \frac{\lambda_1}{\lambda_2} v_c^* + C \dot{v}_c^* \quad (5.9)$$

$$L \frac{di_l}{dt} = \frac{L}{C} \left(\frac{1}{R} - \frac{\lambda_1}{\lambda_2} \right) \left(i_l - \frac{v_c}{R} \right). \quad (5.10)$$

The equilibrium point of the previous system, $(v_c = v_c^*, i_l = v_c^* R^{-1})$, is asymptotically stable if

$$0 < \frac{1}{R} < \frac{\lambda_1}{\lambda_2} \quad (5.11)$$

is fulfilled.

5.2.3 Control law

The control law that guarantees sliding motion on $\sigma(v_c, i_l) = 0$ is:

$$u = \begin{cases} 0 & \text{if } \sigma < -\Delta_k \quad \text{or } (|\sigma| < \Delta_k \ \& \ \dot{\sigma} > 0) \\ 1 & \text{if } \sigma > \Delta_k \quad \text{or } (|\sigma| < \Delta_k \ \& \ \dot{\sigma} < 0). \end{cases}$$

Once the SMC has been designed, the values of the switching function can be now set according to a desired dynamics for the output voltage, employing (5.8). Using the values listed in Table 5.1, the selected values are $\lambda_1 = 0.2$ and $\lambda_2 = 0.38$, which deliver a good transient response with a time constant of 100 μs .

5.3 Switching frequency regulation

As it was briefly introduced, the discrete-time approach is used for regulating the switching frequency of the control action previously designed.

5.3.1 Evaluation of ρ_k^\pm

In order to select the parameter gain γ for the SFC, ρ_k^+ and ρ_k^- are required. Since the problem is intended for regulating a constant voltage at the converter output, such values are particularized to a specific working point, where such values will be treated as parameters, i.e. ρ_*^+ and ρ_*^- . Recalling again (5.4) and (5.7) one gets:

$$\dot{\sigma}(v_c, i_l) = \frac{\lambda_2}{L} E (u_{eq} - u). \quad (5.12)$$

It should be remarked that in this case the working point ($v_c = v_c^*$, $i_l = v_c^* R^{-1}$) leads to an equivalent control that only depends on v_c^* and E (see equation (5.7)). Therefore, (5.12) boils down to:

$$\dot{\sigma}(v_c^*, i_l^*) = \frac{\lambda_2}{L} (v_c^* - E u) \quad (5.13)$$

where $u = u^+ = 1$ or $u = u^- = 0$. According to Section 2.1, the values for ρ_*^\pm are defined as follows:

$$\rho_*^+ = [\dot{\sigma}(v_c^*, i_l^*)_{u=u^-}]^{-1} = \frac{L}{\lambda_2 v_c^*}$$

$$\rho_*^- = [\dot{\sigma}(v_c^*, i_l^*)_{u=u^+}]^{-1} = \frac{L}{\lambda_2 (v_c^* - E)}.$$

Using the data given by Table 5.1, the values are:

$$\begin{aligned} v_c^* = 12 \text{ V} &\rightarrow \rho_*^+ = 4.82 \cdot 10^{-6}; \rho_*^- = -1.61 \cdot 10^{-6}, \\ v_c^* = 24 \text{ V} &\rightarrow \rho_*^+ = 2.41 \cdot 10^{-6}; \rho_*^- = -2.41 \cdot 10^{-6}. \end{aligned}$$

5.3.2 SFC design

The value of γ has to be chosen to guarantee stability of the SFC loop, hence, according to Theorem 1, γ values below $2.07 \cdot 10^5$ implies stability for the 12 V case, being such bound equal to $4.15 \cdot 10^5$ for the 24 V one. Therefore, the stability range becomes $0 < \gamma < 2.07 \cdot 10^5$. The preferred used value for the experimental evaluation will be $\gamma = 2 \cdot 10^4$, although it will be varied for a specific test, as it will be explained. Specifically, for the 12 V case and $\gamma = 2 \cdot 10^4$, the characteristic polynomial results in:

$$p(z) = z^2 - 0.84z + 0.0972$$

where the poles result real and equal to $z_{p1} = -0.138$ and $z_{p2} = -0.7$. Similarly, for 24 V the polynomial results in

$$p(z) = z^2 - 0.885z + 0.048$$

also with real poles equal to $z_{p1} = -0.058$ and $z_{p2} = -0.825$. As a consequence, an overdamped response is expected in all the cases.

5.4 Implementation Details

Before showing the experimental results, some aspects about the implementation methodology are briefly discussed. The implementation of the switching function and the hysteresis comparator have been carried out with analog electronics, as Figures 5.2 depicts.

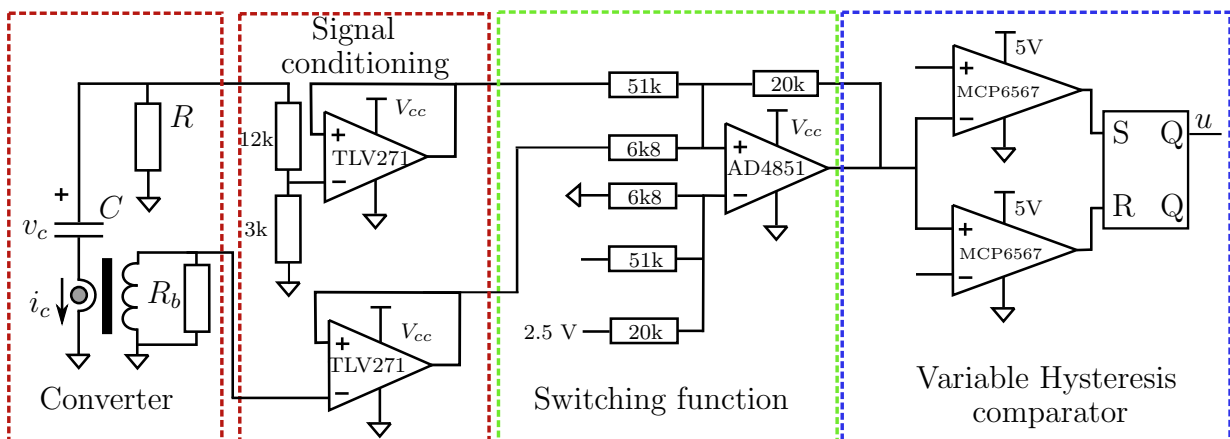


Figure 5.2: Implementation details: the SMC with a variable hysteresis comparator is implemented using analog circuitry.

As it is shown in Figure 5.2, the output voltage is measured through a resistive voltage divider. With regard to the time derivative of v_c , which is required by (5.3), it should be remarked that to perform the time derivation directly over the measured v_c is quite problematic due to the amplification of the switching noise. Instead, a very common strategy [46] is used here, which consists in to measure the current flowing by the output capacitor, i_c , since:

$$i_c = C \frac{dv_c}{dt}.$$

Such measurement is performed with a high frequency current transformer, as it is represented in Figure 5.2. In fact, this is the reason to include C in the switching surface (see (5.3)). The Figure also shows the switching function implementation, which it is based on a common configuration with operational amplifiers (AO). Finally, in the right side block of the Figure, the chosen structure of the variable hysteresis band comparator can be observed, where two high speed comparators together with a Set-Reset flip flop provide the desired operation.

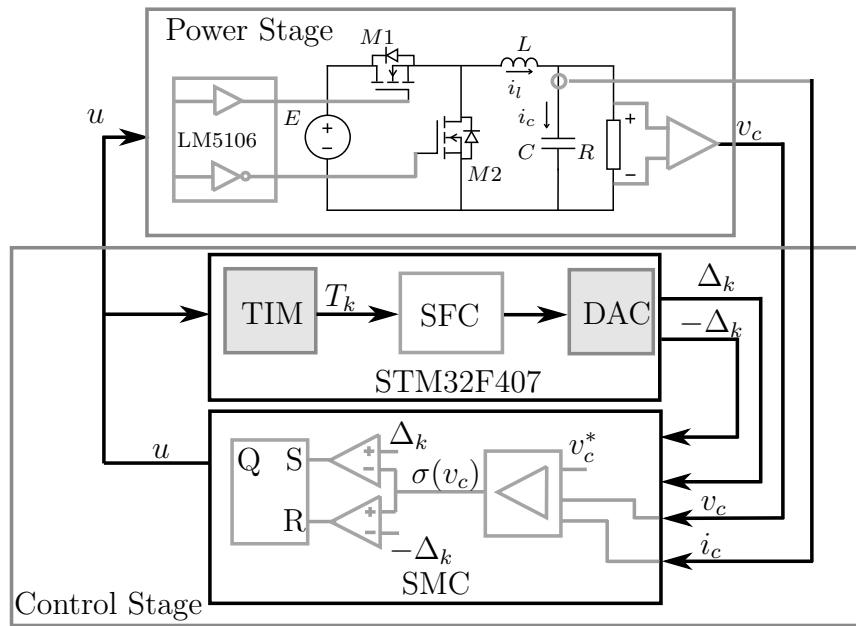


Figure 5.3: Implementation details: the SFC is implemented using the DSP STM32F407.

With regard to the SFC implementation, it is carried out using digital resources. Specifically, the switching period measurement and the generation of hysteresis band values have been performed with the μC STM32F407. Nevertheless, any mid-range performance μC can be used for this purpose, because the system only needs a capture timer peripheral for the switching period measurement, and a digital to analog module (DAC), for updating the hysteresis value. For the switching period measurement, a 32 bits timer (TIM) is programmed as an input capture timer, in the sense that is able to measure the period of u . This TIM is clocked at 168 MHz (CPU clock), which delivers a resolution of 9 ns, enough

for the desired value of $T^* = 10 \mu\text{s}$. Figure 5.3 details the main parts of both controllers (SMC and SFC) denoting the complete scheme of the experimental setup.

The TIM used for measuring the switching period is also employed to synchronize the SFC operation with the control signal u , since for each capture event (rising edge of u) a CPU interrupt is generated. A control routine is associated to such interrupt, where the SFC is implemented. Although the c code routine only needs to do a subtraction, an addition and a multiplication to compute the new hysteresis value, it is important to take into account the amount of time, t_c , that the CPU spends for the execution of the SFC code. In the analysis developed in Section 2.2 this effect was not considered. This computing time, t_c , is shown in Figure 5.4.

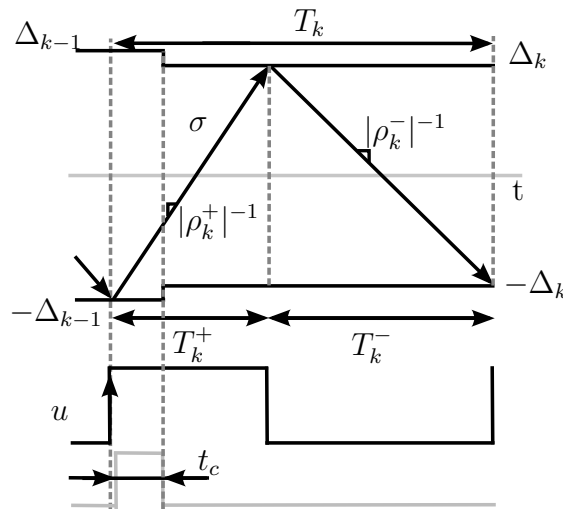


Figure 5.4: Implementation details: effect of the computing time, t_c , in the discrete-time approach of the SFC.

From the Figure, it can be inferred that in conditions where t_c exceeds T_k^+ , from a rigorous point of view, the expression (2.1) should be revisited. For example, in the simplest case where $t_c > T_k^+$ and $t_c < T_k$ the equation (2.1) should be replaced by $T_k = 2 \Delta_{k-1} [\rho_k^+ - \rho_k^-] + \rho_k^- [\Delta_{k-1} - \Delta_k]$. For that expression, all the stability study should be revisited for the SFC stability conditions, as it was presented in Section 2.2. Indeed, whatever relation between t_c and T_k could be considered and analysed in an equivalent procedure.

The expected value for T_k^+ in this experimental evaluation can be estimated using the equivalent control method and the desired switching period. From (5.5) and (5.7), taking into account that the equilibrium point for the designed system is $(v_c = v_c^*, i_l = v_c^* R^{-1})$, the equivalent control in the steady-state sliding motion for the 12 V case at the output becomes:

$$u_{eq} = \frac{v_c^*}{E} = \frac{12}{48} = 0.25,$$

hence

$$T_k^+ = 0.25 \cdot T^* = 2.5 \mu\text{s}.$$

In that case, the computing time results in $t_c = 1.4 \mu s$ (empirically measured using an oscilloscope), while the expected value of T_k^+ is $2.5 \mu s$, thus confirming the usefulness of (2.1).

Finally, an additional aspect about this implementation methodology is discussed. It exists a relation between the resolutions of the used TIM and DAC devices [29]. If the resolution of the DAC is higher than the resolution of the TIM, the hysteresis values could oscillate between two values in steady-state. For this reason, it is advisable to use a TIM with a higher resolution than the DAC one in order to ensure that the hysteresis value becomes constant in steady-state. This effect is also related with the integral gain γ , since the grade of change of Δ ($\Delta_k - \Delta_{k-1}$) is, from (2.13), $e_k \gamma$, and e_k inherits the timer resolution. Therefore, in order to avoid oscillations in the system due to the resolutions of the used peripheral, the inequation (5.14) has to be fulfilled:

$$DAC_R > \gamma TIM_R, \quad (5.14)$$

being DAC_R and TIM_R the corresponding peripheral resolutions.

5.5 Experimental results

The experimental results are presented at this stage. In the following oscilloscope captures, the switching period, T_k , appears converted to voltage with a rate of $0.35 V/\mu s$. Due to implementation aspects, σ has an offset of $2.5 V$ (as it was shown in Figure 5.2). Unless otherwise noted, the SFC gain is set to $\gamma = 2 \cdot 10^4$.

1. SMC performance

The star-up of the converter is illustrated for two different initial values of Δ in Figures 5.5 and 5.6. In these cases the output voltage is regulated to $12 V$. The initial values of Δ have been selected as they become smaller and higher than the steady-state one.

Notice that both v_c and T_k attain their references with a good transient response, while the hysteresis band is adapting till T_k reaches T^* . From both responses, the expected overdamped characteristic can also be confirmed, according to the designs developed at Sections 5.2, 5.3. The switching period, T_k , can be easily measured observing the switching function in the zoomed windows (green signals at the bottom parts of the Figures). As it is noted in (2.13), once T_k reaches the desired value, the hysteresis band Δ_k becomes constant.

In Figure 5.7 a voltage regulation from 12 to $24 V$ and vice-versa, with $R = 4 \Omega$, is tested. In this case v_c^* is step changed and, consequently, the switching function suddenly drops the hysteresis amplitude value and recovers it again in less than one switching period, with a brief and smooth transient of T_k . Again, the expected overdamped behaviour of v_c is confirmed.

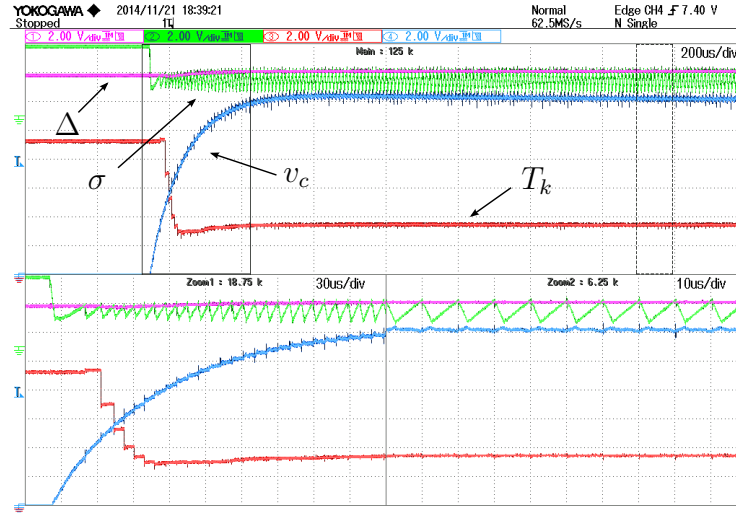


Figure 5.5: Start-up for $v_c^* = 12$ V with $R = 2 \Omega$ and Δ_0 lower than the steady-state value. v_c : blue; σ : green; $|\Delta_k|$: magenta; T_k : red.

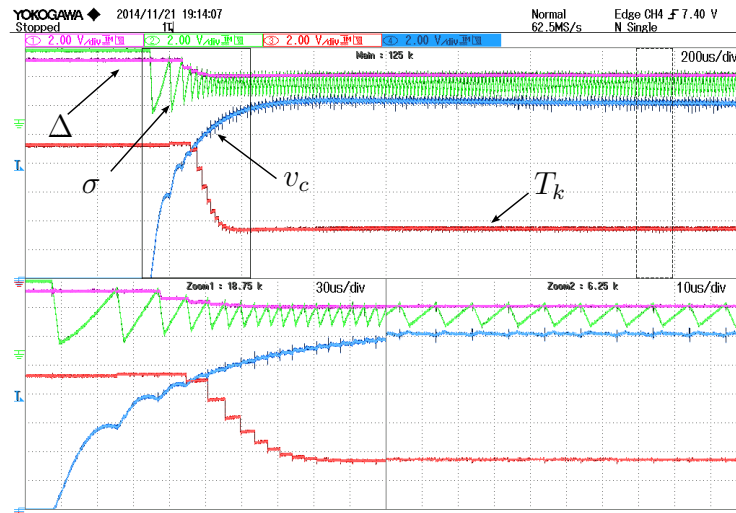


Figure 5.6: Start-up for $v_c^* = 12$ V with $R = 2 \Omega$ and Δ_0 higher than the steady-state value. v_c : blue; σ : green; $|\Delta_k|$: magenta; T_k : red.

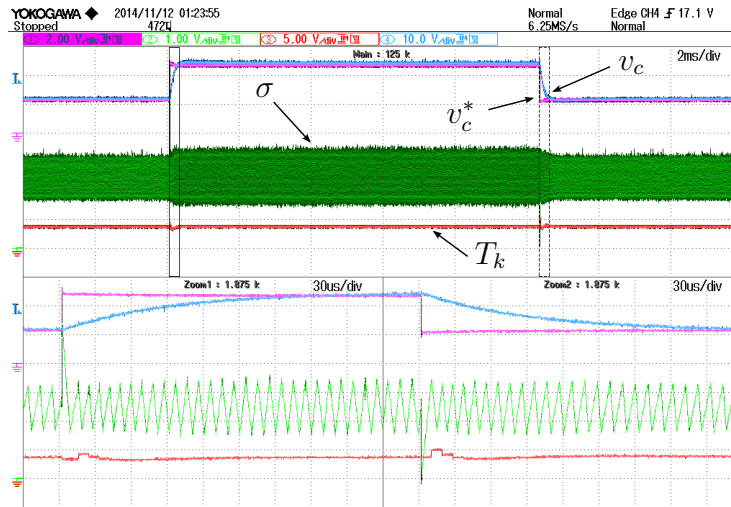


Figure 5.7: Voltage reference, v_c^* , variation from 12 V to 24 V and vice-versa, with $R=4 \Omega$. v_c : blue; σ : green; v_c^* : magenta; T_k : red.

2. SFC performance

In order to evaluate the proper performance of the SFC, several reference step variations are tested in the following. First of all, Figure 5.8 shows the result for a step change of T^* between $12.5 \mu\text{s}$ and $8.3 \mu\text{s}$ with a desired output voltage of 12 V and $R=4 \Omega$. The Figure confirms a good performance of the SFC with an overdamped behaviour, as expected with the used value of γ ($\gamma = 2 \cdot 10^4$).

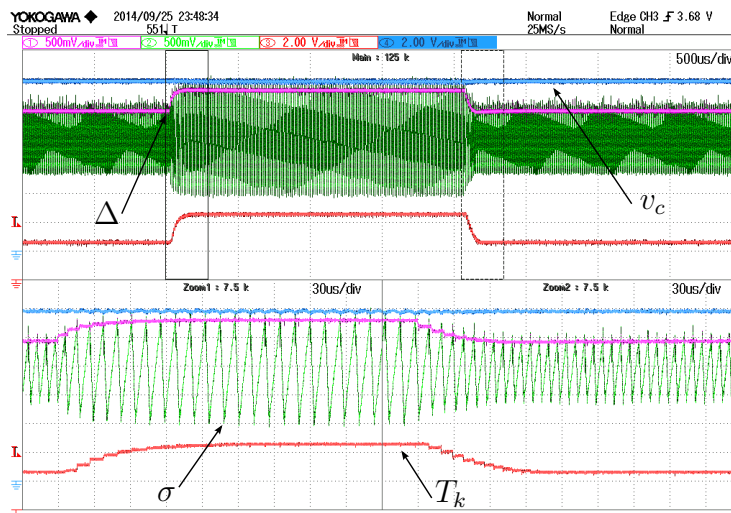


Figure 5.8: Overdamped responses for $\gamma = 2 \cdot 10^4$ with $R=4 \Omega$ and a T^* variation from $12.5 \mu\text{s}$ to $8.3 \mu\text{s}$. v_c : blue; σ : green; $|\Delta_k|$: magenta; T_k : red.

Figure 5.9 shows the result for the same test (step change of T^*), when the integral gain is selected close to the unstable values ($\gamma = 2 \cdot 10^5$, being the stability limit of

$2.07 \cdot 10^5$). In this case T^* is varied from $12.5 \mu\text{s}$ to $14 \mu\text{s}$ and R is kept at 4Ω . The modification of the step values is required to avoid the effects of Δ saturation and the computing time influence that would modify the expected dynamics (see Section 5.4). As γ is now closer to the upper stability limit, both T_k and Δ_k exhibit underdamped transient responses with very low damping ratio, thus confirming the theoretical prediction. It is evident that such response fits with the expected one, as Figure 3.2 denoted in Section 3.1

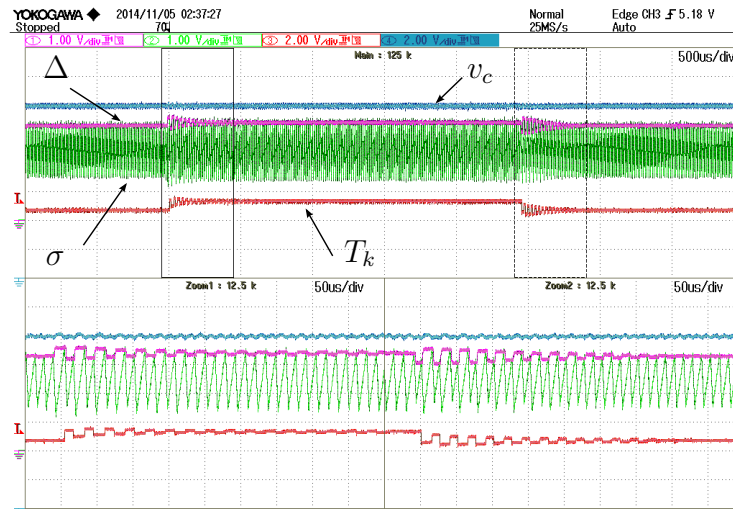


Figure 5.9: Underdamped responses for $\gamma = 2 \cdot 10^5$ with $R=4 \Omega$ and a T^* variation from $12.5 \mu\text{s}$ to $14 \mu\text{s}$. v_c : blue; σ : green; $|\Delta_k|$: magenta; T_k : red.

Finally, the previous test is repeated with different values of γ , in order to confirm the validity of the model developed in Chapter 2. In Figure 5.10 the root locus of the SFC in the case of 12 V is shown, where the poles placement for different values of γ are depicted. Related with such poles, the corresponding responses in the time domain are also shown. All the test are made with a step of T^* from $12.5 \mu\text{s}$ and $8.3 \mu\text{s}$, except for the $\gamma = 2 \cdot 10^5$ case, which is from $12.5 \mu\text{s}$ to $14 \mu\text{s}$.

The switching period (red signal in Figure 5.10) is measured with an analog sensor, which adds some dynamics to the measure. The performance has to be analysed from the Δ response (magenta signal), which is generated through a DAC by the μC , without any delay. From the results shown in Figure 5.10, the SFC model developed at Chapter 2 is fully corroborated.

3. System robustness

Finally, a load transient test is performed at the converter output, in order to confirm that one of the main benefits of the SMC (its robustness) is preserved under the SFC operation. The test consists of suddenly variations of the linear load applied, from 0 to 6 A in the 12 V and 24 V cases. In the Figures 5.11, 5.12, the variable i_o responds

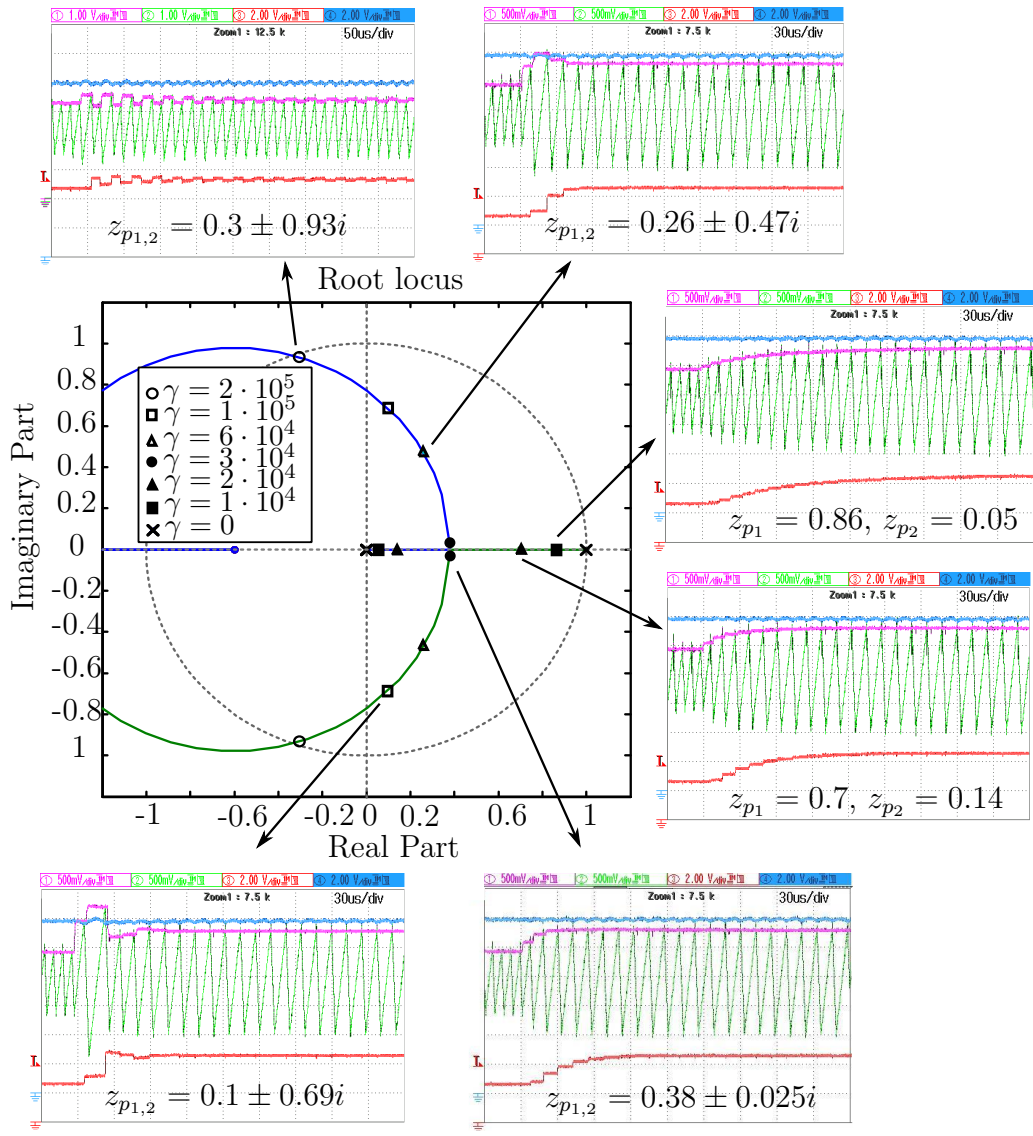


Figure 5.10: Poles placement in the complex plane and the corresponding time domain step responses, with $R = 4 \Omega$. v_c : blue; σ : green; $|\Delta_k|$: magenta; T_k : red.

to:

$$i_o = \frac{v_c}{R}.$$

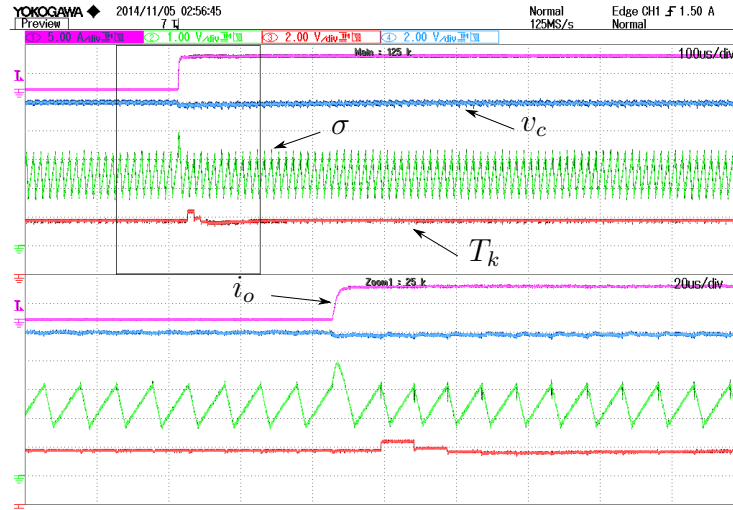


Figure 5.11: Load Transient: responses for $\gamma = 2 \cdot 10^4$ with R from no load to 2Ω , $T^* = 10 \mu\text{s}$ and $v_c^* = 12 \text{ V}$. v_c : blue; σ : green; i_o : magenta; T_k : red.

From Figures 5.11 and 5.12, the good transient response of the SMC is confirmed, since the regulated output voltage is hardly disturbed. In the same way, it is also confirmed that in this design the values of ρ_*^\pm do not depend on the output current, since before and after the transient, the steady-state hysteresis values are essentially the same. This fact confirms the theoretical values found for ρ_*^\pm in Section 5.3.1, as expression (5.12) does not depend on the output load R .

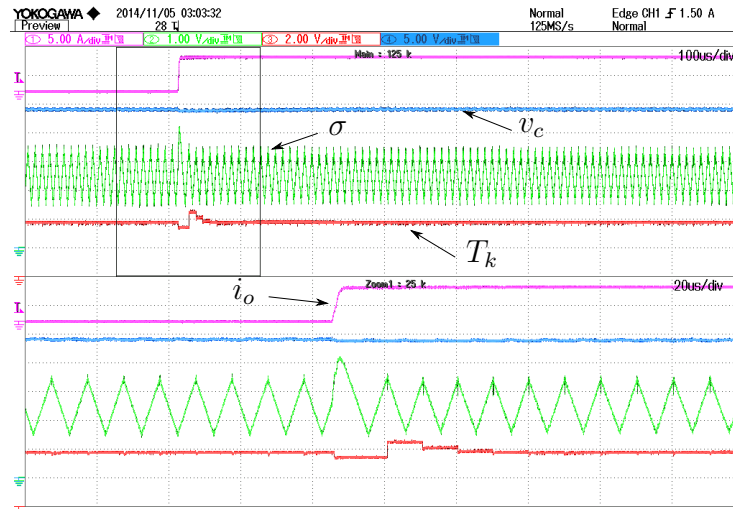


Figure 5.12: Load Transient: responses for $\gamma = 2 \cdot 10^4$ with R from no load to 2Ω , $T^* = 10\mu s$ and $v_c^* = 24$ V. v_c : blue; σ : green; i_o : magenta; T_k : red.

5.6 Conclusions

In this Chapter the design and implementation steps of the SMC and SFC have been described, and several experimental results have been presented corroborating the validity of the proposed procedures, and the models developed in Section 2.2.1. Additionally, a digital implementation of the SFC has been developed using a μC from ST Microelectronics (STM32F407) allowing to demonstrate the expected behaviour of the SFC in the discrete-time approach. The experimental results confirm the output voltage regulation, the operation at fixed switching period, and the system robustness with respect to load and output voltage variations.

Chapter 6

Voltage Regulation in a Multiphase Buck Converter.

The continuous-time approach of the SFC, found in Section 2.3, is applied to a multiphase synchronous Buck converter in the following. The Chapter is structured as follows, in the first Section the power converter data and the sliding mode interleaving operation are briefly introduced. Then, the SMC controller is designed for regulating the output voltage with interleaving operation, followed by the design of the SFC in the continuous-time approach. Finally, the implementation details and the experimental results are presented.

6.1 The multiphase converter

The multiphase synchronous converter is made up by the parallel connection of m Buck converters. Such topology is shown in Figure 6.1. Since this topology is based on the connection of several synchronous Buck converters with their outputs joined in parallel, the corresponding state space equations are equivalent to the ones presented in Chapter 5, extended to a multi-input case.

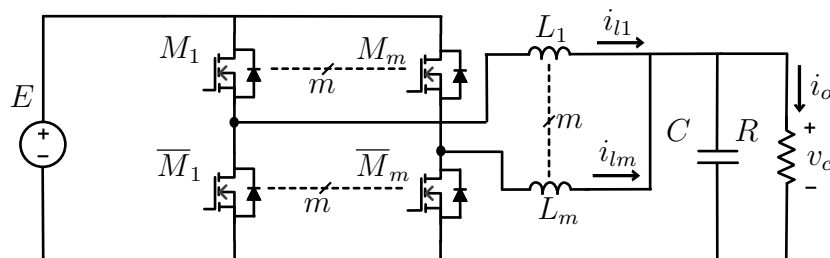


Figure 6.1: Circuit scheme of the m -phase synchronous Buck converter.

Therefore, for the multiphase structure the equations result in:

$$L \frac{di_k}{dt} = -v_c + E u_k; \quad k = 1, \dots, m \quad (6.1)$$

$$C \frac{dv_c}{dt} = \sum_{k=1}^m i_k - \frac{v_c}{R} \quad (6.2)$$

where the control actions u_k take values from the set $\{0, 1\}$, E is the input voltage, v_c the output voltage, i_k is the current flowing through the k -th phase and L , C , R are the inductance, the capacitance and the resistive load, respectively.

An important benefit of the multiphase topology is the possibility to implement interleaving operation. This technique is based on phase shifting the control actions of each converter in such a way that the high frequency current ripple of each inductor are cancelled in the common output connection, thus generating an ideally free ripple current to the output voltage. This technique allows to reduce considerably the output capacitor value, since, in the ideal case, there is no high frequency current ripple to be filtered at the output. Moreover, the distribution of the power through different converters permits the reduction of the component features, as the allowable conduction current of the power switches, or the required heat sinks for losses dissipation, which in some cases can be directly removed from the system. The reduction of the current flowing by the switches also allows to increase the switching frequency, which in turn, would lead to an additional reduction of the value of the reactive components. As a consequence, the multiphase structures have gained interest within the industrial community for different applications due to their high efficiency, good power density, fast transient response, and ability of interleaving operation [47–51].

The control objective is again the output voltage regulation, with the additional task of guaranteeing the interleaving among the phases, which is also controlled by a sliding mode technique. The SMC and the SFC will be implemented by means of analog circuitry, meanwhile the interleaving control is implemented with an FPGA. The parametric data of the assembled multiphase converter are detailed in Table 6.1.

Table 6.1: Multiphase Buck Converter Parameters

| Parameter | Symbol | Value |
|-------------------------------------|----------|--------------------------|
| Input Voltage | E | 48 V |
| Desired Output Voltage Range | v_c^* | 12-24 V |
| Output Capacitor | C | 100 μ F |
| Phase Inductance | L | 22 μ H \pm 10% |
| Number of phases | m | 8 |
| Load Range | I_o | 0-65 A |
| Desired switching period | T^* | 10 μ s |
| Current transformer parameters | L_x, M | 800 μ H, 6.4 μ H |
| Current transformer burden resistor | R_b | 10 Ω |

6.2 Interleaved sliding mode control of the output voltage

The interleaved sliding mode control corresponds to a Master-Slave strategy. One of the Buck converters regulates the output voltage, the Master converter (or Master phase), while the rest of the phases track the control signal of the Master one with the proper phase shifting.

6.2.1 Master switching surface design

The Master switching surface σ_M for output voltage regulation is designed as:

$$\sigma_M := \psi_1 (v_c - v_c^*) + \psi_2 x_M = 0, \quad (6.3)$$

where $\psi_{1,2}$ are the switching surface constants and v_c^* is the desired output voltage. Comparing it with the surface designed for the single Buck converter (see Section 5.2), the first time derivative of e_c is replaced by the signal x_M . As it was discussed in the Section 5.4, it is usual to employ the measured current flowing by the output capacitor instead of time differentiate the output voltage in the implementation set-up. In this case, it is not possible to use the current ripple of the output capacitor since it is ideally cancelled by the interleaving operation. As a consequence, a current transformer is placed in series with the Master phase inductor. The signal x_M is the output of this current transformer, which

adds the following dynamics to the system:

$$L_x \frac{dx_M}{dt} = -R_b x_M + R_b M \frac{di_M}{dt}, \quad (6.4)$$

where i_M is the Master phase current and M and L_x are the mutual inductance and the transformer secondary inductance, respectively. Notice how using the signal x_M the relative degree of the switching function is equal to one, and therefore, the sliding mode can be enforced in $\sigma_M = 0$.

6.2.2 Sliding dynamics of the Master phase

The sliding mode equation for the Master phase becomes:

$$\dot{\sigma}_M = \frac{\psi_1}{C} \left[\sum_{k=1}^m i_k - \frac{v_c}{R} \right] - \psi_1 \dot{v}_c^* - \frac{\psi_2 R_b}{L_x} x_M + \frac{\psi_2 R_b M}{L L_x} [-v_c + E u_M], \quad (6.5)$$

which, assuming that the phases are equal ($\sum_{i=1}^m i_i = m i_M$), it boils down to:

$$\dot{\sigma}_M = -\psi_1 \dot{v}_c^* + \frac{\psi_1 m}{C} i_M - v_c \left[\frac{\psi_2 R_b M}{L L_x} + \frac{\psi_1}{RC} \right] - \frac{\psi_2 R_b}{L_x} x_M + \frac{\psi_2 R_b M}{L L_x} E u_M. \quad (6.6)$$

Therefore, (6.6) can be expressed as:

$$\dot{\sigma}_M = f_1 + \frac{\psi_2 R_b M}{L L_x} E u_M \quad (6.7)$$

being $f_1 = -\psi_1 \dot{v}_c^* + \frac{\psi_1 m}{C} i_M - v_c \left[\frac{\psi_2 R_b M}{L L_x} + \frac{\psi_1}{RC} \right] - \frac{\psi_2 R_b}{L_x} x_M$. It is clear from (6.7) that the sliding motion can be enforced in $\sigma_M = 0$ when

$$\frac{\psi_2 R_b M}{L L_x} E > f_1$$

is fulfilled. In the same way, the equivalent control is found when $\dot{\sigma}_M = 0$ and $\sigma_M = 0$:

$$u_{M_{eq}} = \frac{v_c}{E} + \frac{\psi_1 L}{\psi_2 E M} (v_c^* - v_c) + \alpha \frac{L}{E} (\dot{v}_c^* - \dot{v}_c) \quad (6.8)$$

where

$$\alpha = \frac{\psi_1 L_x}{\psi_2 R_b M}.$$

Placing (6.8) in the original system (6.1), (6.2) as the control inputs, the ideal sliding dynamics is found in (6.9), (6.10):

$$C \frac{d^2 v_c}{dt^2} + \left[m\alpha + \frac{1}{R} \right] \frac{dv_c}{dt} + \frac{m\psi_1}{M\psi_2} v_c = \frac{m\psi_1}{M\psi_2} v_c^*, \quad (6.9)$$

$$\frac{di_k}{dt} = v_c \left(\frac{\alpha}{RC} \right) + \frac{\psi_1}{M\psi_2} (v_c^* - v_c) - i_k \frac{\alpha m}{C} + \alpha v_c^*; \quad k = 1, \dots, m. \quad (6.10)$$

Since all the coefficients in (6.9) and (6.10) are non null and positive, the resulting equilibrium point

$$v_c = v_c^*, i_1 = \dots i_m = \frac{v_c^*}{mR},$$

is asymptotically stable, confirming that in steady-state v_c converges to v_c^* . In order to design the switching function parameters ψ_1 and ψ_2 , the dynamics given by (6.9) for different working conditions of the converter are employed. Specifically, the converter is to undergo variations of the output load, R , and the desired output voltage v_c^* . A strategy adjusting the phase number to the output power could be applied, but in this thesis is not considered, and $m = 8$ always holds. In order to achieve a time constant around $500 \mu s$ for all the cases and keep the overshoot below 20 % for all the load conditions, expression (6.9) allows to design the switching surface constants as $\psi_1 = 0.078$ and $\psi_2 = 2.97$. With such parameters, and with $v_c^* = 24$ V, at the worst case (which occurs at low load $R = 1 k\Omega$) an overshoot around the 20 % is obtained, while for the full load case ($R = 0.4 \Omega$), the response has real poles in $s_{p1} = -43761$ and $s_{p2} = -7502$. The response is dominated by s_{p2} , providing a settling time of $533 \mu s$ (4τ). It has to be remarked that these results are essentially the same for 12 V.

6.2.3 Master phase control law

Finally, the control law enforcing real sliding motion in the vicinity of $\sigma_M = 0$ is:

$$u = \begin{cases} 1 & \text{if } \sigma < -\Delta \quad \text{or } (|\sigma| < \Delta \ \& \ \dot{\sigma} > 0) \\ 0 & \text{if } \sigma > \Delta \quad \text{or } (|\sigma| < \Delta \ \& \ \dot{\sigma} < 0). \end{cases} \quad (6.11)$$

6.2.4 Slaves switching surfaces design. Interleaved Sliding Mode

Assuming that the Master phase corresponds to the phase number 1, the interleaved sliding mode operation is achieved by using the following Slaves switching surfaces:

$$\begin{aligned} \sigma_2 &:= K \int (u_M - u_2) dt = 0 \\ &\vdots \\ \sigma_m &:= K \int (u_{m-1} - u_m) dt = 0 \end{aligned} \quad (6.12)$$

with u_i being the control laws. The hysteretic control laws enforcing sliding motion on the $m - 1$ surfaces are:

$$u_i = \begin{cases} 1 & \text{if } \sigma < -\delta \quad \text{or } (|\sigma_i| < \delta \ \& \ \dot{\sigma}_i > 0) \\ 0 & \text{if } \sigma > \delta \quad \text{or } (|\sigma_i| < \delta \ \& \ \dot{\sigma}_i < 0), \end{cases}$$

for i from 2 to m , being δ the hysteresis width of the comparators (the value of δ in the slaves phases will be, in all the cases, a fixed value). Once the sliding mode occurs in all the surfaces, it holds that

$$\dot{\sigma}_i(u_{eq}) = 0,$$

and the low dynamics (average) of the discontinuous controls (u_1, \dots, u_m) converge. This can be demonstrated equalling all surfaces in (6.12) to 0. Additionally, these surfaces generate a phase shift among the different control signal. Such phase shift among the phases, which leads to an interleaving operation, can be controlled through K , as $T_\phi = \delta/K$ (see [14], [52] for details) being T_ϕ the phase shift among phases. Such phase shift, $T_\phi = T_M/m$, depends on the switching period of the master phase, T_M . In the implementation presented hereafter, the interleaving will be assumed perfect, since the FPGA in charging of implement the aforementioned interleaving control measures the switching period of the Master phase at any time, computing on-line the correct value of K for a proper phase-shifting. This methodology improves the interleaving operation during transients.

6.3 Switching frequency regulation

The switching frequency controller is only designed for regulating the switching period of the Master phase. The slave surfaces presented in (6.12) imply that the switching period of the Master control signal is automatically replicated by all the Slaves ones. Thus, the SFC is only designed for the Master phase. The SFC chosen approach for this case is the continuous-time one, hence, the procedure explained in Section 2.3 is applied.

6.3.1 Evaluation of ρ_k^\pm

From (6.7), and using the equivalent control (6.8), the steady-state values for ρ_*^\pm in the 12 V and 24 V cases are obtained as follows. The sliding mode equation can be expressed as:

$$\dot{\sigma}_M = \beta E (u_M - u_{Meq}), \quad (6.13)$$

with $\beta = \frac{\psi_1}{\alpha L}$. Additionally, the steady-state sliding mode entails that $v_c = v_c^*$, which simplifies (6.8) to $u_{Meq} = \frac{v_c^*}{E}$. Thus, the expressions providing the expected values of $\dot{\sigma}_M$ in the steady-state sliding motion are

$$\begin{aligned} \dot{\sigma}_{M_{u=1}} &= \beta [E - v_c^*], \\ \dot{\sigma}_{M_{u=0}} &= -\beta v_c^*. \end{aligned} \quad (6.14)$$

Once the expressions in (6.14) are found, the values of ρ_*^\pm and λ are evaluated for the expected working conditions and the values of Table 6.1. For $v_c^* = 12$ V arises

$$\rho_*^+ = 2.6 \cdot 10^{-6}; \rho_*^- = -7.8 \cdot 10^{-6}; \lambda = 2.1 \cdot 10^{-5}, \quad (6.15)$$

and for $v_c^* = 24$ V:

$$\rho_*^+ = 3.9 \cdot 10^{-6}; \rho_*^- = -3.9 \cdot 10^{-6}; \lambda = 1.6 \cdot 10^{-5}. \quad (6.16)$$

6.3.2 SFC design

First of all, the values of γ_L that fulfil the Assumption B should be derived. The assumption stated that the linear model developed (see (2.39)) holds when

$$\gamma_L |e_k| \ll \min \left\{ |\rho_*^+|^{-1}, |\rho_*^-|^{-1} \right\}, \quad \forall k \geq k_0$$

is met.

The implemented SM controller has a hardware limited switching period of 4 μ s. In the same way, the limiting values of Δ (see Remark 1) ensure a maximum switching period of $T_k = 50$ μ s, and recalling that $T^* = 10$ μ s, this leads to a maximum period error of 40 μ s. As it was chosen in the simulation of the SFC in the continuous-time approach (see Section 3.3), the factor between the grade of change of Δ and σ_M is set to 20, in order to fulfil the requirement of Assumption B. Therefore, the value γ_{L20} is calculated:

$$\gamma_{L20} |40 \cdot 10^{-6}| = 20 \cdot (7.8 \cdot 10^{-6})^{-1},$$

delivering $\gamma_{L20} = 6.4 \cdot 10^{10}$. As a consequence, if γ_L is selected smaller than γ_{L20} , the real response of the switching period will fit with the model derived in Section 2.3. Moreover, since the switching period is measured by an analog circuit, the characteristic polynomial that determinates the expected response is the one shown by equation (2.42), with $\tau = 65 \cdot 10^{-6}$ (empirically measured). According to (2.42) and Theorem 3, the stable values for γ_L have to satisfy:

$$\gamma_L < \frac{2(10 \cdot 10^{-6} + 2 \cdot 65 \cdot 10^{-6})}{(2.1 \cdot 10^{-5}) \cdot (10 \cdot 10^{-6}) \cdot (10 \cdot 10^{-6} + 4 \cdot 65 \cdot 10^{-6})}$$

for the 12 V case and

$$\gamma_L < \frac{2(10 \cdot 10^{-6} + 2 \cdot 65 \cdot 10^{-6})}{(1.6 \cdot 10^{-5}) \cdot (10 \cdot 10^{-6}) \cdot (10 \cdot 10^{-6} + 4 \cdot 65 \cdot 10^{-6})}$$

for 24 V. Which result in $\gamma_L = 5 \cdot 10^9$ and $\gamma_L = 6.5 \cdot 10^9$, respectively.

Finally, according to the previous results, the chosen value is $\gamma_L = 1.25 \cdot 10^8$ which meets the previous conditions. With this value, the theoretical model delivers a response with a transient response of around 2.5 ms without overshoot, for both 12 and 24 V regulated at

the output.

6.4 Implementation Details

At this stage, several important aspects about the analog implementation are discussed. As it was explained earlier, the controllers are implemented by two different blocks: an analog block containing the SMC of the Master phase and the SFC, and a block based on a FPGA in charging of guaranteeing the interleaving operation among the phases. In this thesis, the first block is detailed hereafter, omitting the FPGA part for the sake of brevity (see [53] for details).

For the design of the converter itself, a modular strategy is used. On the one hand, each Buck converter is built in a single board, and on the other, a motherboard where the phases can be plugged in is designed. This strategy facilitates an eventual maintenance of the converters. The pictures shown at Figures 6.2 and 6.3 depict these boards.

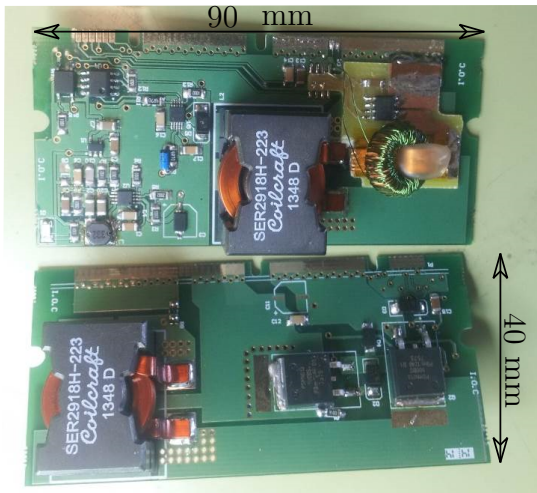


Figure 6.2: Single phase picture.

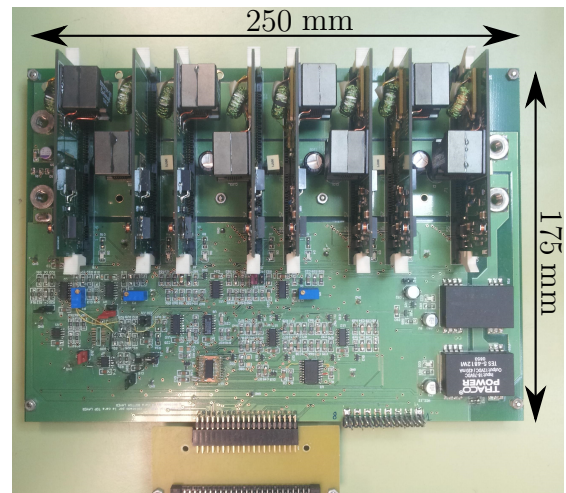


Figure 6.3: Motherboard picture.

As it can be appreciated from Figure 6.2, the single boards are designed being possible the placement of the inductor on both sides, reducing the required space when they are connected in the motherboard (see Figure 6.3).

Each single board includes the power stage and a current transformer in series with the power inductor, in such a way that whatever phase could act as the Master one. The Mosfet circuit driver and a small regulator are also embedded in the converter boards, making possible its supply directly from the main input power (48 V).

The motherboard accommodates the SMC and the SFC control circuits, among other secondary parts (as filters, regulator, etc). The SMC circuit is sketched in Figure 6.4, where the sensing part, the switching function and the variable hysteresis comparator are easily identified. For the output voltage sensing, a voltage divider with an Operational Amplifier (AO) in voltage follower configuration is used. The signal x_M , coming from the Master

current transformer, is directly employed by the AO. For the control law implementation, two high speeds voltage comparators are used.

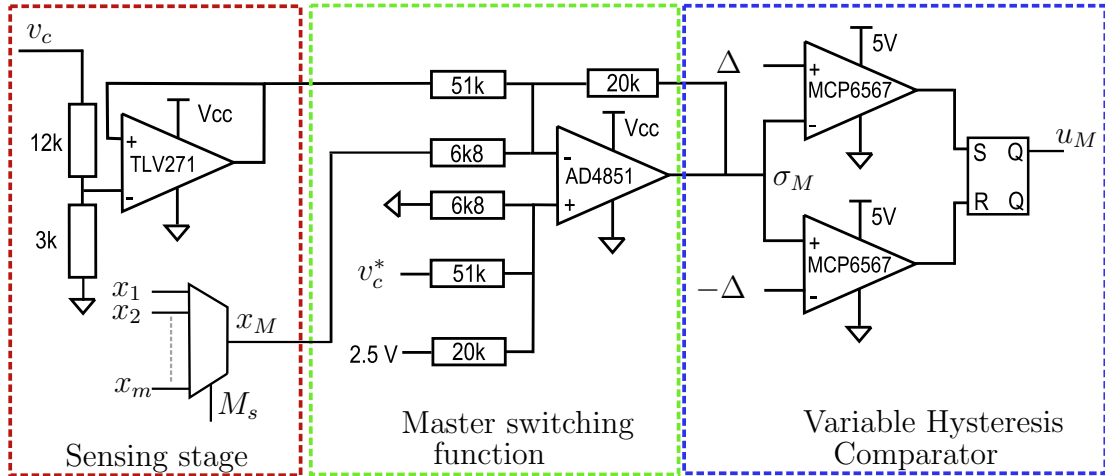


Figure 6.4: Circuit scheme of sliding mode controller using a variable hysteresis comparator.

The SFC circuit contains the switching period sensor and the hysteresis generator, which are depicted in Figure 6.5.

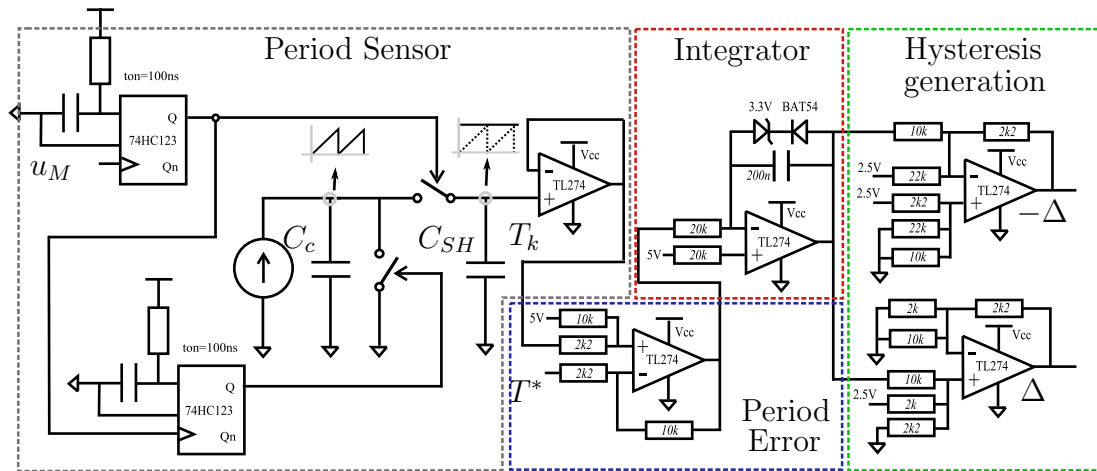


Figure 6.5: Circuit scheme of the period sensor and the analog structure implementing the SFC for the multiphase converter.

The switching period sensor is based on the charge of a capacitor by a constant current source. From the capacitor characteristic equation

$$i_{c_c} = C_c \frac{dv_{c_c}}{dt},$$

it is obvious that with a constant current applied, the resulting voltage is a sawtooth waveform, where the slope is determined by i_{c_c} and C_c . The circuit uses two monostable

circuits, one of them is in charging of synchronizing the capture of the voltage value of the capacitor in a rising edge of the control signal u , while the second one controls the switch that resets this voltage just after the value has been acquired. This behaviour is depicted in the left block of Figure 6.5, called *Period Sensor*. The system works as a sample and hold circuit synchronized with u_M , holding the last measurement until the circuit is triggered again. Although the system delivers discrete-time measurements, the time used to capture the voltage value ($1 \mu\text{s}$) together with the finite value of the sample and hold capacitor ($C_{SH} = 1 \text{ nF}$) add dynamics to the measurement, which can be modelled by a first order response. This model is characterized by τ , which was empirically found to $65 \cdot 10^{-6}$ and used in the previous stability analysis. Such designed circuit is intended to generate 5 V when the switching period is of $10 \mu\text{s}$.

The parts called *Integrator* and *Period Error* make up the SFC. Indeed, as it can be inferred from the Figure, they use standard configuration based on AO for computing the period error and the integral action. Notice how due to the electronics used are unipolar, all the circuits are polarized with a 5 V offset. Despite of the integral action itself, such circuit includes a hardware saturator for the hysteresis value, conformed by a Schottky diode in anti series with a zener diode. This structure implements the maximum increment of Δ , Δ_{max} , being the block called *Hysteresis generator* who fixes the minimum value of Δ , Δ_{min} . Again using AO the Δ and $-\Delta$ are generated, ensuring their symmetrical characteristic.

6.5 Experimental results

Finally, the experimental results obtained in the laboratory with the built prototype are shown at this Section. Firstly, the measured system features as efficiency, line regulation and load regulation are summarized in Table 6.2.

Table 6.2: Experimental results of the Multiphase converter

| Efficiency (%) @65A, $v_c=12/24$. $E=48 \text{ V}$ | Load Regulation (%) $E=48 \text{ V}$, $v_c=12/24$. 0 - 65 A | Line Regulation (%) @ $v_c=24 \text{ V}$, $P_{out}=1 \text{ kW}$. $E=36 \text{ to } 55 \text{ V}$ | Line Regulation (%) @ $v_c=24 \text{ V}$, No load. $E=36 \text{ to } 55 \text{ V}$ |
|---|---|---|---|
| 94.8/97.1 | $\leq 0.97/1.1$ | ≤ 1.7 | ≤ 0.5 |

The data shown at Table 6.2 certify a good performance of the prototype, achieving good levels of efficiency. It should be remarked that such efficiency includes all the power consumption of the system (including, FPGA, drivers, etc). The system also presents a good robustness, which can be inferred from the line and load regulation results.

In order to check the expected features provided by the designed controllers, several tests have been performed in the following. They are organized in four groups, namely:

SMC performance, interleaving, SFC performance and system robustness.

1. SMC performance

The first test consists in step-change variations of the reference voltage from 12 V to 24 V and reversely, with a resistive load of 1 Ω connected at the output. Figure 6.6 portrays the responses of the output voltage, the load current, the switching function and the measured switching period (scaled by 0.5 V/μs). The bottom windows show a zoom view of the transient behaviour when the output voltage reference changes from 12 V to 24 V (left window) and when it decreases from 24 V to 12 V (right window). Notice how the output voltage behaves with a smooth transient response, which corresponds to the ideal sliding motion, and the hysteresis values are adapted such that the switching period reaches the desired value at steady-state.

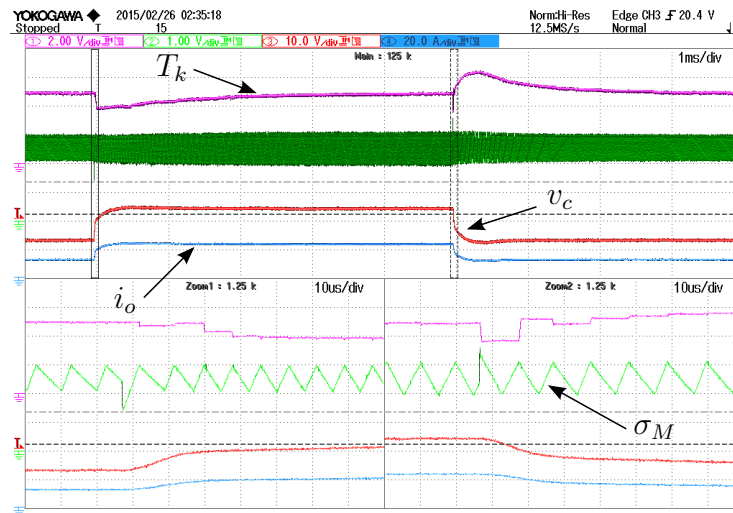


Figure 6.6: Reference change 12-24-12 V with a load of 1 Ω at the output.

2. Interleaving

Figure 6.7 shows the behaviour of the current transformer signals of the 8 phases in the start-up, when the converter supplies a load of 21 A and the output voltage is regulated to 24 V. As it can be seen in the oscilloscope capture, the interleaving operation is started from the second switching period (see current waveforms on the left bottom window) and achieves interleaving at the desired switching frequency of 100 kHz in the steady-state (see right bottom window). Figure 6.8 shows the steady-state behaviours of the current transformer signals of the 8 phases for a load of 65 A with an output voltage of 24 V. From the previous Figures, the proper interleaving operation is fully corroborated.

3. SFC performance

The two following tests are designed with the purpose to validate the SFC operation. In Figure 6.9 the start-up of the multiphase converter for an output voltage reference

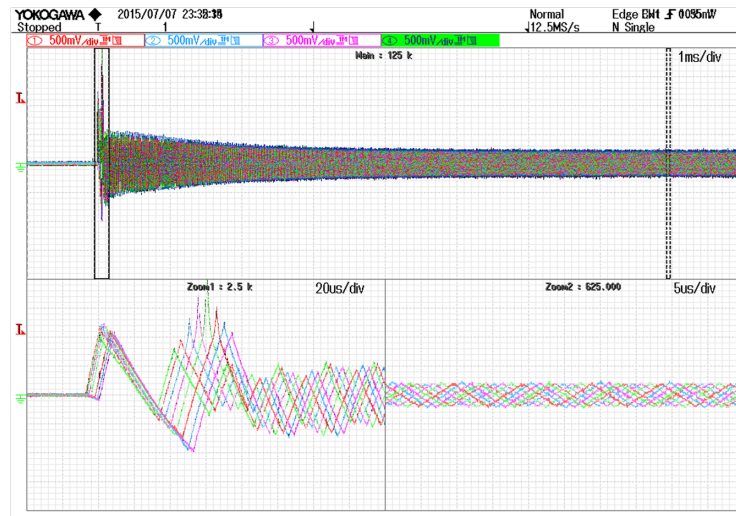


Figure 6.7: Start-up of the current transformer signals of the 8 phases with a load of 21 A for an output voltage of 24 V.

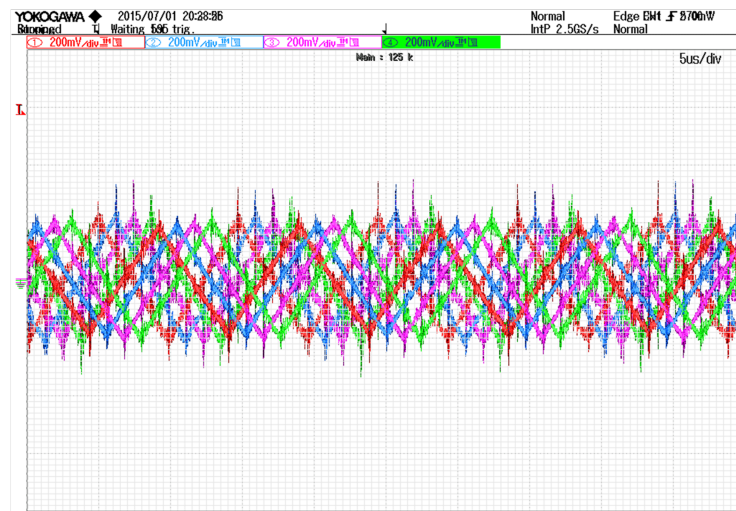


Figure 6.8: Steady-state of the current transformer signals of the 8 phases with a load of 65 A for an output voltage of 24 V.

of 24 V delivering 21 A to the load (at steady-state) is presented. Notice that the initial value of Δ is far away from the steady-state one. Again, the Figure shows the behaviours of the output voltage, the switching function, the Master control signal and the measured switching period. The bottom windows detail the waveforms in the transient state (left window) and in the steady-state (right window). As it can be seen in the Figure, the output voltage reaches the desired voltage with a smooth transient and with a small overshoot. Furthermore, the hysteresis bands are adapted such that the steady-state switching frequency achieves the desired value of 100 kHz with the theoretically predicted overdamped response in the switching period transient (see Section 6.3).

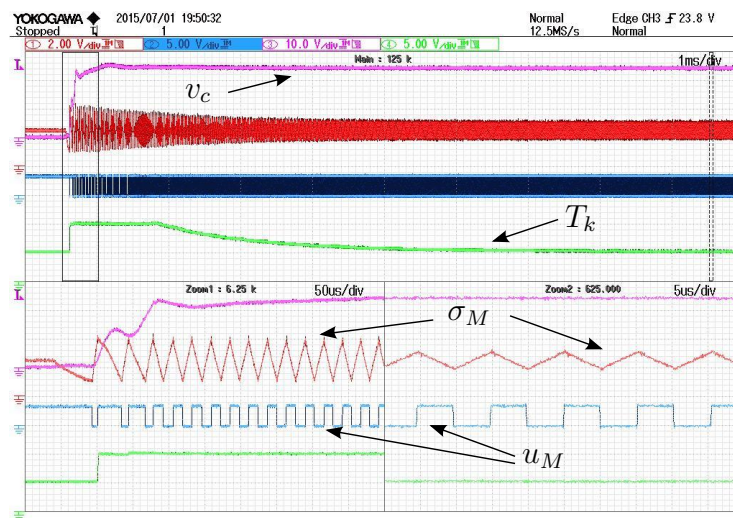


Figure 6.9: Start-up with a load of 21 A for a desired output voltage of 24 V.

The second test is devoted to highlight the switching period tracking of a step-type reference. The switching period reference varies from $8 \mu\text{s}$ to $12 \mu\text{s}$ and vice-versa. The output voltage is regulated to 24 V and there is no load at the output. Figure 6.10 shows the behaviours of the output voltage ripple, Δv_c , the switching function, the switching period, and the switching period reference. The SFC adjusts the hysteresis band value in order to achieve the desired steady-state switching period with the expected motion according to the model derived in Section 6.3. From the Figure, it can be seen how the expected settling time of around 2.5 ms of T_k is qualitatively fulfilled in the real system, validating the developed models and assumptions taken. Besides, the output voltage is not affected by the switching period reference variation, implying that the real sliding mode is not being perturbed by the action of the SFC. This effect can be also inferred from the low output voltage ripple, Δv_c , observed during the entire test. The waveforms detailed in the bottom windows correspond to the steady-state dynamics at $8 \mu\text{s}$ (left window) and at $12 \mu\text{s}$ (right window). Such Figures also confirm the assumption of the piecewise linear behaviour of the switching function.

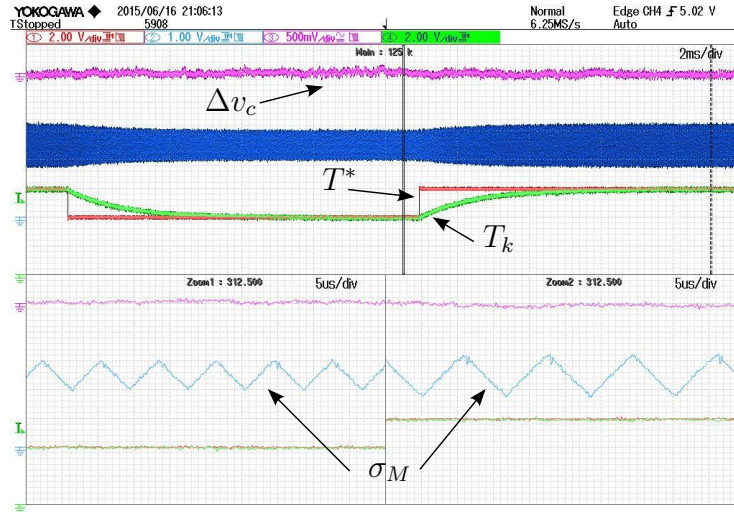


Figure 6.10: Switching period variation from $8 \mu\text{s}$ to $12 \mu\text{s}$ with a desired output voltage of 24 V and no load.

4. System robustness

Finally, the robustness of both controllers are evaluated through sudden variations of the load applied at the output. The following Figures depict the responses of the output voltage, the switching function and the switching period (scaled by $0.5 \text{ V}/\mu\text{s}$) when the load changes from 21 A to 65 A (Figure 6.11) and from 65 A to 21 A (Figure 6.12). In both cases, the output voltage reference is set to 24 V . From these Figures it can be inferred how the converter recovers the desired output voltage after a smooth transient and the switching period is not affected by the load changes. Moreover, it is confirmed that the values of ρ_*^\pm and λ are almost insensitive to load changes, since the hysteresis value, Δ , is nearly the same in both cases.

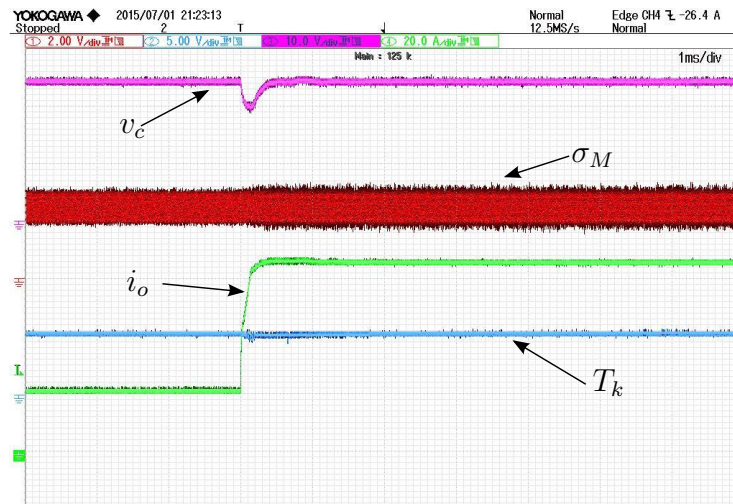


Figure 6.11: Load change from 21 A to 65 A for a regulated output voltage of 24 V.

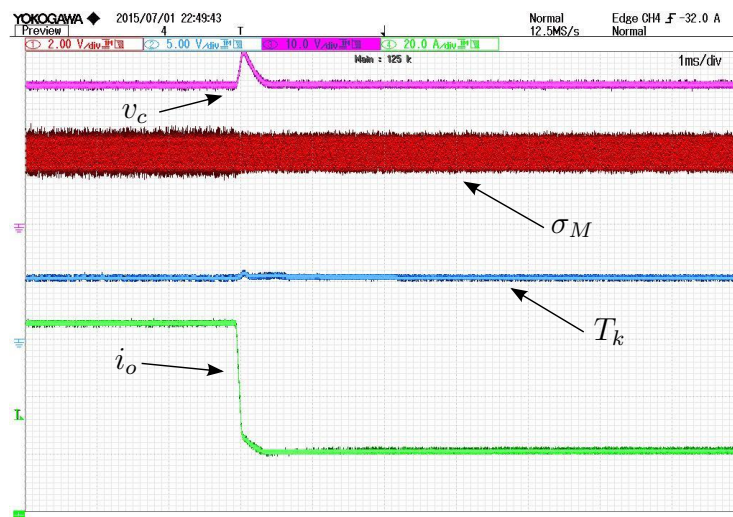


Figure 6.12: Load change from 65 A to 21 A for a regulated output voltage of 24 V.

6.6 Conclusions

Through the experimental results shown above, the proper performance of the SMC together with the SFC is confirmed in a multi input linear system. The expected properties of the full system as output voltage regulation, interleaving operation, steady-state fixed switching period and robustness with respect to load variations have been confirmed. Moreover, the continuous-time approach of the SFC has been successfully implemented by analog circuitry, thus confirming the expected dynamics according to the developed model in Section 2.3.

Chapter 7

Voltage Regulation in a Boost Converter.

The converters implemented in the previous Chapters (Chapters 5 and 6) respond to linear systems with respect to the control input. However, there are power converters that do not fit with this description, as the Boost converter. The equations describing the Boost converter respond to a nonlinear ones, and it is interesting to evaluate the performance of the SFC in this type of structure.

Therefore, the SFC is implemented for regulating the switching period of a Boost converter. The Chapter is structured as follows: firstly the nonlinear equations of the converter and the parametric data of the Boost converter are presented. Then, the SMC will be designed to regulate its output voltage. Next, the design of the SFC in the continuous-time approach is detailed. Finally, the implementation details and the experimental results will be shown.

7.1 The Boost Converter

The circuit scheme of a Boost converter is shown in Figure 7.1. The Boost converter can be understood like a Buck converter where the input is used as the output, and this one as the input. Nevertheless, the state space equations derived from this structure become nonlinear.

The equations describing the dynamics of the Boost converter are shown in (7.1), (7.2).

$$L \frac{di_l}{dt} = E - v_c(1 - u), \quad (7.1)$$

$$C \frac{dv_c}{dt} = i_l(1 - u) - \frac{v_c}{R}, \quad (7.2)$$

where E is the input voltage, v_c the output voltage and L , C , R are the inductance, the capacitance and the resistive load, respectively. In the previous equations, the discontinuous control input, u , takes again the values $\{0, 1\}$. $M1$ and $M2$ work in a complementary

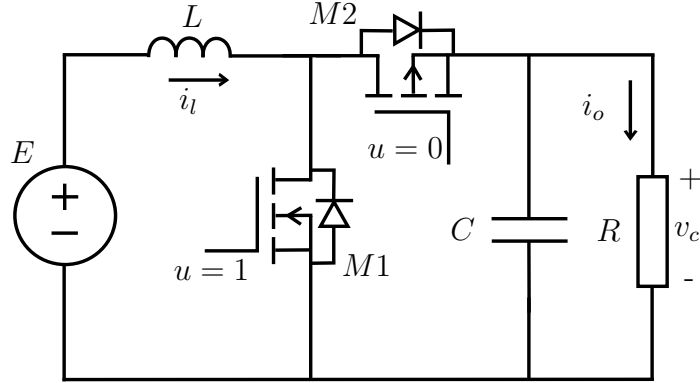


Figure 7.1: Boost converter.

manner, remaining one closed while the other one is open and vice versa. The parametric data of the converter built in the laboratory are shown in Table 7.1.

Table 7.1: Boost converter parameters

| Parameter | Symbol | Value |
|----------------------------|---------|-------------------|
| Input voltage | E | 12 V |
| Output voltage reference | v_c^* | 48 V |
| Output capacitor | C | 132 μF |
| Inductance | L | 20 μH |
| Nominal resistive load | R | 20 Ω |
| Switching period reference | T^* | 10 μs |

The Boost converter, due to its step-up voltage conversion property, is extensively employed in different industrial applications [54–57]. In general, the control of this topology (and other similar ones) involves a complex task due to its nonlinear characteristics, which becomes a challenge from the control point of view.

7.2 Sliding mode control of the output voltage

7.2.1 Switching surface design

The sliding mode controller is designed for regulating the output voltage of the Boost converter. Due to the non minimum phase property of the Boost converter, the direct output voltage regulation using the natural switching function $\sigma(v_c) := v_c^* - v_c$ is not possible, since it results in an unstable behaviour of the inductor current in sliding motion

[10]. Alternatively, an indirect output voltage regulation is proposed with the sliding surface:

$$\sigma(v_c, i_l) := \kappa_1 e_v + \kappa_2 \int e_v(\tau) d\tau - \kappa_3 i_l = 0, \quad (7.3)$$

where the voltage error has been defined as $e_v = v_c^* - v_c$ and the switching surface parameters $\kappa_{1,2,3}$ are assumed positive. Some readers could identify the previous surface as the typical control structure with two nested loops, the inner one regulating the inductor current, and the outer one generating the proper inductor current reference for the inner loop, in order to keep the output voltage at the desired level. In that sense, the terms in (7.3) depending on e_v constitute the outer controller, delivering the aforementioned current reference. In these types of control structures, in order to study the system stability, the inner loop is assumed to be much more faster than the outer one [7]. The difference between that analysis and the one performed here resides in the fact that such hypothesis is not employed.

7.2.2 Sliding dynamics

The time derivative of the switching function is

$$\dot{\sigma}(v_c, i_l) = -\psi_1(v_c, i_l) + (1 - u) \psi_2(v_c, i_l), \quad (7.4)$$

where

$$\psi_1(v_c, i_l) = \frac{E\kappa_3}{L} - \frac{\kappa_1}{RC}v_c - \kappa_2 e_v, \quad \psi_2(v_c, i_l) = \frac{\kappa_3}{L}v_c - \frac{\kappa_1}{C}i_l. \quad (7.5)$$

From (7.4) it is clear that the sliding mode exists when

$$|\psi_2(v_c, i_l)| > |\psi_1(v_c, i_l)|.$$

Using the equivalent control method [7], it is possible to find the ideal sliding dynamics. The u_{eq} , which is found with $\dot{\sigma}(v_c, i_l) = 0$ and $\sigma(v_c, i_l) = 0$, is determined by:

$$u_{eq} = \frac{\psi_2(v_c, i_l) - \psi_1(v_c, i_l)}{\psi_2(v_c, i_l)}, \quad (7.6)$$

leading to an existence range of the sliding mode as:

$$0 < \frac{\psi_1(v_c, i_l)}{\psi_2(v_c, i_l)} < 1. \quad (7.7)$$

The sliding mode dynamics are derived replacing the equivalent control in (7.1)-(7.2):

$$L \frac{di_l}{dt} = E - v_c \frac{\psi_1(v_c, i_l)}{\psi_2(v_c, i_l)}, \quad (7.8)$$

$$C \frac{dv_c}{dt} = i_l \frac{\psi_1(v_c, i_l)}{\psi_2(v_c, i_l)} - \frac{v_c}{R}, \quad (7.9)$$

yielding also a nonlinear state space equations. The point (i_l^*, v_c^*) is an equilibrium point of (7.8), (7.9) that fulfils

$$i_l^* = \frac{v_c^{*2}}{RE}. \quad (7.10)$$

As a consequence, the system stability can be locally disclosed by analysing the stability of the linearized system around this equilibrium point. The linearized system in the error variables $e_1 = i_l - i_l^*$, $e_2 = v_c - v_c^*$, is given by:

$$L \frac{de_1}{dt} = -\frac{E^2 \kappa_1}{C v_c^* \psi_1(v_c^*, i_l^*)} e_1 - \frac{E}{\psi_1(v_c^*, i_l^*)} \left(\kappa_2 - \frac{2\kappa_1}{RC} \right) e_2 \quad (7.11)$$

$$C \frac{de_2}{dt} = \frac{E^2 \kappa_3}{L v_c^* \psi_1(v_c^*, i_l^*)} e_1 + \frac{1}{R \psi_1(v_c^*, i_l^*)} \left(v_c^* \kappa_2 - \frac{2E\kappa_3}{L} \right) e_2, \quad (7.12)$$

where the expressions $\psi_1(v_c^*, i_l^*)$, $\psi_2(v_c^*, i_l^*)$ can be taken from the evaluation of (7.5) under sliding motion, resulting:

$$\psi_1(v_c^*, i_l^*) = \frac{E\kappa_3}{L} - \frac{\kappa_1}{RC} v_c^*, \quad \psi_2(v_c^*, i_l^*) = \frac{\kappa_3}{L} v_c^* - \frac{\kappa_1 v_c^{*2}}{RC E}. \quad (7.13)$$

Stability conditions of (7.11),(7.12) can be derived from its characteristic polynomial:

$$P(s) = s^2 + \frac{1}{\psi_1(v_c^*, i_l^*)} \left(\frac{E^2 \kappa_1}{LC v_c^*} - \frac{\kappa_2 v_c^*}{RC} + \frac{2E\kappa_3}{RLC} \right) s + \frac{E^2 \kappa_2}{LC v_c^* \psi_1(v_c^*, i_l^*)}. \quad (7.14)$$

Therefore, assuming that $v_c^* > 0$, the origin of (7.11),(7.12) is locally asymptotically stable when

$$\frac{E v_c^* \kappa_3}{L} - \frac{\kappa_1 v_c^{*2}}{RC} > 0, \quad (7.15)$$

$$\frac{E^2 \kappa_1}{L} - \frac{\kappa_2 v_c^{*2}}{R} + \frac{2E v_c^* \kappa_3}{RL} > 0. \quad (7.16)$$

Taking into account the values of the converter parameters shown in Table 7.1 and the stability conditions given by (7.15), (7.16), the control parameters are set to $\kappa_1 = 2.2$, $\kappa_2 = 2000$, $\kappa_3 = 0.33$. The goal is to achieve a dominant pole response, being governed essentially by a first order dynamics. Replacing these values in (7.14), the roots of $P(s)$ are: $s_{p1} = -923$, $s_{p2} = -15583$. With these selected gains, the system exhibits a good robustness in the face of load variations, as it will be confirmed in the following experimental results.

7.2.3 Control law

Finally, the control law that enforces sliding motion on the space region given by $|\sigma(v_c, i_l)| < \Delta$ is found using (7.4) as:

$$u = \begin{cases} 0 & \text{if } \sigma \cdot \text{sign}(\psi_2) < -\Delta \quad \text{or } (|\sigma| < \Delta \ \& \ \dot{\sigma} > 0) \\ 1 & \text{if } \sigma \cdot \text{sign}(\psi_2) > \Delta \quad \text{or } (|\sigma| < \Delta \ \& \ \dot{\sigma} < 0). \end{cases} \quad (7.17)$$

It has to be remarked that, from a practical point of view, the design can ensure a constant sign of ψ_2 for a given working conditions, thus avoiding its evaluation by the control law.

7.3 Switching frequency regulation

7.3.1 Evaluation of ρ_k^\pm

The key point for the SFC design is to find the expressions for ρ_k^\pm for a given steady-state sliding motion. Employing the equivalent control derived in (7.6), the equation of $\dot{\sigma}(v_c, i_l)$ in (7.4) is rewritten as:

$$\dot{\sigma}(v_c, i_l) = \psi_2(v_c, i_l)(u_{eq} - u). \quad (7.18)$$

Therefore, the steady-state values of $\dot{\sigma}(v_c, i_l)$ within the hysteresis band boil down to:

$$\dot{\sigma}(v_c^*, i_l^*) = \psi_2(v_c^*, i_l^*) \left(1 - \frac{E}{v_c^*} - u \right).$$

Thus, the values of ρ_*^+ and ρ_*^- result in:

$$\begin{aligned} \rho_*^+ &= \frac{1}{\dot{\sigma}(v_c^*, i_l^*)_{u=0}} = \psi_2(v_c^*, i_l^*)^{-1} \left(1 - \frac{E}{v_c^*} \right)^{-1} \\ \rho_*^- &= \frac{1}{\dot{\sigma}(v_c^*, i_l^*)_{u=1}} = -\psi_2(v_c^*, i_l^*)^{-1} \frac{v_c^*}{E}. \end{aligned}$$

Merging these expressions with the values of the parameters listed in the Table 7.1, one gets:

$$(\rho_*^+, \rho_*^-) = (2.1 \cdot 10^{-6}, -6.3 \cdot 10^{-6}). \quad (7.19)$$

7.3.2 SFC design

Firstly, let us to validate in what conditions the Assumption B is fulfilled, which permits to find the stability conditions through an equivalent linear model of the SFC (see Section 2.3). In the practical implementation, the variable hysteresis band is bounded, leading to a limitation of the feasible switching periods within the range $[2 \mu\text{s}, 20 \mu\text{s}]$, arising an expected maximum error of $10 \mu\text{s}$. As it was shown in the simulation part (see Section 3.3), using a relation of 20 between the grade of change of Δ and $\sigma(v_c, i_l)$ the fulfilment of

Assumption B is guaranteed, then

$$20 \gamma_{L20} |\max e_k| = \min \left\{ |\rho_*^+|^{-1}, |\rho_*^-|^{-1} \right\},$$

and, therefore

$$20 \gamma_{L20} \cdot 10 \cdot 10^{-6} = 1.59 \cdot 10^5 \rightarrow \gamma_{L20} = 7.95 \cdot 10^8.$$

Notice that for $\gamma_L < \gamma_{L20}$, the response of the equivalent model shown in Figure 2.9 will match with the response obtained with the built electronic prototype.

The stability conditions obtained from the linearized model can be found using the Theorem 3 and the equation (2.41). In this case, since the SFC is implemented by analog circuitry, the time constant ($\tau = 65 \mu\text{s}$, empirically measured) of the period sensor has to be taken into account. For the proper evaluation of (2.41), the desired switching period, which is $T^* = 10 \mu\text{s}$, is also required. Hence, from Theorem 3 and equation (2.41) the stability of the linearized system is guaranteed by

$$\gamma_L < \frac{2(T^* + 2\tau)}{\lambda T^*(T^* + 4\tau)} = \frac{2(10 \cdot 10^{-6} + 2 \cdot 65 \cdot 10^{-6})}{1.6 \cdot 10^{-6} \cdot 10 \cdot 10^{-6} \cdot (10 \cdot 10^{-6} + 4 \cdot 65 \cdot 10^{-6})},$$

which yields $\gamma_L < 6.14 \cdot 10^9$.

Finally, the value of the control parameter is set to $\gamma_L = 5 \cdot 10^8$. In this case, the value of γ_L has been tuned close to the limiting value guaranteeing the compliance of Assumption B. With the selected value of γ_L , an overdamped response with low overshoot is expected in the implemented system, as it will be detailed in the experimental part.

7.4 Implementation Details

The Boost converter prototype has been built with the MOSFET power switches PSMN034 from ST Microelectronics (M1 and M2 in Figure 7.1), the inductance SER2918H-223 from Coilcraft, and 4 electrolytic capacitors of $33 \mu\text{F}$ arranged in parallel in order to obtain a total capacitance of $132 \mu\text{F}$ with low equivalent series resistance. The employed MOSFETs driver is the LM5105 from Texas Instruments.

The aforementioned controllers (SMC and SFC) are implemented in a completely analog manner. The switching function, $\sigma(v_c, i_l)$, is generated using a circuitry based on AO, as Figure 7.2 depicts. From this Figure, it can be seen how for the output voltage sensing, v_c , a voltage divider is used together with an AO in voltage follower configuration, ensuring a stage with low output impedance. For the inductor current measurement, i_l , a shunt resistor of $10 \text{ m}\Omega$ with an AO with a high common mode voltage capability is chosen. The selected resistive value for the shunt provides a compromise between low effect Joule losses and a good signal-noise relation. In general, the allowable common mode voltage of a standard AO is equal or close to the used supply voltage. Since the switching function will be, in steady-state, a triangular signal of 100 kHz , a high bandwidth is needed in the AO. A high bandwidth AO usually implies a reduced supply voltage range, as it is the case

here. Therefore, the common mode voltage at the AO inputs should be lower than 5 V (see Figure 7.2). The common mode voltage on both shunt resistor terminals is at least the output voltage (whose desired value is 48 V) plus eventual ringings caused by the Mosfet commutations. It results evident why an AO with a high common mode voltage feature is required. The selected chip is the AD8216 from Analog Devices.

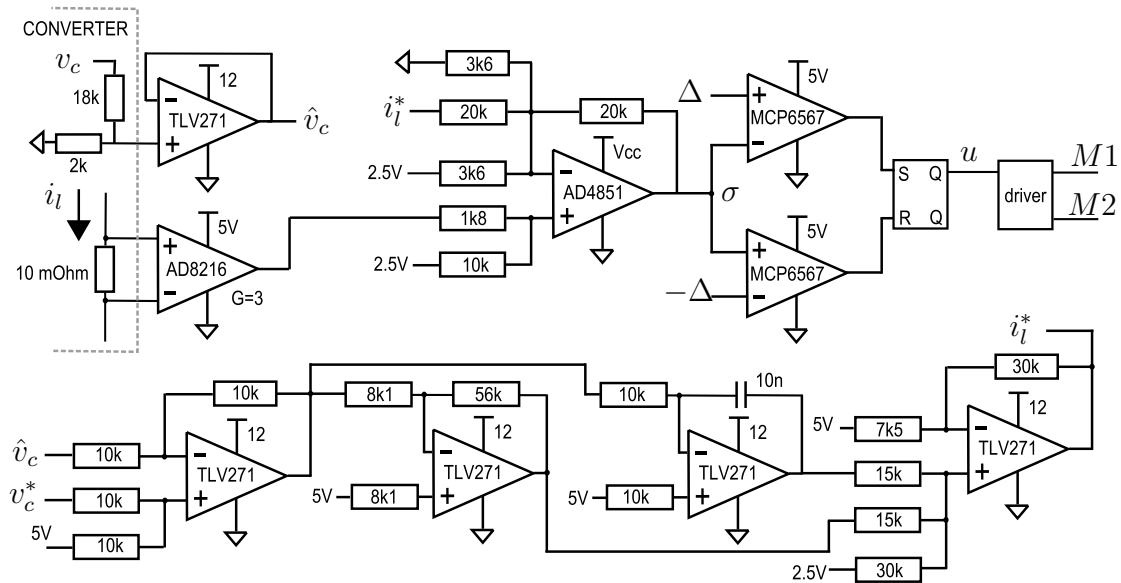


Figure 7.2: Analog electronics implementation of the switching function and the variable hysteresis band comparator.

The variable hysteresis comparator is again built using two high speed comparators from Microchip, specifically the MCP6567 together with a Set-Reset Flip-Flop. For the Flip-Flop implementation a pair of NOR gates are needed (chip 74LS02 or similar) [58]. The selected configuration facilitates the variation of the hysteresis band for the comparator.

The circuitry implementing the switching function has an integral action that could integrate its output prior the start-up of the system. In order to avoid such undesirable effect, which would degrade the expected response, a special circuit has been designed in order to keep the integrator output null until the system starts. Besides, a soft-start strategy has been implemented consisting in an output voltage reference growing linearly from the initial voltage at the output (12 V) up to the desired steady-state one (48 V). The usage of a soft-start is usual in applications with the Boost converter in order to avoid dangerous overvoltage at the output, particularly when the load resistance reaches high values [59]. These systems, have been omitted in Figure 7.2 for the sake of brevity.

Finally, the SFC is implemented with the same structure shown in Section 6.4, but with the updated resistor and capacitor values according to the designed value for $\gamma_L = 5 \cdot 10^8$. The resulting circuit scheme is shown in Figure 7.3.

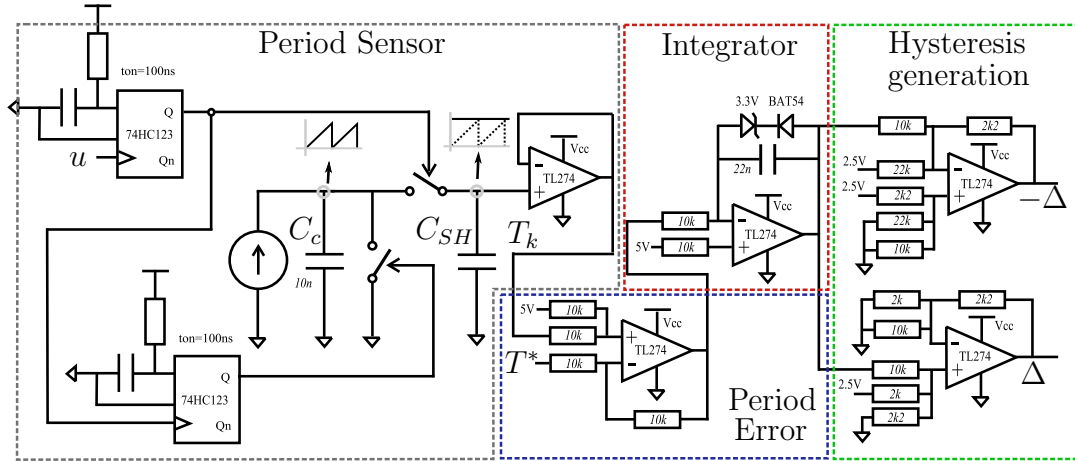


Figure 7.3: Circuit scheme of the period sensor and the analog structure implementing the SFC for the Boost converter.

7.5 Experimental results

The experimental results obtained with the designed system are discussed in this last Section of the Chapter. The results are organized in three groups: SMC performance, SFC performance and system robustness.

1. SMC performance

Figure 7.4 shows the start-up of the converter. The oscilloscope capture illustrates the behaviours of the output voltage, v_c , the switching function, $\sigma(v_c, i_l)$, the control signal, u , and the switching period, T_k ; as it was noted in the previous Chapter, the signal corresponding to the switching period appears converted to voltage with a rate of $0.5 \text{ V}/\mu\text{s}$. In the test, the load resistance is $R=100 \Omega$, which could be understood as a light load condition, being in general the worst scenario for the converter start-up. Notice that the initial value of the output voltage is the value of the input one due to the anti-parallel diode of the M2 switch (see Figure 7.1). From the Figure, it can be seen how the output voltage linearly rises up and how the amplitude of the hysteresis band (see the behaviour of $\sigma(v_c, i_l)$) is adjusted to the required value that provides the desired switching period (see zoomed areas of the steady-state of the waveforms shown in the bottom right window). Besides, the switching period converges to the reference value after a brief transient with a small undershoot. Finally, the bottom left window shows the transient response of the switching function. Notice how in the start-up the switching function reaches quickly the hysteresis region bounded by $-\Delta$ and Δ , from its initial condition. It should be also remarked that the piecewise linear assumption can be taken as a fact almost from the beginning of the test (see the zooms views in the bottom part of the figure).

2. SFC performance

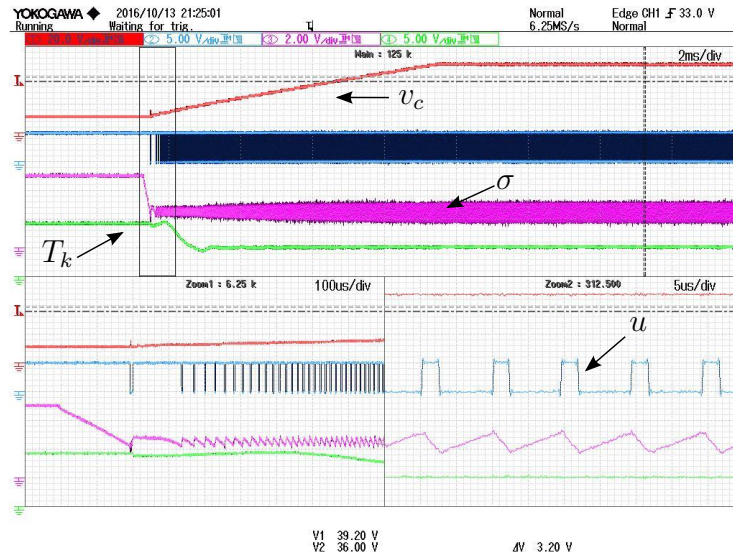


Figure 7.4: Converter start-up. v_c : red, u : blue, σ : magenta, T : green.

The following test is devoted to highlight the switching period regulation capability of the system, with a tracking of a step-type reference. Specifically, the switching period reference varies from $T^* = 8 \mu\text{s}$ to $T^* = 12 \mu\text{s}$ and vice-versa. For this test the load resistance is of $R = 20 \Omega$, corresponding to the full load condition. Figure 7.5 shows the behaviours of the output voltage ripple, Δv_c , the switching function, $\sigma(v_c, i_l)$, the control signal, u , and the switching period, T_k , again scaled at a rate of $0.5 \text{ V}/\mu\text{s}$. The SFC properly adapts the hysteresis band value (see the envelope of σ) in order to achieve the desired steady-state switching period. The experimental result overlaps with the theoretical one. Specifically, the resulting closed-loop transfer function of the model of Figure 2.9 is

$$\frac{T(s)}{T^*(s)} = \frac{\lambda\gamma_L(2 + T^*s)(\tau s + 1)}{p(s)},$$

where $p(s)$ is given by (2.42). In fact, according to the data presented in the Table 7.1, and the designed value $\gamma_L = 5 \cdot 10^8$, the transfer function results in

$$\frac{T(s)}{T^*(s)} = \frac{5.483 \cdot 10^{-6} s^2 + 1.181s + 1.687 \cdot 10^4}{6.5 \cdot 10^{-10} s^3 + 1.4 \cdot 10^{-4} s^2 + 1.916s + 1.687 \cdot 10^4},$$

which fits the experimental oscilloscope capture of Figure 7.5. Notice also that the switching function does not leave the hysteresis band region, and therefore the output voltage is not affected by the switching period reference variation. This fact can be confirmed from the output voltage ripple behaviour, Δv_c , observed during the entire test. The waveforms detailed in the bottom windows correspond to the steady-state dynamics at $T^* = 8 \mu\text{s}$ (right window), and at $T^* = 12 \mu\text{s}$ (left window).

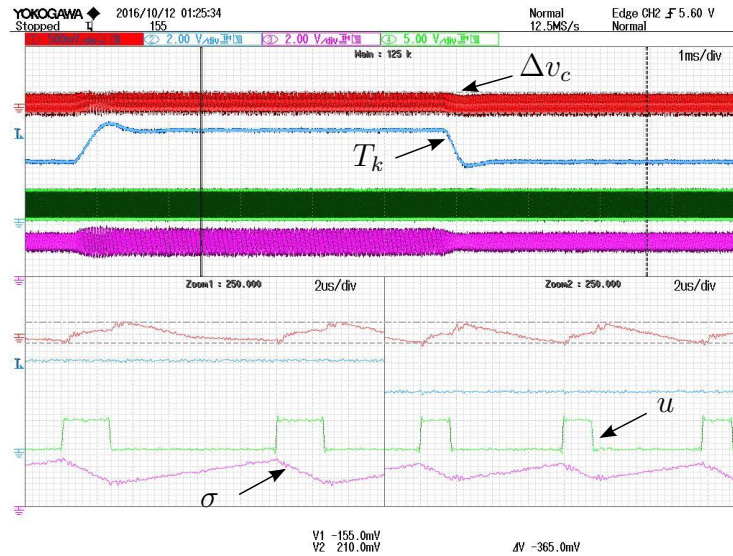


Figure 7.5: Switching period regulation for a step change from $T^* = 8 \mu\text{s}$ to $T^* = 12 \mu\text{s}$ for $v_c^* = 48 \text{ V}$ and $R = 20 \Omega$. Δv_c : red, T : blue, σ : magenta, u : green.

3. System robustness

The two last results show the robustness of the controllers in front of load transients at the converter output. Again, the responses of the output voltage, v_c , the load current, $i_o = \frac{v_c}{R}$, the switching function, $\sigma(v_c, i_l)$, and the switching period (scaled by $0.5 \text{ V}/\mu\text{s}$), T_k , are shown in Figures 7.6 and 7.7, when the resistive load changes from $R = 20 \Omega$ to $R = 100 \Omega$, and from $R = 100 \Omega$ to $R = 20 \Omega$, respectively. In these Figures, one can see how the converter recovers the desired output voltage after a very smooth transient (with a maximum deviation of 2 V around the desired value of 48 V), as expected from the design of Section 7.2, while the switching frequency is only slightly affected by the load change.

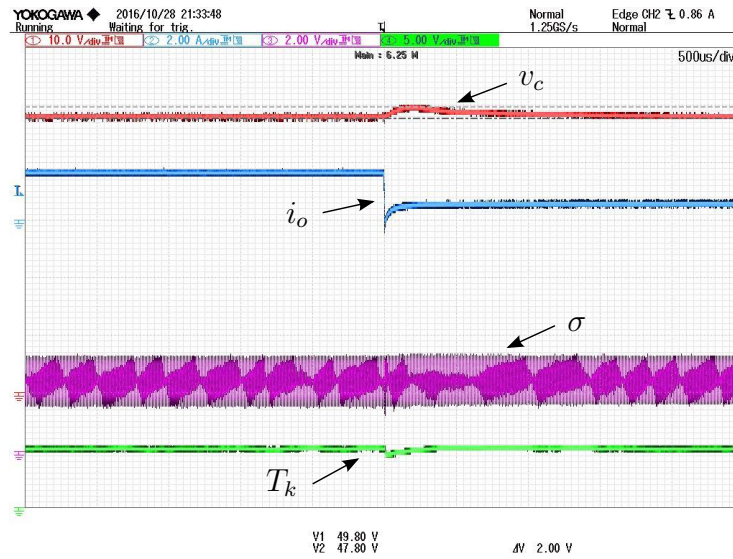


Figure 7.6: Load variation from $R = 20 \Omega$ to $R = 100 \Omega$ for $v_c^* = 48 \text{ V}$. v_c : red, i_o : blue, σ : magenta, T : green.

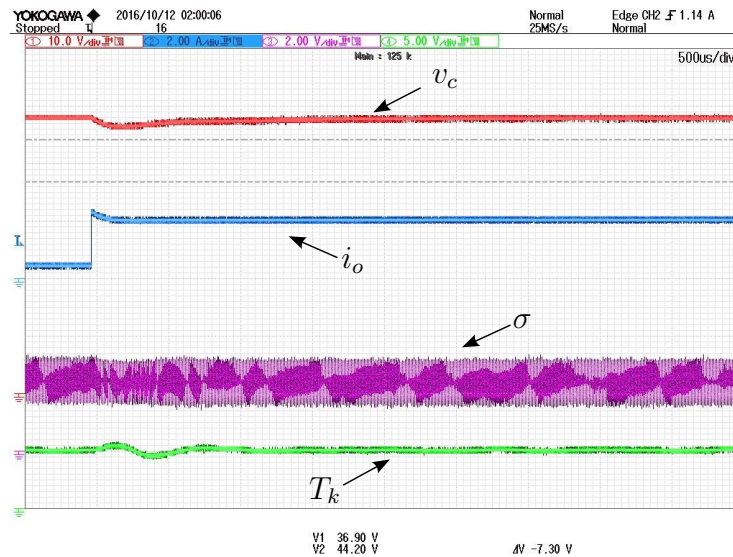


Figure 7.7: Load variation from $R = 100 \Omega$ to $R = 20 \Omega$ for $v_c^* = 48 \text{ V}$. v_c : red, i_o : blue, σ : magenta, T : green.

7.6 Conclusions

The experimental results confirm an overall good performance of the system under the control of the SMC and SFC, and most importantly, they corroborate that the SFC is able to regulate the switching frequency in steady-state without degrading the well-known features of the SMC, as the robustness or the high transient response. The dynamics observed in the laboratory results, highlight the usefulness of the theoretical developments described along the Chapter, for both SMC and SFC controllers. Moreover, the developed model in Section 2.3 is validated for a nonlinear system as the Boost converter is.

Chapter 8

Voltage Tracking in a Voltage Source Inverter.

The applications of the SFC presented in the previous chapters belong to cases where the SMC is under a regulation control task. In this Chapter, the application of the switching frequency regulation strategy in a tracking control problem is set out. Specifically, a voltage source inverter (VSI) is assembled for experimental evaluation in the laboratory. A sliding mode control will be designed in order to generate a sinusoidal voltage at the converter output, thus leading to a tracking control problem. In this experimentation, both controllers, the SMC and the SFC, are digitally implemented by a micro-controller. Moreover, with the purpose of showing results as realistic as possible, the VSI developed in the laboratory has been designed with a medium power-handling capability (up to 2.2 kW). Another important characteristic of the work presented hereafter is that the SMC has been designed with the aim of operating with linear and nonlinear loads connected at the VSI output. Such property allows us to test further the performance of the SFC under a new working scenario.

The Chapter is organized as follows: in the first Section the VSI structure, its parametric data and the corresponding state space equations are introduced. The second Section tackles the sliding mode generation of the AC signal (220 V RMS / 50 Hz) at the VSI output, supporting linear and nonlinear loads. Then, the SFC is designed according to the theory developed at Section 2.2.2. Subsequently, the implementation of both controllers in a digital platform is addressed and discussed. Lastly, the main experimental results are shown in the last Section.

8.1 The voltage source inverter

The VSI circuit scheme is depicted in Figure 8.1. This circuit is commonly employed to generate a sinusoidal signal at its output and it is classified as DC/AC converter. With regard to its structure, the VSI can be understood as a traditional Buck structure with a full bridge of switches. As a consequence, the VSI is able to generate voltages at its output

between E to $-E$. The VSI dynamics are described by the following state space equations:

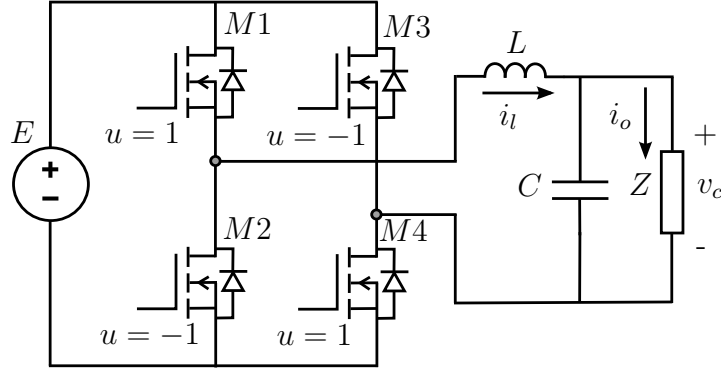


Figure 8.1: Voltage source inverter structure.

$$C \frac{dv_c}{dt} = i_l - i_o, \quad (8.1)$$

$$L \frac{di_l}{dt} = -v_c + E u, \quad (8.2)$$

where i_l is the inductor current, v_c is the output voltage, i_o is the load current, L is the inductance, C is the capacitor and E is the input voltage. The discontinuous control input u takes values in the discrete set $\{-1, 1\}$. This strategy corresponds to the well-known two level modulation in the pulse width modulation (PWM) techniques [60]. The power switches are represented by M_1 , M_2 , M_3 , and M_4 . As it is shown in Figure 8.1, M_1 and M_4 are short circuited when $u = 1$, and remain open when $u = -1$, whereas M_2 and M_3 work in a complementary way. Table 8.1 presents the specific values of the converter parameters used in the experimental setup.

The voltage source inverter is the most used DC/AC converter in the industry [61–65]. Because of its simple structure, the converter has the capability to work with high voltage and manage high powers. As an example of application, VSIs are used in the photovoltaic plants injecting the power generated by the solar cells to the AC power grid. Another application of VSIs can be found in the uninterruptible power supply (UPS) systems, where is common the employment of back-to-back structures [66], being the VSI one of its most important parts. Similarly, the VSI converter is the preferable option for AC machine drives. The AC motors are used, among other, in air conditioner’s compressors, refrigerators, water pumps, electric saw, conveyor belts, electric traction in trains and, increasingly, in the growing market of the electric vehicle.

Table 8.1: Voltage Source Inverter parameters.

| Parameter | Symbol | Value |
|------------------------------------|--------|-----------------|
| Input voltage | E | 420 V |
| Desired output voltage amplitude | A | $220\sqrt{2}$ V |
| Output voltage frequency | f | 50 Hz |
| Inductor | L | 440 μ H |
| Output capacitor | C | 100 μ F |
| Nominal output power (Linear Load) | P | 2.2 kW |
| Peak output power (Linear Load) | P_p | 3.3 kW |
| Switching period reference | T^* | 50 μ s |

8.2 Sliding mode tracking of the output voltage

8.2.1 Switching surface design

In this case, the control objective is to track a time-varying reference voltage at the output. The signal to be tracked is:

$$v_c^* = A \sin \omega t. \quad (8.3)$$

Once the functionality of the VSI has been defined, the following task is to design a switching function that fulfils the desired performance. In the traditional SMC schemes applied to this converter, since the relative degree of the output voltage, v_c , with respect to the control, u , is two, the following first order linear switching surface is typically used [46]:

$$\sigma(v_c, \dot{v}_c) = \psi_1 e_v + \psi_2 C \dot{e}_v = 0, \quad (8.4)$$

where $e_v = v_c - v_c^*$. Notice how (8.4) contains the first time derivative of the output voltage. As it was explained in Section 5.4, it is usual to take the current flowing by the output capacitor as the first time derivative of the output voltage, avoiding the direct differentiation of the measured voltage which always brings noise problems (even in digital differentiation). Such measured current is properly replaced in the switching function written in (8.4), leading to an equivalent expression. However, this technique usually provides good results only with linear loads, degrading its performance with other types of loads. Moreover, from the sliding mode control design, the substitution of the first time derivative by the output capacitor current can compromise the piecewise linear behaviour of the switching function when the load is not pure resistive. As a consequence, in order to design a switching function less sensitive to the type of load applied at the output, an alternative switching function is proposed. The new switching function uses the output signal gener-

ated by a Current Transformer (CT), measuring the inductor current, i_l . Specifically, the proposed switching function is:

$$\sigma(v_c, x_M) := -\psi_1 e_v + \psi_2 C \dot{v}_c^* - \psi_2 \frac{L_x}{MR_b} x_M \quad (8.5)$$

where again v_c^* is the desired output voltage, x_M the signal coming from the current transformer output and $\psi_1, \psi_2 > 0$ are the switching function parameters. L_x , M and R_b are CT parameters, and C is the capacitance of the output VSI filter. As it was already introduced in Section 6.2, the state space equation generated by the CT inclusion is:

$$L_x \frac{dx_M}{dt} = -R_b x_M + R_b M \frac{di_l}{dt}. \quad (8.6)$$

In order to illustrate the lack of piecewise linear behaviour in the switching function if i_c is used as $C \dot{v}_c$, a simulation of the system designed and experimented in this Chapter is early introduced at this step. Figure 8.2 depicts the simulation result for a nonlinear load, where the signal i_c and \hat{x}_M are shown, being \hat{x}_M :

$$\hat{x}_M = x_M \frac{L_x}{MR_b}.$$

Therefore, expression (8.5) can be rewritten as:

$$\sigma(v_c, x_M) := -\psi_1 e_v + \psi_2 C \dot{v}_c^* - \psi_2 \hat{x}_M.$$

The behaviour of the CT can be understood as a high pass filter, since, from (8.6), it can be derived that:

$$I_l(s) = \frac{sL_x + R_b}{sR_bM} X_M(s).$$

The gain of the previous filter in the band pass can be found solving the following limit:

$$\lim_{s \rightarrow \infty} \frac{sL_x + R_b}{sR_bM} = \frac{L_x}{R_bM},$$

and hence \hat{x}_M is proportional to the high frequency ripple of i_l .

The nonlinear load used in the simulation corresponds to a diode rectifier with a filtering capacitor supplying a resistor (see Figure 8.10). When the diodes are closed ($|v_c| \geq V_{dc}$), the load connected at the VSI is a capacitor in parallel with a resistor (assuming ideal diodes). When the diodes stay open ($|v_c| \leq V_{dc}$), the VSI is in no load condition. From the result in Figure 8.2, it is clear that when the diodes are switched on and there is current flowing to the load, i_c loses the piecewise linear behaviour while \hat{x}_M does not. Such results justify the selection of the switching function shown in (8.5).

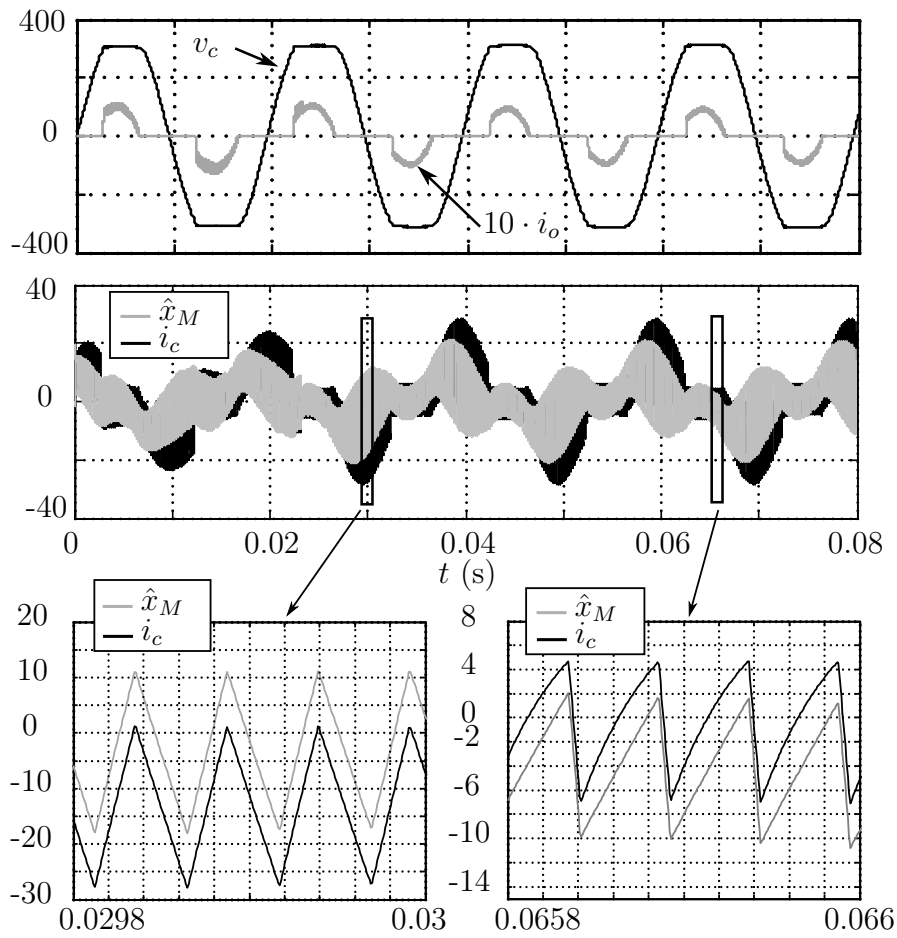


Figure 8.2: Details of the signals i_c and \hat{x}_M when the inverter is loaded by a nonlinear load.

8.2.2 Ideal sliding dynamics

The SMC design is derived from the first time derivative of the switching function:

$$\dot{\sigma}(v_c, x_M) = -\psi_1 \dot{e}_v + \psi_2 C \ddot{v}_c^* + \frac{\psi_2}{M} x_M - \frac{\psi_2}{L} [E u - v_c]. \quad (8.7)$$

Moreover, the dynamics enforced by the sliding motion on $\sigma(v_c, x_M) = 0$ can be found from (8.5) as:

$$x_M = \frac{M R_b}{\psi_2 L_x} [\psi_1 (v_c^* - v_c) + \psi_2 C \dot{v}_c^*], \quad (8.8)$$

and, therefore

$$\dot{\sigma}(v_c, x_M) = -\psi_1 \dot{e}_v + \psi_2 C \ddot{v}_c^* - \beta (\psi_1 e_v - \psi_2 C \dot{v}_c^*) - \frac{\psi_2}{L} [E u - v_c] \quad (8.9)$$

where $\beta = \frac{R_b}{L_x}$. Thanks to the inclusion of x_M in (8.5), the relative degree between the switching function and the control input is one, as it corroborates the fact that u appears in $\dot{\sigma}(v_c, x_M)$. Arranging terms in (8.9) one gets (notice that $e_v = v_c - v_c^*$):

$$\dot{\sigma}(v_c, x_M) = f^* + f^e - \frac{\psi_2}{L} E u \quad (8.10)$$

where $f^* = \psi_2 C \ddot{v}_c^* + \beta \psi_2 C \dot{v}_c^* + \frac{\psi_2}{L} v_c^*$, $f^e = \left(\frac{\psi_2}{L} - \beta \psi_1 \right) e_v - \psi_1 \dot{e}_v$. From (8.10) it can be figured out that a sliding motion can be enforced in $\sigma(v_c, x_M) = 0$ when the term depending on control dominates the rest of terms, or

$$\frac{\psi_2}{L} E > |f^* + f^e|.$$

From (8.10) the equivalent control is easily found:

$$u_{eq} = (f^* + f^e) \frac{L}{\psi_2 E}. \quad (8.11)$$

Once the equivalent control and the sliding mode equation have been found, it is time to analyse the resulting sliding dynamics in order to check if the desired tracking of v_c^* by v_c is achieved. Replacing the equivalent control, (8.11), in the original system (8.1), (8.2), the state space equations that arise are:

$$\psi_2 \frac{di_l}{dt} = f^* + f^e - \frac{\psi_2}{L} v_c, \quad (8.12)$$

$$C \frac{dv_c}{dt} = i_l - i_o. \quad (8.13)$$

Let us analyse the sliding dynamics for the tracking error e_v . Combining equations

(8.12) and (8.13), the resulting dynamics for the tracking error, $e_v = v_c - v_c^*$, can be found:

$$C\ddot{e}_v + \frac{\psi_1}{\psi_2}\dot{e}_v + \frac{\psi_1 R_b}{\psi_2 L_x}e_v = \frac{R_b C}{L_x}\dot{v}_c^* - \dot{i}_o. \quad (8.14)$$

As expected, the sliding mode dynamics of the output voltage includes the evolution of the load current. In this thesis, three types of loads are studied, namely: resistive loads, reactive loads and nonlinear loads. Each of those cases are analysed separately in the coming Sections 8.2.4, 8.2.5 and 8.2.6 for further understanding.

8.2.3 Control law

The control law that ensures sliding motion in $\sigma(v_c, x_M) = 0$ regardless of the type of load applied to the VSI, is obtained from (8.10) as:

$$u = \begin{cases} -1 & \text{if } \sigma < -\Delta_k \quad \text{or } (|\sigma| < \Delta_k \ \& \ \dot{\sigma} > 0) \\ 1 & \text{if } \sigma > \Delta_k \quad \text{or } (|\sigma| < \Delta_k \ \& \ \dot{\sigma} < 0). \end{cases} \quad (8.15)$$

8.2.4 Sliding dynamics for pure resistive load

The specific case for a pure resistive load is characterized by $i_o = \frac{v_c}{R}$, which, using (8.14), boils down to the equation:

$$C\ddot{e}_v + \frac{\psi_1}{\psi_2}\dot{e}_v + \frac{\psi_1 R_b}{\psi_2 L_x}e_v = \frac{R_b C}{L_x}\dot{v}_c^* - \frac{\dot{v}_c}{R}. \quad (8.16)$$

The dynamics in (8.16) depends on the VSI parameters and the controller gains. The selection procedure of L and C values is omitted for the sake of brevity, but, summarizing, it follows setting the cut-off frequency of the output LC filter at least a decade below the switching frequency, thus reducing the output voltage ripple [2]. Therefore, the parameters to design are ψ_1 , ψ_2 , L_x and R_b . Notice that the CT parameters are treated as switching surfaces gains, including the sensor dynamics in the design. Let us define the following parameters in order to clarify the future developments:

$$\alpha = \frac{\psi_1}{\psi_2}, \quad \beta = \frac{R_b}{L_x}, \quad \gamma = \frac{1}{RC},$$

Replacing those definitions in the sliding mode dynamics, (8.16) results in:

$$C\ddot{e}_v + [\alpha + \gamma C]\dot{e}_v + \alpha\beta e_v = C\dot{v}_c^* [\beta - \gamma]. \quad (8.17)$$

From (8.17) it can be easily derived that if $\beta = \gamma$ a perfect tracking of the output voltage is achieved, since (8.17) has $e_v = 0$ as an asymptotic stable equilibrium point. The problem is that the output load is not fixed and can vary under different situations. As a consequence, the strategy followed in this study is to adjust β for the worst load case, which corresponds

to the output peak power. Hence, the value of β is fixed as:

$$\beta = \frac{1}{R_p C},$$

being

$$R_p = \frac{A^2}{2P_p}.$$

The value of α is the remaining design parameter. The design criterion for α has several implications in the tracking error dynamics. One of the design criteria for this value is the amplitude and phase error committed in v_c with respect to v_c^* at steady-state. From (8.17) it can be derived the transfer function that relates v_c and v_c^* :

$$\frac{V_c(s)}{V_c^*(s)} = \frac{s^2 C + s[\alpha + \beta C] + \alpha \beta}{s^2 C + s[\alpha + \gamma C] + \alpha \beta}. \quad (8.18)$$

Figure 8.3 shows the frequency response of (8.18), for α values from 0.5 to 2, for a condition where the applied load is not the maximum one ($R \neq R_p$). Specifically, in these curves $R = 200 \Omega$, being such value far away from the used value for designing β , which is $R_p = 14.7 \Omega$. This value implies one of the worst-case scenarios from the tracking error point of view. In the graph, the desired frequency of the VSI output voltage (50 Hz) is highlighted. From the Figure, it is clear that both amplitude and phase error at 50 Hz decrease as α increases, being such error acceptable when $\alpha \geq 1$.

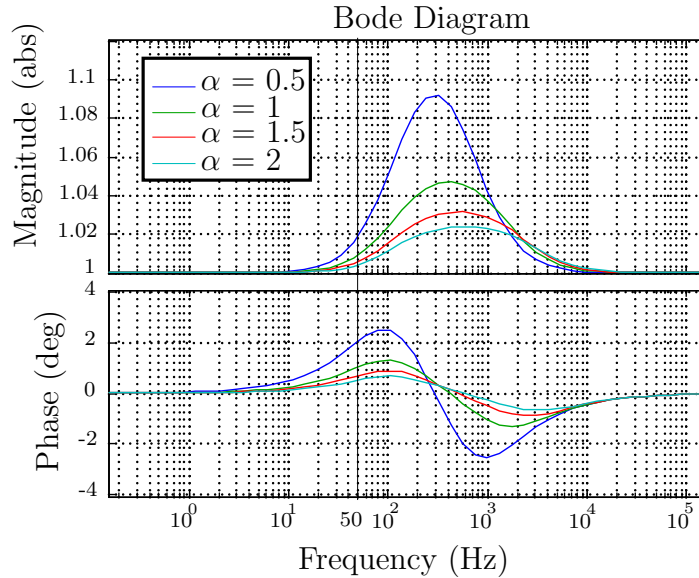


Figure 8.3: Bode plots of expression (8.18) with α as a parameter. $\beta C = 1/R_p = 0.068$, $\gamma C = 0.005$.

The α parameter has also influence in the transient response of the error dynamics. From equation (8.17), it is obvious that the characteristic polynomial governing such dy-

namics is:

$$Cs^2 + [\alpha + \gamma C]s + \alpha\beta = 0. \quad (8.19)$$

Using (8.19), an equivalent closed-loop system can be found as its closed-loop poles coincide with the roots of (8.19). This methodology allows us to plot the root locus as a function of α value. Notice that (8.19) is equivalent to:

$$1 + \frac{\alpha}{C} \frac{s + \beta}{s^2 + \gamma Cs} = 0. \quad (8.20)$$

Figure 8.4 depicts the resulting root locus using a load value satisfying $\gamma = 0.5\beta$. On the Figure, it can be seen the values of the breakaway and break-in points, s_1 , s_2 , and the corresponding values of α for those points.

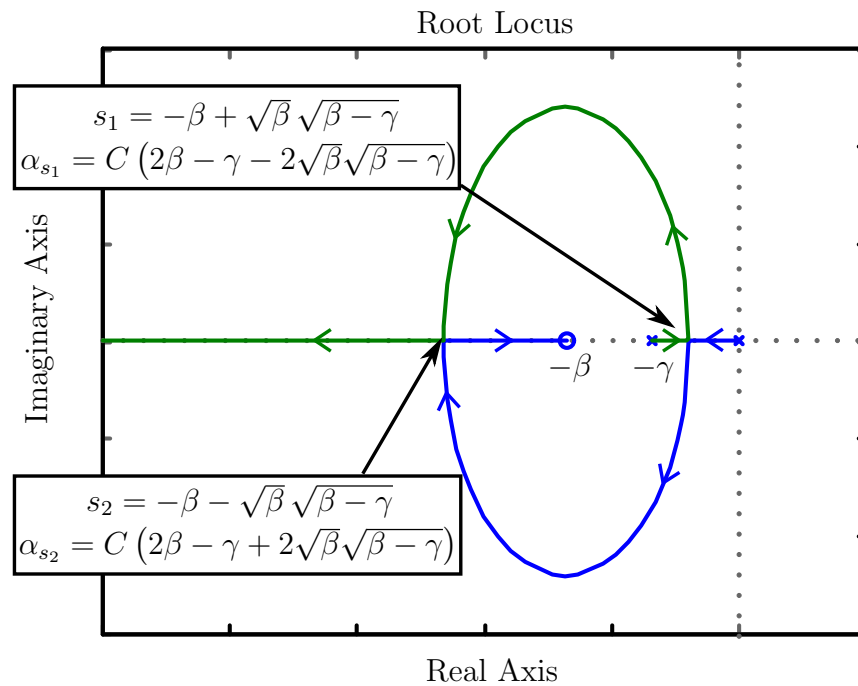


Figure 8.4: Root locus of system shown in (8.20). $\gamma = 0.5\beta$.

The interesting point is s_2 (break-in point), since the closed-loop poles becomes higher in absolute value, providing a fast transient response. Let us analyse the conditions for α in the working range of γ such that the closed-loop poles departure always from s_2 , thus providing overdamped responses. Selecting R_p as the minimum resistive load, the working range for γ is defined according to the expected load level in the inverter:

$$R_p < R \quad \rightarrow \quad 0 < \gamma < \beta.$$

The value of α corresponding to the break-in point s_2 is (as it is shown in Figure 8.4):

$$\alpha_{s_2} = C \left(2\beta - \gamma + 2\sqrt{\beta} \sqrt{\beta - \gamma} \right),$$

which results, for the limiting values:

$$\gamma = 0 \quad \rightarrow \quad s_2 = -2\beta, \alpha_{s_2} = 4\beta C,$$

$$\gamma = \beta \quad \rightarrow \quad s_2 = -\beta, \alpha_{s_2} = \beta C.$$

Therefore, if the α parameter fulfils

$$\alpha > 4\beta C = \frac{4}{R_p},$$

the responses will be overdamped for all the loads conditions. For the case analysed in this thesis, using the data shown at Table 8.1, the requirement for α results in $\alpha > 0.26$. Additionally, according to Figure 8.4, it is clear that (8.19) will have a root in the range $(s_2, -\beta)$, thus entailing a transient response with a time constant, τ , at least equal or higher than $1/(2\beta)$ and always smaller than $1/\beta$.

According to the previous discussion, it is reasonable to use an $\alpha \geq 1$. However, it exists an inconvenient from a practical point of view that could appear if α is too high, which is the lack of piecewise linear behaviour of σ . This nondesirable effect is related to the high frequency ripple in the state variables i_l and v_c , produced by the switched characteristic of u . Let us study such phenomena through expression (8.10). At this point, it is important to remind that the switching frequency is designed as high as, in a switching interval, the system dynamics related to ω (frequency of the desired VSI output voltage v_c^* , equation (8.3)) can be considered constant ($T^* \ll 2\pi/\omega$). Unlike v_c^* , that only has harmonics in ω , in the real sliding mode v_c and i_l have harmonics at the switching frequency. This can be easily proved from (8.1) and (8.2). From (8.2), it is evident that the action of the discontinuous action u induces high frequency harmonics in i_l (E is a constant value). Similarly, such ripple in i_l produces a high frequency ripple in v_c , as (8.1) states.

Recalling (8.10), it can be observed that f^* only depends on v_c^* and, as a consequence, it can be treated as a constant value, F^* , during a specific switching interval. This does not happen with f^e , since it depends on v_c , which has high frequency ripple. Therefore, the expression for the switching function time derivative in the real sliding motion can be approximated as:

$$\dot{\sigma}(v_c, x_M) = F^* - \alpha\psi_2(\beta e_v + \dot{e}_v) - \frac{\psi_2}{L}(Eu - e_v). \quad (8.21)$$

The error e_v appearing on the right term in (8.21) is not worrying since $E \gg e_v$ and, in practise, e_v can be neglected. Nevertheless, it is evident how with high values of α the term on the middle could take relevance, since e_v has high frequency components due to v_c . As a result, a high α amplifies the effect of e_v in (8.21), compromising the assumption of piecewise linear behaviour of the switching function.

Therefore, in order to select an α value providing: a good transient response in the overall load range, a low phase and amplitude tracking error in steady-state and preserving, as far as possible, the piecewise linear characteristic of σ , $\alpha = 1$ is chosen.

Finally, the resulting frequency responses of (8.18) with the α , β selected for different loads are shown in Figure 8.5. The bode plots correspond to load values, from $R = 15 \Omega$ up to $R = 200 \Omega$. From the curves, it can be inferred how with the designed values the best responses are obtained when the output power increases (as expected). However, it is clear also from the Figure that with light load conditions the phase and amplitude error are really small at the working frequency of 50 Hz, being of 1.5° and 1%, respectively, in the worst case. It should be remarked that the maximum load case ($\gamma = \beta C$) has been omitted since the response becomes a straight line equal to one (perfect tracking).

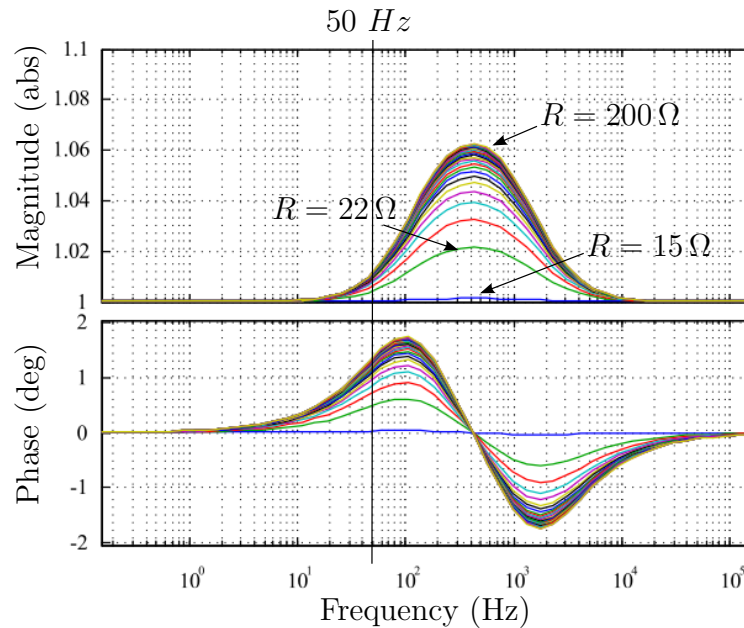


Figure 8.5: Bode plots of expression (8.18) with the applied load at the output as a parameter.

8.2.5 Sliding dynamics for reactive linear load

The previous Section has shown how to design the switching function parameters when the loads applied to the VSI are purely resistive, and how to minimize the tracking error for a given load range. However, it is also interesting to analyse the sliding mode dynamics for different loads connected at the VSI output. Let us define a general impedance, $Z(s)$, as:

$$Z(s) = \frac{a_n s^n + a_{n-1} s^{n-1} + \dots + a_0}{b_m s^m + a_{m-1} s^{m-1} + \dots + b_0}. \quad (8.22)$$

The function shown in (8.22) can be treated as a positive real function, (from now on PR) [67], [68]. As it is stated in Chapter 3 of reference [67], whatever realization of an impedance network consisting of resistors, capacitors or inductors delivers a PR function. Therefore, a general analysis carried out considering that the output impedance of the

inverter $Z(s)$ is a PR function would apply for whatever type of load, as R-L, R-C, R-L-C, etc. The main properties of a PR function, among others (see [67] for details) are summarized in the Definition 1.

Definition 1. *A PR function, $Z(s)$, fulfils that:*

1. *No poles or zeros must be in the right half of the s -plane.*
2. *Poles of $Z(s)$ and poles of $1/Z(s)$ on the finite imaginary axis must be simple and have real and positive residues.*
3. *$|n - m| \leq 1$; no poles and zeros at infinity must be simple.*
4. *$|\arg Z(s)| \leq \pi/2$ for $|\arg s| \leq \pi/2$.*
5. *A sum of PR functions is also PR.*
6. *Being $Z(s)$ PR, $1/Z(s)$ is also PR.*

The PR characteristic does not only belong to linear impedances, whatever function can be PR if some requirements are fulfilled. The Definition 2 states the conditions for a rational function with real coefficients, $Q(s)$, to be PR [67].

Definition 2. *A rational function, $Q(s)$, is PR if:*

1. *$Q(s)$ must have no poles in the right-half side of the complex plane.*
2. *$Q(s)$ may have only simple poles in the imaginary axis ($j\omega$) with positive and real residues.*
3. *$\text{Re } Q(j\omega) \geq 0 \quad \forall \omega$.*

At this step, a general analysis of the output voltage dynamics is performed. The output current is characterized in the s domain as follows:

$$I_o(s) = \frac{V_c(s)}{Z(s)}.$$

Using such expression, and applying the Laplace transform to (8.14), one gets:

$$s^2 C E_v(s) + s\alpha E_v(s) + \alpha\beta E_v(s) = s\beta C V_c^*(s) - sV_c(s) \frac{1}{Z(s)}. \quad (8.23)$$

Since $E_v(s) = V_c(s) - V_c^*(s)$

$$s^2 C E_v(s) + s\alpha E_v(s) + \alpha\beta E_v(s) = s\beta C V_c^*(s) - s [E_v(s) + V_c^*(s)] \frac{1}{Z(s)}. \quad (8.24)$$

Using expression (8.24) the equivalent block diagram of the resulting dynamics is sketched in Figure 8.6. From Figure 8.6 the closed-loop transfer function can be also deduced, which results in

$$T(s) = D(s) \frac{G(s)}{1 + G(s)H(s)}, \quad (8.25)$$

where

$$H(s) = 1/Z(s), \quad D(s) = \left[\frac{R_b C}{L_x} - \frac{1}{Z(s)} \right], \quad G(s) = \frac{s}{s^2 C + s \frac{\psi_1}{\psi_2} + \frac{\psi_1 R_b}{\psi_2 L_x}}.$$

First of all, from the defined transfer function $D(s)$, it is clear that the zeros of the impedance connected to the output become closed-loop poles. The function $D(s)$ is intended to represent realizations of real impedances, having always a dissipative characteristic, resulting in roots with real parts lower than zero. Therefore, from the PR characteristic of $Z(s)$, and assuming always real parts lower than zero, all the zeros and poles of $Z(s)$ will be located in the left side of the complex plane, which does not compromise the system stability.

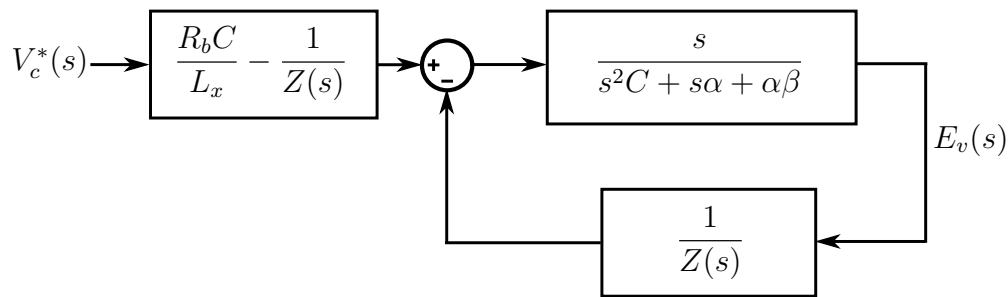


Figure 8.6: Equivalent diagram of the ideal sliding mode dynamics in the s domain. General case in function of $Z(s)$.

The remaining poles of (8.25) are determined by:

$$P(s) = 1 + G(s)H(s). \quad (8.26)$$

The stability analysis could be performed over the equation described in (8.26) for a specific load applied to the VSI, substituting the corresponding impedance in the s domain. However, it is interesting to perform a general analysis trying to take advantage of the early presented properties of a PR function.

It has already been noted that $Z(s)$ is PR due to its construction, and also its inverse $H(s) = 1/Z(s)$. According to (8.26), in order to obtain a phase margin greater than zero (which implies stability), the argument of $G(s)H(s)$, should be within $\pm\pi$. From the PR characteristic of $H(s)$, its phase fulfils $|\arg H(s)| \leq \pi/2$. If $G(s)$ would respond to a PR function, its phase would be within $|\arg G(s)| \leq \pi/2$ as well, and $|\arg G(s)H(s)| \leq \pi$.

The requirements for a function to be PR were detailed in Definition 2. The function $G(s)$ has no poles in the right-half side since its denominator is a second order expression

with positive coefficients, implying that $G(s)$ is Hurwitz [69] and the conditions 1 and 2 of Definition 2 are met. Let us check the third condition in Definition 2. The evaluation of the real part of $G(j\omega)$ is presented as follows:

$$G(j\omega) = \frac{j\omega}{-\omega^2 C + j\omega \frac{\psi_1}{\psi_2} + \frac{\psi_1 R_b}{\psi_2 L_x}} = \frac{\omega^2 \frac{\psi_1}{\psi_2} + j\omega \left(\frac{\psi_1 R_b}{\psi_2 L_x} - \omega^2 C \right)}{\left(\frac{\psi_1 R_b}{\psi_2 L_x} - \omega^2 C \right)^2 + \omega^2 \frac{\psi_1^2}{\psi_2^2}} \quad (8.27)$$

being the real part of the complex impedance,

$$Re G(j\omega) = \frac{\omega^2 \frac{\psi_1}{\psi_2}}{\left(\frac{\psi_1 R_b}{\psi_2 L_x} - \omega^2 C \right)^2 + \omega^2 \frac{\psi_1^2}{\psi_2^2}}, \quad (8.28)$$

always positive. Therefore, the condition 3 of the Definition 2 is also met and $G(s)$ is PR. As a consequence, the phase of $G(s)H(s)$, fulfils $|argG(j\omega)H(j\omega)| \leq \pi$.

The stability of the resulting system can also be found through the Nyquist stability criterion. Since $|argG(j\omega)H(j\omega)| \leq \pi$, the resulting path of $G(j\omega)H(j\omega)$ in the complex plane describing the contour $-j\omega$ to $j\omega$, with $0 \leq \omega \leq \infty$, cannot cross from the second to the third quadrant or vice versa, and it is therefore impossible that the point $-1 + j0$ be encircled [6].

In Figure 8.7 a table with different configurations of loads, $Z(s)$, connected to the VSI is shown. The objective is to demonstrate that the Nyquist diagrams of $G(s)H(s)$ with these loads do not encircle the point $-1 + j0$. Such results are depicted in Figure 8.8. With the aim of assigning values to the different load configurations in Figure 8.7, the loads have been designed to provide an approximate apparent power between 0.5 and 1.5 kVA at 50 Hz in all the cases. Figure 8.8 confirms that the Nyquist curves in the complex plane do not encircle the point $-1 + j0$. For the derivation of the plots shown in Figure 8.8, the designed values for ψ_1 , ψ_2 and β obtained in Section 8.2.4 have been used. Notice, however, that such values could be redesigned in order to achieve a optimized tracking performance for a specific impedance connected at the VSI.

Finally, the bode diagrams of the frequency responses of the transfer functions, $T(s)$, defined in (8.25) are shown in Figure 8.9. From such frequency responses, it can be corroborated that in all the cases the tracking errors are small in magnitude, being around of 2.5 % in the worst case for the load $Z_4(s)$.

8.2.6 Sliding dynamics for nonlinear load

There are different types of loads that exhibit a nonlinear consumption from the power source they are connected. In the power electronics field, some rectifiers (converters from AC to DC voltages) produce nonlinear currents, as the uncontrolled rectifier (diode rectifier), which is the nonlinear load studied in this Section. The diode rectifier, shown in Figure 8.10, is widely used in industry, appliances, etc. The rectifier provides a DC voltage

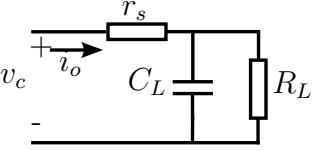
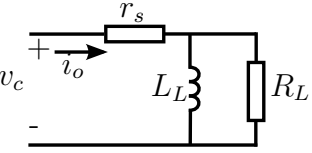
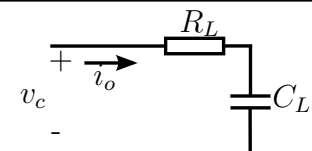
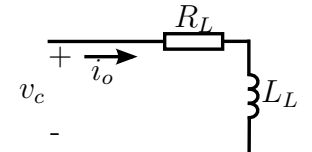
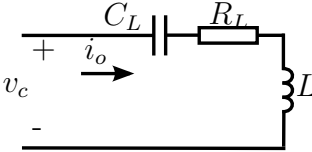
| | | |
|--|--|---|
| $Z_1(s) = \frac{R_L + r_s + sC_L R_L r_s}{1 + sC_L R_L}$ |  | $R_L = 8 \Omega$ $r_s = 30 \Omega$ $C_L = 0.1 \text{ mF}$ |
| $Z_2(s) = \frac{r_s R_L + sL_L (r_s + R_L)}{R_L + sL_L}$ |  | $R_L = 10 \Omega$ $r_s = 30 \Omega$ $L_L = 2 \text{ mH}$ |
| $Z_3(s) = \frac{1 + sC_L r_s}{sC_L}$ |  | $R_L = 60 \Omega$ $C_L = 0.1 \text{ mF}$ |
| $Z_4(s) = r_s + sL_L$ |  | $R_L = 50 \Omega$ $L_L = 50 \text{ mH}$ |
| $Z_5(s) = \frac{s^2 C_L L_L + s R_L L_L + 1}{s C_L}$ |  | $R_L = 40 \Omega$ $L_L = 2 \text{ mH}$ $C_L = 6 \text{ mF}$ |

Figure 8.7: Several configurations of output impedance, $Z(s)$, connected at the VSI output with their parametric values.

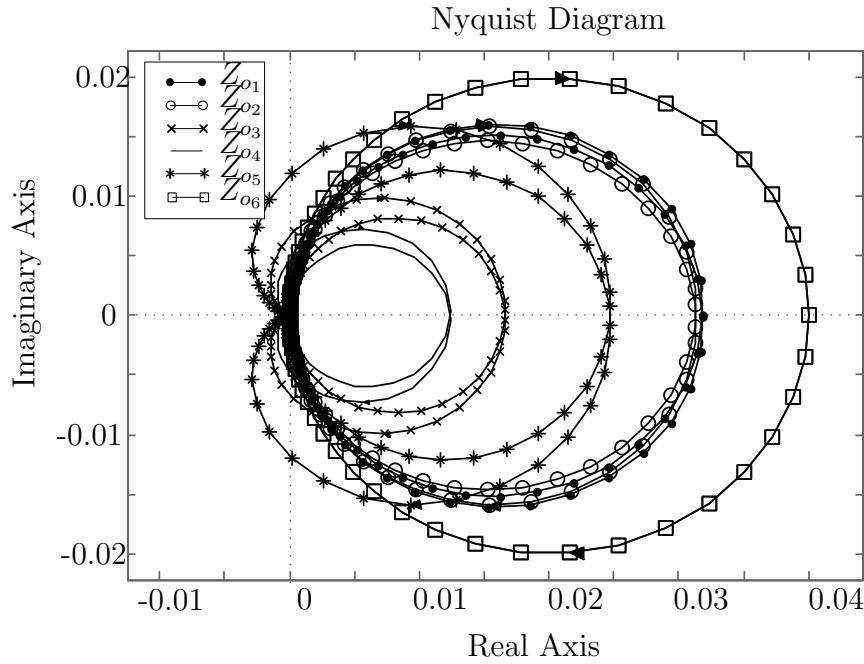


Figure 8.8: Nyquist diagram for the different conditions for the output impedance shown in Figure 8.7. The case of Z_{o6} is the pure resistive case with $R = 25 \Omega$.

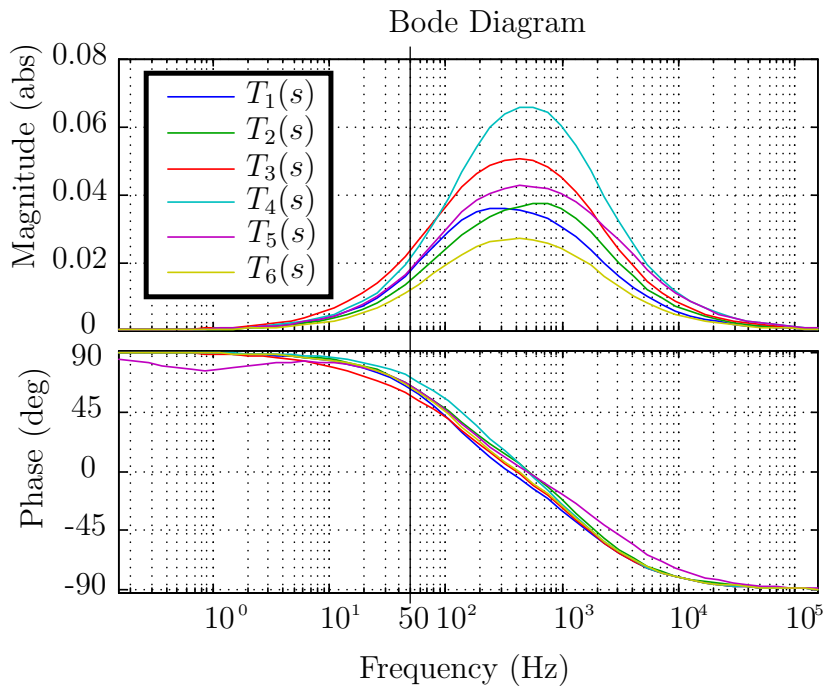


Figure 8.9: Bode responses of the tracking errors of the SMC with the output impedances, $Z(s)$, shown on the table of Figure 8.7. The case of $T_6(s)$ is the case for the pure resistive load of $R = 25 \Omega$.

from an AC input voltage, which in this case will be the output voltage of the VSI designed in this Chapter.

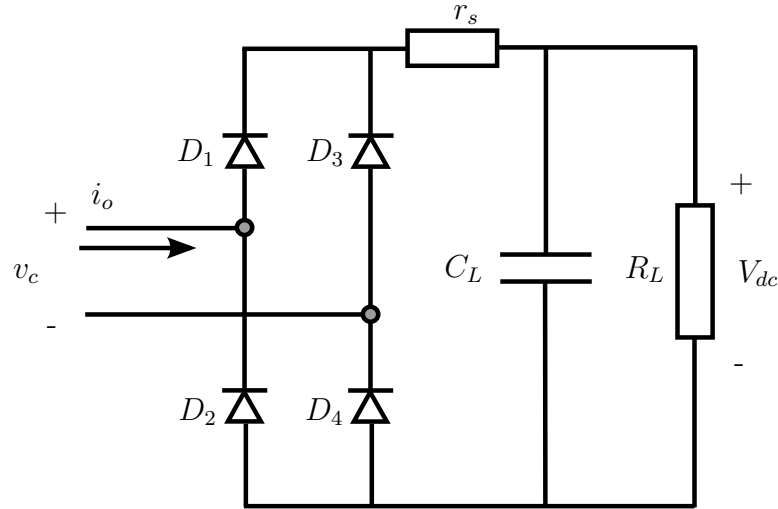


Figure 8.10: Diode rectifier topology.

The nonlinear characteristic of this structure comes from the behaviour of the diodes together with the output capacitor, C_L . The diodes act as switches, taking two discrete states, closed or open. According to this behaviour, the rectifier dynamics can be divided in two alternating topologies: one when the load is connected to the output of the VSI through the diodes (diodes ON) and other when the diodes remain in open circuit and the VSI is in no load condition (diodes OFF). The resulting topologies of the VSI with the rectifier connected at its output for the two states of the diodes are shown in Figure 8.11. When the diodes are closed (ON), the resulting load is linear and reactive, and the analysis developed in Section 8.2.5 can be applied. When the diodes remain open (OFF), the equivalent output resistor is $R = \infty$, which fits with the analysis of Section 8.2.4. Since the generated output voltage, v_c , is a sinusoidal waveform, the aforementioned topologies occur two times per cycle. Specifically, there exist 4 different time intervals, two of them corresponding to a no load condition ($i_o = 0$ A) and two corresponding to a reactive load (see top plot of Figure 8.2).

From the stability conditions stated in Sections 8.2.4 and 8.2.5, it is clear that the closed-loop systems of the resulting topologies are stable. Therefore, the nonlinear tracking error in steady-state will be bound by known values if the settling times of each topology, with respect to the duration of the expected time interval, are fast enough. In the case that only one of the settling times is fast enough to achieve the steady-state error, such tracking error at least will reach a known value two times per cycle, corresponding to a tracking error which can be also bounded. In the case when both topologies present slow settling times with respect to their time intervals, the stability of the system is not guaranteed.

Notice that the found stability conditions depend on several aspects as the expected topologies, their corresponding settling times and the time interval application of each

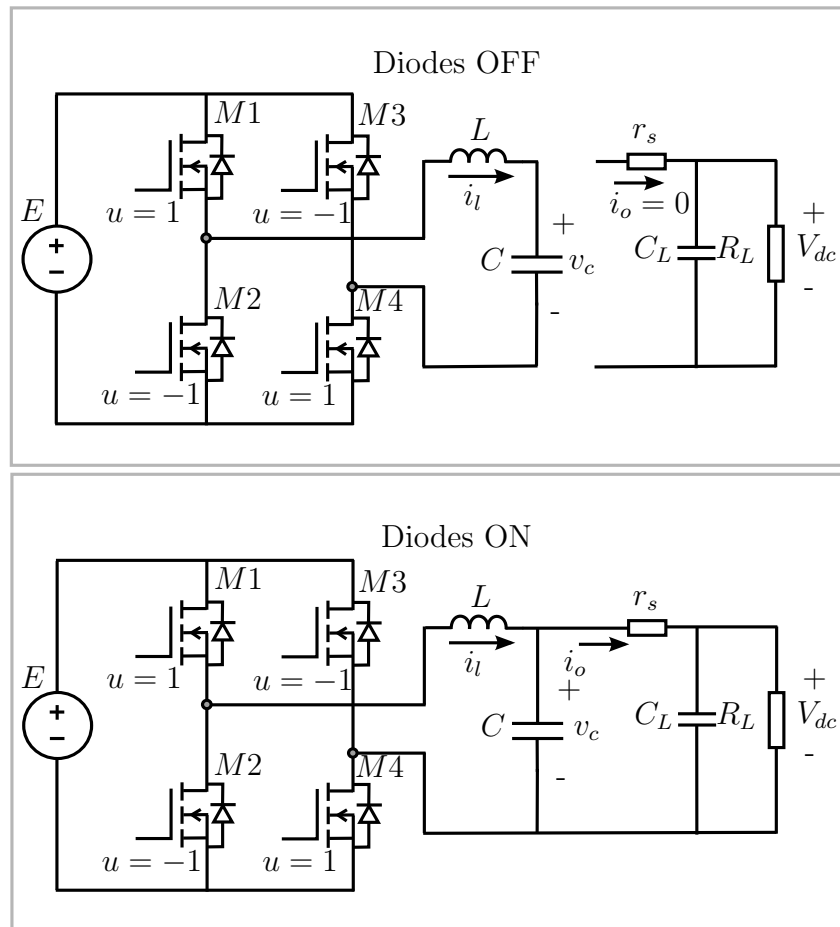


Figure 8.11: Resulting topologies with the VSI and a diode rectifier connected as output load.

topology. In that sense, the stability conditions should be checked for a certain system. Let us analyse the rectifier used in the laboratory. The values of the nonlinear load are (see Figure 8.10):

$$R_L = 132 \Omega, \quad r_s = 1 \Omega, \quad C_L = 6.6 \text{ mF}.$$

For the calculations, the diodes are assumed ideal. According to the equivalent systems in sliding motion obtained in (8.18), (8.25) the expected tracking errors, e_t , and settling times at 95 % of the final value, $t_{s95\%}$, for each state are found (it should be noticed that the parameters α and β have been already designed to $\alpha = 1$, $\beta = 680$):

$$\begin{aligned} \text{Diode OFF} &\rightarrow e_t = 2.7\% t_{s95\%} = 4.1 \text{ ms}, \\ \text{Diode ON} &\rightarrow e_t = 30\% t_{s95\%} = 30 \text{ ms}. \end{aligned}$$

The case for the diodes connected produces a very slow transient and a considerable tracking error, due to the load capacitor, C_L , is really big in value. As a consequence, taking into account that the period of the output voltage will be 20 ms, it is clear that this state will not reach the steady-state behaviour. The corresponding case to the diodes switched off provides a faster settling time, producing also a smaller amplitude error. This second settling time is of 4.1 ms, and assuming that the signal period is of 20 ms, it is reasonable to figure out that the resulting time interval for this topology would be larger than 4.1 ms, making possible to achieve the steady-state amplitude error of 2.7%. This result will be corroborated in the experimental part.

8.3 Switching frequency regulation

The next step is to design the SFC controller in order to provide steady-state fixed switching frequency to the VSI. Again, the parameters ρ^\pm should be derived for the steady-state sliding motion. Since in this case the control problem belongs to a tracking scheme, the SFC structure defined in Section 2.2.2 applies. Firstly, the expression yielding the evolution of ρ_k^\pm for the steady-state sliding motion, ρ_{k*}^\pm , are found from (8.10). In the previous Sections, it has been explained that the perfect tracking performance can be only achieved when a resistive load of a specific value, R_p , is connected at the output. Anyhow, it was also demonstrated that although the load varies, even including elements as capacitors and inductors at the output load, it is possible to adjust the control parameters such as the tracking error becomes negligible. As a consequence, in the following study, it is assumed that, under steady-state sliding motion, $v_c = v_c^*$ holds.

Recalling (8.10), the first time derivative of the switching function at steady-state sliding motion becomes:

$$\dot{\sigma}(v_c^*, x_M) = \omega\beta CA \cos(\omega t) - \omega^2\psi_2 CA \sin(\omega t) + \frac{\psi_2}{L} (A \sin(\omega t) - Eu). \quad (8.29)$$

From (8.29), it is immediate to derive the expressions for ρ_*^\pm just replacing the two

possible values of the control signal u , which are $u^+ = 1$ and $u^- = -1$. Notice that once the discontinuous control input is replaced by one of its possible states, the expressions for ρ_{*k}^\pm become continuous functions of time, $\rho(t)^\pm$. The sampling of these functions at any switching period interval, T^* , yields:

$$\rho_{*k}^+ = [\dot{\sigma}(v_c^*, x_M)_{u=-1}]^{-1} = \left[\omega\beta CA \cos(\omega k T^*) - \omega^2 \psi_2 CA \sin(\omega k T^*) + \frac{\psi_2}{L} (A \sin(\omega k T^*) + E) \right]^{-1}$$

$$\rho_{*k}^- = [\dot{\sigma}(v_c^*, x_M)_{u=1}]^{-1} = \left[\omega\beta CA \cos(\omega k T^*) - \omega^2 \psi_2 CA \sin(\omega k T^*) + \frac{\psi_2}{L} (A \sin(\omega k T^*) - E) \right]^{-1}.$$

Once the expressions for ρ_{*k}^\pm are found, the stability values for γ can be found applying

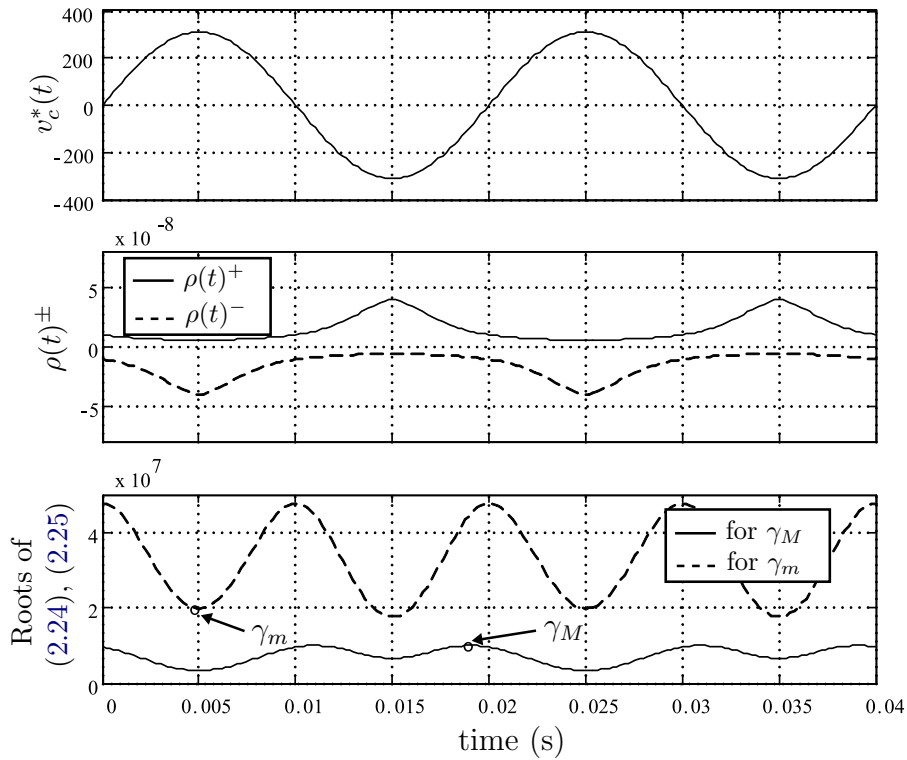


Figure 8.12: From top to bottom. 1- Desired output voltage, v_c^* . 2- Dynamic evolution of ρ_{*k}^+ and ρ_{*k}^- . 3- Roots of the conditions set in Theorem 2.

Theorem 2 (Section 2.2.2), which is sketched in Figure 8.12. Specifically, in the top plot, Figure 8.12 shows the desired output voltage, v_c^* , and the dynamic evolution of $\rho(t)^+$, $\rho(t)^-$ in the mid plot. Finally, the set of solutions of the condition stated at Theorem 2 for the resulting values of ρ_{*k}^+ , ρ_{*k}^- are presented in the bottom plot. With such signals, it is straightforward to find the maximum and minimum values guaranteeing stability of the SFC. The exact values that define the stability margin are numerically found in $\gamma_M = 1.76 \cdot 10^7$ and $\gamma_m = 9.98 \cdot 10^6$, i.e. $9.98 \cdot 10^6 < \gamma < 1.76 \cdot 10^7$.

However, through simulations and experimental testing, the stability of the system with values below the minimum value, γ_m , has been confirmed. It is worth remarking here that

Theorem 2 gives sufficient but not necessary stability conditions. Indeed, γ values below the range provide a much more reliable performance in practise. As a consequence, in the experimental evaluation, some different values of γ will be tested, including values within and outside of the range.

Remark 8. *In the early developed analysis, it has been assumed that under steady-state sliding motion the output voltage, v_c , perfectly tracks the reference signal v_c^* . As it was explained in the previous Section, just for a certain load condition such perfect tracking occurs. However, the switching surface parameters are designed to ensure that the output voltage tracking error can be neglected in all the load conditions, as Figures 8.5, 8.9 depict. As a consequence, the applied load does not influence in the switching functions slopes, and the aforementioned stability condition applies for whatever load applied to the VSI.*

8.4 Implementation details

In this Section, the methodologies used to implement the designed controllers are explained. It is important to remark here that the implementation is based on a micro-controller (μC). The digitalization of the switching function and of the hysteresis comparator will deserve a special attention. Hence, this Section will be organized in several parts divided as follows: in the first Subsection the effects of sampling the hysteresis comparator are presented; in the second Subsection, a strategy able to emulate the operation of the ideal hysteresis comparator using digital devices is introduced, followed by the third Subsection, where the discretization of the switching function is detailed. The fourth Subsection deals with the digital implementation of the SFC in the tracking case. Fifthly, a Subsection describing the available procedures in order to estimate the switching functions slopes (and their inverse values, ρ_k^\pm) is presented. Finally, the details of the assembled system in the laboratory are given.

8.4.1 Effects of the hysteresis comparator discretization

As it has been explained in Section 2.1, a sliding motion enforced in a fixed hysteresis band comparator provides a known switching frequency. From the implementation point of view, the hysteresis comparator can be accurately built using analog circuitry, as it was made in the experimental evaluations of Chapters 5, 6 and 7. However, the implementation in digital processors degrades its performance if the sampling effect is not taken into account.

Figure 8.13 shows the behaviour of a switching function, σ , working with an ideal hysteresis comparator, being T its related switching period. Analogously, the expected performance of the same switching function under the effect of discretization is sketched through σ_z , and its corresponding switching period, T_z .

Notice that the sampling process includes a least a delay equal to the sampling time, t_s , since the required actions to be performed cannot be executed up to the next sampling period. This contemplates that the computing time, t_c , which is the time spent by the μC

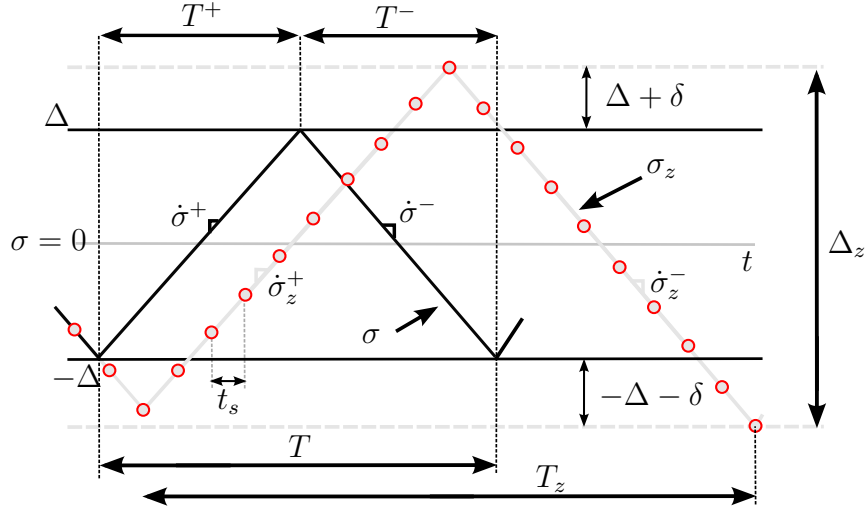


Figure 8.13: Hysteresis comparator discretization effect on the switching surface and related switching period.

to evaluate a certain algorithm according to the sampled signals, is lower than t_s . If this t_c is higher than t_s , a higher delay should be considered.

This effect produces that the switching function is no longer confined within the hysteresis band in sliding motion, inducing stationary errors in the state variables. In this scenario, as it is illustrated in Figure 8.13, a new and larger boundary layer appears, defined as $|\sigma_z| < \Delta + \delta$. According to Figure 8.13, in the best case the system will switch with a delay of one sampling period (just one sample within δ). In the worst scenario the delay will be of $2t_s$. Notice that the expected switching period will not be constant even at steady-state, due to such discretization effect. However, it is possible to qualitatively analyse these errors. The maximum and minimum values of δ are defined in (8.30).

$$\begin{aligned} \delta_{min}^+ &= t_s \dot{\sigma}^+; & \delta_{min}^- &= -t_s \dot{\sigma}^- \\ \delta_{max}^+ &= 2t_s \dot{\sigma}^+; & \delta_{max}^- &= -2t_s \dot{\sigma}^-, \end{aligned} \quad (8.30)$$

where $\dot{\sigma} = \dot{\sigma}_z$ has been assumed. Then, the maximum and the minimum Δ_z values will be:

$$\begin{aligned} \Delta_{z_{max}} &= 2\Delta + \delta_{max}^+ - \delta_{max}^- \\ \Delta_{z_{min}} &= 2\Delta + \delta_{min}^+ - \delta_{min}^-. \end{aligned} \quad (8.31)$$

Replacing (8.30) in (8.31) the maximum and minimum values are:

$$\begin{aligned} \Delta_{z_{max}} &= 2\Delta + 2t_s [\dot{\sigma}^+ + \dot{\sigma}^-] \\ \Delta_{z_{min}} &= 2\Delta + t_s [\dot{\sigma}^+ + \dot{\sigma}^-]. \end{aligned} \quad (8.32)$$

Using the previous expressions, the maximum and minimum switching periods in a fixed hysteresis band could be found applying equation (2.1), placing $\Delta_{z_{max}}$ and $\Delta_{z_{min}}$ instead of Δ , respectively. Even though it is possible to bound the switching periods, such bounds

depend on $\dot{\sigma}^+$, $\dot{\sigma}^-$, which are time-varying signals in a tracking control case, leading to a nondesirable situation.

Remark 9. From now on, the subindex n will identify the sampling related with the μC operation's, t_s , keeping k for the ones related to the switching periods events, T^* .

8.4.2 Digital emulation of the ideal hysteresis comparator

In order to recover the ideal switching period derived in Section 2 (see expressions (2.1), (2.9)) for an ideal hysteresis comparator, an emulation of this ideal behaviour is developed using a discrete-time algorithm. The control law is properly modified such that the response shown in Figure 2.1 is recovered in a discretized system. The procedure is able to deliver the proper control action $u(t)$, in such a way the switching function, σ , changes its slope sign just when it hits the hysteresis band Δ . The desired performance is illustrated in Figure 8.14.

Since the μC is able to perform actions only at the sampling time instants, t_{n+1}, t_{n+2}, \dots , in order to make the switching action at time instant $t = t_1 + t_{n+1}$, a pulse width modulated (PWM) control signal is applied. The definition of the desired values of $u(t)$ in the time interval t_n to t_{n+3} are (see Figure 8.14):

$$u(t) = \begin{cases} -1 & \text{for } t_n < t < t_{n+1} \\ -1 & \text{for } t_{n+1} < t < t_1 + t_{n+1} \\ 1 & \text{for } t_1 + t_{n+1} < t < t_{n+2} \\ 1 & \text{for } t_{n+2} < t < t_{n+3} \end{cases}. \quad (8.33)$$

The following duty cycles, computed according to the values presented in ((8.33)), have to be updated in the pulse width modulator at time instants (t_n, t_{n+1}, t_{n+2}) , as:

$$d = \begin{cases} d_n & = 0 & \text{at } t = t_n \\ d_{n+1} & = t_1/t_s & \text{at } t = t_{n+1} \\ d_{n+2} & = 1 & \text{at } t = t_{n+2} \end{cases} \quad (8.34)$$

The duty ratio d_{n+1} updated at $t = t_{n+1}$ makes possible the commutation at the desired time instant $t = t_{n+1} + t_1$. This value, according to Figure 8.14, is defined as:

$$d_{n+1} = \frac{\Delta - \sigma_{n+1}}{\sigma_{n+2} - \sigma_{n+1}}. \quad (8.35)$$

It is worth remarking that d_{n+1} depends on the future sample σ_{n+2} . At this point, a prediction of the value of σ_{n+2} is required. Furthermore, an additional delay should be taken into account, due to the computing time t_c . This means that the duty cycle which can be applied at $t = t_{n+1}$, has to be calculated with the available information at $t = t_n$. Referred to the equation (8.35), this implies a prediction of σ_{n+1} and σ_{n+2} at time instant $t = t_n$.

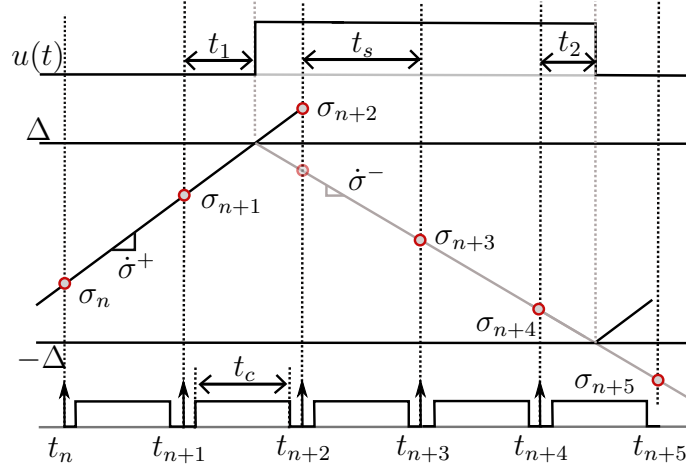


Figure 8.14: Sampling switching surface desired behaviour.

Summarizing, the digital implementation of the hysteresis comparator is achieved through the prediction of the next two switching function samples, $\hat{\sigma}_{n+1}$, $\hat{\sigma}_{n+2}$, and the proper calculation of the next PWM duty cycle. The control law defined in (8.15) is updated for the time instant $t = t_n$ as:

$$\begin{cases} \text{if } \hat{\sigma}_{n+2} > \Delta \text{ then} & d_{n+1} = \frac{\Delta - \hat{\sigma}_{n+1}}{\hat{\sigma}_{n+2} - \hat{\sigma}_{n+1}} \\ \text{if } \hat{\sigma}_{n+2} < \Delta \text{ then} & d_{n+1} = 0 \end{cases} \quad (8.36)$$

The question to answer now is how to perform the switching function predictions. The strategy proposed to predict the future samples exploits the piecewise linear characteristic of the switching function. Under this assumption, the required future samples can be easily estimated according to (8.37).

$$\begin{cases} \hat{\sigma}_{n+1} = \sigma_n + m_n t_s \\ \hat{\sigma}_{n+2} = \sigma_n + 2m_n t_s, \end{cases} \quad (8.37)$$

where m_n is the time derivative of σ at sample n . With the knowledge of the values for the switching function slopes, m_n , the emulation of the hysteresis comparator is achieved through (8.36) and (8.35).

The estimation of the switching function slopes is not only required for this emulation strategy but also by the SFC implementation discussed later. The available possibilities to estimate these parameters will be addressed in the coming Subsection 8.4.5.

Remark 10. The equations (8.34), (8.35) and (8.36) are developed to produce the commutation when $u(t)$ changes from -1 to 1 at the desired time instant $t = t_{n+1} + t_1$. Notice from Figure 8.14 that the duty cycle for the commutation case of $u(t)$ from 1 to -1 at time instant $t = t_{n+4} + t_2$ is given by $d_{n+4} = t_2/t_s$. Following the same procedure used to deduce equation (8.36), an analogue expression of the duty cycle can be obtained but the switching of $u(t)$ yields in a complementary form. This fact has to be taken into account in the PWM

configuration.

Remark 11. *The proposed method for the digital emulation of the hysteresis comparator in sampled systems can be applied as long as the piecewise linear characteristic of the switching function is met.*

8.4.3 Switching function digitalization issues

For the switching function calculation, expression (8.5) has to be digitally evaluated. The measured signals are v_c and x_M , since v_c^* and \dot{v}_c^* are generated by the μC , and the rest of the parameters are assumed constants. The acquisition of such signals is performed using an Analog to Digital converter (ADC). The ADC operates at the sampling time, t_s , it acquires v_c and x_M and the μC computes (8.5) one time per sampling period.

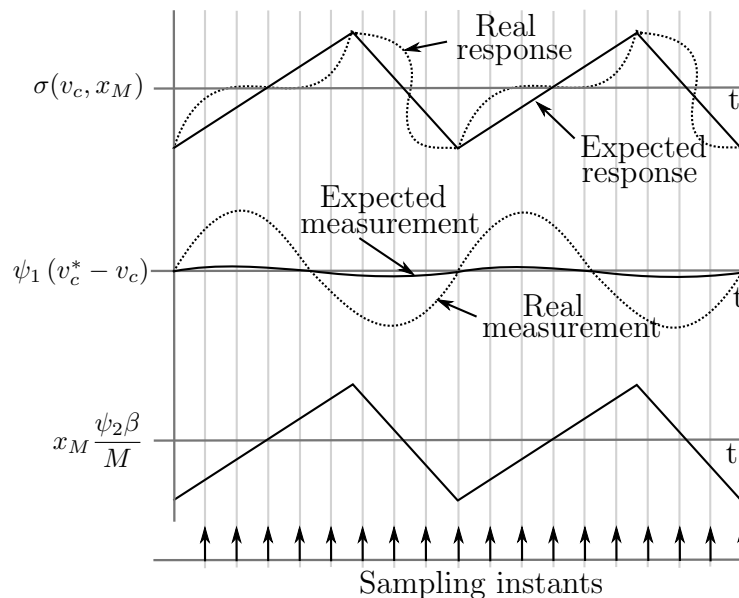


Figure 8.15: Noise effect in the measurement of v_c in the switching function.

As it was explained in Section 8.2.4, equation (8.21), high frequency harmonics on v_c can compromise the piecewise linear behaviour of σ . Furthermore, apart from the natural ripple produced by the switched characteristic of u in v_c , in the experimental prototype can appear other effects as switching noise or bus voltage oscillations which could increase the output voltage ripple, leading to an additional lack of the piecewise linear behaviour of σ . Figure 8.15 shows such phenomena. In the Figure, the two main terms of (8.5) are shown for two different scenarios, one according to the theoretical response, and the other considering an unexpected noise in the output voltage. If this noise is considerable, the piecewise linear behaviour could be lost, as it was stated in (8.21). It is obvious that with the switching function represented by dotted lines the expected performance is compromised.

The solution chosen hereafter to recover the piecewise linear behaviour of the switching function consists in performing an averaging of the v_c measured values during a switching period, and use such averaged value in the next switching interval. Therefore, the value of v_c is replaced by its mean value calculated in the previous subinterval as:

$$\langle v_c \rangle_{k-1} = \frac{\sum_{n=1}^N v_{c_n}}{N} \quad (8.38)$$

where v_{c_n} are the acquired values at each sampling period, n , and N is the number of acquired values during the $k - 1$ switching interval. As a consequence, the switching function samples computed in the time interval from T_{k-1} to T_k by the μC are:

$$\sigma(v_c, x_M)_n := \psi_1(v_{c_n}^* - \langle v_c \rangle_{k-1}) + \psi_2 C \dot{v}_{c_n}^* - \psi_2 \frac{L_x}{MR_b} x_{M_n} \quad (8.39)$$

with n going from 1 to N . Using this mean value, the piecewise linear of the switching function is preserved, even in presence of switching noise or unexpected disturbances.

Remark 12. *With regard to the proposed averaging strategy, some considerations must be taken into account. In the one hand, the mean value used during a switching interval corresponds to the average of the measured values of the previous switching interval. Such assumption becomes acceptable if the switching frequency is high enough with respect to the low frequency component of v_c . In the other hand, it is obvious that such methodology could affect the sliding mode transient response. However, in the experimentation results presented later (Subsection 8.5), it will be shown that the dynamics provided by the implemented system is very close to the theoretical one, thus confirming that the impact of such averaging procedure on v_c can be neglected.*

Theoretically, a sampling time, t_s , ensuring a couple of σ samples per control signal state should be enough to properly estimate $\langle v_c \rangle$ and to emulate the hysteresis comparator. It is clear however, that this only happens in the ideal case without unexpected disturbances. Conversely, since the normal situation in real system is to have disturbances, decreasing the sampling period t_s with respect to T , leads to a more accurate averaged value calculation, improving the overall system performance.

8.4.4 Digital emulation of the SFC for a tracking control task

At this stage, the digital implementation of the SFC is addressed. From Section 2.2.2, it is clear that for a SMC working in a tracking case, for a fixed switching period operation, Δ_k has to be updated according to (2.18). The tracking SFC structure is not only more complex than the regulation case one but also the generation of Δ_k depends on the ρ_k^\pm values, in order to implement the feedforward action, Ω_k , as (2.20) states. The value of Ω_k requires the knowledge of the current switching function time derivatives at period k . It is obvious that the value Δ_k should be calculated at the beginning of the period, when the available information is that of the $k - 1$ switching period, and as consequence, Ω_k has to

be calculated with this information. Such effect was already noted in Remark 3 (Section 2.2.2). Therefore, the implemented value of Ω_k is approximated by Ω_{k-1} , as:

$$\Omega_k \simeq \Omega_{k-1}.$$

With regards to the estimation of ρ_k^\pm , or equivalently, the estimation of the switching function slopes, there are several possibilities to do that, as it was noted in the previous Subsection. In the next Subsection, the alternatives for estimating those parameters are discussed, explaining which estimation strategy are used for this case.

Finally, the SFC implementation is carried out using (2.18), being γ designed according to Subsection 8.3, and the expression of Ω_k approximated by Ω_{k-1} , using the proper strategy for ρ_k^\pm estimation (explained in the following).

8.4.5 Estimation of switching function slopes

As it was already noted in the previous Subsections, the estimation of ρ^\pm (or their inverses, $\dot{\sigma}^\pm$) can be carried out through several strategies. The most intuitive approximation can be derived from Figure 8.14, as:

$$\dot{\sigma}_n^\pm = (\rho_n^\pm)^{-1} \simeq \frac{\sigma_n - \sigma_{n-1}}{t_s}. \quad (8.40)$$

This strategy is the simplest one, and does not require any additional hardware, which is its main advantage. However, this approximation fails considerably if an error measurement occurs in the acquisition of σ_n, σ_{n-1} .

The values of $\dot{\sigma}^\pm$ could also be achieved using the sliding mode control theory. If under sliding motion, the equivalent control, u_{eq} , is measured through low pass filtering the real control action, u , [7], using (8.10) one gets

$$\dot{\sigma}(v_c, x_M) = \frac{\psi_2 E}{L} (u_{eq} - u) \quad (8.41)$$

and, therefore

$$\dot{\sigma}_n^\pm = (\rho_n^\pm)^{-1} \simeq \frac{\psi_2 E}{L} (u_{eqn} - u(t)_n). \quad (8.42)$$

The estimations based on (8.42) have as main drawback that they require the knowledge of E , and need a dedicated hardware for measuring the equivalent control.

From the hypothesis of the piecewise linear behaviour of σ , and assuming known the values Δ_k, Δ_{k-1} (indeed, they are generated by the SFC) the switching function time derivatives can be estimated as (see Figure 2.2, Section 2.2):

$$\rho_{k-1}^+ = \frac{T_{k-1}^+}{\Delta_{k-1} + \Delta_{k-2}}, \quad \rho_{k-1}^- = \frac{T_{k-1}^-}{2\Delta_{k-1}}, \quad (8.43)$$

where T_{k-1}^+ and T_{k-1}^- periods are measured, cycle by cycle, by the μC Timer in charging of

measure T_k .

Finally, as it was performed for the average value of v_c in equation (8.38), the switching function slopes can be averaged along a switching period interval as:

$$\dot{\sigma}(v_c, x_M)_k^+ = \frac{\sum_{n=1}^{N_T^+} \dot{\sigma}_n^+}{N_T^+} \quad (8.44)$$

where N_T^+ is the number of samples inside T_k^+ and

$$\dot{\sigma}(v_c, x_M)_k^- = \frac{\sum_{n=N_T^+}^N \dot{\sigma}_n^-}{N - N_T^+} \quad (8.45)$$

with N denoting the samples within the switching period T_k .

The expressions in (8.40), (8.42), (8.43) and (8.44), (8.45) are, from a theoretical point of view, the same one. However, using one or another entails different implications from a practical point of view. The following Remarks state such implications.

Remark 13. *From a theoretical point of view, whatever approximation can be employed in order to estimate the slopes of the switching function (or their inverses) and used in the prediction algorithm and in the SFC. However, from a practical point of view, is not equivalent to use one or another. Mainly, the differences among them for ρ_k^\pm (or their inverses) estimation are related to the noise immunity of these expressions, and also to the required signals to be measured.*

The first one based on (8.40) does not require anything more apart from the digitalization of the switching function, which is already done for the SMC, but is the most sensitive to noise. On the other hand, the estimation based in (8.42) has a better rejection to noise, but requires the additional measurements for the equivalent control. Finally, (8.43) or (8.44)-(8.45) lead to a low sensitive noise estimations of ρ_k^\pm , without the necessity to include additional hardware.

Remark 14. *It is obvious that the estimation based on (8.43) or (8.44)-(8.45) delivers the result a switching period delayed. As a consequence, such approximation is useful when the switching period is low enough with respect to the period of v_c^* . Notice that this hypothesis has been a key consideration throughout the entire work.*

Since in this case the desired switching period ($T^* = 50 \mu\text{s}$) is low with respect to the period of the desired output voltage, v_c^* (20 ms), the selected approximation for ρ^\pm are (8.43) for the SFC and (8.44)-(8.45) for the emulation of the hysteresis comparator in the SMC. Although both controllers are implemented in the same μC , their sampling ratios are different. The SFC sampling coincides with the switching period of the control action, T_k and strictly speaking, it is not totally fixed. The SMC one, t_s , is the sampling of the μC itself, and it is fixed. This fact hinders to share the single estimated information of ρ^\pm by both algorithms. This is the reason why the ρ^\pm estimations are performed twice, one by the SFC and another by the SMC.

8.4.6 Controller implementation

The SMC and the SFC are implemented using the μC F28377S from Texas Instrument. The details of this devices can be checked in the datasheet provided by the manufacturer ([70]). This device includes all the peripheral needed by a power electronics implementation (ADC, PWM, etc.), a CPU with a floating point unit and a dedicated trigonometric unit (TMU). Moreover, the F28377S provides a second processor able to perform floating point operations as well, called control law accelerator (CLA). This core is intended to deal with time-critical control task, having direct access to the main peripherals. Both cores, together with the TMU, can work up to 200 MHz and in parallel, leading to a very good computing capability.

The embedded ADC can work with resolutions up to 16 bits, although in our case the 12 bit resolution is enough. The ADC can be clocked up to 50 MHz, which is fast enough for this application. In the same way, the PWM embedded in the F28377S has a lot of programming options, making possible the strategy proposed in Subsection 8.4.2. Finally, one of the general purpose 32 bit timers of the μC is programmed for measuring the switching period of the control signal.

The controller routines are programmed in *c* language. Since the F28377S allows some level of task paralleling, such feature is exploited in order to obtain an execution as fast as possible. The Figure 8.16 sketches the structure that implements the SMC and the SFC. Both the CPU and the CLA execute code. A detailed explanation of what code is executed for each one is presented hereunder.

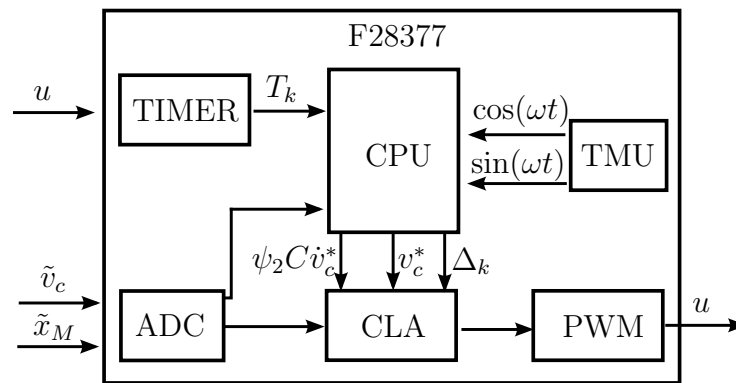


Figure 8.16: Diagram of the peripheral used for the implementation of the SMC and the SFC in the processor F28377S.

- Main CPU.

The main CPU is in charging of initializing all the system in the start-up, including the configuration of the peripherals and the CLA. The initialization procedure configures the Timer for generating a CPU interrupt at any rising event of the control signal, where the SFC is implemented. Also the synchronization of the ADC is configured, which will be triggered with a sampling of 1 MHz ($t_s = 1 \mu\text{s}$). Once the

ADC ends the conversions, a CPU interrupt is generated. The CPU also configures the CLA to execute code once the ADC has ended the conversion.

Besides the initialization, the main CPU executes the SFC, using the expressions found in (2.18), (2.19) and (2.20). For the calculation of Ω_k , expressions in (8.43) are employed for ρ_k^\pm estimation. The resulting Δ_k is stored in an accessible memory region by the CLA. The sampling of this routine is the one generated by the control action, u . Another task performed by the main CPU is the generation of the voltage reference for the SMC, v_c^* , through (8.3). The term $\psi_2 C \dot{v}_c^*$ is also computed by the CPU. For both expressions, the TMU provides a very fast computation of the *cos* and *sin* functions. Such code is placed in the CPU interrupt executed at the sampling of 1 MHz.

Finally, since the CPU has also access to the ADC outputs, a security code is implemented monitoring the IGBT temperature, the bus voltage, the overcurrents and overvoltages, in order to protect the system in front of fault conditions. Moreover, in the experimental evaluation the CPU is programmed to take out some internal signals (as σ) through two DACs, in order to be shown by an oscilloscope.

- CLA.

The CLA executes the SMC, including the emulation of the hysteresis comparator detailed in Subsection 8.4.2. Firstly, the switching function is computed using (8.39), where the average value of v_c has been calculated in the preceding switching interval, according to (8.38). The resulting value of σ is used to perform the predictions detailed in (8.37), but using the averaged slopes found in (8.44) and (8.45), according to the state of the control input, u . Therefore the implemented predictions in the switching interval from T_{k-1} to T_k are:

$$\begin{cases} \hat{\sigma}_{n+1} = \sigma_n + \dot{\sigma}(v_c, x_M)_{k-1}^+ t_s \\ \hat{\sigma}_{n+2} = \sigma_n + 2\dot{\sigma}(v_c, x_M)_{k-1}^+ t_s \end{cases} \quad (8.46)$$

when $u = 1$ and

$$\begin{cases} \hat{\sigma}_{n+1} = \sigma_n + \dot{\sigma}(v_c, x_M)_{k-1}^- t_s \\ \hat{\sigma}_{n+2} = \sigma_n + 2\dot{\sigma}(v_c, x_M)_{k-1}^- t_s \end{cases} \quad (8.47)$$

for $u = -1$.

Once $\hat{\sigma}_{n+2}$ and $\hat{\sigma}_{n+1}$ are found, the PWMs are properly updated using the control law defined in (8.36).

8.4.7 Assembled converter and devices employed

The power plant assembled for experimental evaluation is depicted in Figure 8.17. The converter incorporates two capacitors at its input forming a virtual neutral point which is connected to the ground. This structure reduces considerably the common mode noise of the system, improving the quality of the measured signals. These capacitors ($2 \times 10 \mu\text{F}$)

also help to attenuate the high frequency voltage oscillations at the converter input. For the same reason, the output inductor is split in two equal inductors, leading to a further reduction of the common mode voltage. The inductors are built using gapped ferrite cores, where the windings have been wound with copper litz wire. The used power switches are the IGBT 50MT060WTHA from Vishay. This device has a breakdown voltage of 600 V, being able to manage continuous currents up to 50 A. In order to avoid short circuit of the input source, a dead time of $2 \mu\text{s}$ is included in the control signals by the μC . The output capacitance is formed by two capacitors (C4AEGBW5500A3LJ) disposed in parallel, in order to reduce the equivalent series resistance.

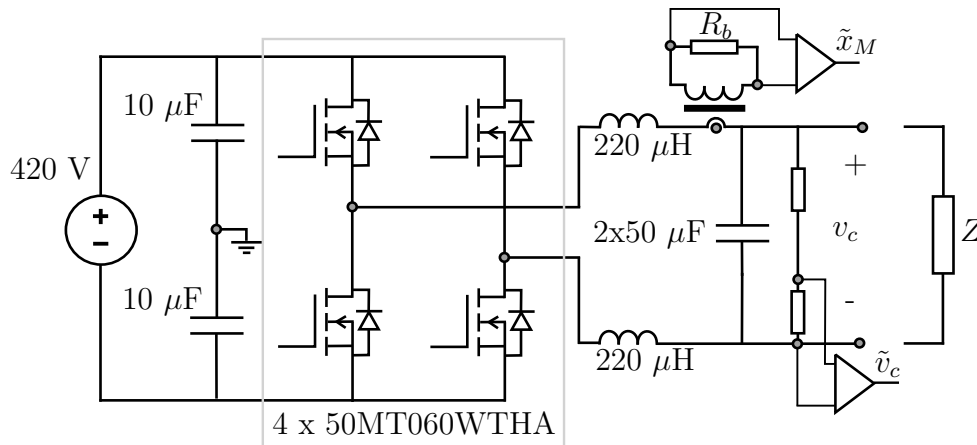


Figure 8.17: Power plant built for experimental evaluation.

Regarding the sensing part, the Figure also sketches the current transformer and the voltage divider employed for v_c and x_M measurements, respectively. The current transformer, CT, is manually wound using a toroidal ferrite core of 3C90 material from Ferroxcube. The number of turns is 300, and the required values of M and L_x are adjusted adding an air gap in the core. The CT provides an isolated measurement, so no additional isolation amplifier is required. A standard structure based in AO is implemented in order to adapt the measurement to the ADC input, which is identified as \tilde{x}_M . Such adapting process is due to the ADC which holds values from 0 to 3 V in its input. The output voltage is measured using a voltage divider. In this case, an isolation amplifier is required, using for such purpose the chip AMC1301. Again, the signal \tilde{v}_c is adapted in order to be acquired properly by the ADC. The standard AO structures adapting \tilde{v}_c and \tilde{x}_M have been omitted for the sake of brevity.

To conclude, the designed control parameters are summarized in Table 8.2.

Table 8.2: Controller parameters.

| Parameter | Value |
|-----------|--|
| ψ_1 | 100 |
| ψ_2 | 100 |
| M | 33 μ H |
| L_x | 10 mH |
| R_b | 6.8 Ω |
| γ | $1 \cdot 10^4 < \gamma < 1 \cdot 10^7$ |

8.5 Experimentation results

The experimental results obtained with the aforementioned prototype are presented at this stage. First of all, Table 8.3 summarizes the obtained steady-state tracking errors under different load conditions. The Table also contains the Total Harmonic Distortion (THD) of the output voltage related to the fundamental frequency of 50 Hz for each load level. With regard to the VSI efficiency, a value around 95 % has been measured at nominal load condition (2.2 kW).

The main features to be experimentally evaluated are the related to the SMC and SFC dynamics. The experimental results aimed to show the performance of each controller have been divided in three main blocks, namely: SFC performance, SMC performance and nonlinear load test.

8.5.1 SFC performance

Firstly, the result of Figure 8.18 shows the converter performance when the SFC is disable, and the SMC operates with a fixed hysteresis band. Under this scenario, the switching period becomes variable as the FFT calculated by the oscilloscope evidences (bottom part of Figure 8.18). The switching frequency harmonics are distributed along the range 12 kHz - 29 kHz, almost with the same amplitude.

The Figure 8.19 shows the same test but in this case with the SFC enabled. It is clear how the SFC generates a time-varying hysteresis value (see magenta signal in the Figure). The resulting FFT for this case is now similar to the expected one assuming a constant switching frequency of the control action. Thus, the proper performance of the SFC under a tracking case is confirmed. It should be noticed that in this case the value of $\gamma = 2.5 \cdot 10^6$ is not within the range found in Section 8.3 ($9.98 \cdot 10^6 < \gamma < 1.76 \cdot 10^7$). However, the stability of the SFC is confirmed from the experimental result. Moreover, the results in Figures 8.18, 8.19 also validate the previous implementing methodologies (switching function predictions and PWM modulations detailed in Section 8.4) developed

Table 8.3: Experimental results of the VSI

| Linear Load | | | | |
|----------------------|--------------------|------------------------|---------------|----------------------|
| Output Power (kW) | THD Voltage (%) | Voltage error (Vpp) | Vout (Vpp) | Voltage error (%) |
| 0 | 0.2 | 3.7 | 626 | 0.59 |
| 0.5 | 0.3 | 4.6 | 626 | 0.73 |
| 1 | 0.3 | 5.6 | 626 | 0.89 |
| 1.8 | 0.3 | 6.1 | 626 | 0.97 |
| 2.2 | 0.3 | 6.6 | 626 | 1.04 |

| Nonlinear Load | | | | |
|----------------------|----------------------------|---------------------|-------------------|----------------------|
| Output Power (kW) | THD Voltage/Current (%) | Peak Current (A) | Crest Factor - | Voltage error (%) |
| 0.63 | 1.1/81.2 | 17.6 | 3.4 | 3.3 |

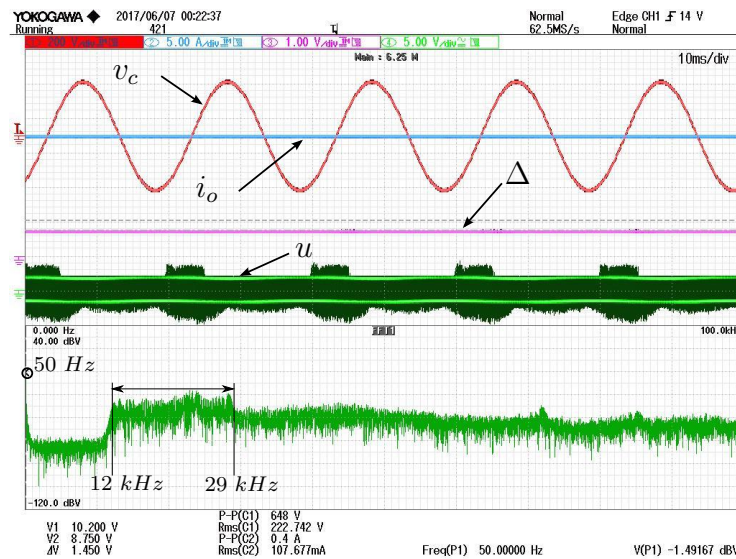


Figure 8.18: VSI response with the system tracking the desired output voltage in no load condition. SFC is disabled and Δ has a constant value. FFT details on the bottom.

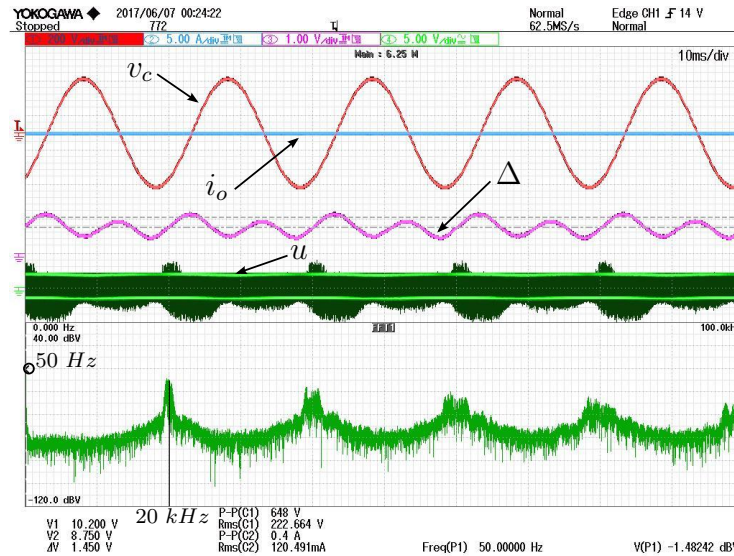


Figure 8.19: VSI response with the system tracking the desired output voltage in no load condition. SFC is enabled and $\gamma = 2.5 \cdot 10^6$. FFT details on the bottom.

in order to recover the ideal response of the hysteresis comparator in a sampled system.

The test shown in Figure 8.20 shows the same case of Figure 8.19, but with a linear load of 2.2 kW connected at the VSI output. From direct comparison of the FFT's responses depicted at Figures 8.19 and 8.20, it is obvious that the system has essentially the same response despite of the applied load level.

Figure 8.21 shows the difference between operate with and without SFC. In this case, the value of $\gamma = 1 \cdot 10^7$ is within the range provided by the Theorem 2 (Section 2.2.2), which was found in Section 8.3 to be $9.98 \cdot 10^6 < \gamma < 1.76 \cdot 10^7$. The FFT of Figure 8.20 is replaced by the measured switching period, T , in Figure 8.21 for a better understanding (T is generated by a DAC of the μC , corresponding 1.5 V to 50 μs). From this test two facts can be observed: on the one hand, the different performances of the system with and without the SFC, and, in the other hand, the fast transient of the switching period to the desired value once the SFC is enabled.

Finally, the results of Figures 8.22 and 8.23 present variations of the desired switching period. From these results, the proper SFC regulation is confirmed in both cases. Notice how the employment of a smaller value of γ than in the previous case ($\gamma = 2.5 \cdot 10^6$) produces a smoother transient in the switching period.

8.5.2 SMC performance

Different tests in order to evaluate the performance of the SMC while the SFC is enabled are presented below. The first one presented in Figure 8.24 shows the tracking capability of the designed SMC. Specifically, the Figure 8.24 shows the output voltage, v_c , the tracking error, $v_c - v_c^*$, and the output current, i_o . The tracking error is calculated by the μC and

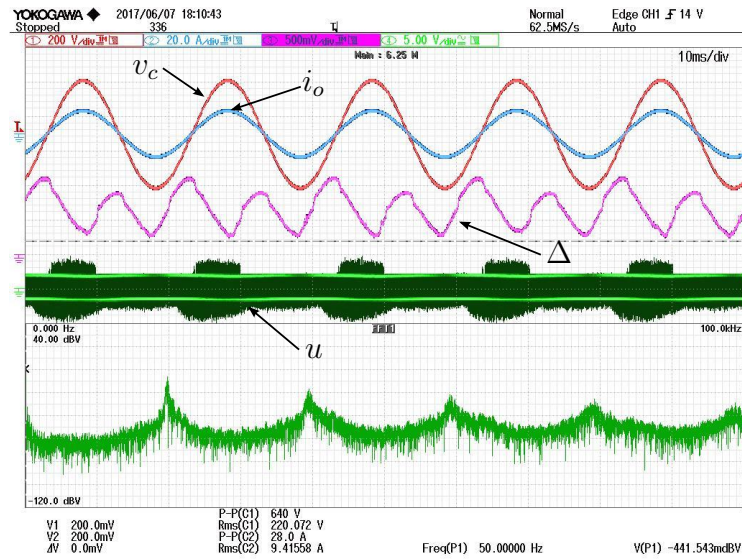


Figure 8.20: VSI response with the system tracking the desired output voltage with 2.2 kW at the output. SFC is enabled and $\gamma = 2.5 \cdot 10^6$. FFT details on the bottom.

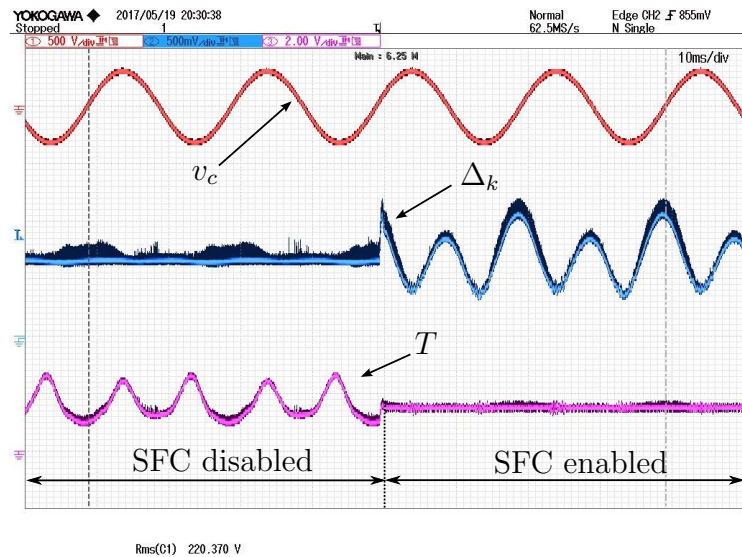


Figure 8.21: VSI response with the system tracking the desired output voltage in no load condition. SFC on-off and $\gamma = 1 \cdot 10^7$.

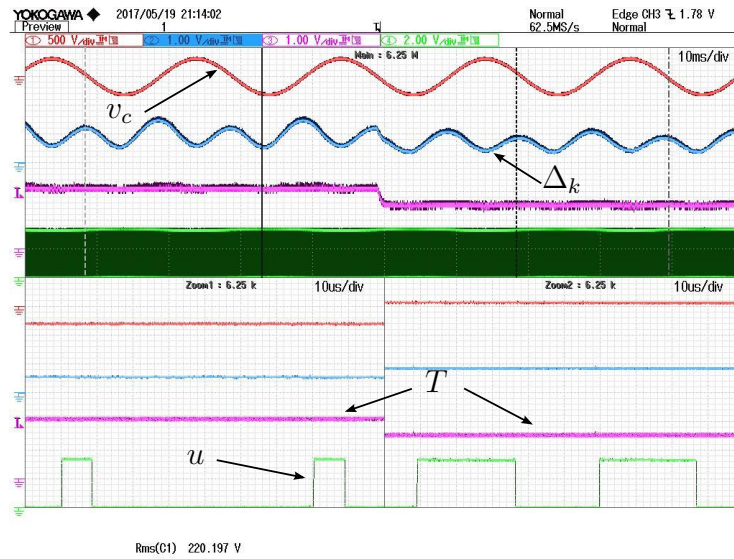


Figure 8.22: Switching frequency regulation from $T^* = 70 \mu s$ to $T^* = 50 \mu s$ in no load condition. SFC is enabled and $\gamma = 2.5 \cdot 10^6$.

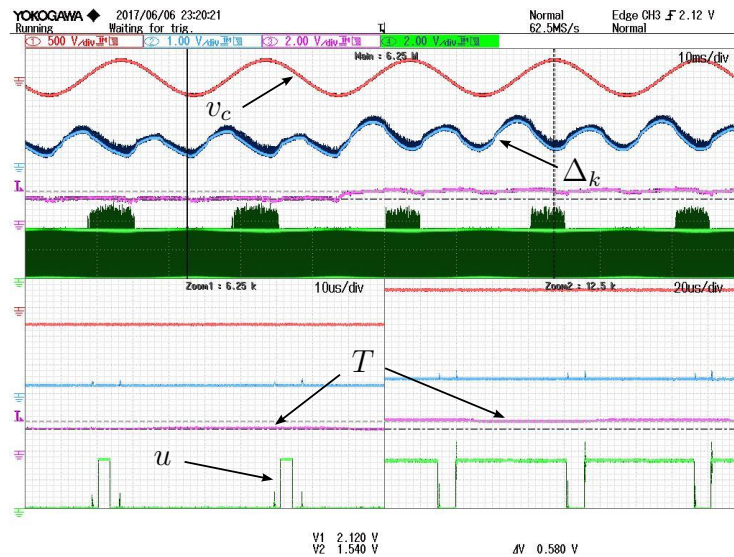


Figure 8.23: Switching frequency regulation from $T^* = 50 \mu s$ to $T^* = 70 \mu s$ with 2.2 kW load at the output. SFC is enabled and $\gamma = 2.5 \cdot 10^6$.

visualized through a DAC output port. The resulting scale is 247.18 V/V in order to pass from the signal generated by the μC to the real tracking error. As a consequence, the tracking error for a no load condition is of 3.7 V peak to peak, representing an error of 0.6 % of the nominal value. The result of Figure 8.25 shows the same curves but for a load condition of 2.2 kW. For that scenario, the voltage error is of 1 %, approximately. The Table 8.3 details the measured tracking errors for different output power levels.

The results shown in that Table differ from the expected condition according to the theoretical study developed in Section 8.2.4. According to that Section, the amplitude of the error should decrease as the load level increases. However, in the experimental prototype this tendency is not observed. The reader should realize that the system losses of the reactive components and IGBT switching losses, among others, were not considered in the theoretical analysis. It should be remarked that these losses increase as the output power does, thus confirming that with higher load levels the tracking error tends to increase.

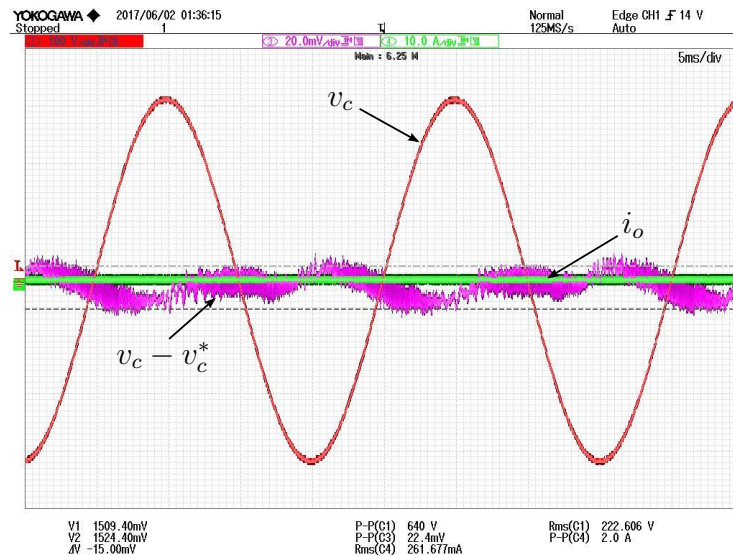


Figure 8.24: SMC steady-state tracking performance with no load. Detailed voltage error $v_c - v_c^*$. SFC with $\gamma = 2.5 \cdot 10^6$.

In the result of Figure 8.26, a sudden load change from no load to 2.2 kW is performed at the VSI output. The maximum error, just after the transient, reaches the 15 V, representing a 5 % of the output voltage peak amplitude. Moreover, it should be noted from the dynamics of the tracking error that the settling time is around 4 ms, which is the expected value according to the ideal sliding mode derived in Section 8.2.4. This result confirms the theoretical prediction, validating all the assumptions made in the design and the implementation stages.

Finally, the Figure 8.27 shows how the SMC rejects during all the tests an input voltage oscillation of two times the desired output frequency (100 Hz). This oscillation is produced by the non ideal characteristic of the input power supply. This result gives further evidence of the system robustness.

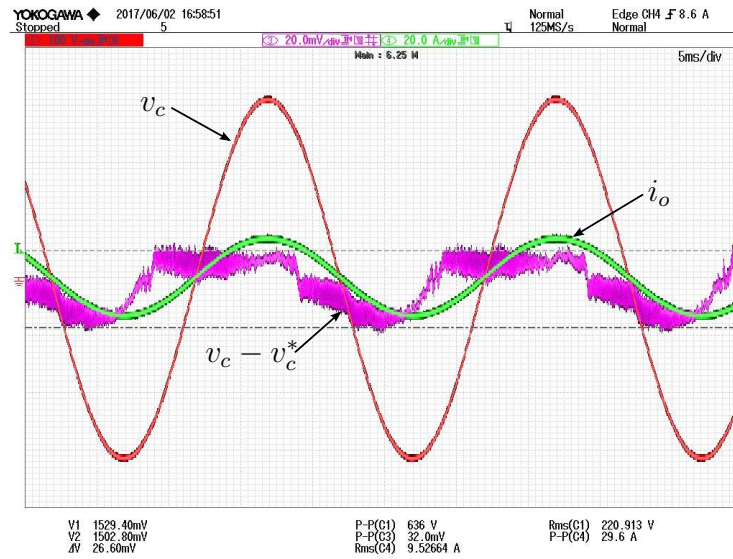


Figure 8.25: SMC steady-state tracking performance with 2.2 kW load. Detailed voltage error, $v_c - v_c^*$. SFC with $\gamma = 2.5 \cdot 10^6$.

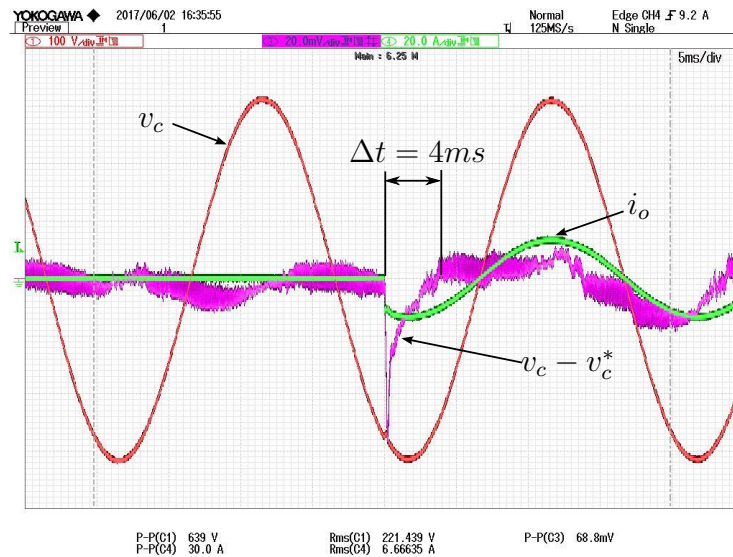


Figure 8.26: Load Transient from no load to 2.2 kW load. Detailed voltage error, $v_c - v_c^*$. SFC with $\gamma = 2.5 \cdot 10^6$.

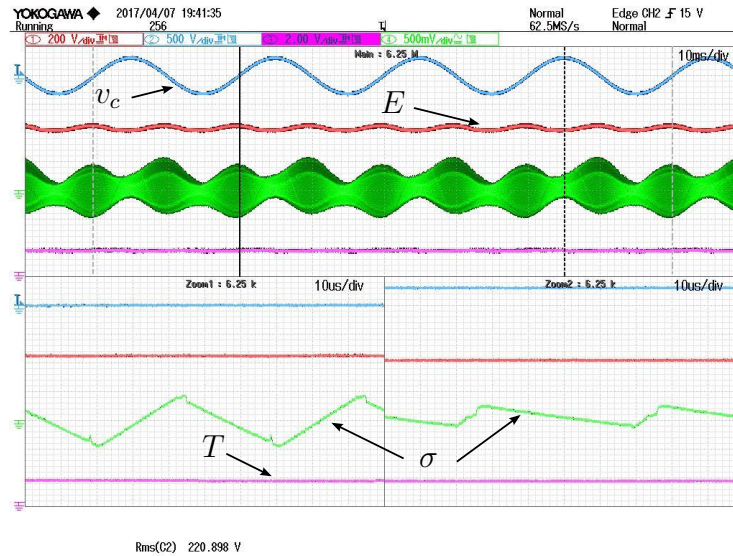


Figure 8.27: Input voltage oscillation rejection by the SMC. No load condition. SFC with $\gamma = 2.5 \cdot 10^6$.

8.5.3 Nonlinear load test

The influence of a nonlinear load at the output of the VSI is tested at this stage. It should be remarked that one of the main applications of the VSI designed in this Chapter will be the emulation of a power grid from an island photovoltaic system or similar. Due to the different nature of the loads typically connected to the power grid, it is interesting to see how the SMC and the SFC behave when this type of loads are connected to the VSI. As it was presented in Section 8.2.6, the evaluated load is a diode rectifier, with the parametric data provided in Section 8.2.6. Firstly, the general performance of the SMC and SFC with a nonlinear load producing current peaks around 18 A is shown in Figure 8.28. Notice that the resulting crest factor is around 3.4, which is considerably high. It can be observed from the Figure that, although the responses (output voltage and switching period) slightly differ from the reference ones, the system keeps an overall good performance.

From Figure 8.29 the presented result in Section 8.2.6 can be now corroborated. The time interval corresponding to the topology where the diodes are OFF (load disconnected from the VSI) is around 8 ms, which is higher than the expected settling time for this topology of 4 ms. As expected, the time interval where the diodes are ON is too short to reach the corresponding steady-state error. However, since one of the alternating topologies achieves its steady-state value, the tracking error results bounded. From the Figure, it can be inferred that the maximum tracking error is of 22 V peak to peak, representing a 3.3 % of the desired peak to peak voltage.

Finally, the FFT of the nonlinear case is depicted in Figure 8.30. From the Figure, the performance shown in Figure 8.20 is qualitatively preserved, although the nonlinear consumption of the diode rectifier slightly degrades the performance with respect to the linear case.

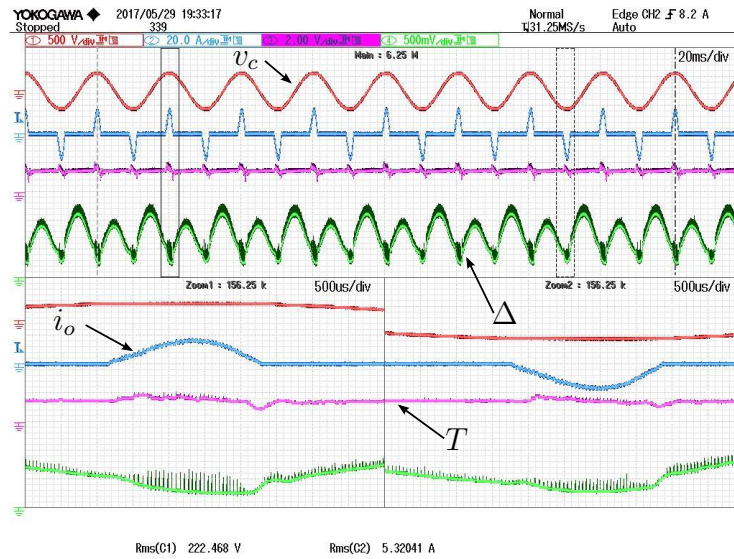


Figure 8.28: System performance with nonlinear load. SFC with $\gamma = 1 \cdot 10^4$.

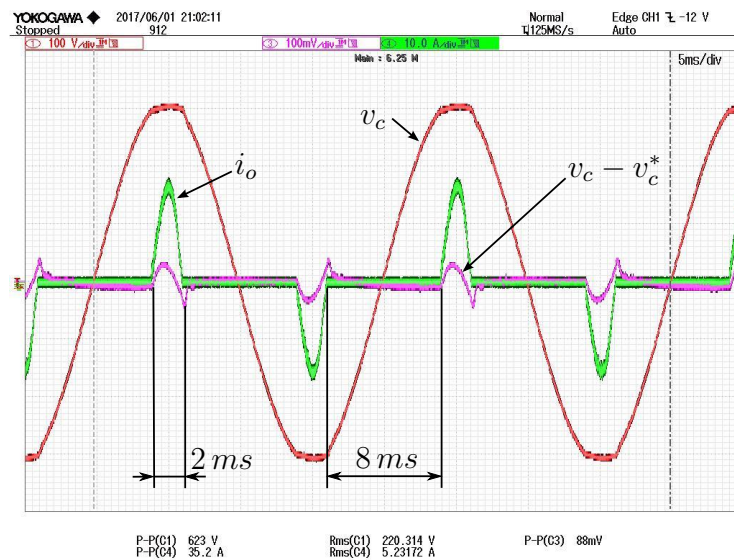


Figure 8.29: System performance with nonlinear load. Tracking error detail. SFC with $\gamma = 1 \cdot 10^4$.

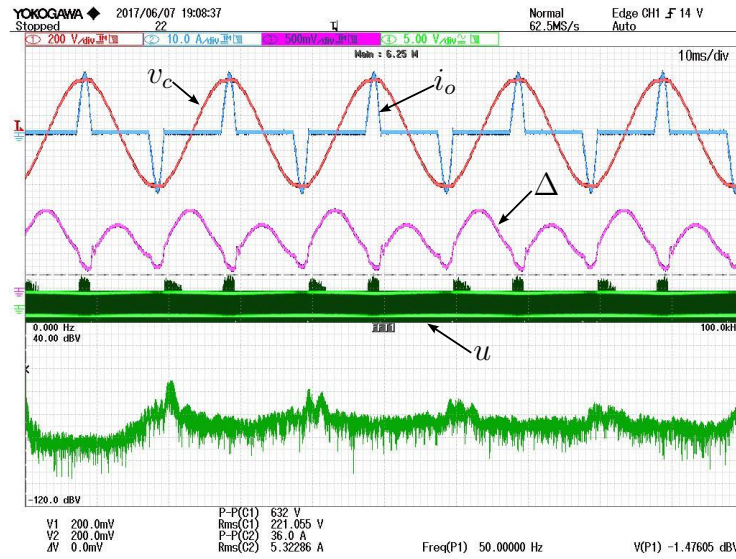


Figure 8.30: System performance with nonlinear load. FFT of the control action at the bottom part. SFC with $\gamma = 1 \cdot 10^4$.

8.6 Conclusions

All the experimental results shown confirm an overall good performance of the VSI generating an AC signal at its output, when the SMC operates with the proposed SFC in a tracking control problem. Through the experimental evaluation, the expected VSI features as robustness, insensitive to type of load and fixed switching period operation have been confirmed. In the Chapter, not only the SFC design has been shown. A detailed analysis of the resulting sliding dynamics has been developed taking into account the different loads that the VSI could supply, as linear resistive, linear reactive and nonlinear load. The expected dynamics of the system matches with the theoretical predictions developed in the design stage, corroborating the validity of the analysis.

Moreover, both controllers have been digitally implemented by a single μC , with the advantage that this entails as: flexibility, embedded system, communications capabilities, repeatability, etc. Furthermore, the Chapter has included the implementation details of each controller in a discrete-time system, which becomes a useful methodology for applying the designed SFC and SMC controllers in whatever power converter through a digital platform.

Part IV

Conclusions and Future Research.

Chapter 9

Conclusions and Future Research.

9.1 Conclusions

Nowadays, the electric power processing has become a key aspect due to its widespread use in the industry, in appliances and, increasingly, in the field of renewable energy and electrical vehicles. Therefore, to improve the features of the switched power converters, which are the most efficient option to process the electric power, is of the utmost importance. It is well known that the power converters are designed to operate with fixed switching frequency, for which its performance is optimal. The sliding mode control is a control strategy that can provide benefits to the power converters features as improved robustness or faster transient response. The most intuitive and common application of the sliding mode control comes from the substitution of the sign function by a comparator with hysteresis, leading to a bounded but variable switching frequency. This phenomena hinders the sliding mode control application in power converters. This thesis proposes a simple control solution that regulates the switching frequency of operation without degrading the performance provided by the ideal sliding mode to the power converters.

The control structure presented in this thesis adds a control loop measuring the switching period of the control action, T , and updates the hysteresis bandwidth, Δ , of the comparator implementing the sliding mode discontinuous control law. Even though the switching period regulation structure itself can not be treated as a thesis contribution, since it was already proposed in some works for hysteretic controllers. However the application of this structure to the sliding mode control, and the developed analysis about the loop stability conditions do represent a contribution to the field.

The thesis has been divided in two main parts. The first one deals with the switching period regulation structure modelling, and the analysis of its stability conditions according to different working scenarios. The second part is devoted to the application of the proposed control structure in different power converters. Therefore, it is reasonable to split the thesis contributions in two main groups.

9.1.1 Theoretical analysis of the proposed solution and study of the resulting sliding dynamics

In this first part of the thesis, the theoretical procedures applied to derive the stability conditions of the new loop and the parametric design of the switching frequency controller were addressed. Through such studies, the following results were achieved:

- The development of the models describing the behaviour of the switching frequency control loop were derived in Chapter 2. As a peculiarity of this control structure, the way to update the hysteresis bandwidth of the comparator affects the equation relating the control system input, Δ , with its output, T . The discrete-time approach, where Δ becomes a set of discrete values, and the continuous-time approach, where Δ is a function of time, have been presented in this work. In this thesis, a control structure based on an integral action has been studied for both discrete-time and continuous-time approaches. However, the models for other controllers can also be derived following analogous procedures to the ones shown in Chapter 2.
- Once the models were achieved, the stability conditions for the resulting closed-loop dynamics were provided in Chapter 2. Specifically, the stability conditions (and design guidelines) have been found for the main working scenarios of the sliding mode control, namely: the regulation case and the tracking case. In the case of the discrete-time approach in a regulation control problem, the stability conditions were derived applying the well-known Jury test. The stability conditions of the discrete-time approach in a tracking scheme were found through the inclusion of a feedforward action in the control structure, and the application of the Lyapunov discrete-time criterion. In this case, the stability conditions are sufficient but not necessary. With regard to the continuous-time approach, a linearization of the resulting nonlinear system was required, leading to a stability conditions based on ensuring the validity of the linearized system. Finally, the good performance of the developed structures were validated through a set of numerical simulations in Chapter 3. In this Chapter, the proposed approaches (the discrete-time and the continuous-time) were tested in a simple linear system under the regulation and the tracking cases. The simulation results not only provide evidences of the proper behaviour of the proposed control structure but, also, an useful guidelines of how to design the switching frequency controller.
- The last contribution achieved, from a theoretical point view, was the analysis of how the new control loop affects to the real sliding motion, which was developed in Chapter 4. Firstly, it was demonstrated that if a piecewise linear switching function confined in a symmetric boundary layer, Δ , becomes T -periodic, the mean values in T of the real and the ideal sliding motion converge both to zero. Therefore, the piecewise linear characteristic of the switching function not only supports the validity of the thesis development but also provides a real sliding mode matching, in average, the ideal one in steady-state. This case can be fully applied to the

regulation case, where the switching function becomes T -periodic and the hysteresis value is constant in steady-state. The aforementioned T -periodicity does not occur neither in the tracking case nor in transients and, as a consequence, the averaged real sliding mode differs from the ideal one. However, the Chapter gave some guidelines for the switching frequency controller design such that its influence in the real sliding mode can be neglected.

9.1.2 Application of the proposed solution to power converters.

The second part of the thesis deals with the application and experimental evaluation of the developed control structures in several converter prototypes. Despite of the experimental evaluation itself, during the procedures required to carry out such tasks, additional contributions, related to implementation issues were also achieved. The power converters employed, and the approaches applied to each case, were designed with the aim of covering all the cases analysed in the theoretical part:

- The discrete-time approach in a regulation control case was experimentally tested in Chapter 5, where an output voltage regulation in a Buck converter was performed with good results, showing robustness and switching frequency regulation. This converter is characterized by a linear state space equation with a discontinuity produced by the control action in the right-hand side. The Buck converter is, surely, the most popular power conversion topology.
- A multiphase Buck structure with interleaving operation was presented in Chapter 6 in a regulation control problem. In this case, the continuous-time approach for the switching frequency regulator was chosen. With this converter, the switching frequency control is applied to a multi input structure, which is becoming increasingly popular due to its good efficiency. The built system achieved very good levels of efficiency, robustness and, as expected, steady-state fixed switching frequency.
- The popular Boost converter, with a well-known nonlinear characteristic, has been also tested in this thesis, controlling its output voltage to a desired constant value, entailing a regulation case. For this application, described in Chapter 7, the continuous-time approach was used. The importance of the good results obtained in this experimental part is not only related to the proper operation of the technique but also to confirm that the proposed solution can be used in both linear and nonlinear systems.
- A tracking control problem is proposed in Chapter 8, using for such purpose a voltage source inverter (VSI), which is the most employed DC/AC converter. The results obtained in the laboratory validated the feedforward action proposed for the tracking cases. Additionally, the sliding mode control was designed such that different type of loads can be connected to the converter without a lack of stability. Specifically, the sliding dynamics were analysed assuming resistive load, reactive load and nonlinear load, and the corresponding theoretical tracking errors for each scenario were also

reported. In the experimental evaluation, the overall good system performance in all the expected load cases was corroborated, including fixed switching frequency of operation in all conditions.

- The implementation approaches, the discrete-time and the continuous-time, and the sliding mode control structure, have led us to follow different strategies in the controllers implementation. In the experimentation of the Buck converter, the sliding mode controller was implemented by means of analog circuitry being, the SFC one completely digital. Otherwise, for the continuous-time approach used in the multiphase and Boost converters, both the sliding mode control and the switching frequency regulator was assembled using only analog circuitry.
- Finally, a fully digital controller implementation was used in the VSI experimentation. Included in Chapter 8, the issues related to the implementation of the controllers in a digital platform were widely detailed and discussed, becoming an useful implementing guide for the application of the proposed controllers to arbitrary converters under sliding mode control and switching frequency regulation.

9.2 Future research

Through the thesis development, there were several points which represent future research topics. The open problems have been classified as follows.

9.2.1 Open problems in the theoretical part

- In the thesis, although the proposed control structures have been analysed under discrete-time and continuous-time approaches, all the studies have been developed assuming a simple integral action as switching frequency controller. As a consequence, it would be interesting to explore the resulting dynamics provided by different controllers.
- As regards to the continuous-time approach, the thesis only analysed the regulation control task, remaining pending the tracking case. It should be noticed that in the continuous-time approach, the resulting model was nonlinear, which implied a more difficult analysis, even, in the regulation control problem. Therefore, to find out stability conditions for a tracking case in the continuous-time approach will be an additional contribution to the work developed in this thesis.
- Another pending aspect is related with the procedure followed for deriving the stability conditions in the discrete-time approach when a tracking case is studied, where a feedforward action was proposed. As it was previously stated, the stability condition was found using a Lyapunov discrete-time criterion, being such condition sufficient but not necessary. Indeed, in both numerical simulations and experimental testing,

it was shown that the additional loop presents stable behaviour with values not fulfilling the stability criterion. Therefore, it should exist different Lyapunov function candidates providing wider range of stable values for the switching frequency control gain. An interesting topic would be to explore new Lyapunov functions yielding new (and wider) stability conditions.

- The conditions found for the tracking case were based on the employment of a feedforward action, removing the non-homogeneous part of the equation that characterizes the closed-loop dynamics. However, through the simulations one realized that in some conditions, without the inclusion of the feedforward action, the switching period error becomes really small, being negligible in practise. As a consequence, the prediction of the bounds for the switching period error for certain conditions, making unnecessary the feedforward action usage, constitutes a further research subject.
- In Chapter 4, the impact of the switching frequency controller in the real sliding dynamics was tackled. The developed analysis provided qualitative results. A procedure to quantitative analyse such dynamics variations for a specific situation would lead to a further contribution.

9.2.2 Open problems in the application part

The open problems from the application point of view are focused on the further testing of the switching frequency regulation control loop to other power converters topologies. Moreover, since the technique is not only useful for power converters, its application to another type of systems would become interesting for the applicability of the proposed solution.

Bibliography

- [1] A. Pressman, *Switching power supply design*. McGraw-Hill, Inc., 1997. 4
- [2] R. W. Erickson and D. Maksimovic, *Fundamentals of power electronics*. Springer Science & Business Media, 2007. 4, 5, 80, 127
- [3] N. Mohan and T. M. Undeland, *Power electronics: converters, applications, and design*. John Wiley & Sons, 2007. 4
- [4] K. H. Billings and T. Morey, *Switchmode power supply handbook*. McGraw-Hill, 2011. 4
- [5] B. C. Kuo, *Automatic control systems*. Prentice Hall PTR, 1987. 5
- [6] K. Ogata and Y. Yang, *Modern control engineering*. Prentice-Hall Englewood Cliffs, NJ, 1970. 5, 134
- [7] V. Utkin, J. Guldner, and J. Shi, *Sliding mode control in electro-mechanical systems*, vol. 34. CRC press, 2009. 6, 7, 8, 9, 53, 111, 147
- [8] J.-J. E. Slotine, W. Li, *et al.*, *Applied nonlinear control*, vol. 199. Prentice hall Englewood Cliffs, NJ, 1991. 6, 7
- [9] H. K. Khalil, “Nonlinear systems,” *Prentice-Hall, New Jersey*, vol. 2, no. 5, pp. 5–1, 1996. 6
- [10] V. Utkin, “Sliding mode control of DC/DC converters,” *Journal of the Franklin Institute*, vol. 350, no. 8, pp. 2146–2165, 2013. 9, 111
- [11] R. Venkataramanan, *Sliding mode control of power converters*. PhD thesis, California Institute of Technology, 1986. 9, 11
- [12] F. Bilalovic, O. Music, and A. Sabanovic, “Buck converter regulator operating in the sliding mode,” *Proceedings VII International PCI*, pp. 331–340, 1983. 9
- [13] H. Bühler, *Réglage par mode de glissement*. Presses polytechniques et universitaires romandes, 1986. 11

- [14] H. Lee, V. I. Utkin, and A. Malinin, “Chattering reduction using multiphase sliding mode control,” *International Journal of Control*, vol. 82, no. 9, pp. 1720–1737, 2009. [11, 98](#)
- [15] V. Repecho, D. Biel, and A. Arias, “Fixed switching period discrete-time sliding mode current control of a PMSM,” *IEEE Transactions on Industrial Electronics*, 2017. [12](#)
- [16] C. Chiarelli, L. Malesani, S. Pirondini, and P. Tomasin, “Single-phase, three-level, constant frequency current hysteresis control for UPS applications,” in *Fifth European Conference on Power Electronics and Applications*, pp. 180–185, 1993. [12](#)
- [17] R. Guzman, L. G. de Vicuña, J. Morales, M. Castilla, and J. Matas, “Sliding-mode control for a three-phase unity power factor rectifier operating at fixed switching frequency,” *IEEE Transactions on Power Electronics*, vol. 31, no. 1, pp. 758–769, 2016. [12](#)
- [18] D. G. Holmes, R. Davoodnezhad, and B. P. McGrath, “An improved three-phase variable-band hysteresis current regulator,” *IEEE Transactions on Power Electronics*, vol. 28, no. 1, pp. 441–450, 2013. [12](#)
- [19] L. Malesani, L. Rossetto, G. Spiazzi, and A. Zuccato, “An AC power supply with sliding-mode control,” *IEEE Industry Applications Magazine*, vol. 2, no. 5, pp. 32–38, 1996. [12](#)
- [20] P. Mattavelli, L. Rossetto, G. Spiazzi, and P. Tenti, “Sliding mode control of Sepic converters,” in *Proceedings European Space Power Conference (ESPC)*, pp. 173–178, 1993. [12](#)
- [21] J. Ruiz, S. Lorenzo, I. Lobo, and J. Amigo, “Minimal UPS structure with sliding mode control and adaptive hysteresis band,” in *16th Annual Conference of IEEE Industrial Electronics Society (IECON)*, pp. 1063–1067, 1990. [12](#)
- [22] P. Mattavelli, L. Rossetto, G. Spiazzi, and P. Tenti, “General-purpose sliding-mode controller for DC/DC converter applications,” in *24th Annual IEEE Power Electronics Specialists Conference (PESC)*, pp. 609–615, 1993. [12](#)
- [23] J. F. Silva and S. S. Paulo, “Fixed frequency sliding mode modulator for current mode PWM inverters,” in *24th Annual IEEE Power Electronics Specialists Conference (PESC)*, pp. 623–629, 1993. [12](#)
- [24] E. Fossas, R. Griñó, and D. Biel, “Quasi-sliding control based on pulse width modulation, zero averaged dynamics and the L2 norm,” *Advances in Variable Structure System, Analysis, Integration and Applications*, pp. 335–344, 2001. [13](#)

-
- [25] R. R. Ramos, D. Biel, E. Fossas, and F. Guinjoan, "A fixed-frequency quasi-sliding control algorithm: application to power inverters design by means of FPGA implementation," *IEEE Transactions on Power Electronics*, vol. 18, no. 1, pp. 344–355, 2003. 13
- [26] J. Mahdavi, A. Emadi, and H. Toliyat, "Application of state space averaging method to sliding mode control of PWM DC/DC converters," in *32th Annual Conference on Industry Applications (IAS)*, vol. 2, pp. 820–827, 1997. 15
- [27] S.-C. Tan, Y. Lai, C. K. Tse, and M. K. Cheung, "A fixed-frequency pulse width modulation based quasi-sliding-mode controller for buck converters," *IEEE Transactions on Power Electronics*, vol. 20, no. 6, pp. 1379–1392, 2005. 15
- [28] S.-C. Tan, Y.-M. Lai, and K. T. Chi, "General design issues of sliding-mode controllers in DC-DC converters," *IEEE Transactions on Industrial Electronics*, vol. 55, no. 3, pp. 1160–1174, 2008. 15
- [29] S. C. Huerta, P. Alou, O. Garcia, J. A. Oliver, R. Prieto, and J. Cobos, "Hysteretic mixed-signal controller for high-frequency DC-DC converters operating at constant switching frequency," *IEEE Transactions on Power Electronics*, vol. 27, no. 6, pp. 2690–2696, 2012. 15, 86
- [30] S. C. Huerta, P. Alou, J. A. Oliver, O. Garcia, J. A. Cobos, *et al.*, "Nonlinear control for DC-DC converters based on hysteresis of the current with a frequency loop to operate at constant frequency," *IEEE Transactions on Industrial Electronics*, vol. 58, no. 3, pp. 1036–1043, 2011. 15
- [31] W.-T. Yan, K. T. Au, C. N.-M. Ho, and H. S.-H. Chung, "Fixed-frequency boundary control of buck converter with second-order switching surface," *IEEE Transactions on Power Electronics*, vol. 24, no. 9, pp. 2193–2201, 2009. 15
- [32] M. Castilla, L. G. de Vicuna, J. M. Guerrero, J. Miret, and N. Berbel, "Simple low-cost hysteretic controller for single-phase synchronous buck converters," *IEEE transactions on Power Electronics*, vol. 22, no. 4, pp. 1232–1241, 2007. 15
- [33] H. Sira-Ramire, "Differential geometric methods in variable-structure control," *International Journal of Control*, vol. 48, no. 4, pp. 1359–1390, 1988. 25
- [34] V. Repecho, D. Biel, and E. Fossas, "Fixed switching frequency sliding mode control using a hysteresis band controller," in *13th International Workshop on Variable Structure Systems (VSS)*, pp. 1–6, 2014. 28
- [35] W. J. Rugh, *Linear system theory*, vol. 2. Prentice Hall Upper Saddle River, NJ, 1996. 32
- [36] J. G. Truxal and L. Weinberg, "Automatic feedback control system synthesis," *Physics Today*, vol. 8, p. 17, 1955. 36

- [37] V. Utkin, *Sliding modes in optimization and control problems*. Springer Verlag, New York, 1992. 53, 54, 56
- [38] J. Olm, D. Biel, V. Repecho, and Y. B. Shtessel, “On average real sliding dynamics in linear systems,” in *The 20th World Congress of the International Federation of Automatic Control, IFAC 2017, Toulouse, France*, 2017. 53, 56, 57
- [39] G. Teschl, *Ordinary differential equations and Dynamical Systems*, vol. 140 of *Graduate Studies in Mathematics*. American Mathematical Society, 2012. 57
- [40] A. D. Lewis, “A mathematical approach to classical control,” *Queens University*, 2003. 60
- [41] C. Nan, R. Ayyanar, and Y. Xi, “A 2.2 MHz active-clamp buck converter for automotive applications,” *IEEE Transactions on Power Electronics*, 2017. 80
- [42] E. Vidal-Idiarte, A. Marcos-Pastor, R. Giral, J. Calvente, and L. Martinez-Salamero, “Direct digital design of a sliding mode-based control of a PWM synchronous buck converter,” *IET Power Electronics*, vol. 10, no. 13, pp. 1714–1720, 2017. 80
- [43] S.-Y. Kim, Y.-J. Park, I. Ali, T. T. K. Nga, H.-C. Ryu, Z. H. N. Khan, S.-M. Park, Y. Pu, M. Lee, K. C. Hwang, *et al.*, “A design of a high efficiency DC-DC buck converter with two-step digital PWM and low power self tracking zero current detector for IoT applications,” *IEEE Transactions on Power Electronics*, 2017. 80
- [44] J.-I. Seo, B.-M. Lim, and S.-G. Lee, “A 96.5% efficiency current mode hysteretic buck converter with 1.2% error auto-selectable frequency locking,” *IEEE Transactions on Power Electronics*, 2017. 80
- [45] F. J. Sebastián Zúñiga, P. Fernández Miaja, F. J. Ortega González, M. Patino, and M. Rodríguez, “Design of a two-phase buck converter with fourth-order output filter for envelope amplifiers of limited bandwidth,” *IEEE Transactions on Power Electronics*, 29 (11), 2014. 80
- [46] M. Carpita and M. Marchesoni, “Experimental study of a power conditioning system using sliding mode control,” *IEEE Transactions on Power Electronics*, vol. 11, no. 5, 1996. 84, 123
- [47] O. Garcia, P. Zumel, A. De Castro, J. Cobos, *et al.*, “Automotive DC-DC bidirectional converter made with many interleaved buck stages,” *IEEE Transactions on Power Electronics*, vol. 21, no. 3, pp. 578–586, 2006. 94
- [48] O. García, A. De Castro, P. Zumelis, J. Cobos, *et al.*, “Digital-control-based solution to the effect of nonidealities of the inductors in multiphase converters,” *IEEE Transactions on Power Electronics*, vol. 22, no. 6, pp. 2155–2163, 2007. 94

- [49] A. Garcia-Bediaga, I. Villar, A. Rujas, I. Etxeberria-Otadui, and A. Rufer, “Analytical models of multiphase isolated medium-frequency DC–DC converters,” *IEEE Transactions on Power Electronics*, vol. 32, no. 4, pp. 2508–2520, 2017. 94
- [50] S. Jensen and D. Maksimovic, “Fast tracking electrosurgical generator using two-rail multiphase buck converter with GaN switches,” *IEEE Transactions on Power Electronics*, vol. 32, no. 1, pp. 634–641, 2017. 94
- [51] J. Quintero, A. Barrado, M. Sanz, C. Fernández, and P. Zumel, “Impact of linear–nonlinear control in multiphase VRM design,” *IEEE Transactions on power electronics*, vol. 26, no. 7, pp. 1826–1831, 2011. 94
- [52] R. Ramos, D. Biel, E. Fossas, and R. Griño, “Sliding mode controlled multiphase buck converter with interleaving and current equalization,” *Control Engineering Practice*, vol. 21, no. 5, pp. 737–746, 2013. 98
- [53] V. Repecho, D. Biel, R. Ramos-Lara, and P. G. Vega, “Fixed-switching frequency interleaved sliding mode eight-phase synchronous buck converter,” *IEEE Transactions on Power Electronics*, vol. 33, no. 1, pp. 676–688, 2018. 100
- [54] Y.-T. Chen, T.-M. Li, and R.-H. Liang, “A novel soft-switching interleaved coupled-inductor boost converter with only single auxiliary circuit,” *IEEE Transactions on Power Electronics*, 2017. 110
- [55] A. Leon-Masich, H. Valderrama-Blavi, J. M. Bosque-Moncusi, J. Maixe-Altes, and L. Martinez-Salamero, “Sliding-mode-control-based boost converter for high-voltage–low-power applications,” *IEEE Transactions on Industrial Electronics*, vol. 62, no. 1, pp. 229–237, 2015. 110
- [56] R. Haroun, A. El Aroudi, A. Cid-Pastor, G. Garcia, C. Olalla, and L. Martinez-Salamero, “Impedance matching in photovoltaic systems using cascaded boost converters and sliding-mode control,” *IEEE Transactions on Power Electronics*, vol. 30, no. 6, pp. 3185–3199, 2015. 110
- [57] S.-C. Tan, Y.-M. Lai, K. T. Chi, L. Martinez-Salamero, and C.-K. Wu, “A fast-response sliding-mode controller for boost-type converters with a wide range of operating conditions,” *IEEE Transactions on Industrial Electronics*, vol. 54, no. 6, pp. 3276–3286, 2007. 110
- [58] D. D. Gajski, *Principles of digital design*. Pearson, 1997. 115
- [59] L. Martinez-Salamero, G. Garcia, M. Orellana, C. Lahore, and B. Estibals, “Start-up control and voltage regulation in a boost converter under sliding-mode operation,” *IEEE Transactions on Industrial Electronics*, vol. 60, no. 10, pp. 4637–4649, 2013. 115

- [60] D. G. Holmes and T. A. Lipo, *Pulse width modulation for power converters: principles and practice*, vol. 18. John Wiley & Sons, 2003. 122
- [61] S. Yin, Y. Liu, Y. Liu, K. Tseng, J. Pou, and R. Simanjorang, “Comparison of SiC voltage source inverters using synchronous rectification and freewheeling diode,” *IEEE Transactions on Industrial Electronics*, 2017. 122
- [62] S. Jayalath and M. Hanif, “Generalized LCL-filter design algorithm for grid-connected voltage-source inverter,” *IEEE Transactions on Industrial Electronics*, vol. 64, no. 3, pp. 1905–1915, 2017. 122
- [63] J. Chavarria, D. Biel, F. Guinjoan, C. Meza, and J. J. Negroni, “Energy-balance control of PV cascaded multilevel grid-connected inverters under level-shifted and phase-shifted PWMs,” *IEEE Transactions on Industrial Electronics*, vol. 60, no. 1, pp. 98–111, 2013. 122
- [64] G. Shen, D. Xu, L. Cao, and X. Zhu, “An improved control strategy for grid-connected voltage source inverters with an LCL filter,” *IEEE Transactions on Power Electronics*, vol. 23, no. 4, pp. 1899–1906, 2008. 122
- [65] A. García-Cerrada, P. Roncero-Sanchez, P. García-González, and V. Feliú-Batlle, “Detailed analysis of closed-loop control of output-voltage harmonics in voltage-source inverters,” *IEE Proceedings-Electric Power Applications*, vol. 151, no. 6, pp. 734–743, 2004. 122
- [66] B. Wu and M. Narimani, *High-power converters and AC drives*. John Wiley & Sons, 2017. 122
- [67] W. H. Kim and H. E. Meadows, *Modern network analysis*. Wiley, 1971. 131, 132
- [68] B. D. Anderson and S. Vongpanitlerd, *Network analysis and synthesis: a modern systems theory approach*. Courier Corporation, 2013. 131
- [69] F. Kuo, *Network analysis and synthesis*. John Wiley & Sons, 2006. 134
- [70] “F28377s overview.” <http://www.ti.com/tool/LAUNCHXL-F28377S>, 2015. Accessed: 2017-12-13. 149

